Development of combinatorial methods to tailor electrical and mechanical properties of Cu-based thin-film structures

Dissertation
zur
Erlangung des Grades
Doktor-Ingenieur

der
Fakultät für Maschinenbau
der Ruhr-Universität Bochum

von

Tobias Oellers

Aus Dortmund

Bochum 2022

Dissertation eingereicht am: 25.02.2022

Tag der mündlichen Prüfung: 27.04.2022

Erstgutachter: Prof. Dr. Alfred Ludwig

Zweitgutachter: Prof. Dr. Gerhard Dehm

Acknowledgements

I want to extend my thanks and gratitude to the many people who contributed to the making of this work and supported me throughout the last years. Firstly, I want to express my gratitude to Prof. Dr. Alfred Ludwig for giving me the possibility to make this thesis. I am thankful for the continuous support and guidance without which this work would not have been possible. I also want to thank Prof. Dr. Gerhard Dehm for his guidance as my second supervisor.

I also want to give big thanks to my close collaboration partner Dr. Viswanadh Gowtham Arigela for his great effort in developing his testing device which was essential for this work and the amazing teamwork he made possible. Further I want to thank Prof. Dr. Christoph Kirchlechner, Dr. Janine Pfetzing-Micklich, Dr. Jiwon Jeong, Dr. Nadine Ziegler, Dr. Dennis Naujoks, Dr. Nicolas Peter, Steffen Salomon, and Matthias Wambach who all contributed to this thesis through assistance with analysis, technical discussion or through inspiration of new ideas

Lastly, I want to thank my family for their continuous patience and never-ending support which kept me going throughout the years.

Kurzfassung

Kombinatorische Materialuntersuchungen haben das Potential die Erforschung neuer und verbesserter Materialien mittels Hochdurchsatzsynthese und -analyse von Materialproben signifikant zu beschleunigen. Besonders für die Durchführung von Hochdurchsatzuntersuchungen wird allerdings der Einsatz spezieller Untersuchungsmethoden benötigt, welche auf schnelle Probenherstellung, kurze Analysezeiten und Automatisierung optimiert sind. Kern dieser Arbeit ist die Entwicklung neuer Methoden für die Herstellung von Dünnschichtstrukturen welche die korrelative Hochdurchsatzuntersuchung mechanischer, elektrischer und mikrostruktureller Eigenschaften für die Erforschung und Optimierung leitfähiger Materialien in elektronischen Systemen ermöglichen. Ein Fokus ist dafür die Entwicklung eines neuartigen Prozesses für die Fertigung von Zugproben mit mikroskaligen Abmessungen bei gleichzeitiger Kompatibilität mit der kombinatorischen Herstellung von Materialbibliotheken. Im Rahmen dieser Arbeit wurden verschiedene Fertigungskonzepte und -iterationen entwickelt, welche auf der Fertigung von strukturierten Dünnschicht-Materialbibliotheken mittels Photolithographie basieren. Für eine erste Validierung der Funktionalität wurden Zugproben aus Cu-Schichten hergestellt und analysiert. In einer zweiten Stufe wurde die Kompatibilität der entwickelten Prozesse mit kombinatorischen Fertigungs- und Analysemethoden evaluiert. Für die Evaluierung wurden Materialbibliotheken mit binären, Cu-basierten Legierungen Cu-Ag und Cu-Zr hergestellt und untersucht. Cu-Ag zeigte gute elektrischen Eigenschaften (bis zu 94 % „International Annealed Copper Standard" im geglühten Zustand), eine signifikante Verbesserung der mechanischen Eigenschaften bei Raumtemperatur (Härte bis zu 2 GPa und Zugfestigkeit bis zu 900 MPa im geglühten Zustand) und eine geringfügige Verbesserung der mechanischen Eigenschaften bei erhöhten Temperaturen (Zugfestigkeit > 70 MPa bei 400 °C) im Vergleich zu Cu. Cu-Zr zeigte dagegen eine deutliche Verschlechterung der elektrischen Eigenschaften (bis zu 44 % „International Annealed Copper Standard" im geglühten Zustand) und eine signifikante Verbesserung der mechanischen Eigenschaften bei Raumtemperatur (Härte bis zu 3.2 GPa und Zugfestigkeit bis zu 1350 MPa im geglühten Zustand) und erhöhten Temperaturen (Zugfestigkeit > 700 MPa). Für alle Materialien wurden ergänzend weiterführende mikrostrukturelle Untersuchungen für eine Diskussion der zugrundeliegenden Einflüsse auf die funktionellen Eigenschaften durchgeführt.

Abstract

Combinatorial investigations of materials have the potential to significantly accelerate the exploration of novel and improved materials through the application of high-throughput synthesis und -analysis. But especially the execution of high-throughput investigations requires the use of specific investigation methods, optimized for rapid sample synthesis, short analysis times and automation. This study is dedicated to the development of methods for fabrication of thin-film structures that can be utilized for the correlative high-throughput characterization of mechanical, electrical, and microstructural properties for the exploration and optimization of conductor materials in electronic devices. A focus was the development of a novel fabrication process for micro-scale thin-film tensile-test structures, compatible with the synthesis of combinatorial materials libraries. Within this work multiple fabrication concepts and iterations were developed, based on the fabrication of thin-film material-libraries through photolithography. Initial investigations were performed with Cu for validation of the functionality of the developed materials libraries. For evaluation of the applicability to combinatorial processes, binary Cu-based alloys Cu-Ag and Cu-Zr were utilized. Materials libraries were subsequently fabricated and evaluated. Cu-Ag showed high retention of electrical conductivity (up to 94 % „International Annealed Copper Standard" in the annealed state), with significant improvement of mechanical properties at room temperature (hardness up to 2 GPa and ultimate tensile strength up to 900 MPa in the annealed state), and a small improvement at elevated temperatures (ultimate tensile strength > 70 MPa at 400 °C), in comparison to Cu. Cu-Zr, in comparison, showed only intermediate electrical conductivity (up to 44 % „International Annealed Copper Standard" in the annealed state) with significant improvement of mechanical properties at room temperature (hardness up to 3.2 GPa and ultimate tensile strength up to 1350 MPa in the annealed state) and at elevated temperatures (ultimate tensile strength > 700 MPa). Microstructural investigations were performed for discussion of the different contributions to the functional properties.

List of abbreviations

BHF	Buffered hydrofluoric acid
BS	Backside
BSED	Backscatter electron detector
CSM	Continuous stiffness measurement
DRIE	Deep reactive ion etching
EBSD	Electron backscatter diffraction
EDS	Energy dispersive X-ray spectroscopy
FS	Frontside
GS	Grain size
HAADF	High angle annular darkfield
MA	Measurement area
MEMS	Micro-electro-mechanical-systems
ML	Materials library
MS	Maximum stress
NEMS	Nano-electro-mechanical-systems
PVD	Physical vapor deposition
RIE	Reactive ion etching
SED	Secondary electron detector
SEM	Scanning electron microscope
TEM	Transmission electron microscopy
UV	Ultraviolet
XRD	X-ray diffraction

This work was performed with collaborations from Dr. Viswanadh Gowtham Arigela from the "Max Plank Institut für Eisenforschung" (MPIE), Düsseldorf and his contributions are duly acknowledged throughout this thesis in all the associated chapters. The individual contributions in the corresponding chapters involving collaborations are listed below.

Chapter	Contribution
2.7	FIB milling was performed by Nadine Ziegler (Ruhr-Universität Bochum).
3.1	T. Oellers did the sample fabrication. T. Oellers and Dr. V. G. Arigela performed the experiments for the optimization of the design jointly. T. Oellers did the microstructural, and electrical characterization and Dr. V. G. Arigela performed the tensile experiment and analysis. T. Oellers did fractography of the samples. Hardness measurements were performed by Dr. Janine Pfetzing-Micklich (Ruhr-Universität Bochum). XPS measurements were performed by Dr. Dennis Naujoks (Ruhr-Universität Bochum).
3.2	T. Oellers did the sample fabrication. Dr. Jiwon Jeong (MPIE) and Nicolas Peter (MPIE) performed TEM analysis. T. Oellers did the microstructure characterization by SEM and EBSD. Dr. V. G. Arigela performed tensile experiments at room temperature and at 400 °C. T. Oellers did fractography of the samples. Hardness measurements were performed by Dr. Janine Pfetzing-Micklich (Ruhr-Universität Bochum). XRD measurements were performed by Steffen Salomon (Ruhr-Universität Bochum).
3.3	T. Oellers did the sample fabrication. Dr. Jiwon Jeong (MPIE) performed TEM analysis. T. Oellers did the microstructure characterization by SEM and EBSD. Dr. V. G. Arigela performed tensile experiments at room temperature and at 400 °C. T. Oellers did fractography of the samples. Hardness measurements were performed by Dr. Janine Pfetzing-Micklich (Ruhr-Universität Bochum).

Table of contents

1 Introduction

Ever since their inception, the research areas of micro- and nanoelectronics systems, as well as microelectromechanical and nanoelectromechanical system (MEMS / NEMS) experienced continuous advancements to realize devices that delivered ever increasing performance at constant size, or similar performance at smaller device dimensions. This trend is best observed in the development of integrated circuit devices for which the engineer Gordon Moore in 1965 predicted that the density of transistors in an integrated circuit will double every year over the next ten years. Though the timeframe for each doubling proved to be closer to 20 months, the prediction still holds true today, more than 50 years later, and is famously known as Moores´s law [1]. Maintaining such rapid progress requires constant research and progress in many interconnected fields with especially, the introduction of novel technologies and materials, as well as the research in improving the understanding of underlying characteristics and properties of the technologies that are utilized.

In the context of micro- and nanoelectronics systems, as well as MEMS and NEMS, the further miniaturization of materials and structures and the development of functional materials is of particular importance. There are numerous reasons for the miniaturizations of devices, such as the obvious realization of smaller device dimensions for easier transportation, easier integration into other products, minimizing resource requirements and costs for fabrication, or lower power consumption [2]. This ultimately allows us to make devices with complex functionalities such as smartphones, lab-on-chip medical tests, or light emitting diode technology available to everyday consumers at affordable prices. While miniaturization plays a critical role in making such devices readily available and affordable, it is also the development of functional materials that enables the integration of functions and improvement of performance in small scale devices. Functional materials can for example act as transducers to convert one form of energy (e.g. thermal, mechanical, electrical, magnetic, chemical and radiant energy) into another [3,4] to enable sensor/actuator functions, or to improve characteristics such as e.g. electrical/thermal conductance to improve device performance and reliability. But the integration of materials in small scale devices can be challenging, as material behavior can change significantly at smaller dimension in comparison to bulk materials at the macro-scale. These behaviors are often described as scaling effects and encompasses multiple properties such as size-dependent mechanical behavior with typically increasing strength at smaller

dimensions ([5–11]). Therefore, it is required to investigate properties on a length scale which is representative of the system where the material is applied.

To facilitate these challenges, it is required to have investigation tools and concepts available that allow us to determine properties at the relevant scale in an effective manner. Effective investigations are increasingly more important today as functional materials in general are becoming increasingly more complex with regards to their elemental and microstructural composition such as multinary shape-memory alloys [12,13], high-entropy alloys [14,15] or photovoltaic materials [16,17]. Screening for the desired functional properties over the available compositional, or microstructural space of such complex materials by serial sample synthesis and investigation requires considerable time. To accelerate this process the field of combinatorial science, which focuses on the concept of rapid and often automated synthesis and characterization of materials libraries (MLs), can be applied. Such libraries can encompass e.g., the entire compositional space of a multinary material. With high-throughput investigations it is possible to significantly reduce both time, and cost of developments. However, for the successful application of combinatorial investigations suitable high-throughput fabrication and characterization techniques must be available [18–21].

In the field of materials science, a prominent combinatorial concept is the fabrication of thin-film MLs using physical vapor deposition. This approach is very appealing for materials research targeted at small-scale applications, as the utilized thin-film synthesis technologies are widely used for the fabrication of micro- and nanoelectronics systems as well as MEMS and NEMS. But the concept is also widely applied to materials that are used outside of these fields. A wide range of characterization methods have already been adapted for high-throughput analysis such as thin-film thickness, elemental composition, or functional property characterization (e.g., mechanical [22,23], microstructural [24], electrical [25], magnetic [26], optical [27] properties). Despite this broad range, there are still many properties that cannot be characterized effectively in high-throughput such as mechanical properties through tensile testing, which are typically characterized in high-throughput by nanoindentation experiments. While nanoindentation is routinely used to measure properties such as hardness or Young´s modulus, it is much more difficult to characterize mechanical behavior with regards to plastic deformation or fracture mechanics. Both characteristics are important for all devices that operate under mechanical strain or are subject to mechanical failure and their understanding plays a vital role in improving the reliability of devices. The main limitation for high-throughput tensile testing is the fabrication of test specimens which requires a high amount of machining and the fabrication of precise geometries.

To overcome these limitations, this work was dedicated to the development of methods for fabrication of thin-film structures which can be utilized in MLs for mechanical characterization through tensile testing and corelative MLs for the characterization of electrical, and microstructural properties. The developed methods were applied for the exploration and optimization of conductor materials in electronic devices. Multiple fabrication concepts were explored including development, prototype testing and assessment of the different approaches. The most promising concept was further applied to model systems to investigate the reliability of the tensile tests, the applicability to combinatorial investigations, and to determine the need for further improvements to the tensile structure fabrication processes.

1.1 High-throughput investigation of thin film mechanical properties – requirements and challenges

The understanding of mechanical properties of materials is important for many applications as improved mechanical behavior can play a significant role in achieving higher performance and lifetime of devices. While mechanical testing methods are well established on various length-scales, they are typically focused on facilitating detailed investigations at a low throughput. On the other hand, rapid investigation approaches such as combinatorial materials science are becoming increasingly important to face the challenges for investigating increasingly complex materials over significant compositional and microstructural spaces efficiently and for the generation of experimental datasets that can be utilized for machine learning and data driven developments [28]. Of special interest for high-throughput investigations are thin-film-based techniques, as the rapid fabrication of thin-film MLs is well established. But as the geometrical scale of thin films is typically on the micro- or nanoscale for film thickness, the investigation of mechanical properties requires techniques that are capable of probing material volumes or structures on the appropriate length-scale. Micro-scale investigations are typically performed by nanoindentation ([29,30]), or alternatively with defined sample geometries by pillar-compression ([6,31,32]), bending-cantilever ([6,33,34]) and tensile test experiments ([34–37]). In practice, experimental methods for high-throughput testing are typically selected under consideration of cost and time required for execution, as well as the actual mechanical property of interest. Time, due to the necessary processing speed to make high-throughput investigations time efficient and costs, as investigations are typically executed under a restricted budget. In practice, an additional limitation for execution is fabrication

requirements, as characterization on the micro-scale has high demands towards the geometrical accuracy of fabricated thin films and the subsequently machined test geometries. The fabricated dimensions of the structures must conform closely to predetermined target dimensions and process execution must be reproducible and automated for entire MLs. Beyond fabrication aspects, high-throughput micro-scale testing also imposes high requirements on the execution of measurements with regards to automation and actuation. To characterize MLs, the high quantity of measurement areas (MAs) requires automation to make investigations time efficient. As such, positioning, actuation of the measurement systems must be executed with repeatable precision and conformity to ensure artifact free and repeatable results.

1.2 State of the art in microscale and high-throughput tensile testing

One of the most common techniques for high-throughput and small-scale investigations of mechanical properties is nanoindentation by indenting a material surface with a geometrically standardized tip. Properties are determined by characterizing the interdependent relation of indentation depth and force. With the resulting indentation depth over indentation force data and the indent topography, characterization of properties such as e.g., hardness and Young´s modulus, or elastic and plastic mechanical behavior is possible [38]. Nanoindentation is often utilized for high-throughput characterizations, because commercial setups that allow for fully automated measurements and range of motion to investigate MLs are available. Further, nanoindentation is versatile with regards to processable samples with applicability to thin film and bulk materials, as well as microscale geometries such as pillars and bending beams. As a limitation, nanoindentation has high demands towards low roughness of the indented surface, as the indentation depth is typically in the order of tens to hundreds of nanometers, which is in a similar order as the roughness of as-fabricated material surfaces before further polishing. A too high roughness can result in high measurement inaccuracies. This makes prior surface treatment or selection of synthesis techniques and processing parameters which yield low surface roughness mandatory for nanoindentation.

Alternatively, high-throughput investigations on the micro-scale can also be executed by tensile testing. Tensile testing is commonly used for low-throughput mechanical testing with microstructures that are fabricated from bulk or thin-film materials by focused ion beam (FIB) milling, or other subtractive processing methods. FIB milling is utilized frequently, because it

allows very flexible fabrication of complex 3-dimensional structures with high accuracy to accommodate for different test structure geometries and preexisting fixture geometries. But FIB milling is not well suited for high-throughput fabrication, because sequential removal of material by sputtering with the focused ion beam, fabrication of a tensile structure geometry and structure release for manipulation during testing requires the removal of high material volumes which requires high processing time. Subsequently, the number of samples that can be fabricated and tested for individual studies with this approach is limited. This is especially relevant for combinatorial approaches, where MLs with well-defined gradients are fabricated rapidly in high-throughput processes.
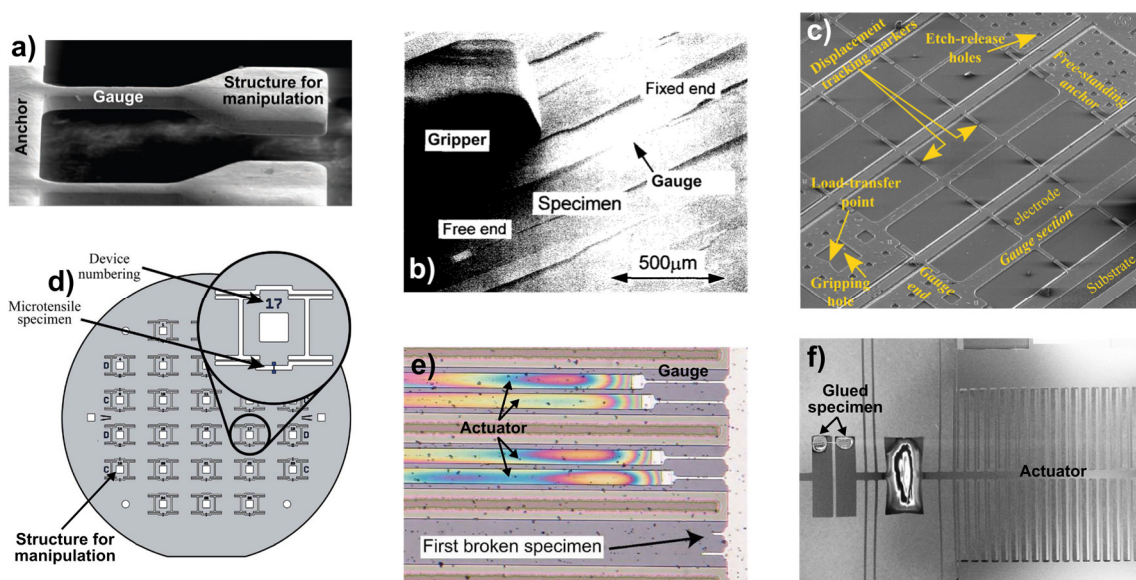
Fig. 1: Overview of different concepts for high-throughput tensile-structure fabrication and testing. [After 39–44]

Examples for rapid tensile-structure fabrication typically utilize thin-film, wafer-based fabrication techniques derived from semiconductor fabrication. These techniques are capable of parallel fabrication over full wafer substrate surfaces with subtractive and additive techniques. Approaches that can be found in literature can be divided into three categories. Firstly, tensile-test structure fabrication on the wafer substrate where the wafer is only utilized as a carrier and testing is performed in a separate setup after dicing of the wafer and actuation is performed on the thin-film structure via a gripper. Secondly, tensile-test structure fabrication on a wafer substrate and fabrication of a mechanism on the wafer that can be actuated with a separate setup without the need for dicing of the wafer. Thirdly, tensile structure fabrication on a wafer substrate and fabrication of a mechanism on the wafer with integrated actuation that does not require an external actuation setup or dicing of the wafer.

14

The work of Smolka et al. [39] is an example for the first approach where fabrication of the test material was executed by galvanic deposition and machining of the tensile-test structure by photolithography on a Si wafer substrate (Fig. 1 a)). Tensile-test structures were released from the wafer substrate by etching targeted regions of the Si substrate underneath the structure with a potassium hydroxide (KOH) wet etchant. The tensile structure material was protected from the wet etchant by a SiO$_2$ etch barrier which was removed by wet etching with a diluted hydrofluoric acid (HF) solution. After etching and final cleaning, the tensile-test structures were separated by manual breaking of the substrate for mounting in the straining device. Throughout this study Cu was utilized exclusively for fabrication of structures. Advantages of this process were the easy and inexpensive availability of most utilized processes. Wet etching and manual structure separation did not require significant investments and could easily be performed on lab scale. The main limitation was the availability of a photolithography setup in a cleanroom environment. Further, the parallel processing allowed for the fabrication of high quantity of structures in parallel (in order of hundreds), which significantly reduced fabrication time in comparison to traditional serial machining. Primary limitations for practical application to combinatorial synthesis and high-throughput characterization were the utilization of wet etching which required sufficient etch selectivity against the exposed materials, as well as the manual structure separation and handling. For combinatorial testing, the limiting step was the removal of the SiO$_2$ etch barrier, as it relied on a high etch selectivity of the barrier against the tensile-test structure material to avoid damage and subsequent influence on characterization. This limited investigations to materials inert against HF, which significantly limited the scope of materials combinations that could be applied for a combinatorial investigation. The second limitation regarded the manual handling of structures and the requirement to perform experiments in a separate, single measurement, straining device. This limited the level of automation that could be implemented for a high-throughput approach and lead to long investigation times.

Magagnose et al. [45] demonstrated a concept where structures were fabricated by femtosecond laser machining. This concept was comparable to the first category with the difference, that no wafer substrate was required. Instead, structures were machined directly from thin material foils by scanning with a focused laser source. Structures were fabricated with a "dog-bone" geometry and testing was executed with a separate straining device with integrated structure fixation. The laser-based machining provided a significant advantage, as it could be applied to process a wide range of materials. Because structures were machined from foils without a supporting substrate, structure release through etching and further

post-processing was not required. This reduced the need to consider material compatibilities within the process flow, subsequently widening the range of materials for investigation. Primary limitations for combinatorial application were structure handling after machining and characteristics of the laser processing. As tensile-test structures were fabricated individually and without additional mechanical support structures, individual manual handling was required for transfer to the straining device, as well as individual positioning, alignment, and actuation within the device. Automation of these aspects would have been challenging and served as the main bottleneck for measurement time and achievable throughput. The laser processing limited the direct applicability to MLs because process parameters would likely have required in-situ adaption for machining changing material compositions along gradients of a ML.

Two similar fabrication processes which correspond to the approach of the second category were developed by Tsuchiya et al. [40] and Bergers et al. [41] (Fig. 1 b), c)). Both processes were based on surface micromachining, where the tensile-test structures were fabricated from a material layer deposited on the surface of a Si wafer, with an additional sacrificial layer in between. Fabrication of the tensile geometry was done by lithography and etching, and structure release for testing was achieved by selective etching of the sacrificial layer. Structures were designed, that the tensile-test structures remain attached to the substrate through an anchor structure on one side and the freestanding gauge with a structure for gripping and actuation on the other side. The freestanding end of the tensile-test structures was actuated by an external device. The main difference in between both processes were the physical way of actuation, and the materials utilized for investigation and as sacrificial layer. Tsuchiya et al. utilized polycrystalline Si for investigation and SiO_2 as a sacrificial layer, whereas Bergers et al. utilized Al and $Al_{99}Cu_1$ for investigation and Si as a sacrificial layer. Both processes utilized thin films with constant elemental compositions over the substrate, because the main limiting factor for elemental variations was the necessary etch selectivity in between the material for investigation and the sacrificial material which is difficult to achieve for multiple compositions. This limited possible material combinations and subsequent applicability to combinatorial investigations.

An alternative approach of the second category was developed by Gaspar et al. [42] who utilized bulk micromachining to fabricate a straining mechanism with external mechanical actuation (Fig. 1 d)). The straining mechanism consisted of a spring suspended frame, fabricated by deep reactive ion etching (DRIE). Displacement of the tensile-test structure, fixed in between the movable frame and the wafer substrate, and measurement of the applied force were achieved with an external mechanical manipulator. As the tensile-test structures were connected to the

Si wafer substrate on both ends, the structures were protected against damage from physical shock or handling mistakes. This resulted in an improved reliability in comparison to the processes of Tsuchiya et al. [40] and Bergers et al. [41] which only feature one anchor point for the test structures. Polycrystalline Si, Si$_3$N$_4$ and Al were utilized as tensile-test structure materials in individual studies and structures were always fabricated with constant elemental compositions over the substrate. Similar to the processes of Tsuchiya et al. [40] and Bergers et al. [41], the main limit for incorporation of compositional variations was the required etch selectivity of the test materials against the utilized reactive ion etching (RIE) etching and DRIE processes. This again served as the main limitation for possible material combinations and subsequent applicability to combinatorial investigations. Throughout literature, similar fabrication processes which focused on the fabrication of a Si-based straining device with varying geometries and external actuation are available. The focus of such publications is typically on the fabrication of devices for low-throughput investigations. As the fabrication processes were typically performed on Si-wafers, an upscaling to parallel device fabrication on wafer level for high-throughput testing could be achieved for most of the available processes. But the established limitations for compatibility of subtractive Si wafer processing with deposited MLs with compositional variations remained true as the main limitation for the application to combinatorial investigations.

One approach of the third category with full integration of tensile structures and actuation mechanisms that were independent from external manipulation was presented by André et al. [46], and Fabregue et al. [47] in a preliminary version with the optimized iteration (Fig. 1 e)) presented by Gravier et al. [43]. For this process, freestanding thin-film tensile-test structures were fixed to the substrate on one side and the other end was connected to a freestanding thin-film actuator structure. The force for actuation was generated by the intrinsic stress of the material of the actuator. As the applied force was defined by the geometrical dimensions of the actuator structure, a specific actuator geometry could only generate one specific stress-strain state. To generate a full stress-strain plot, comparable to a standard tensile test, multiple structures with different actuator geometries had to be fabricated to generate the required data. For device fabrication, the tensile-test structure and actuator material were deposited by physical or chemical vapor deposition on a Si wafer and patterned by photolithography and RIE. The release step to fabricate freestanding structures was done by underetching using RIE. The process had been applied for investigation of materials such as single- and polycrystalline Si, Al, Pd and metallic glasses. Investigations were always performed with constant elemental compositions over the substrate surface. The main

limitations for incorporation of compositional variations were the required etch selectivity of the test materials against RIE and the actuation through intrinsic stress. As the etch selectivity for materials with different composition was difficult to predict and materials could be incompatible with the required etch processes, possible material combinations were limited. The actuation through intrinsic stress relied on precise process control to generate the required tensile stress and knowledge of the intrinsic stress state of the tensile-test structure material, as the net-force applied to the tensile-test structure was the result of the interplay in between the stress states of the actuator and tensile-test structure materials. This complicated the applicability to combinatorial investigations, as intrinsic stress of the tensile-structure material was likely to change along compositional gradients, influencing the applied net-force. Therefore, it would have been necessary to investigate the intrinsic stress of the tensile-structure material in a separate investigation to determine the experimental conditions for evaluation of the tensile-test experiments.

A second approach of the third category was developed by Gupta et al. [44] with integration of structure actuation and displacement/load measurements in a MEMS fabricated straining device (Fig. 1 f)). The device was fabricated by bulk micromachining from a Si wafer by photolithography with RIE and DRIE. A particularity of this approach was, that tensile structure fabrication was not integrated into the device fabrication process and structures were fabricated externally and attached to the finished straining device during post-processing. Displacement of the tensile-test structure was achieved by electrostatic actuation and measurement of the applied force with a capacitive sensor. As fabrication of the straining device and tensile-test structures were executed separately, the approach was potentially compatible with all materials. This resulted in a good compatibility with combinatorial approaches with regards to varying compositions, as process incompatibilities in between tensile-test structure and straining device fabrication were of no concern due to the external fabrication of tensile structures. The main limitation for throughput was the required time for individual, and precisely aligned fixation of the tensile-test structures before testing. Structure manipulation for fixation was performed manually with a tungsten tip and structures were glued to the device for final fixation.

As presented, many approaches were developed to engage the difficult task of high-throughput tensile testing on the micro-scale and smaller. While the described processes featured very particular differences, they could generally be divided into the three mentioned categories with common traits and similarities. In the context of high-throughput testing and combinatorial investigations, these traits determined how the different approaches performed

with respect to achievable throughput/time efficiency, material compatibility and fabrication complexity/cost. These characteristics are typically achieved as tradeoffs against each other where a focus on one of the characteristics comes to the detriment of another characteristic. Due to this interdependent relation the different categories all had their own merits, as they could provide distinct advantages for specific applications. The main tradeoffs occurred in between throughput on one side with material compatibility and fabrication complexity on the other side. An increase in throughput by higher automation and functional integration typically required more fabrication steps and more complex microfabrication processes, which in turn constricted the choice of usable materials, and further depended on the availability of specific fabrication machines.

Table 1: Qualitative comparison of different approach categories for tensile-test structure and straining device fabrication.

	Throughput and time efficiency	Material compatibility	Fabrication complexity and cost
Category 1	-	+	+
Category 2	0	0	0
Category 3	+	0	-

2 Experimental methods

2.1 Photolithography

Photolithography is an important technique for pattern transfer that is used for fabrication of thin-film structures [2]. The pattern transfer process requires multiple process steps which are based on the deposition of a photosensitive polymer on a substrate and a subsequent exposure to light radiation with a specific wavelength (e.g. UV-light with $\lambda \approx 365$ nm to 435 nm [48]), which changes the chemical behavior of the polymer. Upon exposure, solubility of the light-sensitive polymers, typically called photoresists, can be modified to be either soluble or insoluble in a chemical removal process. By applying radiation in defined areas, it is possible to fabricate geometrically defined resist patterns. Typical approaches for defined exposure are serial techniques by scanning of a focused radiation source (e.g. lasers), or parallel techniques where radiation is applied over larger areas (e.g. mercury-vapor lamps) and patterns are defined by a radiation absorbing mask in between source and resist. The mask is patterned corresponding to the desired target pattern in the resist. Resists are typically applied on substrates to transfer the fabricated resist pattern onto the substrate by subsequent application of additive/subtractive fabrication techniques.

Different resist sidewall geometries can be produced which are optimized for different pattern transfer techniques. For lift-off process used for patterning by additive processes, as illustrated in Fig. 2 a-c), the photoresist is dissolved after deposition to remove material deposited on the resist from the substrate. The resist is dissolved wet chemically in a solvent, which requires direct access to the resist by the solvent. This is achieved by fabricating an undercut which allows for access to the resist after deposition of a material. The undercut can be formed by different techniques such as multilayer resist systems [49] or depth dependent exposure [50] during patterning. The thickness of the material that can be deposited is limited by the thickness and undercut geometry of the resist, because solvent access to the resist can be blocked by uninterrupted deposition in the area of the undercut (Fig. 2 d). For subtractive techniques such as dry or wet etching, resists with vertical sidewalls are utilized to optimize accuracy of pattern transfer (Fig. 2 e)).
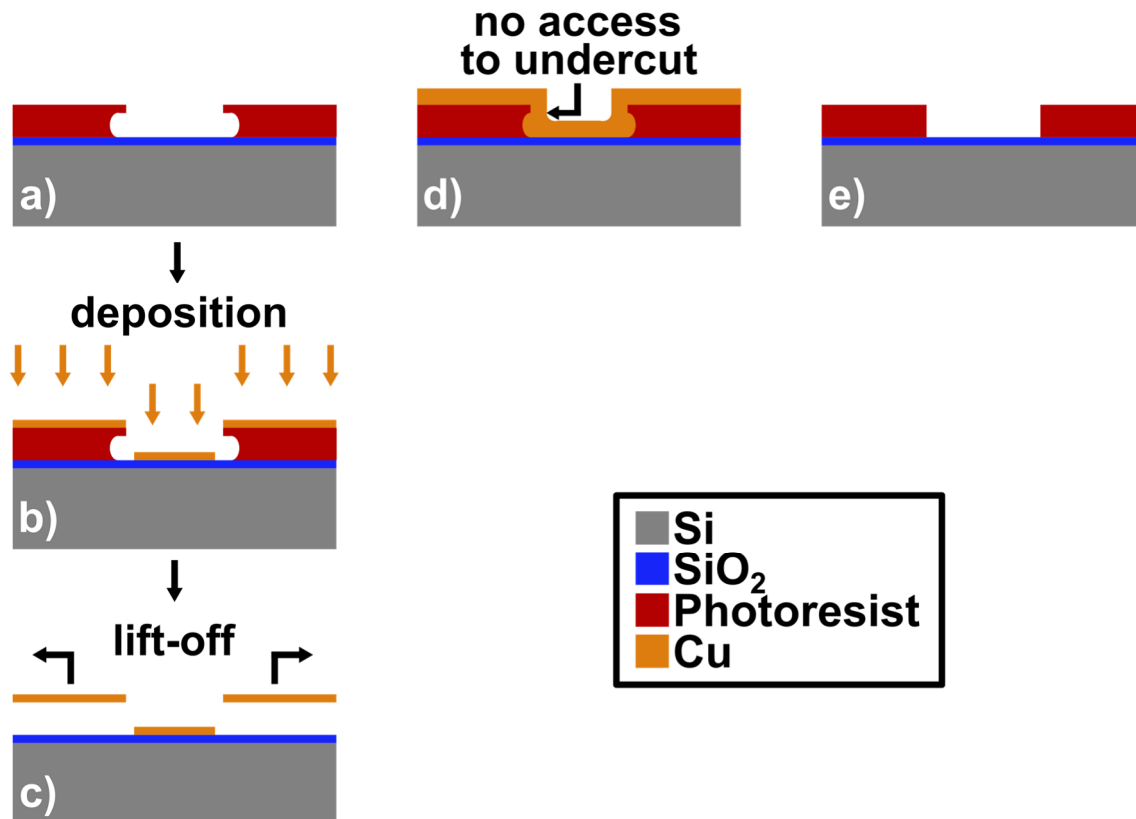
Fig. 2: Schematic of the two utilized resist profiles with (a-c) undercut resist profile required for a lift-off with the schematic lift-off process, (d) illustration of too thick deposition on a lift-off resist which blocks solvent access, (e) vertical sidewall for an accurate transfer of the mask image to the fabricated structure.

Throughout this work spin-coating was used for application of liquid photoresists on Si wafer substrates. The utilized photoresists are mentioned along the corresponding fabrication concepts. Coatings were performed on a "POLOS 200" spin-coater with manual dispense. For resist exposure, a laser lithography system (µPG 101, Heidelberg Instruments Mikrotechnik GmbH) with a laser wavelength of 405 nm and spot size of 5 µm, as well as a mask aligner system (MA6/BA6, Süss Microtec) with a 1000 W mercury vapor lamp were used. Minimum feature sizes that could be achieved were approximately 5 µm for the laser lithography system and approximately 1 µm for the mask aligner system.

2.2 Additive fabrication

Additive fabrication of metallic thin films was, within this work, executed exclusively by magnetron sputter deposition (short: magnetron sputtering). Magnetron sputtering is a thin-film deposition technique that utilizes the physical sputtering process to eject particles from a solid source material (target) which subsequently condenses on the surface of a substrate

under vacuum. Fig. 3 shows a schematic illustration of a magnetron sputter setup and process. In the most basic configuration, the target and substrate are positioned parallel to each other. Target and substrate are operated as electrodes and a high, negative potential is applied to the target. Due to the potential, ions (typically Ar ions) that are generated in between the electrodes are accelerated towards the target, bombarding its surface. High kinetic energy of the ions causes sputtering of the target material as primarily neutral atoms through physical momentum transfer. The sputtered particles move in line-of-sight direction through the plasma towards the substrate. Divergence from the line-of-sight movement can occur by scattering at gas atoms with the magnitude depending on gas pressure in the deposition chamber. [2]
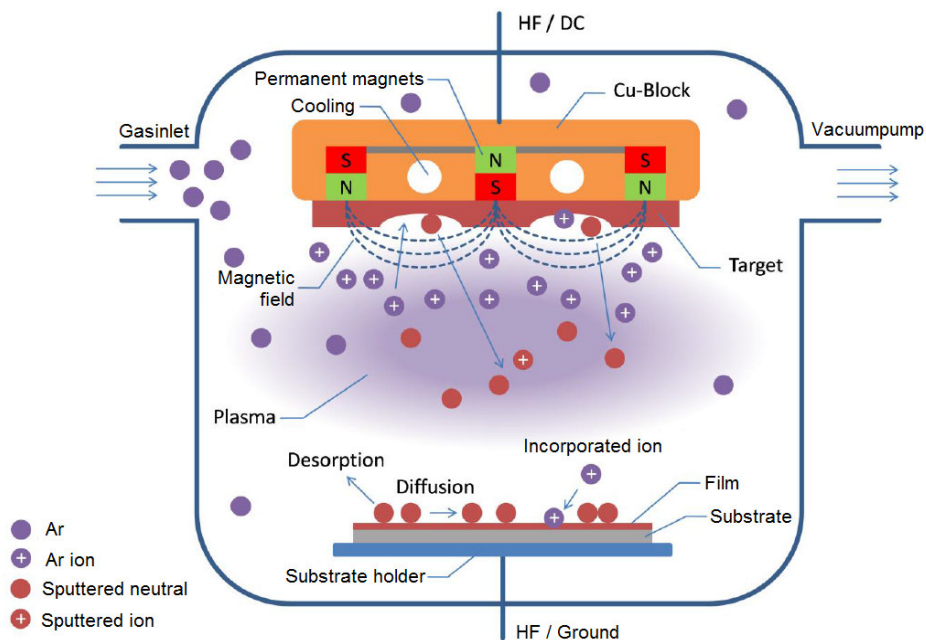
Fig. 3: Schematic illustration of a magnetron sputter system and the associated sputtering process. A basic sputtering process with a parallel target / substrate placement is shown. Ar-ions, generated in a plasma in between the target and substrate, are accelerated onto the target and sputter the material. The sputtered material moves towards the substrate and condenses on the surface. [51]

With sputtering, almost all solid materials can be deposited, since the energy of the ions sputtering the target is high in comparison to the bond strength of most materials. It is possible to deposit metallic and nonmetallic elements, alloys, ceramics, polymers, and compounds such as oxides, nitrides and carbides through reactive processing with an additional process gas [52,53]. Thin-film properties are highly dependent on process parameters, but generally follow the rule that increased energy of the sputtered species result in higher diffusion of the deposited material which increases crystallinity and phase formation. Typical process parameters for property adaption are substrate temperature, process pressure and substrate bias of which the

22

general influence on microstructure can be visualized by Thornton diagrams and extended Thornton diagrams [54–56]. The diagrams show the expected microstructure in a 2-D plot over the adapted process parameters with temperature on one axis and a second parameter on the second axis.

Throughout this work, a magnetron sputter system with a confocal target setup was used (ATC 220-V, AJA INTERNATIONAL). The system featured 4 sputter sources placed circularly around the substrate carrier with a 90° spacing in between the sources (Fig. 4). The target configuration was generally set up with two diametrically opposing sources of the same element (Fig. 4 A) to deposit a thin-film with improved thickness homogeneity without the use of substrate rotation. The other sources were used with different elemental targets to either superposition of a second element with the homogeneous coating to form a composition gradient (Fig. 4 B), or to deposit an adhesion promoting layer in between substrate and the thin-film for investigation (Fig. 4 C).
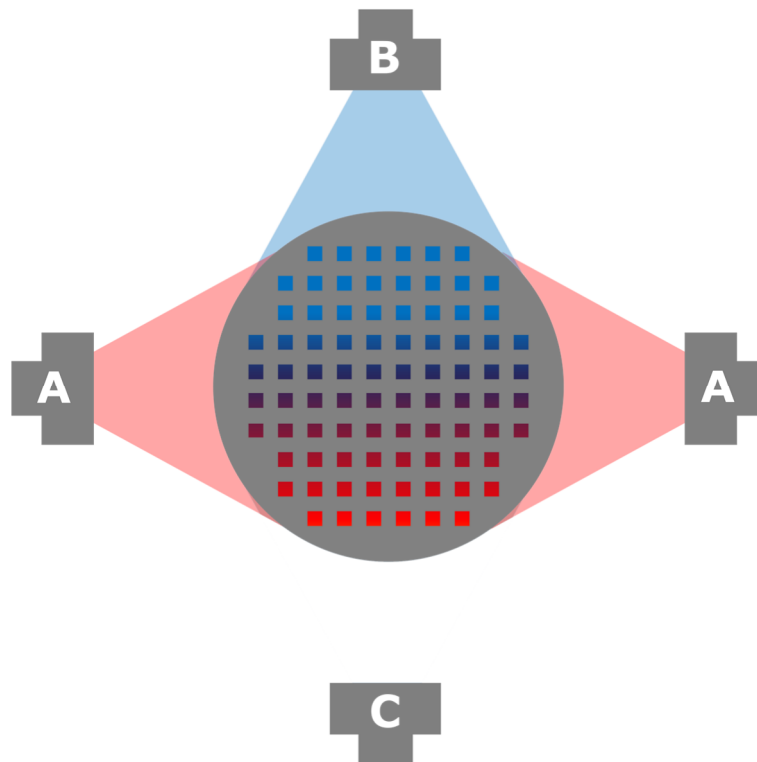
Fig. 4: Schematic illustration of the cathode and target arrangement of the utilized sputter geometry. The distribution of elements on the cathode positions is indicated for the fabrication of binary MLs with low thickness variation over the substrate. The colored squares indicate the MAs and the elemental distribution over the ML is indicated by the color gradient. Target arrangement for binary MLs consisted of two diametrically opposed targets of the same element (A) and one orthogonally positioned target of a second element (B). A fourth cathode was available for an additional element (C).

2.3 Microstructural and compositional property analysis

Scanning electron microscope (SEM) image analysis was performed on SEM images acquired by use of secondary electron detectors (SED) and backscatter electron detectors (BSED). SED image contrast is based on the sample topography which was used to investigate geometry and surface characteristics. BSED image contrast is based on elemental and microstructural characteristics and was used to investigate elemental distribution and microstructural variations. For SEM image acquisition "JEOL 5800" and "JEOL JSM-7200F" microscopes were utilized.

Quantitative compositional analysis was performed by energy dispersive X-ray spectroscopy (EDS) on a "JEOL 5800" SEM fitted with an "INCA X ACT" EDS detector. The system parameters were set to an acceleration voltage of 20 kV at a 600x magnification and a working distance of 10 mm. A Co bulk standard was used for calibration and the system had an accuracy of approximately ± 0.5 at.%. For further qualitative analysis of small features a "JEOL JSM-7200F" SEM with an "OXFORD INSTRUMENTS X-Max^n" EDS detector was utilized with an acceleration voltage of 20 kV and a working distance of 10 mm.

Depth dependent profiles of the elemental composition profiles along the thickness of the thin-films were investigated by X-ray photoelectron spectroscopy. Investigations were performed on a "KRATOS ANALYTICAL AXIS Nova" XPS system. Depth profiles were acquired in steps of sequential measurement and Ar-ion-etching. For calibration of the actual depth increments of the profile the material dependent etch rate was calibrated by measuring the time that was required to etch through a different MA with identical composition and known thin-film thickness.

Electron backscatter diffraction (EBSD) was utilized for microstructural and crystallographic investigations. For measurements, a "JEOL JSM-7200F" SEM with an "OXFORD INSTRUMENTS SYMMETRY" EBSD detector was used. EBSD measurements were performed with an acceleration voltage of 20 kV and a working distance of 15 mm.

For high resolution structural and crystallographic investigations orientation mapping analysis was carried out using a 200 kV TEM (2200FS, JEOL) equipped with ASTARTM (Nanomegas Inc.). Analyses were performed in nanobeam diffraction mode (NBD) with a beam size of 0.5 nm and a condenser aperture size of 20 μm. The scanning area was 500×500 nm^2 with a scan step size of 2 nm (250×250 pixels). Precision electron diffraction mode was applied during nanobeam scanning with the precession frequency of 100 Hz and precession angle of 0.5°. For post-processing, the orientation data was exported to the format compatible to an

orientation imaging analysis software (TSL OIM™, EDAX Inc.). The detailed data processing method is described in [57]. TEM sample preparation was done by Ar+ ions with 3 kV acceleration voltage and 6 ° inclination of the ion beam under liquid nitrogen cooling condition to obtain an electron transparent area. A final polishing was done by low energy milling with 0.5 kV acceleration voltage to remove surface damage caused by prior ion bombardment.

Additional structural investigations were performed by X-ray diffraction (XRD) for crystal structure and phase identification. For measurements, a "BRUKER D8 DISCOVER" XRD system was used in theta-two theta geometry with a Copper K-α X-ray source. The XRD system could be optionally equipped with a heating stage for in-situ investigation at elevated temperatures. For measurements at elevated temperatures the sample was placed in a heating device under vacuum with a Beryllium cover for transmission of the X-ray beam.

2.4 Geometrical property analysis

Thickness measurements were performed by tactile profilometry "Ambios XP 2" profilometer. For investigation of coating thickness, the measurements were performed on substrate-bound MAs from the top of the coating down to the substrate surface at a lithographically fabricated step.

2.5 Electrical property analysis

Electrical resistivity was obtained by sheet resistance measurements on substrate-bound MAs utilizing a custom-built 4-point probe system [58]. Measurements were performed in a series of 5 measurements per MA with a current of 50 mA. Resistivity values were calculated from the film thickness (t) and sheet resistance (R) with a correction factor (C') of 4.0653 [59] according to the following formula [60]:

$$\rho = C'Rt \qquad (1)$$

The correction factor considers the thickness and in-plane geometry of the investigated MAs. In the context of this work, film thickness was < 5 μm with a square in-plane geometry with edge length of 4.5 mm.

2.6 Mechanical property analysis

Mechanical properties were investigated by two different techniques with nanoindentation on substrate-bound and tensile testing on tensile-test structure MLs. Indentation was performed with an MTS Nanoindenter XP equipped with a diamond Berkovich indenter. Measurements were performed with a standard CSM (continuous stiffness measurement) method (45 Hz, 2 nm harmonic displacement) with an indentation depth of 200 nm. Tensile experiments were performed with a custom build straining device at room temperature (RT) and at elevated temperatures of 400 °C. Details about the setup and execution of tensile experiments can be found in [61,62].

2.7 Tensile-test structure fabrication

2.7.1 Requirements

A primary objective of this study was to develop processes for the fabrication of MLs with specific and well-defined MA geometries to enable characterization of the required properties. The main properties of interest for characterization were mechanical properties investigated through tensile-testing, and electrical resistivity/conductivity through 4-point sheet resistivity measurements. In addition, the ML design also had to allow for the investigation of supplementary properties such as MA geometry (in-plane and thickness), chemical composition and microstructure. Main requirements for the fabrication process were compatibility with thin-film synthesis by sputtering on wafer substrates, parallel processing for rapid ML fabrication and the possibility to perform heat treatments during post processing.

As the tensile tests required structuring of a MA and the 4-point sheet resistivity measurements were best performed on structures with a regular and uninterrupted geometry (see section 2.5) it was decided to design separate MAs that were dedicated to specific characterization techniques. Additionally, it was decided to not fabricate the different MA designs in a single ML, but to fabricate separate MLs where each individual library was dedicated to a single MA design. Fabrication of both designs on a single ML would have been possible by alternating the designs on the grid where the MAs were placed and assuming an adjacent pair of designs as a single MA. But this would have reduced compositional resolution over the library and complicated property correlation, as the two structures would have always had a difference in composition due to the gradient over the library. With two separate libraries it was possible to align the placement of the MA grids during design and fabrication to ensure identical placement and therefore identical chemical composition of the corresponding MAs on both MLs. This way MAs fabricated on different MLs were easily comparable and property correlation was possible.

2.7.2 Library design

For both ML designs the MA placement on the wafer substrate was based on a rectangular grid (4.5 mm pitch) with 15 rows and 14 columns for a total of 210 MAs. The geometry of the grid was selected to conform with preexisting measurement and analysis standards of the utilized characterization systems. The grid was adapted for binary alloy

systems, as initial case studies were intended for the investigation of binary alloys within the scope of this work. MLs of binary alloys were fabricated with the compositional gradient along a length axis of the substrate, with the aim of characterizing properties along the direction of the gradient. As the gradient was oriented along the columns of the MLs, more rows than columns of MAs were fabricated to increase the compositional range that could be investigated. Fabrication of more columns to match the number of rows was not possible, because MAs would have been placed too close to the edge of the wafer substrate which would have resulted in fabrication defects. The boundary of the grid was therefore constrained to the rectangular grid (15 rows, 14 columns) to consider the constraints of the substrate geometry (100 mm diameter Si wafer).

The MAs of MLs for electrical characterizations were designed as square thin-film structures (4 mm width/height) which were oriented in the center of the MAs (Fig. 5 a)). With a pitch of 4.5 mm, adjacent structures were separated by a gap of 0.5 mm. The gap in between the thin-film structures was fabricated to avoid cutting through the thin-film during separation of the MAs with a wafer saw, as this could have resulted in damage to the thin-film in contact with the saw blade and could have caused subsequent delamination from the substrate.
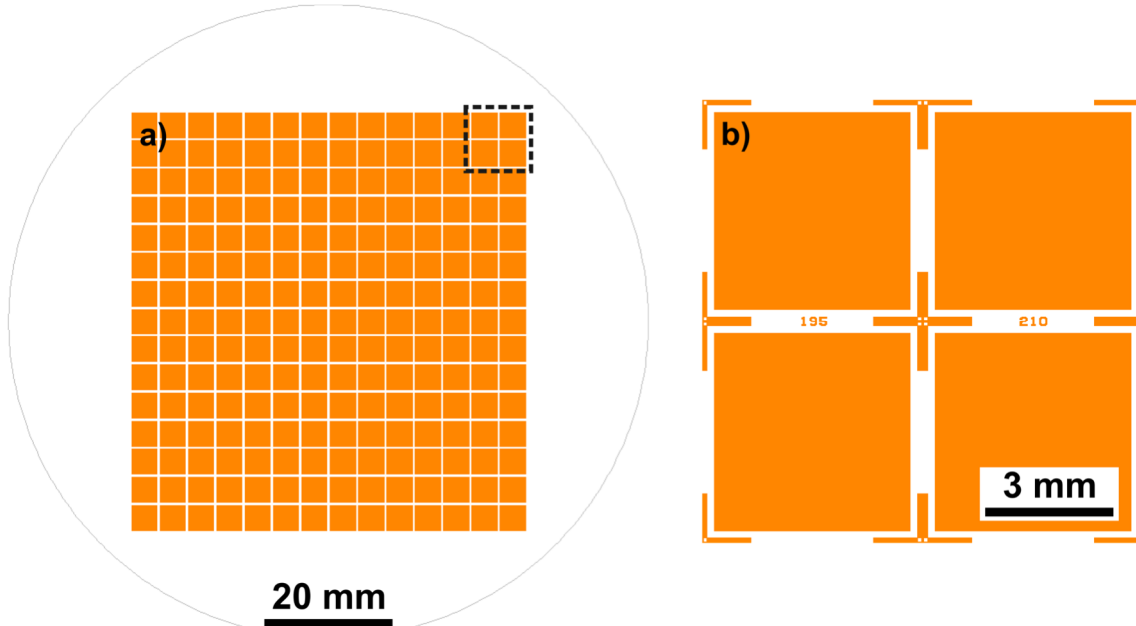
Fig. 5: Schematic illustration of (a) a ML design for substrate-bound MAs with (b) a magnified view of 4 MAs. MAs were arranged in a rectangular array with 15 rows and 14 columns. Every MA was labeled with a unique identifying number next to the rectangular structure and surrounded by cross-shaped markers for orientation.

The MAs of MLs for tensile testing required structuring of the thin film with a tensile-test structure geometry (Fig. 6 a)), followed by a structure release to fabricate

28

freestanding tensile-test structures. The planned nominal dimensions of the tensile-test structures are shown in Fig. 7 a). The main dimensions important for mechanical testing were gauge length, gauge width and film thickness (nominal values: 100 µm, 25 µm, 5 µm respectively). Corners in the transition area from the gauge to the "head" and handle structures were designed with a radius of 10 µm to reduce stress concentrations. Dimensions were selected to follow "DIN EN ISO 6892-1" for structures with rectangular cross-sections as closely as possible, following the approach by Smolka et al. [39]. The gauge length was adjusted relative to the structure thickness that could be achieved for the tested fabrication approaches. Detailed fabrication processes will be described in the following sections.

MAs were arranged on rectangular grid with identical pitch as described for substrate-bound MLs for electrical characterization and both ML types were placed with the same absolute position and orientation relative to the wafer substrate. This was done to allow for correlation of the experimental results.
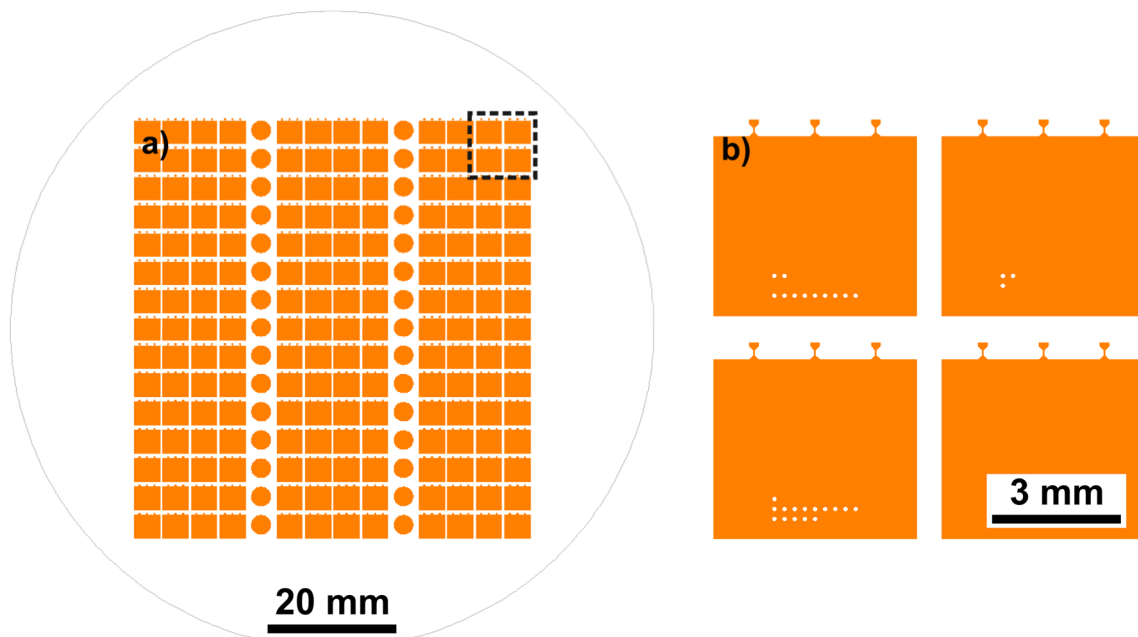
Fig. 6: Schematic illustration of (a) a ML design with MAs for tensile testing and (b) a magnified view of 4 tensile-test structure MAs. Two columns were fabricated with round discs as a pre-product for fabrication of samples for transmission electron microscopy. MAs were arranged in a rectangular array with 15 rows and 14 columns. All MAs were labeled with a unique identifying number on the structures.

For both ML types a numbering scheme was implemented where all MAs were assigned a unique number for clear identification. For substrate-bound MLs numbers were placed below the MAs (Fig. 5 b)). For tensile-test structure MLs the numbering was achieved by holes that were fabricated in the handle section instead of actual numbers (Fig. 6 b)). This approach was

selected to limit the removal of material at the handle, as the size of numbers that would have been required for unassisted identification by eye would have significantly compromised stability of the handle, freestanding after release. With the selected, hole based, numbering scheme it was possible to limit the removal of handle material and it was possible to identify the holes with less ambiguity by eye, without assistance of an optical microscope. The holes were read from bottom to top and left to right. The bottom holes were equivalent to 0 to 9 in increments of 1, the middle row 0 to 90 in increments of 10, and the top row 0 to 900 in increments of 100. For both ML types, the holes for numbering were structured during the lithography step of the structure fabrication processes.

For the planned structure design of the MAs, the actual tensile-test structures gauge where the properties were measured were offset from the center of the MA by approximately 1.7 mm, while the substrate-bound ML properties were measured at the center of the respective MAs. The offset would have resulted in a compositional deviation for the acquired properties. To minimize this error the absolute positions of the two ML types on the wafer substrates were offset by 1.7 mm during fabrication (Fig. 7 b)).

Fig. 7 Schematic illustrations of (a) the design of a tensile structure MA with the associated structure dimensions and (b) the offset in between the MA placement of tensile-test structure MLs and substrate-bound MLs for improved comparability in between tensile-tests and substrate-bound investigations.

2.7.3 Approach V1 – Structure fabrication by two-step lift-off lithography

2.7.3.1 Design

The first investigated fabrication process was based on photoresist-based lift-off lithography to pattern the tensile-test structures and wet etching to release the fabricated structures from the substrate. The overall process was adapted from Smolka et al. [39] and was altered to substitute tensile-test structure fabrication by photolithography and electrochemical deposition with lift-off lithography and PVD (magnetron sputtering).

The use of lift-off lithography and confocal sputter deposition required multiple design considerations for the overall structure geometry and fabrication process. This concerned primarily the achievable minimal structure size and cross-section geometry. The confocal deposition theoretically prevented fabrication of structures with dimensions in the same order and thicker than the thickness of the lift-off photoresist and caused geometrical artifacts at the structure edges due to deposition on the photoresist. To avoid these limitations, the fabrication concept was designed to utilize the material deposited on top of the lift-off resist for fabrication of the tensile-test structure. By deposition on the resist, the surface was fully exposed to the sputtered material flux and not constrained by the height of the resist sidewalls. This resulted in a more homogeneous deposition over the cross-section and allowed fabrication of structures with in-plane dimension smaller than the lift-off resist thickness. This approach required additional processing to connect the deposited material with the substrate by an anchor structure, as the material on top of the lift-off resist was, by design, not connected to the substrate and would have been removed during lift-off. The connection to the anchor structure had to be mechanically stable enough to withstand forces during a tensile test and had to be designed geometrically for a linear flux of force from the point where force is applied during tensile testing to the point where the force is absorbed in the anchor structure. This was important to avoid out of plane bending of the tensile-test structures upon loading (Fig. 8).
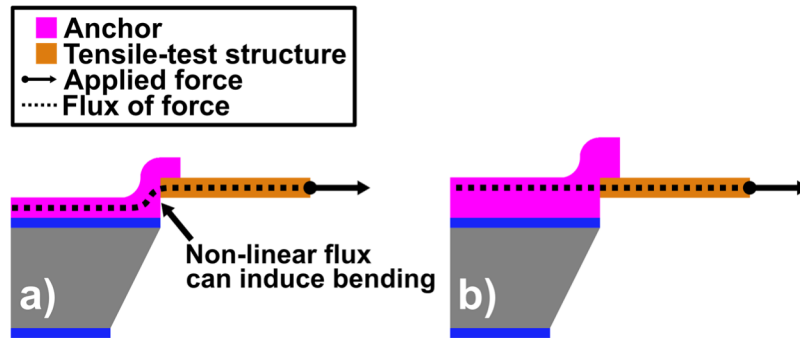
Fig. 8: Schematic illustration of the flux of force for different anchor structures. (a) A bend in between tensile-test and anchor structure results in a non-linear flux which is prone to induce bending in the structure upon loading. (b) With tensile-test and anchor structure in-line the flux is linear, and bending is avoided.

With deposition on top of the lift-off resist the setup of the fabrication process had to ensure, that the resist was fully removed during lift-off/cleaning with no residues, as it could have caused defects during annealing and testing due to contaminations. The critical step in this process was removal of resist underneath the tensile-test structure. The structure incorporated multiple features with big surface areas, which would have required long immersion for lift-off if the only access for the solvent was from the structure edges. But lift-off time had to be limited, as Cu-based materials, which were the focus of this work, were not resistant against stronger solvents (e.g.: NMP, DMSO) that were required to dissolve the lift-off resist. Therefore, the etch grooves that were fabricated during backside Si etching for release of the tensile-test structure had to be positioned to also provide direct access for the solvents to the resist from the backside of the substrate.

For this approach tensile-test structures were connected to the substrate with an anchor structure. Consequently, the MAs with the tensile-test structures had to be separated after fabrication for testing. For this, the fabrication of V-grooves for manual breaking of the substrate was incorporated during etching of the Si substrate. The MAs were placed on a rectangular grid with a pitch of 4.5 mm by 4.5 mm 15 rows and 14 columns of MAs. Two separate sets of grooves were designed, to cleave the 4.5 mm by 4.5 mm MAs in a first step, and subsequently remove the protective Si frame around the tensile-test structures in a second step.

2.7.3.2 Tensile-test structure fabrication process and material synthesis

Si wafers were used as a substrate for the fabrication process. The wafers were double side polished with orientation (100), thickness 525 μm, diameter 100 mm and were thermally oxidized with a 2.1 μm thick SiO_2 diffusion/etch barrier (Fig. 9 a)).

In a first step a positive tone resist (AZ1518, Microchemicals) was spin coated on the wafer backside (BS). The dispense was performed dynamically at a rotational speed of approximately 8.3 1/s (500 rpm) over a time of 5 s, with a final rotation speed of approximately 66.7 1/s (4000 rpm) for 30 s and an acceleration of approximately 183.3 rad/s^2 (1750 rpm/s). A softbake was performed at 100 °C for 50 s on a hotplate. Subsequently, AZ1518 was spin coated on the frontside under identical conditions. Cleanroom paper was placed in between the wafer and hotplate to prevent adhesion of the backside resist to the hot surface and prevent scratching of the resist on the metal hotplate surface. Afterwards, exposure of the backside resist was performed with a laser lithography system (μPG 101, Heidelberg Instruments Mikrotechnik GmbH) with a dose of approximately 55 mJ/cm^2. After exposure, the resist system was processed by immersion development in an aqueous-alkaline developer (AZ 726 MIF, Microchemicals) for approximately 35 s, followed by a rinsing cascade in deionized water (Fig. 9 b)). A subsequent hardbake was performed at 100 °C for 1800 s on a hotplate and the wafer was again placed on cleanroom paper. In a next step the thermally oxidized SiO_2 on the backside was selectively etched in buffered hydrofluoric acid (BHF, BOE 7:1, Microchemicals), followed by a rinsing cascade in deionized water. Etch time for the 2.1 μm thick SiO_2 was approximately 1500 s. After etching the resist on both wafer sides was removed in a cleaning cascade of acetone and isopropanol (600 s each) with ultrasonic agitation, followed by a final rinsing with isopropanol and spin drying (Fig. 9 d)).

For pattering of the tensile-test structures a bilayer of non-photosensitive lift-off photoresist (LOR 20 B, MicroChem Corp.) with a combined thickness of approximately 6.6 μm was spin coated on the frontside (FS). The two layers were deposited by two successive spin coating steps which were performed with a waiting time of 5 s in between the coatings. The individual coatings were performed with a dynamic dispense at a rotational speed of approximately 8.3 1/s (500 revolutions per minute (rpm)) over a time of 5 s, with a final rotation speed of approximately 16.7 1/s (1000 rpm) for 35 s and an acceleration of approximately 183.3 rad/s^2 (1750 rpm/s). After deposition of the bilayer a softbake was performed at 160 °C for 120 s. In the next step a positive tone photoresist (AZ1518, Microchemicals) was spin coated. The dispense was performed dynamically at a rotational speed of approximately 8.3 1/s

(500 rpm) over a time of 5 s, with a final rotation speed of approximately 66.7 1/s (4000 rpm) for 30 s and an acceleration of approximately 183.3 rad/s^2 (1750 rpm/s). The softbake was performed at 100 °C for 50 s. Exposure of the top resist was performed with a mask aligner (MA6/BA6, Süss Microtec) with a broadband UV Hg-vapor lamp with a dose of approximately 55 mJ/cm^2. The exposure mask was aligned to markings on the backside of the wafer fabricated during BHF etching. After exposure, the resist system was processed by immersion development in an aqueous-alkaline developer (AZ 726 MIF, Microchemicals) for approximately 60 s, followed by a rinsing cascade in deionized water (Fig. 9 e)). After fabrication of the resist lift-of structure the deposition of the tensile-test structure material was performed. For deposition, a magnetron sputter system with a confocal target setup was used (ATC 220-V, AJA INTERNATIONAL). The thin-film was deposited by simultaneous sputtering of two diametrically opposed Cu targets (4-inch diameter, 99.999 at.% purity). The deposition powers (direct current) for both Cu targets were adjusted for a similar sputter rate of approximately 0.18 - 0.2 nm/s. Depositions were performed at a pressure of approximately 0.666 Pa (5 mTorr) with an Ar plasma at room temperature and a base pressure < 2.7*10^{-5} Pa. Deposition time was adjusted to achieve a film thickness of up to 5 μm (Fig. 9 f)).

After deposition, a bilayer of non-photosensitive lift-off photoresist (LOR 20 B, MicroChem Corp.) with a combined thickness of approximately 8 μm was spin coated on the frontside. The two layers were separately spin coated and softbaked. The individual coatings were performed with a dynamic dispense at a rotational speed of approximately 8.3 1/s (500 revolutions per minute (rpm)) over a time of 5 s, with a final rotation speed of approximately 16.7 1/s (1000 rpm) for 35 s and an acceleration of approximately 183.3 rad/s^2 (1750 rpm/s). After deposition of the bilayer a softbake was performed at 160 °C for 120 s. In the next step a positive tone photoresist (AZ1518, Microchemicals) was spin coated. The dispense was performed dynamically at a rotational speed of approximately 8.3 1/s (500 rpm) over a time of 5 s, with a final rotation speed of approximately 66.7 1/s (4000 rpm) for 30 s and an acceleration of approximately 183.3 rad/s^2 (1750 rpm/s). The softbake was performed at 100 °C for 50 s. Exposure of the top resist was performed on a mask aligner (MA6/BA6, Süss Microtec) with a broadband UV Hg-vapor lamp with a dose of approximately 55 mJ/cm^2. The exposure mask was aligned to markings on the frontside of the wafer fabricated during the first sputter deposition. After exposure, the resist system was processed by immersion development in an aqueous-alkaline developer (AZ 726 MIF, Microchemicals) for approximately 60 s, followed by a rinsing cascade in deionized water (Fig. 9 g)). After fabrication of the resist lift-off structure the deposition of the tensile-test structure material was performed. For deposition,

a magnetron sputter system with a confocal target setup was used (ATC 220-V, AJA INTERNATIONAL). The thin-film was grown by simultaneous sputtering of two diametrically opposed Cu targets (4-inch diameter, 99.999 at.% purity). The deposition powers (direct current) for both Cu targets were adjusted for a similar sputter rate of approximately 0.18 - 0.2 nm/s. Depositions were performed at a pressure of approximately 0.666 Pa (5 mTorr) with an Ar plasma at room temperature and a base pressure $< 2.7*10^{-5}$ Pa. Deposition time was adjusted to achieve a film thickness of approximately 8 μm (Fig. 9 h)).

In a next step the wafer frontside was coated with a non-photosensitive, KOH resistant resist (AR-PC 503, Allresist) by spin-coating (Fig. 9 i)). To improve step coverage multiple dispenses were performed to cover the whole wafer surface with liquid resist before starting rotation with a final speed of approximately 66.7 1/s (4000 rpm) for 30 s and an acceleration of approximately 183.3 rad/s^2 (1750 rpm/s). A subsequent softbake was performed at 180 °C for 120 s on a hotplate. After application of the protective resist the substrate was etched from the backside with KOH (30 % wt. in H_2O) at a temperature of 70 °C. Etching was continued until the frontside SiO_2 etch barrier was reached. During etching the wafer frontside was isolated from the etchant by clamping in a protective wafer holder (Tandem series, AMMT). After etching the wafer was cleaned in a rinsing cascade with deionized water followed by spin drying (Fig. 9 j)).

In a next step the frontside SiO_2 etch barrier was etched from the backside through the opening in the Si wafer with BHF (BOE 7:1, Microchemicals) (Fig. 9 k)). The etching was followed by a rinsing cascade in deionized water. Etch time for the 2.1 μm thick SiO_2 was approximately 1500 s. After etching the resists on the wafer frontside were removed in multiple cleaning steps. Firstly, AR-PC 503 and AZ1518 were removed by immersion in acetone for a time of approximately 12 hours. Long immersion times were necessary to ensure that AZ1518 underneath the deposited Cu layers was fully dissolved. Detached Cu layers were subsequently removed to expose the underlying LOR 20 B resist. The remaining LOR 20 B was dissolved by immersion in NMP heated to 40 °C. Immersion time was limited to 1800 s to avoid damage to the Cu structures by chemical reaction with the NMP. Cleaning in NMP was followed by a cleaning cascade of acetone and isopropanol (600 s each) with manual agitation, followed by a final rinsing with isopropanol and drying in air (Fig. 9 l)).

In a last step the structures were cleaved from the Si substrate along the V-grooves fabricated during KOH etching. Grooves were indicated in Fig. 9 k) (backside) by marking B and C. Grooves B had a depth of approximately 300 μm and grooves C approximately 200 μm. Etch depths were selected to provide sufficient mechanical stability for handling and spin

coating/drying. The depth of grooves C was reduced in comparison to B to preferentially cleave the rectangular MAs while the protective frame remained around the tensile-test structure. Cleaving was performed manually and had to be performed carefully to avoid damage to the tensile-test structure. After removal of the Si frame the structures were ready for testing.
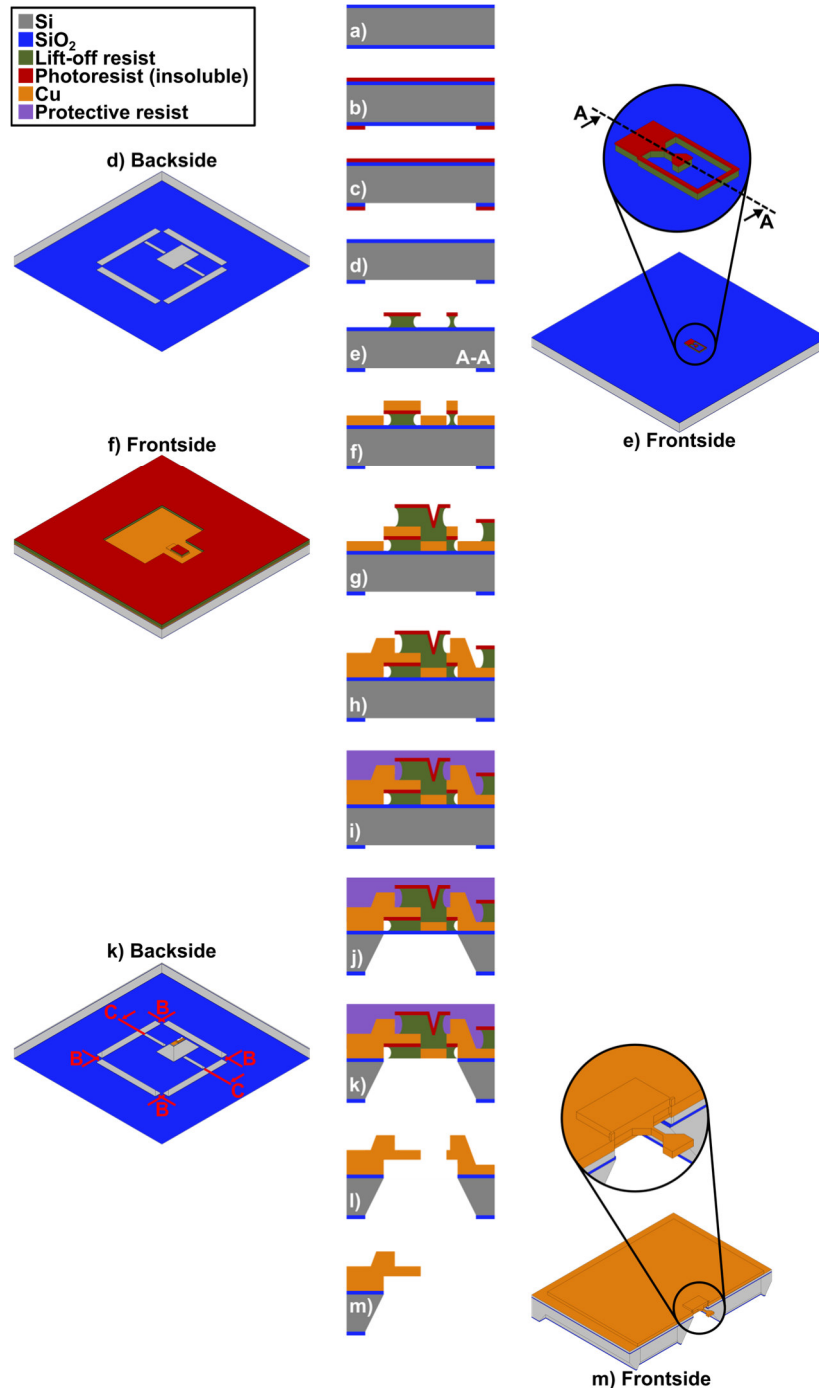
Fig. 9: Schematic process flow for fabrication approach V1 (not to scale). (a) thermally oxidized Si wafer, (b-d) BS structuring of SiO$_2$ by photolithography and BHF etching, (e) FS photolithographic structuring of lift-off resist, (f) FS Cu sputter deposition, (g) FS photolithographic structuring of lift-off resist, (h) FS Cu sputter deposition, (i) FS spin coating of KOH protective resist, (j) BS etching of Si with KOH and SiO$_2$ with BHF, (l-m) final cleaning cascade with NMP, acetone, isopropanol, and structure separation by cleaving.

36

2.7.3.3 Important design features

In the following sub-section selected features were described/reiterated with the aim to clarify their purpose within the design. The features were presented in a separate section to highlight their importance, as they were essential to the overall process.

The first feature concerns the fabrication of a "frame" around the tensile-test structure that was fabricated during deposition on top of the lift-off resist and consisted of the same material as the tensile-test structure itself (Fig. 10 a) (C)). The frame was designed to avoid damage to the tensile-test structure during cleaving of the substrate for structure release. Due to the small gap ($< 5\ \mu m$) in between the substrate-bound Cu film and the tensile-test structure that was given by the geometry of the resist, both films would have been prone to touching and subsequent bending during mechanical cleaving. To avoid this, a frame was utilized to separate the Cu layer deposited directly on the substrate surface during the first deposition (Fig. 9 f)) into two separate areas (D and E in Fig. 10 a)). The film inside the frame (Fig. 10 a) (F)) was positioned in such a way, that it remained fully disconnected from the substrate during the last lift-off/cleaning step and was washed away in the solvent without strong mechanical interaction (Fig. 9 k)). To remove the frame during final structure release, the second deposition (Fig. 9 h)) was structured to connect the frame with the substrate through a connection with a small width to reduce mechanical stability of the connecting point (Fig. 10 b) (F)). With this the frame could be removed during cleaving of the Si substrate and the Cu frame around the tensile-test structure would easily fracture.
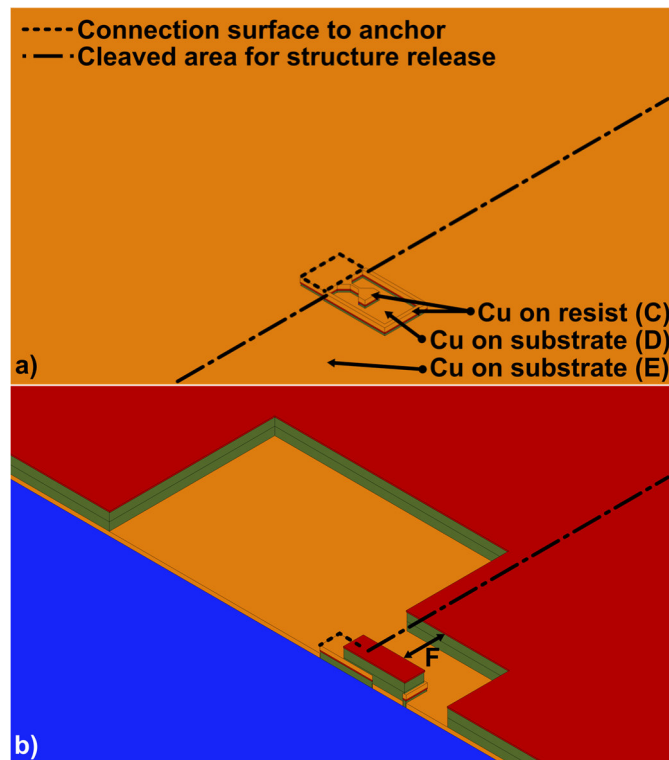
Fig. 10: Schematic illustration of intermediate steps in the process flow to illustrate the connection of the tensile structure to the substrate, as well as the fabrication and placement of design features for structure separation by cleaving (not to scale). Illustrations corresponded to fabrication steps Fig. 9 f) and Fig. 9 g) in the process flow.

The second feature concerned the etch groove to remove the Si underneath the tensile-test structure. As indicated in the design subsection, the dimensions of the groove after etching were selected to cover the tensile-test structure and the adjacent, rectangular area that connected to the anchor structure. The size was selected to improve access of the solvents to the resist during cleaning. Without access from the FS, the solvent had to penetrate elongated gaps (300 µm length with 5 µm height for the smallest tensile-test structure tested here) by diffusive transport to remove resist (Fig. 11 a)) which would have increased process time considerably. With additional access from the BS after etching (Fig. 11 b)) the resist structure was homogenously exposed to the solvent, which resulted in an accelerated removal. This design adaption was essential for the investigation of Cu-based materials which were the focus of this work because these materials were chemically not resistant against prolonged exposure to the strong required solvents such as NMP and DMSO dissolve the lift-off resist (LOR 20 B). If the process was adapted for different materials, the chemical compatibility with the solvent would need to be evaluated first to avoid chemical attack on the test material.

38
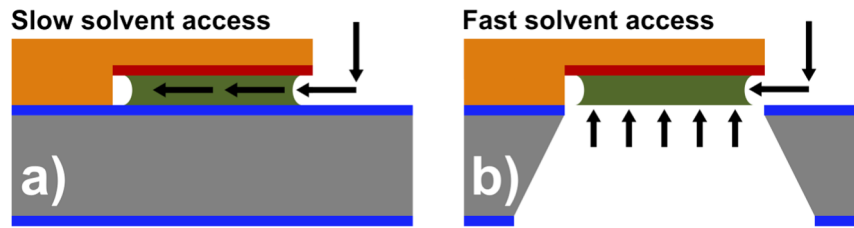
Fig. 11: Schematic illustration of different approaches for removal of the bi-layer lift-off resist for release of tensile structures in a cross-section view (not to scale) with (a) slow resist removal from the side without access from the substrate BS and (b) fast resist removal with access from the side and trough an etched opening from the BS.

A third feature was the design of the mask for etching of the V-grooves on the BS of the substrate (see Fig. 9 k)) BS, feature (B). The KOH etch mask that was fabricated in the SiO_2 layer was not one continuous opening, but instead consisted of four separated, rectangular openings. This design was selected to avoid underetching of convex corners in KOH. Had the opening been designed as one continuous mask, convex corners would have been present that would have resulted in extensive underetching of the MA and would have led to a loss of structural integrity of the Si wafer during etching. With four separate structures the etch masks consisted exclusively of concave corners which were underetched slowly according to the <111> crystal planes with no significant underetching of the MA.

2.7.3.4 Discussion

To evaluate the viability of the fabrication process, multiple wafers with tensile-test structures were fabricated. Fig. 12 shows a processed wafer from the FS after (a) the last BHF etching step (see Fig. 9 k)) before final cleaning and structure separation and (b) after a partial final cleaning (see Fig. 9 k-l)). After cleaning (Fig. 12 b)), multiple MAs with discontinuous coatings could be observed by eye, which indicated successful lift-off and removal of the substrate-bound Cu layer. But these also included MAs where also the tensile-test structures were removed. Intact structures were subsequently cleaved from the wafer and inspected. The structure yield for the shown example was low with approximately 20 % intact MAs. This was partially due to the fact, that the Si etching in KOH was stopped before all structures were fully released to avoid damage to the released structures by overetching and also due to several issues in the process that prevented repeatable and reliable structure fabrication.
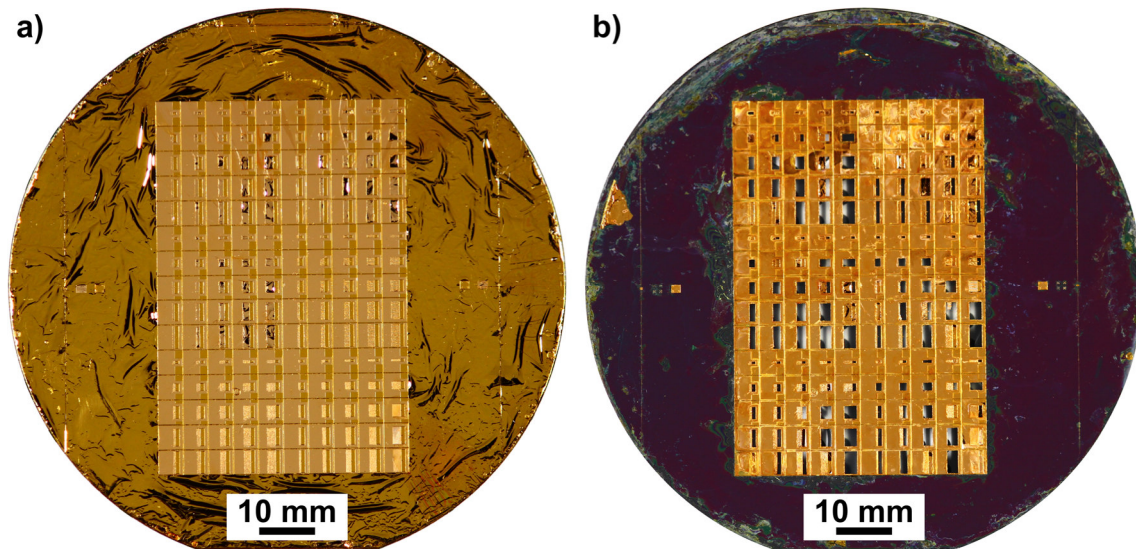
Fig. 12: Photos of a wafer processed according to approach V1 with FS views a) after the last BHF etching step and b) after partial final cleaning and before cleaving. Before cleaning significant warping of the Cu on top of resist was observed outside of the MA array. After cleaning failure of multiple MAs was observed with detachment of the tensile-test structures.

A significant issue that was clearly visible by eye was delamination of the Cu film deposited on top of "AZ 1518" photoresist (Fig. 13 a)). Delamination occurred during heat treatment on a hotplate for softbake of resist layers that were coated following a Cu deposition (see Fig. 9 g) and i)). Delamination happened specifically at the interface in between Cu and the "AZ 1518" photoresist during softbake of resists "LOR 20 B" and "AR-PC 503". The effect was attributed to the softbake temperatures that were required for both resists, which were 160 °C and 180 °C respectively. The "AZ 1518" photoresist had a softening temperature of approximately 100 °C, so softbake temperatures ≥ 160 °C were sufficient to trigger resist reflow. The resist softening and movement during reflow could have triggered delamination, especially as the Cu films were not optimized in terms of intrinsic stress. With the reduced adhesion in between Cu and the reflowing resist, forces from intrinsic stress could have increased the probability for delamination. Delamination of the tensile-test structures (Fig. 13) occurred primarily during heat treatment of "LOR 20 B" coated after the first Cu deposition (see Fig. 9 f-g)) while delamination of larger areas as observed towards the wafer edge (Fig. 13 a)) occurred during heat treatment of "AR-PC 503". Delamination of the tensile-test structures did not occur anymore after the second Cu deposition, because the deposition connected the structures to the substrate by the anchor structure. A substitution of "LOR 20 B" and "AR-PC 503" to reduce softbake temperatures was not possible at the time, because no alternative non-photosensitive and KOH-resistant resists with lower softbake temperatures were available. Alternatively, a substitution of the "AZ 1518" photoresist with a negative tone
40

resist would have been possible. Such resists typically feature higher softening temperatures due to higher polymer cross-linking during exposure. This was not evaluated due to the increased difficulty to remove heavily cross-linked resists which typically requires long immersion in strong solvents such as NMP or DMSO. Immersion times in these solvents during final cleaning (Fig. 9 k)) already had to be limited due to reactions with the Cu. As such, further increase of the cleaning times due to the use of a negative resist was not considered as a viable alternative.
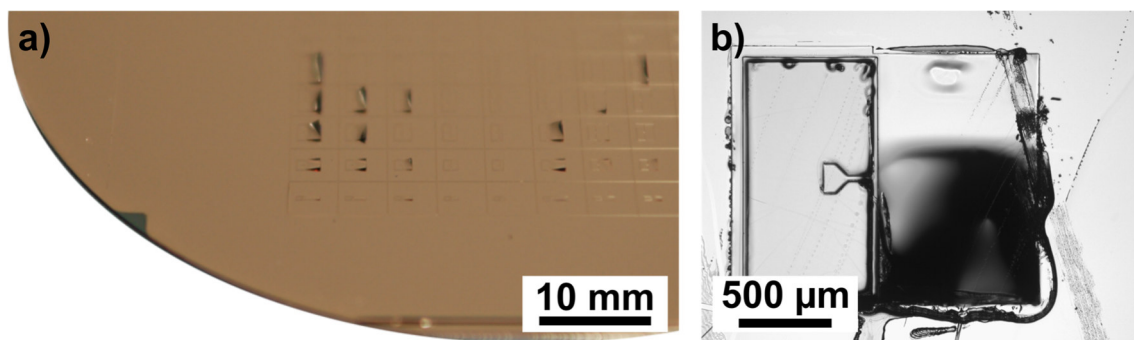
Fig. 13: a) Photo of a wafer-section and b) a magnified optical microscope image of a tensile-test structure after the first Cu deposition. Both images showed delamination of Cu from the lift-off resist for several structures primarily at the structure handle.

A second issue was connected to resist contaminations at the tensile-test structures which were located primarily at the outer edge of the tensile-test structure. The resist contaminations were critical, because the polymer would have chemically decomposed during elevated temperatures of following annealing steps and would have resulted in chemical contaminations of the tensile-test structure material itself. Fig. 14 a) shows the contaminations that remain after development of the lift-off resist system (see Fig. 9 g)) for the second Cu deposition. The contaminations were then buried underneath the subsequently deposited Cu film (see Fig. 9 h)) and could not be removed after the final cleaning step (Fig. 14 b)). The reason for the contaminations was related to the spin coating characteristics of the "LOR 20 B" resist due higher viscosity (~ 0.00028 m^2/s approximated from data sheet). During spin coating over the preexisting tensile-test structure, the resist formed contaminations locally at the structure corners and elongated streaks that follow the flow of the resist at the structure edges which faced away from the wafer center. After softbake, the contaminations featured a significantly reduced development rate relative to normal "LOR 20 B" and prolonged development times resulted in the removal of the entire lift-off resist structure before contamination could be removed. Substitution of the "LOR 20 B" was considered, but no viable alternatives for non-photosensitive lift-of resists that could be fabricated with

comparable thicknesses and lower viscosity were found available. Negative-tone lift-off resists were not considered here, as they conceptually have smaller undercuts which were not compatible with sputter-type PVD and, as explained above, require extended cleaning processes due to the increased polymer cross-linking which were not compatible with the used Cu material.
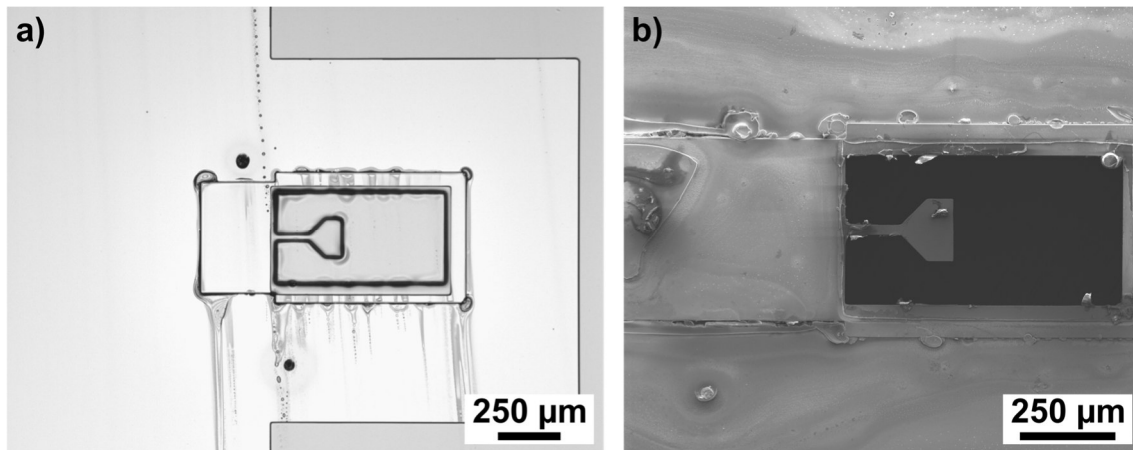
Fig. 14: a) Optical microscope image of a tensile-test structure after deposition of the second lift-off resist layer (Fig. 9 g)) and b) SEM SED image of a tensile-test structure after final cleaning and before cleaving. In both states, resist contaminations from the lift-off resist were visible a) directly after development and b) underneath the subsequently deposited Cu.

One potential issue that was not evaluated here was the compatibility of the second BHF etching step (see Fig. 9 k)) with other materials. By design, the material of the tensile-test structure should have been separated from the etchant by the lift-off resist system which was sufficiently resistant against BHF for the applied etch times. But separation in between the etchant and tensile-test structure could not be evaluated, as the Cu material that was used was not significantly etched in BHF within the applied etching time. As such, compatibility of the fabrication process must be evaluated first, if different materials are processed.

Tensile tests were not performed with the fabricated structures, because the last cleaving step to remove the Si frame surrounding the tensile-test structure was never performed successfully for all fabricated structures. For removal of the Si frame, it was also necessary to cleave through the deposited Cu layer. The Cu did not break with the Si due to the layer thickness and ductility. Increased mechanical forces to break the layer always resulted in detachment of the tensile-test structure from the anchor. This could have been alleviated by addition of mechanical weak points in the Cu layer during photolithography, but this was not implemented due to advancements with other fabrication concepts.

As the structures were not tested in tensile experiments it was not possible to evaluate the mechanical stability of the connection from the tensile-test structure to the substrate under load. It was planned to connect the substrate and the tensile-test structure by deposition of a layer with sufficient thickness to "overgrow" the lift-off resist system and attach to the film on top (Fig. 9 h)). Consequently, the strength of the connection would have been primarily dependent on the adhesion at the interface where the deposited films connected. The fact that the tensile-test structures remained attached to the substrate after lift-off and cleaning (see Fig. 14 b)) indicated that the connection formed successfully. But during later investigations of structures deposited on similar lift-off structures (see approach V3 and V5 for further details) and under similar sputter conditions clearly showed, that no connection in between the layers on the substrate and resist was formed and structures were easily separated during lift-off. For the structure fabricated here, it might have been possible that resist residues that were not fully removed remained at the interface and formed the connection. As a result, it was highly likely that the connection was only formed superficially and would not have been able to withstand the load during testing. It might have been possible to improve the connection by adaption of sputter parameters (e.g., higher deposition pressure for improved conformity of the deposition at edges). But with sputtering a significant improvement of the coverage of the resist structure would have been difficult due to the line-of-sight characteristic of the material flux, which would have likely left the connection as a limiting constraint.

2.7.3.5 Conclusion

With the presented process the optical inspection after fabrication showed, that structures with the planned geometry could be fabricated and that that the general structure release, as well as separation of the MAs into 4.5 mm by 4.5 mm dies was successful. The main advantages of this fabrication approach were, that only lift-off lithography was utilized for structuring of the tensile-test structure and that the structures remained attached to a handle that was directly fabricated from the Si wafer substrate. With the exclusive use of lift-off lithography for structuring the process was compatible to practically all materials that could be deposited by sputtering and the integrated fabrication of the handle reduced the need for manual post-processing. But several limitations remained with regards to cleaning, the final removal of the Si frame to access the structure during testing, the mechanical stability of the connection from the tensile-test structure to the substrate under load and possible heat treatments. With regards to heat treatment, the sputter deposition was constrained to RT processes, as it was

performed on top of resist for structuring. As such, it was only possible to perform heat treatments during post processing. The main concern for this approach was the mechanical stability of the connection from structure to handle. The current solution by sputter deposition required high process time and, with respect to experiences from other approaches, was mechanically unreliable. Due to the deposition characteristics of the sputter process, it was unlikely to sufficiently strengthen the connection by adaption of the deposition parameters and the approach was not further developed.

2.7.4 Approach V2 - Structure fabrication by structuring a continuous thin-film with photolithography and wet etching

2.7.4.1 V2 Design

The second fabrication process was based on fabrication of the tensile-test structures by structuring a continuous thin-film with photolithography and wet etching. The overall process was adapted from Smolka et al. [39] and was primarily altered to substitute tensile-test structure generation by photolithography and electrochemical deposition with PVD (magnetron sputtering), photolithography and subtractive wet etching.

In this approach the tensile-test structures were fabricated from a substrate-bound thin-film. Primary considerations were the selection of a suitable etchant and etch parameters to fabricate structures according to the geometrical demands with regards to lateral dimensions, as well as surface quality and geometry of the etched surfaces. Etch parameters had to be optimized to yield etched surfaces which were vertical in relation to the substrate for optimal application of force during testing and roughness had to be reduced as much as possible to avoid the influence of notches on the mechanical properties during tensile-testing. Two Cu etchants were evaluated for application in this process (FeCl$_3$ 37 wt. % + HCl 3 wt. % in H$_2$O and APS-100 (Transene Company ((NH$_4$)$_2$S$_2$O$_8$ 15 - 20 wt. % in H$_2$O)).

Identical to the first approach, MAs with the tensile-test structures were placed on a rectangular grid with a pitch of 4.5 mm by 4.5 mm with 15 rows and 14 columns of MAs. After fabrication the substrate-bound MAs were separated by cleaving of the substrate which was done by fabrication of a similar set of V-grooves in the Si substrate as shown in approach V1.

2.7.4.2 Tensile-test structure fabrication process and material synthesis

Si wafers were used as a substrate for the fabrication process. The wafers were double side polished with orientation (100), thickness 525 µm, diameter 100 mm and were thermally oxidized with a 2.1 µm thick SiO$_2$ diffusion/etch barrier (Fig. 15 a)).

In a first step a TiW diffusion/etch barrier and a Cu thin-film for fabrication of the tensile-test structures were deposited. For deposition, a magnetron sputter system with a confocal target setup was used (ATC 220-V, AJA INTERNATIONAL). The TiW film was deposited from a compound target (nominal composition: 80 at.% W and 20 at.% Ti, 4-inch

diameter, 99.95 at.% purity). The deposition power (radio frequency) was 150 W for a sputter rate of approximately 0.15 nm/s. Depositions were performed at a pressure of approximately 0.666 Pa (5 mTorr) with an Ar plasma at room temperature and a base pressure $< 2.7*10^{-5}$ Pa. Deposition time was adjusted to achieve a film thickness of 50 nm. Directly following, the Cu thin-film was deposited by simultaneous sputtering of two diametrically opposed Cu targets (4-inch diameter, 99.999 at.% purity). The deposition powers (direct current) for both Cu targets were adjusted for a similar sputter rate of approximately 0.18 - 0.2 nm/s. Depositions were performed at a pressure of approximately 0.666 Pa (5 mTorr) with an Ar plasma at room temperature. Deposition time was adjusted to achieve a film thickness of up to 5 µm (Fig. 15 b)).

After deposition, a positive tone resist (AZ1518, Microchemicals) was spin coated on top of the Cu. The dispense was performed dynamically at a rotational speed of approximately 8.3 1/s (500 rpm) over a time of 5 s, with a final rotation speed of approximately 66.7 1/s (4000 rpm) for 30 s and an acceleration of approximately 183.3 rad/s^2 (1750 rpm/s). A softbake was performed at 100 °C for 50 s on a hotplate. Afterwards, exposure of the resist was performed with a laser lithography system (µPG 101, Heidelberg Instruments Mikrotechnik GmbH) with a dose of approximately 55 mJ/cm^2. After exposure, the resist system was processed by immersion development in an aqueous-alkaline developer (AZ 726 MIF, Microchemicals) for approximately 35 s, followed by a rinsing cascade in deionized water (Fig. 15 c)). The patterned resist was subsequently used as an etch mask during wet etching of the Cu thin film. Wet etching was performed in a mixture of $FeCl_3$ based etchant ($FeCl_3$ 37 wt. %, HCl 3 wt. %, in H_2O) at a temperature of 60 °C without additional stirring (other etchants and parameters were also evaluated, but the process flow was identical). After etching, the wafer was cleaned in a rinsing cascade with deionized water, followed by spin drying (Fig. 15 d)). After etching the resist was removed in a cleaning cascade of acetone and isopropanol (600 s each) with ultrasonic agitation, followed by a final rinsing with isopropanol and spin drying (Fig. 15 e)).

In a next step a positive tone resist (AZ1518, Microchemicals) was spin coated on the wafer BS. The dispense was performed dynamically at a rotational speed of approximately 8.3 1/s (500 rpm) over a time of 5 s, with a final rotation speed of approximately 66.7 1/s (4000 rpm) for 30 s and an acceleration of approximately 183.3 rad/s^2 (1750 rpm/s). A softbake was performed at 100 °C for 50 s on a hotplate. Subsequently, AZ1518 was spin coated on the frontside under identical conditions. Cleanroom paper was placed in between the wafer and hotplate to prevent adhesion of the BS resist to the hot surface and prevent scratching of the resist on the metal surface. Exposure of the BS resist was performed on a mask aligner

(MA6/BA6, Süss Microtec) with a broadband UV Hg-vapor lamp with a dose of approximately 55 mJ/cm^2. The exposure mask was aligned to markings on the frontside of the wafer fabricated during wet etching of Cu. After exposure, the resist system was processed by immersion development in an aqueous-alkaline developer (AZ 726 MIF, Microchemicals) for approximately 35 s, followed by a rinsing cascade in deionized water (Fig. 15 f)). A subsequent hardbake was performed at 100 °C for 1800 s on hotplate. During treatment, the wafer was placed on cleanroom paper. In a next step (Fig. 15 g)) the thermally oxidized SiO$_2$ on the backside was selectively etched in BHF (BOE 7:1, Microchemicals), followed by a rinsing cascade in deionized water. Etch time for the 2.1 μm thick SiO$_2$ was approximately 1500 s. After etching, the resist on both wafer sides was removed in a cleaning cascade of acetone and isopropanol (600 s each) with ultrasonic agitation, followed by a final rinsing with isopropanol and spin drying (Fig. 15 h)).

In a next step, the wafer FS was spin-coated with a non-photosensitive, KOH resistant resist (AR-PC 503, Allresist), shown in Fig. 15 i). To improve step coverage, multiple dispenses were performed to cover the whole wafer surface with liquid resist before starting rotation with a final speed of approximately 66.7 1/s (4000 rpm) for 30 s and an acceleration of approximately 183.3 rad/s^2 (1750 rpm/s). A subsequent softbake was performed at 180 °C for 120 s on a hotplate. After application of the protective resist the substrate was etched from the BS with KOH (30 % wt. in H$_2$O) at a temperature of 70 °C. Etching was continued until the frontside SiO$_2$ etch barrier was reached (Fig. 15 j)). During etching the wafer frontside was isolated from the etchant by clamping in a protective wafer holder (Tandem series, AMMT). After etching, the wafer was cleaned in a rinsing cascade with deionized water followed by spin drying (Fig. 15 k)).

In a next step, a positive tone resist (AZ1518, Microchemicals) was spin coated on the wafer FS. The dispense was performed dynamically at a rotational speed of approximately 8.3 1/s (500 rpm) over a time of 5 s, with a final rotation speed of approximately 66.7 1/s (4000 rpm) for 30 s and an acceleration of approximately 183.3 rad/s^2 (1750 rpm/s). A softbake was performed at 100 °C for 50 s on a hotplate, followed by a hardbake at 100 °C for 1800 s on hotplate (Fig. 15 l)). Afterwards, the SiO$_2$ etch barrier was selectively etched in BHF from the BS, followed by a rinsing cascade in deionized water. Etch time for the 2.1 μm thick SiO$_2$ was approximately 1500 s. After etching, the wafer was cleaned in a rinsing cascade with deionized water followed by spin drying. In a subsequent etching step, the exposed TiW film was removed by wet etching in a mixture of H$_2$O$_2$ (8 wt. %) and NH$_3$ (0.5 wt. %) in H$_2$O at 60 °C from the BS. Process time was adapted by observation during etching until the TiW was

fully removed. Etching was followed by a rinsing cascade with deionized water and spin drying (Fig. 15 m)). After etching, the resist on wafer FS was removed in a cleaning cascade of acetone and isopropanol (600 s each), followed by a final rinsing with isopropanol and spin drying (Fig. 15 n)).

In a last step, the structures were cleaved from the Si substrate along the V-grooves fabricated during KOH etching to prepare for testing. Grooves were indicated in Fig. 15 n) (Backside) by markings B and C. Grooves B had a depth of approximately 300 µm and grooves C approximately 200 µm. Etch depths were selected to provide sufficient mechanical stability for handling and spin coating/drying. Depth of grooves C was reduced in comparison to B to preferentially cleave the rectangular MAs while the protective frame remained around the tensile-test structure. Cleaving was performed manually and had to be performed carefully to avoid damage to the tensile-test structure. After removal of the Si frame the structures were ready for testing (Fig. 15 o)).
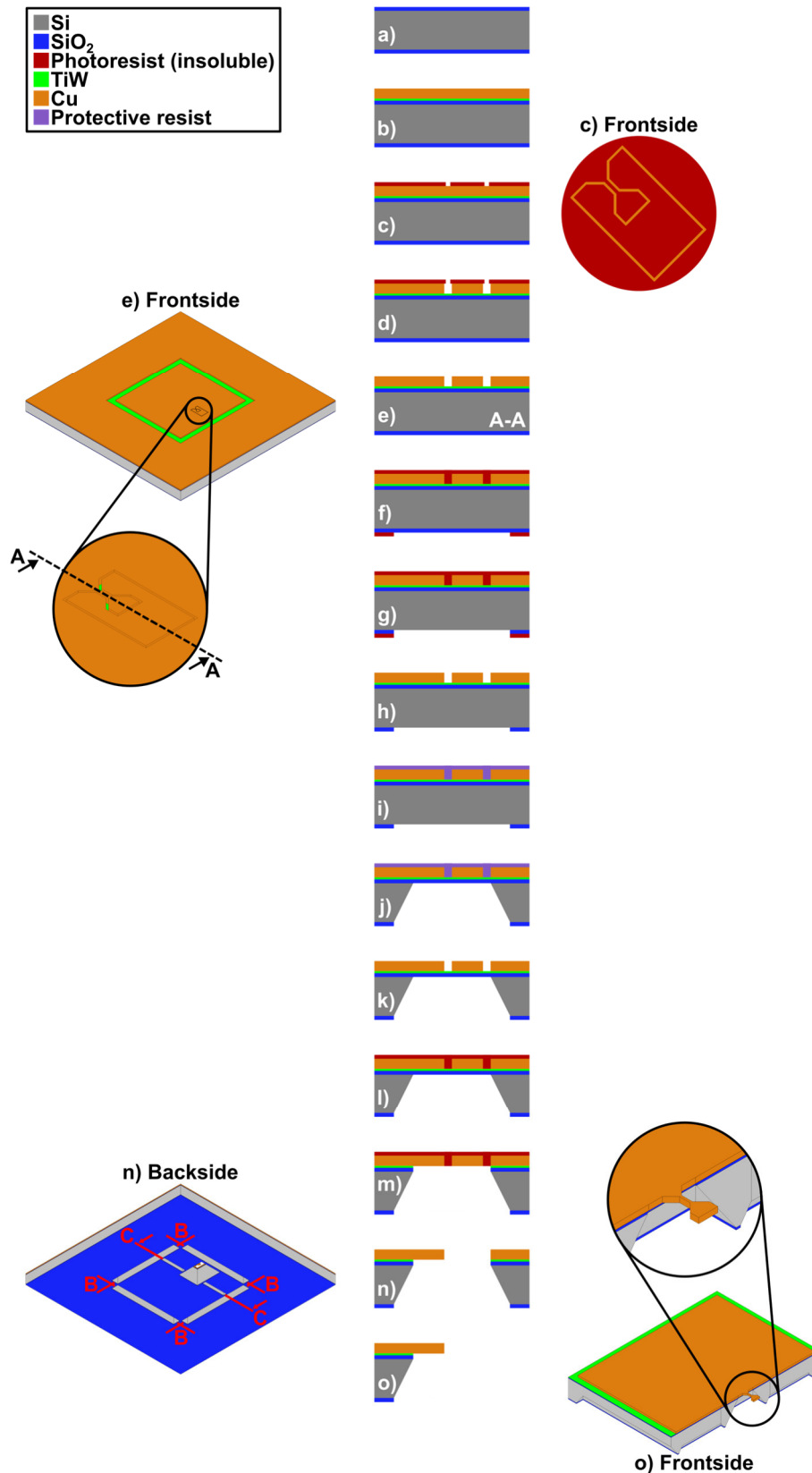
Fig. 15: Schematic process flow for fabrication approach V2 (not to scale). (a) thermally oxidized Si wafer, (b) FS TiW and Cu sputter deposition, (c-e) FS photolithographic structuring of photoresist and Cu etching, (f-h) BS photolithographic structuring of photoresist and SiO₂ etching, (i-k) FS deposition of KOH protective resist and BS KOH etching, (l-m) FS deposition of protective resist and BS etching, (n-o) final cleaning cascade with acetone, isopropanol, and structure separation by cleaving.

2.7.4.3 Important design features

In the following sub-section selected features are described/reiterated with the aim to clarify their purpose within the design. The features are presented in a separate section to highlight their importance, as they were essential to the overall process.

The first feature concerned the mask design that was used to transfer the geometry of the tensile-test structure into the Cu layer. To etch the geometry of the tensile-test structures, the etch mask was fabricated in form of a trench along the outer dimension (Fig. 16 a)) instead of etching the Cu over a larger area (Fig. 16 b)). This mask geometry was selected to ensure homogenous etching along the entire lateral geometry of the tensile-test structure. Fig. 16 c) and d) showed a comparison of structures etched according to the masks depicted above. The geometry of the tensile-test structure defined by an etched trench was significantly more homogenous in comparison to the structure etched along a large area mask opening. The trench structure only showed a small change in sidewall geometry of the Cu where the etched trench changed width (Fig. 16 c)). This error originated from the serial exposure of the used laser lithography system and was corrected in later versions. The structure etched according to the large area mask opening shown here was overetched on purpose to exaggerate the etching inhomogeneities for better visibility. Main inhomogeneities were tapering of the gauge width along the gauge length and accelerated etch rate at convex corners. The reason for the variation in etch rate was the supply of fresh etchant to the Cu surface. At convex corners, the ratio of available etchant to etched Cu surface was higher in comparison to straight sections and at concave corners the ratio was lower. This resulted in an increased etch rate at convex corners, and a decreased etch rate at concave corners. This effect explained both, the increased etching at the corners (convex) of the structure head, as well as the tapering of the gauge, as it was positioned in between two concave corners where the etch rate was locally reduced relative to the straight middle section of the gauge. In contrast, etching along the trench structure had a high ratio of masked to unmasked (exposed to etchant) surface area, so the etched area was not subjected to a limited etchant supply, which lead to more homogenous structure etching.

A second feature was the design of the mask for etching of the V-grooves on the BS of the substrate (see Fig. 15 n)) Backside, feature B). The KOH etch mask that was fabricated in the SiO_2 layer was not one continuous opening, but instead consisted of four separated rectangular openings. This design was selected to avoid underetching of convex corners in KOH. Had the opening been designed as one continuous mask, convex corners would have been present that would have resulted in extensive underetching of the MA and would have led

50

to a loss of structural integrity of the Si wafer during etching. With four separate structures, the etch masks consisted exclusively of concave corners which were underetched slowly according to the <111> crystal planes with no significant underetching of the MA.

Fig. 16: Schematic illustration of photoresist etch-mask designs for etching of the Cu tensile-test structures (not to scale) and optical microscope images of the fabricated structures after etching. Etch-mask designs were for a) etching through a trench opening with constant width and b) and large surface area opening. Photoresist is indicated in red and Cu in orange color. After etching the c) trench opening showed homogenous reproduction of the etch-mask geometry in the Cu, while the d) large area opening showed very inhomogeneous underetching of the etch-mask geometry. For the large area opening the photoresist mask was retained for better illustration of the underetching.

One feature was the order of the process flow. It was necessary to perform the $FeCl_3$ based Cu etching prior to the BHF etching of the SiO_2 on the wafer BS. Generally, it was preferable to perform BHF etching before other materials were deposited to avoid potential chemical reactions which could influence the tensile-test structure material. For this process it was tested to etch the SiO_2 prior to the Cu. But it was observed during later KOH etching of the substrate, that the Si was etched with inhomogeneities in form of significant local reductions in etch rate. Fig. 17 shows a comparison between partially etched rectangular cavities for structure release which were fabricated with different process flows. For the first cavity (Fig. 17 a)) the

BHF etching was performed prior to FeCl$_3$ etching and for the second cavity (Fig. 17 b)) FeCl$_3$ etching was performed prior to BHF etching. Etch rates in the areas with dark contrast were approximately 1/30 of the nominal <100> Si etch rate. The inhomogeneities were assumed to originate from reactions of the FeCl$_3$ based etchant with residues of the BHF etchant at the Si surface that remained on the wafer BS after etching of the SiO$_2$. In literature [63] it was observed that mixtures of FeCl$_3$ and HF could cause enhanced formation of porous Si. The irregular crystal orientation exposed by porous Si could have explained the slow etch rate, as a clean <100> surface with high etch rate was not available. To avoid this issue, it was possible to either coat the BHF etched Si with a protective resist layer to avoid reaction with the FeCl$_3$ etchant, or to perform the step prior to BHF etching. The later variant was used, as there were no significant chemical reactions in between the Cu material utilized throughout this work and BHF. Additionally, the alternative coating with resist still retained the risk of porous Si formation through defects in the resist layer (e.g., pinholes, scratches).
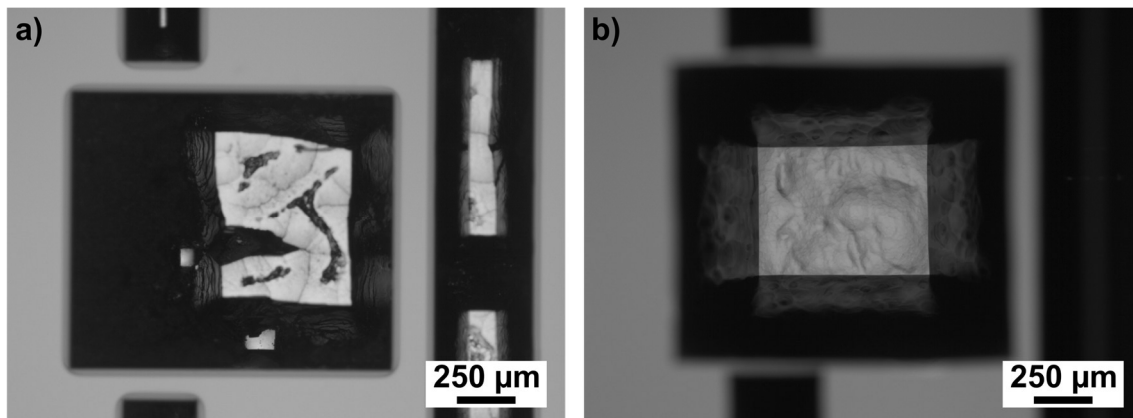
Fig. 17: Optical microscope images of the etched cavities underneath the tensile-test structures from the wafer BS after partial KOH etching. Structures were processed by a) etching of Cu with FeCl$_3$ after SiO$_2$ etching with BHF and b) etching of Cu with FeCl$_3$ prior to SiO$_2$ etching with BHF. Image a) showed inhomogeneous etching with reduced, indicated by the dark regions.

2.7.4.4 Discussion

Prior to testing the fabrication process, the etch characteristics of both tested Cu etchants were evaluated. The parameters for the FeCl$_3$ based etchant were investigated with regards to temperature, concentration, composition, and etchant agitation. Fig. 18 shows a comparison of Cu structures etched at a) 40 °C, b) 60 °C and c) 80 °C. Etch times were approximately 40 s, 30 s and 20 s respectively with variations of ± 5 s. Interruptions of the etching for observation of the progress had significant influences on the final etch time, so it was important to determine

etch rates prior in a separated experiment and etch the tensile-test structures in a single, uninterrupted process. The tensile geometries of the structures were etched homogeneously along the edges and etch rate for underetching of the mask was close to the etch rate in thickness direction for all temperatures. Variations in the gauge width of the etched structures Fig. 18 a) – c) were due to different dimensions of the initial photoresist mask and were not connected to the etch characteristics. Magnified views Fig. 18 d) – f) showed development of the surface quality for etched sidewalls at d) 40 °C, e) 60 °C and f) 80 °C. From 40 °C to 60 °C sidewalls appear vertical for both temperatures with reduced surface roughness at 60 °C and similar surface morphology. Further increase of the process temperature revealed the breakdown of an outer layer during etching with a second surface underneath which showed distinctly lower roughness.
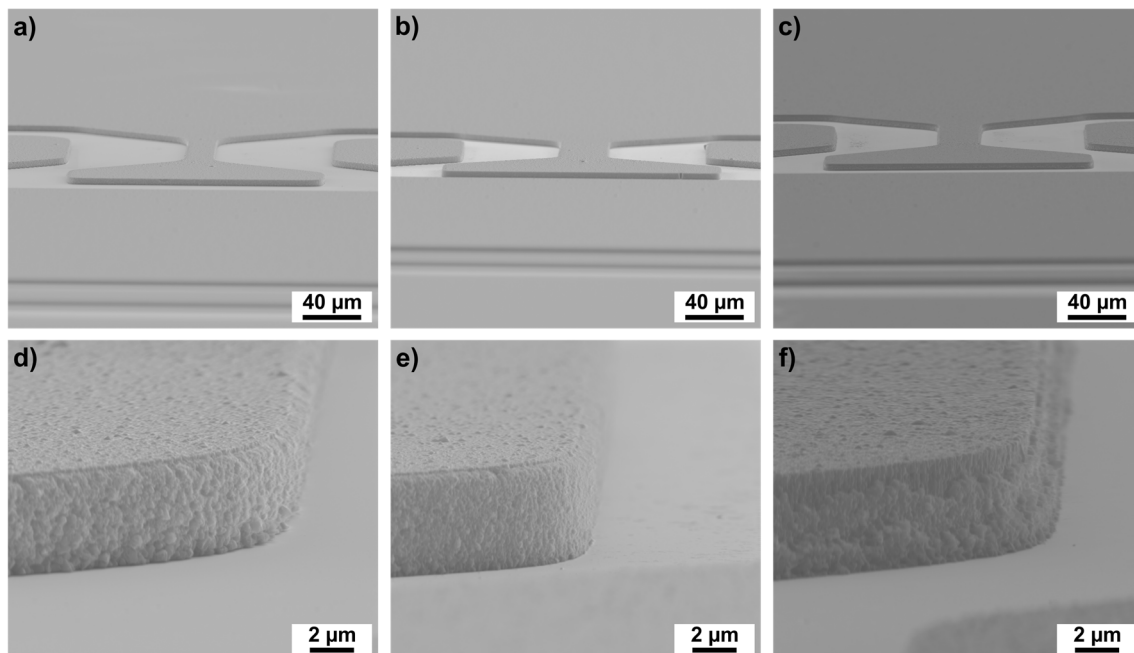
Fig. 18: SEM SED images of tensile-test structures after FeCl$_3$ etching processes with increasing temperature at a) 40°C, b) 60°C and c) 80°C with respective images at higher magnification of the structure sidewalls processed at d) 40°C, e) 60°C and f) 80°C.

An investigation of the surface etched at 80 °C by area resolved EDS revealed the presence of Cl in the additional surface layer which covered the etched Cu surface (Fig. 19 a-c)). This indicated that the additional layer was a reaction product formed during the FeCl$_3$ etching that remained attached to the surface. To avoid issues of chemical contamination by the Cl during further processing and possible influences of the additional layer during mechanical characterization the etching process was adapted to remove the reaction product. This was achieved by addition of 3 wt. % HCl to the etchant which removed the reaction products [64,65].

A structure processed with the adapted etchant (60 °C, 20 s, with stirring) is shown in Fig. 19 d). Etch homogeneity along the structure edges and characteristics for underetching of the etch mask were not affected by the addition of HCl. A magnified view of the etched Cu surface (Fig. 19 e)) revealed full removal of the secondary layer. The etched Cu surface featured reduced roughness in comparison to the surface etched in the etchant without HCl addition (Fig. 18 e)), but a few, blade-like structures remained orthogonal to the Cu surface. The reason for the formation of these structures remained unclear.
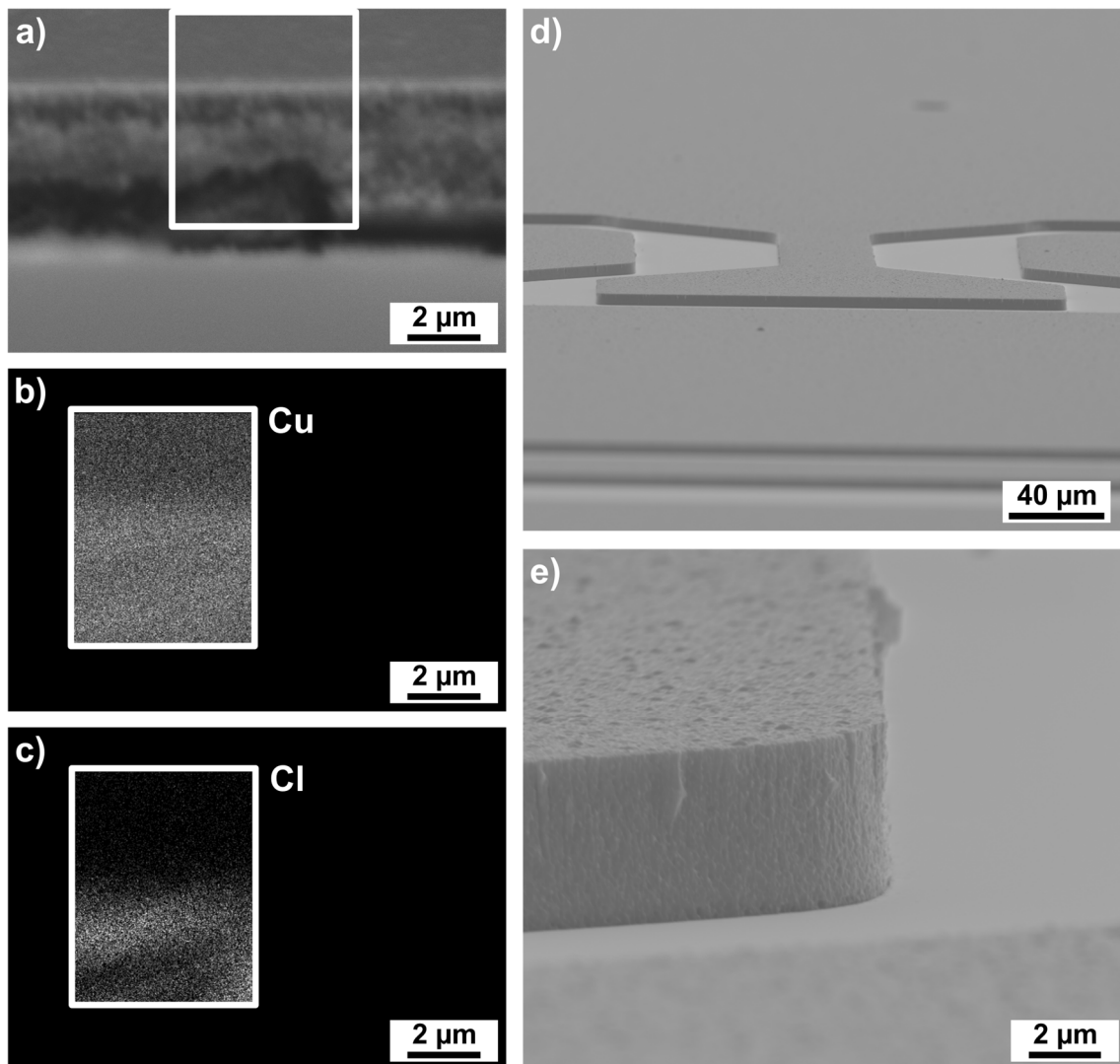
Fig. 19: a) SEM BSED image of a Cu tensile-test structure sidewall after etching with $FeCl_3$ with local elemental distribution of b) Cu and c) Cl in the area indicated by the highlighted rectangle. Mismatch of the area in between the images was due to initial drift. d) SEM SED image of a Cu tensile-test structure after etching with $FeCl_3$ + HCl with e) a magnified view of the sidewall geometry.

The influence of stirring on the etch characteristics was also investigated to evaluate influences on the underetching of the etch mask with regards to verticality of the structure

sidewalls. Fig. 20 shows a comparison between two Cu structures etched at 40 °C a) with and b) without stirring. Stirring was performed in a beaker with a rotating magnetic stirring bar. Etch rates were generally faster for stirred etchants. The rate of underetching in both cases remained close to the thickness of the Cu layer, but the stirred etchant showed a reduction of the underetching rate with increasing etch depth which caused a more vertical sidewall geometry after etching. This effect was assumed to be caused by the reaction kinetics that occurred in the gap in between etch mask and substrate. During underetching of the Cu in the gap, the etchant supply was primarily dominated by diffusive transport in the unstirred, and convective transport in the stirred solution. As a result, the ratio of etch rate in depth direction relative to the underetching rate was higher in the stirred case which led to the more vertical sidewall geometry. But under the assumption of differing rates for underechting it remained unclear, why the magnitude of the final underetching was in the order of the Cu thickness in both cases. With a higher rate of vertical etching to underetching, the unstirred solution should have shown reduced underetching in comparison. It was assumed, that the generally lower etch rate in the unstirred etchant, which caused longer process times, also incidentally led to a relative increase in the underetching time. With this it could have been possible that the structures processed with stirring were overetched longer in comparison to unstirred solutions, which could have led to the similar appearance in underetching for both etchants.
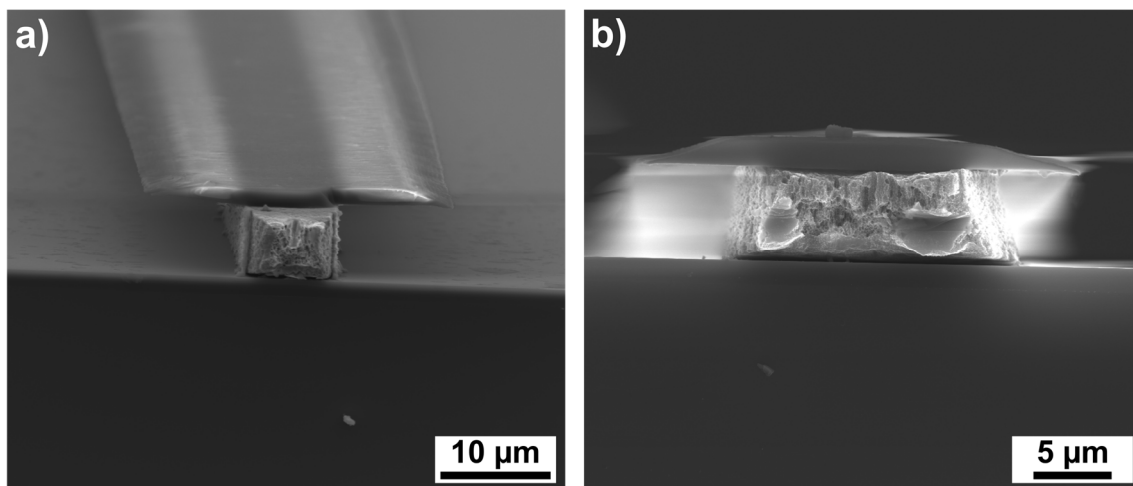
Fig. 20: SEM SED cross-sectional images of Cu structures after etching with FeCl₃ at 40 °C. For etching executed a) with stirring a vertical sidewall was observed and b) without stirring a more isotropic sidewall geometry was observed.

In general, control of the etch times was difficult due to the high etch rates (approximately 125 to 250 nm/s at 40 °C to 80 °C) which resulted in low control over the final structure geometry due to underetching and variations in manual handling. A reduction in etch

rate was evaluated by testing lower etching temperatures, or dilution of the etchant. But in both approaches a loss in etch homogeneity along the structure edges was observed which prevented repeatable structure fabrication. Therefore, these approaches were not investigated further.

As an alternative to the $FeCl_3/HCl$ based solution, the etch characteristics of a second, commercially available, Cu etchant (APS-100 $((NH_4)_2S_2O_8$ 15 - 20 wt. % in $H_2O))$ were evaluated. Etch characteristics were primarily investigated at different process temperatures without stirring. Etching at 30 °C, recommended by the etchant manufacturer, showed a low etch rate of approximately 7 nm/s with significant underetching (Fig. 21 a,d)). Etching did not yield well defined tensile-test structures and were unsuitable for mechanical actuation during tensile testing. Fig. 21 b) and e) show a structure etched at 70 °C with an etch rate of approximately 170 nm/s. Verticality of the sidewalls improved with increasing etch temperatures, while the structure still showed partially isotropic geometry, especially close to the substrate surface. Roughness values of the etched surfaces generally were higher in comparison to the $FeCl_3/HCl$ based etchant. By extending the overetching time (Fig. 21 c,f)) it was possible to further reduce the curvature at the sidewalls while retaining the etch homogeneity along the structure edges. A further increase in process temperatures was not considered due to the further reduction in etch time which would have again led to reduced control over the final structure geometries. Etching at 70 °C allowed for structures with geometries comparable to processing with the $FeCl_3/HCl$ based etchant at better control due to the longer etch times (50 s of etching and overetching). But surface roughness was higher which could have had an influence on tensile testing, as the surface morphology might have acted as notches and could have negatively impacted mechanical properties.
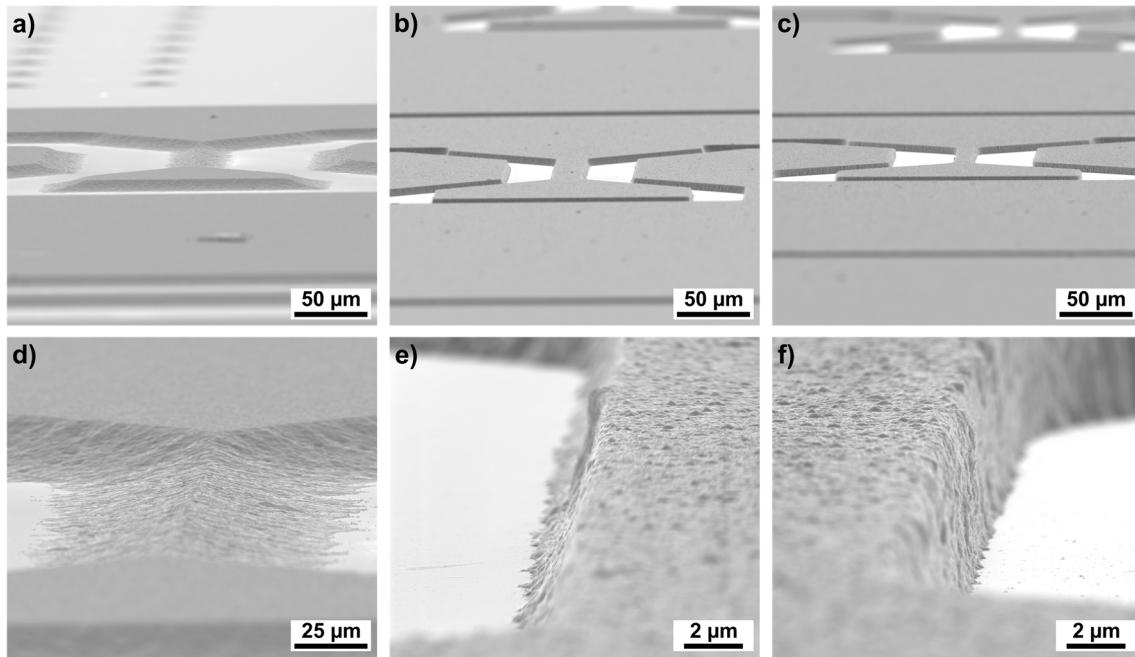
Fig. 21: SEM SED images of tensile-test structures after an APS-100 etching processes with increasing temperature at a) 30°C, b) 70°C and c) 70°C with increased overetching time and respective images at higher magnification of the structure sidewalls processed at d) 30°C, e) 70°C and f) 70°C with increased overetching time.

After evaluation, the FeCl$_3$/HCl based etchant at a temperature of 60 °C without stirring was selected as the etchant for the fabrication process, as it was the best compromise of surface roughness, sidewall geometry and process control related to the etch time of the tested etchants.

After selection of the etchant, the full fabrication process was tested to evaluate the fabrication of tensile-test structures. All test processes that were performed had to be stopped towards the end of the KOH etching step where the Si substrate was etched for structure release. Fig. 22 shows SEM images of two different tensile-test structures after KOH etching before removal of the SiO$_2$ layer from the a) FS and b) BS. The structure seen from the FS (Fig. 22 a)) showed a bright discoloration in the SiO$_2$ layer that was located at the trench that was etched in the Cu layer at the gauge and base of the tensile-test structure. The bright contrast was caused by the topography of the SiO$_2$. The layer deformed by buckling after intrinsic stress of the SiO$_2$ was released by removal of the underlying Si substrate due to the high compressive stresses of thermally oxidized SiO$_2$. Fig. 22 a) represents a rare case where the SiO$_2$ layer remains intact after release. In most cases the SiO$_2$ layer ruptured (Fig. 22 b)) at the base of the tensile test structure where the SiO$_2$ was not supported by the remaining Cu layer.
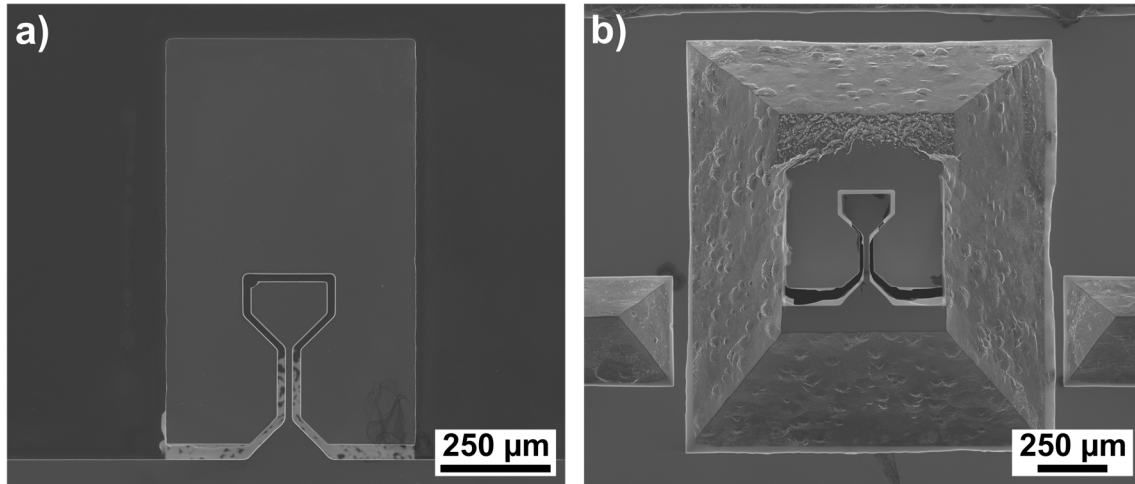
Fig. 22 SEM SED images of partially processed tensile-test structures after KOH etching from a) the FS and b) the BS of the wafer. Image a) shows a structure where the SiO_2 layer is intact, but locally under high strain, indicated by the bright contrast of the gap surrounding the tensile-test structure. Image b) shows a structure with a fractured SiO_2 layer due to strain.

With failure of the SiO_2 layer the only remaining protection for the tensile-test structure was the KOH protective resist. After fracture of the SiO_2, the resist quickly delaminated from the wafer FS due to the mechanical movement of the SiO_2 layer and chemical reactions in areas where the KOH was in contact with the now exposed Cu structures. The structure shown in Fig. 22 b) appeared undamaged by the etchant, which was most likely attributed to the fact, that the etching was coincidentally stopped at the time when the SiO_2 fractures and the tensile-test structure was still undamaged. It was not possible to transfer this time sensitive manual etch stop to an entire wafer of structures due the combination of Si thickness and etch rate variations over the area of the substrate which were unavoidable. Because of these variations it was necessary to perform a short overetching at the end of the KOH etching process to ensure that all fabricated cavities were etched all the way through to the SiO_2 etch barrier. This overetching typically required a time < 600 s, but this time was already too long and resulted in damage to most structures on the wafer as illustrated in Fig. 23. Fig. 23 a) showed a partially processed wafer towards the end of KOH etching and after removal of the protective resist. Fig. 23 b-f) shows magnified light microscope images from the wafer BS, for different process states with b) a cavity where a thin layer of Si remained, c) a cavity directly after failure of the SiO_2 layer and d) - f) different stages of overetching. The structures were positioned in adjacent MAs along a column as indicated in Fig. 23 a). Even over short distances on the wafer, the Cu tensile-test structures showed rapidly increasing damage from MA to adjacent MA due to etching with KOH. As a result, it was not possible to achieve the necessary overetching while protecting the structures.

58
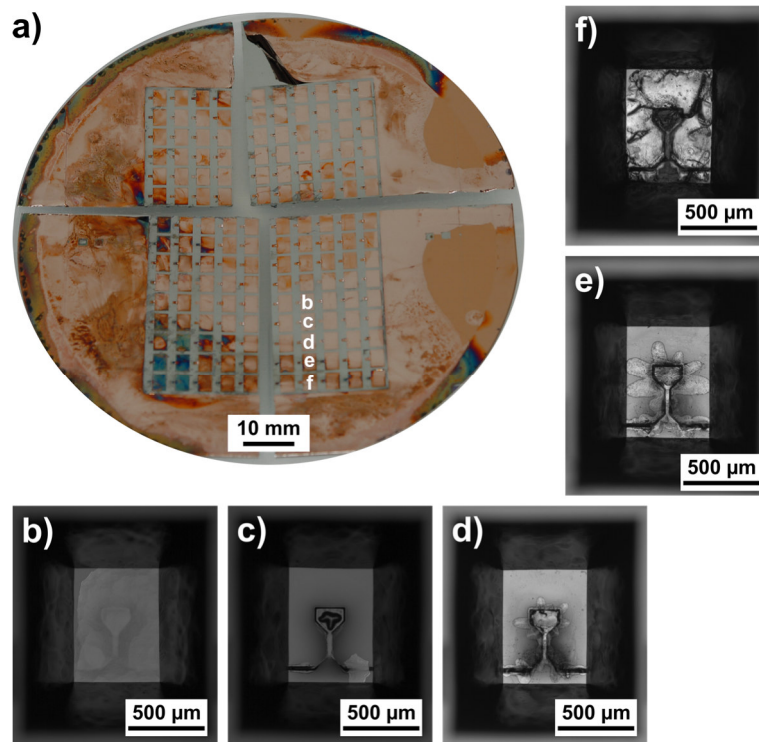
Fig. 23: a) Photo of a partially processed wafer after cleaning, fractured into four pieces due to manual handling. Processing was stopped shortly before KOH etching was complete. Discoloration of the Cu on the FS indicated an etch attack on the FS during KOH etching. Optical microscope images showed adjacent tensile-test structures from the BS b) shortly before full removal of Si in KOH, c) during etching of last Si residues with fracture of the SiO$_2$ layer, d) first etching of Cu through the fractured SiO$_2$ opening, e) increasing damage to the Cu due to KOH exposure and f) etch attack on the entire tensile-test structure.

To avoid breaking of the SiO$_2$ layer, multiple approaches were tested by changing parameters of the protective resist coating, decreasing the thickness of the SiO$_2$ barrier and different structuring of the Cu layer. For the protective coating, the resist types and their thickness were varied to observe influences on the stabilization of the SiO$_2$ layer. Tested resists were AR-PC 503 (Allresist), AZ 1518 (Microchemicals), LOR 20 B (MicroChem Corp.), SU-8 3010 (MicroChem Corp.) and PEB (utilized by Smolke at al. [39]) with different thicknesses. No tested coating prevented failure of the SiO$_2$ layer. The main limitation was assumed to be due to the high compressive stress of the thermally oxidized SiO$_2$. The resulting buckling was likely sufficient to cause delamination from the resist layer and induced initial defects in the SiO$_2$ which quickly propagated and resulted in fracture. This issue was not encountered by Smolka et al. in the original process. This was attributed to the custom fabricated SiO$_2$ deposited by plasma enhanced chemical vapor deposition, which typically featured reduced intrinsic stress. To improve stabilization during release, the SiO$_2$ thickness was reduced to 500 nm to improve the relative impact of the remaining Cu and resist on stabilization. But the thickness reduction showed no improvement and failure of the devices occurred in the same way during

KOH etching. Alternatively, it was evaluated if the geometry of the trench etched into the Cu affected failure. Main deformation and failure in the SiO_2 preferentially occurred towards the base of the tensile-test structure (see Fig. 22). It could have been possible, that the SiO_2 was initially deformed in that location due to intrinsic stress of the surrounding Cu layer. To test this, the Cu surrounding the tensile-test structure was removed after etching of the trench in a second etching process. Fig. 24 a) shows a light microscope image of a structure where the Si was almost fully removed during KOH etching. In all areas where the Si was removed, the freestanding SiO_2 showed significant buckling and exhibited quick failure after full removal of the Si (Fig. 24 b)) and subsequent etching of the Cu tensile-test structure.
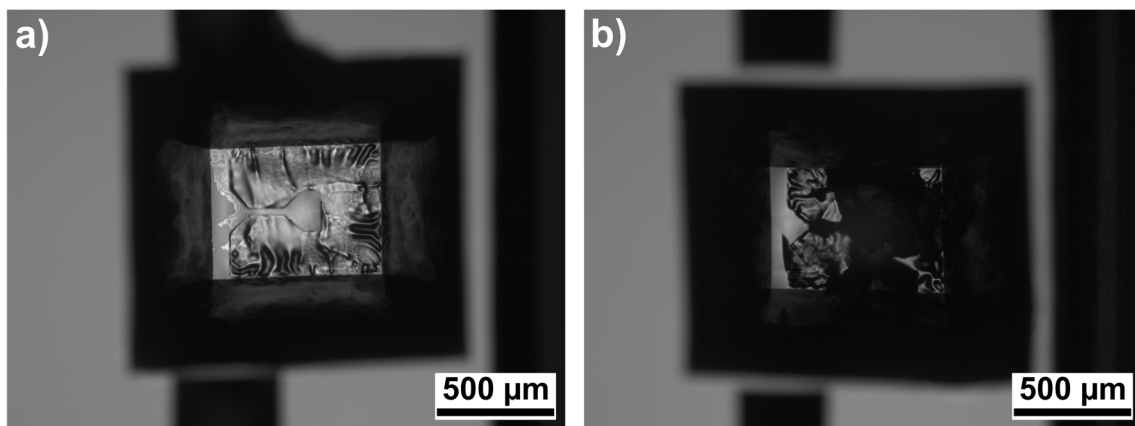
Fig. 24: Optical microscope images of tensile-test structures from the BS after partial KOH etching. For the shown wafer, all Cu material apart from the tensile-test structure was removed in an additional Cu etching step. Image a) shows the state during etching of the last remaining Si with significant warping of the SiO_2 etch barrier due to stress in areas where Si was fully removed. Image b) shows the state shortly after all Si was removed with fracture of the SiO_2 etch barrier due to stress and etch attack on the Cu structure.

A possible solution to overcome the limitation would have been the replacement of the thermally oxidized SiO_2 barrier with a different etch barrier material with lower intrinsic stress to avoid buckling and failure during release. An optimal stress state would have been low tensile stress, as it would have significantly reduced deformation after structure release. A possible candidate was low stress Si_3N_4 deposited by low pressure chemical vapor deposition techniques [66]. But removal of such a film after Si etching would have required dry etching, as possible wet etchants (e.g. concentrated HF ($\sim$ 50 wt. %), or hot (180 °C) H_3PO_4) were incompatible with a multitude of materials which would have significantly limited application of the approach [65]. Both, chemical vapor deposition and dry etching were not available at the time, so the process was not pursued further.

2.7.4.5 Conclusion V2

Within the second approach it was not possible to achieve successful fabrication of the tensile-test structures. With optimization of the etching process, it was possible to structure the Cu layer with the intended tensile-test geometry, but all fabrication tests ultimately failed during structure release due to intrinsic stress of the SiO_2 etch barrier. To overcome this issue, it would have been required to replace the thermally oxidized SiO_2 barrier with a low stress barrier (e.g. Si_3N_4, or SiO_2 optimized for low stress). Changes to the barrier material would have required selection of suitable etchants for later removal of the barrier during structure release. The main limitation of this approach was the transfer from processing of single element tensile-test structures to multinary MLs for combinatorial investigations due to constraints during the wet etching processes. Because material composition significantly influences etch characteristics, structure fabrication with consistent geometries would have been difficult. As such, universal applicability of the fabrication process to arbitrary multinary materials could not be ensured. If available, the wet etching processes should be replaced by dry etching such as RIE for etch barrier and ion beam etching for structuring of the tensile-test structure materials. Especially the change to ion beam etching would be essential for this approach, because the low etch selectivity and range of materials that can be etched is unmatched by individual wet etchants. If the limitations of the etching processes and stability of the etch barrier could be resolved, the process would be highly competitive with other approaches due to the range of materials that could be processed and the possibility to perform heat treatments prior to structuring.

2.7.5 Approach V3 – Freestanding structure fabrication by lift-off lithography

2.7.5.1 V3 Design

The next approach was based on photoresist-based lift-off lithography process which was similar to structure patterning in approach V1 where the tensile-test structures were structured by deposition on top of a lift-off resist. For this approach it was selected to perform lift-off directly after deposition to utilize the structures in the as-deposited thin-film form and omit anchoring to the wafer substrate and subsequent release by wet etching and cleaving. Without anchoring to the substrate, it was required to fabricate a structure for clamping in the

straining device that had to be attached to the tensile-test structure in post processing. Due to utilization of a lift-off process similar to approach V1, the following approach was subject to similar constraints in terms of in-plane structure geometry and structure thickness. The overall design of a fabricated sample encompassed two main elements. The tensile-test structure itself for mechanical characterization and a rectangular section, which was utilized as a handle for manual manipulation and attachment of the structure for clamping in the straining device.

Identical to the first approach, MAs with the tensile-test structures were placed on a rectangular grid with a pitch of 4.5 mm by 4.5 mm with 15 rows and 14 columns of MAs. After fabrication, the MAs were already separated into individual freestanding MAs due to the lift-off process and could be directly utilized for further processing without the need for cleaving/dicing.

2.7.5.2 Tensile-test structure fabrication process and material synthesis

Si wafers were used as a substrate for the fabrication process. The wafers were single side polished with orientation (100), thickness 525 µm, diameter 100 mm and were thermally oxidized with a 1.5 µm thick SiO_2 diffusion barrier (Fig. 25 a). In a first step a bilayer of non-photosensitive lift-off photoresist (LOR 20 B, MicroChem Corp.) with a combined thickness of approximately 6.6 µm was spin-coated (Fig. 25 b). The resist thickness was selected to be higher than the nominal thickness of the tensile-structures (in the order of 2/3 of the resist thickness) to ensure a successful lift-off process. The two layers were deposited by two successive spin coating steps which were performed with a waiting time of 5 s in between the coatings. The individual coatings were performed with a dynamic dispense at a rotational speed of approximately 8.3 1/s (500 revolutions per minute (rpm)) over a time of 5 s, with a final rotation speed of approximately 16.7 1/s (1000 rpm) for 35 s and an acceleration of approximately 183.3 rad/s^2 (1750 rpm/s). After deposition of the bilayer, a softbake was performed at 160 °C for 120 s. In the next step, a positive tone photoresist with a thickness of approximately 1.5 µm (AZ1518, Microchemicals) was spin-coated (Fig. 25 c). The dispense was performed dynamically at a rotational speed of approximately 8.3 1/s (500 rpm) over a time of 5 s, with a final rotation speed of approximately 66.7 1/s (4000 rpm) for 30 s and an acceleration of approximately 183.3 rad/s^2 (1750 rpm/s). The softbake was performed at 100 °C for 50 s. Exposure of the top resist was performed with a laser lithography system (µPG 101, Heidelberg Instruments Mikrotechnik GmbH) with a dose of approximately 55 mJ/cm^2 (Fig. 25 d). After exposure, the resist system was processed by immersion development in an

aqueous-alkaline developer (AZ 726 MIF, Microchemicals) for approximately 60 s, followed by a rinsing cascade in deionized water (Fig. 25 e).
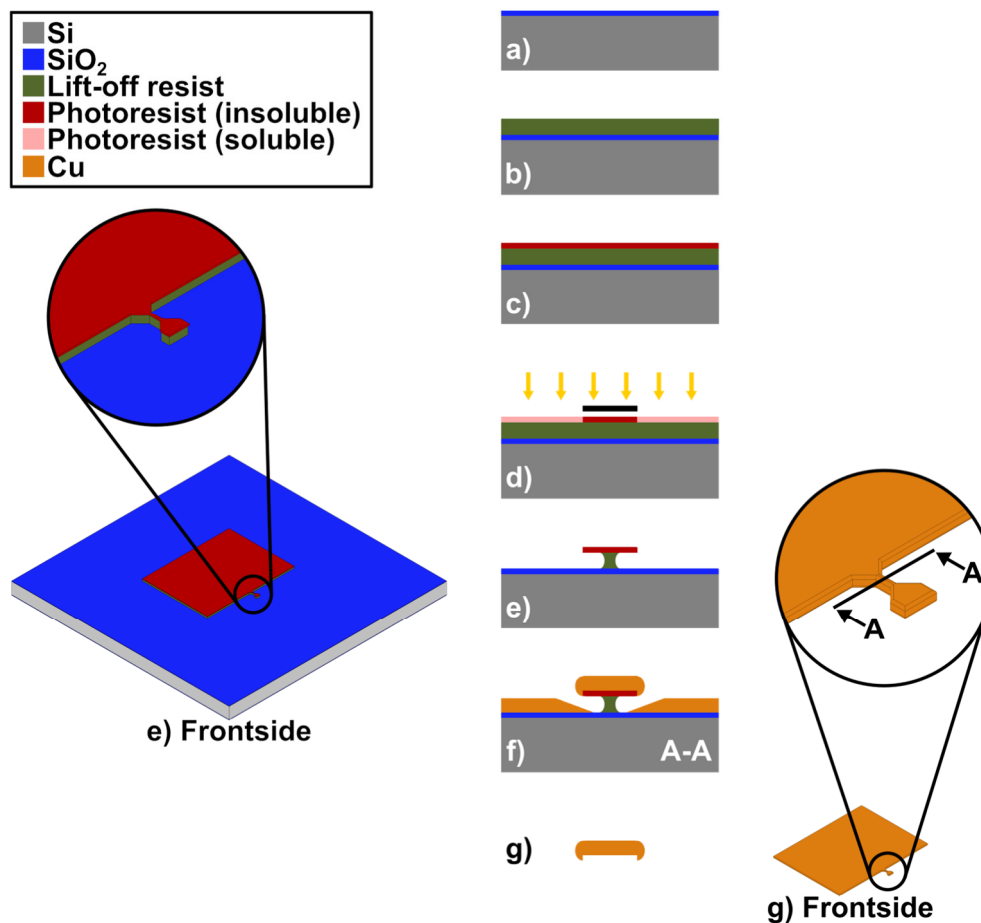
Fig. 25: Schematic process flow for fabrication approach V3 (not to scale). (a) thermally oxidized Si wafer, (b-c) FS bi-layer lift-off resist deposition, (d-e) FS photolithographic structuring of photoresist, (f) FS Cu deposition, (g) structure lift-off in acetone and final rinsing cascade with acetone and isopropanol.

After fabrication of the resist lift-of structure, the deposition of the tensile-test structure material was performed (Fig. 25 f). For deposition, a magnetron sputter system with a confocal target setup was used. The thin film was deposited by simultaneous sputtering of two diametrically opposed Cu targets (4-inch diameter, 99.999 at.% purity). The deposition powers (direct current) for both Cu targets were adjusted for a similar sputter rate of approximately 0.18 - 0.2 nm/s. Deposition time was adjusted to achieve a film thickness of up to 5 µm. Sputter parameters were adjusted to achieve low changes of intrinsic stress along the film thickness and low porosity within the freestanding films. Low sputter pressure and additional bias were used to achieve increased incidence energy during deposition resulting in dense films. Literature sources were used as an initial guide to achieve stress compensation: low sputter pressure, typically resulting in compressive stress, could be compensated by substrate bias, which can

result in tensile stress [67–69]. After deposition of the tensile-test structure material the lift-off was performed by dissolving the top photoresist layer in acetone. The bottom resist layer was selected to be insoluble in acetone which ensured a clean and consistent lift-off of the tensile-test structure. Lift-off was continued until the structures were fully detached from the substrate and photoresist residues on the structure surface were fully dissolved. After lift-off, the structures were removed from the acetone individually and cleaned with a rinsing cascade of acetone and isopropanol to remove last remaining contaminations.

After lift-off, the freestanding structures were fixed in between two rectangular Si plates with Ag glue (G 3692, PLANO GmbH) to have a mechanically more stable assembly for subsequent handling and attachment to a holder that was fitted into the setup for mechanical testing (Fig. 26). The setup with Si plates and holder was used during initial testing. For later testing the setup was simplified by omitting the attachment to the holder and directly clamping the tensile-test structure at the glued Si plates.
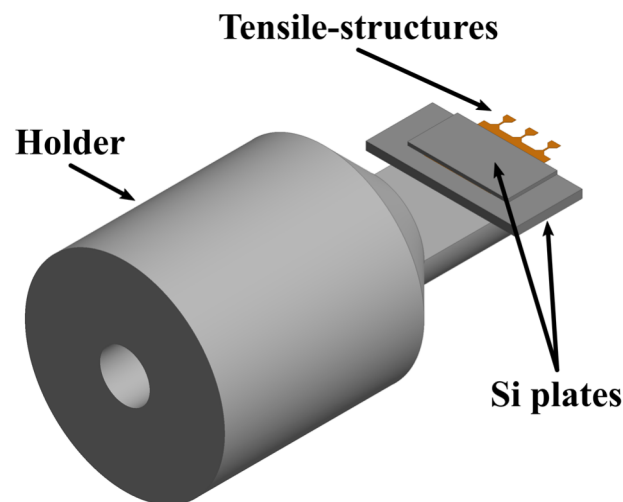
Fig. 26: Schematic assembly of the tensile-test structures and the holder that is fitted into the initial test setup. The structures were fixed in between two Si plates which were then attached to the holder.

2.7.5.3 Discussion

For evaluation of the fabrication process and mechanical testing, Cu tensile-test structures were fabricated. A freestanding tensile-test structure is shown in Fig. 27 a). With the selected process parameters, the structures remained in a flat shape after lift-off, which was of high importance for mechanical testing. To characterize the actual structure dimensions and influences of the polymer structure on the final geometry, cross-sections of the tensile-test

structures were prepared before lift-off while the structures were still attached to the Si substrate. The structure shown in Fig. 27 b) had a width and thickness of approximately 23 µm and 4.6 µm, respectively. Deviations of the structure thickness from the nominal value of 5 µm were caused by variations over the tensile structure array due to the sputter configuration with increasing thickness for substrate positions closer to the sputter sources. The top photoresist structure showed a curvature along the width of the gauge section which was reproduced in the deposited Cu film (Fig. 27 b)). The curvature was attributed to insufficient mechanical stability of the top resist layer due to the undercut of the lift-off resist underneath. During the development step of the fabrication process a lateral undercut with a size similar to the thickness of the lift-off resist was generated. The undercut was required for the lift-off step but approximately two thirds of the top resist remain mechanically unsupported, which resulted in the deformation. An additional influence on the geometry was deposition on the sidewalls of the top resist layer, which resulted in a triangular shaped overhang at the edge of the gauge. The deposition on the sidewall also extended to the side of the gauge area, which resulted in a semicircular sidewall geometry with increasing film thickness. The geometry at the sides was mainly caused by the confocal setup of the deposition system. With the low sputter pressure, the material flux was generally inclined towards a line-of-sight characteristic which allowed for more pronounced deposition on the structure sidewalls.
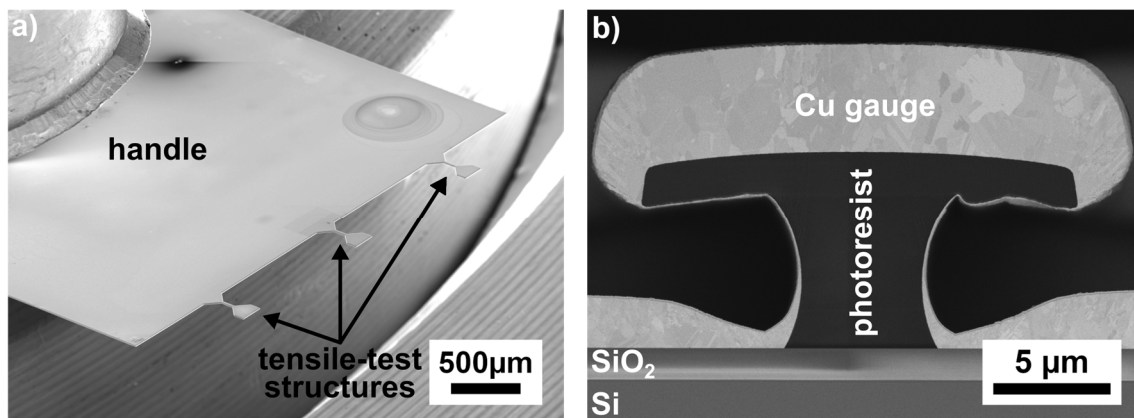
Fig. 27: SEM SED image of a) a fabricated thin-film structure with handle and three tensile-test structures. A circular discoloration in the corner of the handle structure was caused by residues that remained during evaporation of isopropanol during the last cleaning step. b) SEM image of a cross-section through the gauge of a Cu tensile-test structure, orthogonal to the gauge before release of the structure from the bi-layer photoresist.

Both, the curvature, and the overhang resulted in a process-related deviation from a rectangular cross-section. The cross-sectional area of the gauge was measured to be approximately 105 µm^2 by image analysis, which accounted for all geometrical features such

as curvature along the gauge width and the semicircular deposition on the sides into account. Coincidentally, this area was close to the area of a rectangle without geometrical deviations with a cross-sectional area of 105.8 μm^2 for the same dimensions of 23 μm width and 4.6 μm height. A drawback of the triangular shaped overhang was the possibility of stress concentrations in that area during loading which could have resulted in premature failure. This effect could be amplified when load imperfections (e.g., misalignment) were present, which could be detrimental in particular for brittle materials.

Execution of the tensile-test experiments required a specific orientation of the structure in the tensile-test apparatus. Initial tests showed significant deformations at the head of the tensile-test structures which resulted in undefined mechanical loading which could not be used to probe the material properties (Fig. 28 a)). It was observed, that under load, the head structure started buckling and bent in direction of the top surface. The deformation was caused by the shape of the structure sidewalls (semicircular) and gripper (straight). Upon loading, the initial contact in between the gripper and tensile-test structure occurred at the outer edges of the rounded sidewalls. In an ideal case the force would have been applied in horizontal direction as illustrated by red arrows in Fig. 28 b). The direction of the applied force was offset from the center of mass of the tensile gauge. Due to this effect a momentum was induced, which resulted in an initial upwards bending of the head structure, followed by subsequent buckling around the long axis of the structure. To counteract buckling of the head, the tensile-test structures had to be placed with the bottom surface facing upwards in the gripper structure. Additionally, the tensile-test structure was positioned in contact to the bottom surface of the gripper before the tensile test. In this configuration the moment was still induced upon loading but buckling of the structure head was constrained by the bottom surface of the gripper. To prevent pre-bending, the gripper and structure were not placed in direct contact, but with a remaining gap (≤ 1 μm) before testing. Due to the gap an out-of-plane bending of the structure head towards the gripper still occurred during the experiment which caused unwanted strain at the transition from gauge to the head. With the distance in between both structures a bending of approximately < 0.5 ° was expected. This behavior made it critical that fracture did not occur close to the structure head to perform valid experiments.
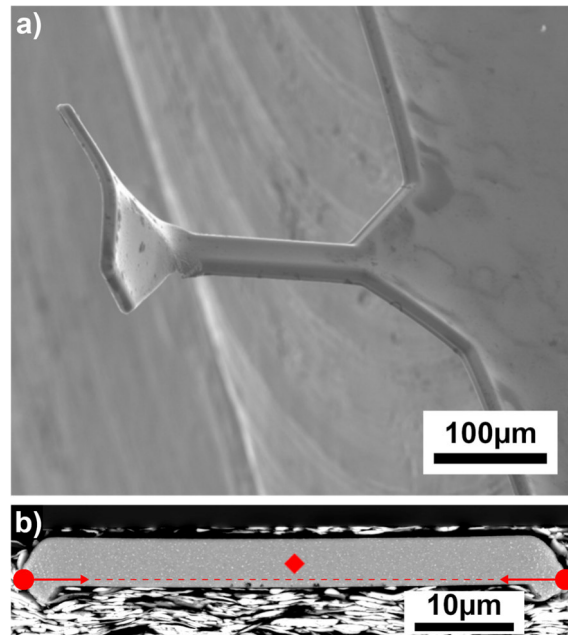
Fig. 28: a) SEM SED image of a failed tensile-test experiment due to bending and buckeling of the structure head. The head was bend in direction of the top surface. The experiment was stopped before fracture to illustrate the deformation. b) SEM BSED image of a cross-sectional cut through the head of a tensile-test structure. Indicated were the position of the first contact of the gripper structure with the tensile-test structure (●), the direction of the applied force (→) and the approximate center of mass (♦) of the cross-section.

An additional artefact from the fabrication process was observed at the bottom surface of the structure. Localized at the edges of the structure an additional, thin layer was visible (Fig. 29). The layer formed during thin-film deposition where a small fraction of sputtered atoms coated the underside of the photoresist structure by scattering in the Ar plasma (Fig. 29 a)). During lift-off the layer fractured at the connection in between the top and bottom resist layers, which was a mechanical weak point. After fracture, the layer on the underside of the top resist attached to the bottom surface of the structure and remained after drying (Fig. 29 b)). The layer had a thickness < 20 nm, approximately 0.4 % of the structure thickness. During execution of the tensile tests no detrimental effects on the stress-displacement data which correlate with failures in the artifact layer were observed. This was attributed to the low thickness relative to the structure thickness. But the layer could disturb image analysis during and after testing by blocking view on the structure surface.
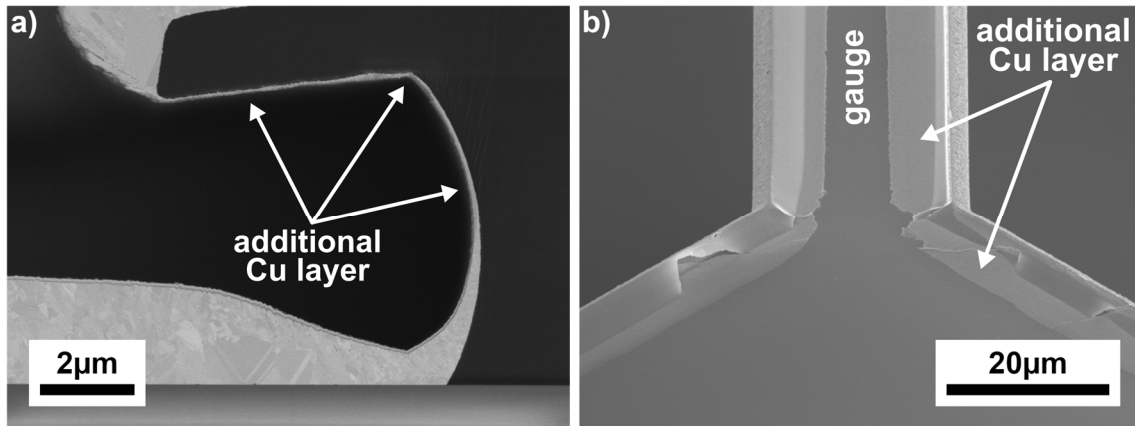
Fig. 29: SEM inlense detector image of a) a magnified view of a cross-section cut through the gauge on the lift-off photoresist. A thin Cu layer was located along the bottom and sidewall of the photoresist surface. b) SEM SED image of a tensile-test structure bottom surface at the transition region from the head to the gauge. An attached layer with a thickness < 20 nm was observed towards the edge of the tensile-test structure.

As the deposited material was in direct contact with the photoresist during deposition it was investigated if the resist acted as a source of contamination for the thin film. The investigation was required, because photoresists have limited stability under vacuum conditions or increased temperatures which were both present during deposition conditions and could have resulted in emission of contaminations through outgassing or thermal breakdown of the resist polymer. For characterization, depth dependent XPS measurements were performed on freestanding MAs starting from the bottom side which was in contact with the resist during deposition. Contaminations were investigated with regards to C and O contaminations which would have been expected as characteristic components of the polymer. H might also have been a possible contamination but was excluded during investigation as it was not possible to characterize H by XPS. Measurements were performed in depth increments of approximately 4.5 nm and compositional data was recorded for every step. At the MA surface significant C, O and Cu contents were measured with approximately 52 at.%, 33 at.% and 15 at.%, respectively. For increasing depth increments the contaminations decreased rapidly to a combined C and O content of approximately 1.2 at.% at a depth of approximately 4.5 nm and approximately 0.2 at.% at a depth of approximately 9 nm.

For both measurements below the surface the magnitude of the contamination content was within the standard deviation of the measurements. This indicated that contaminations were only present at the MA surface and the inner volume could be considered contamination free. Further it could be concluded that deposition on photoresist did not have a relevant influence on the contamination content of the deposited material.

68
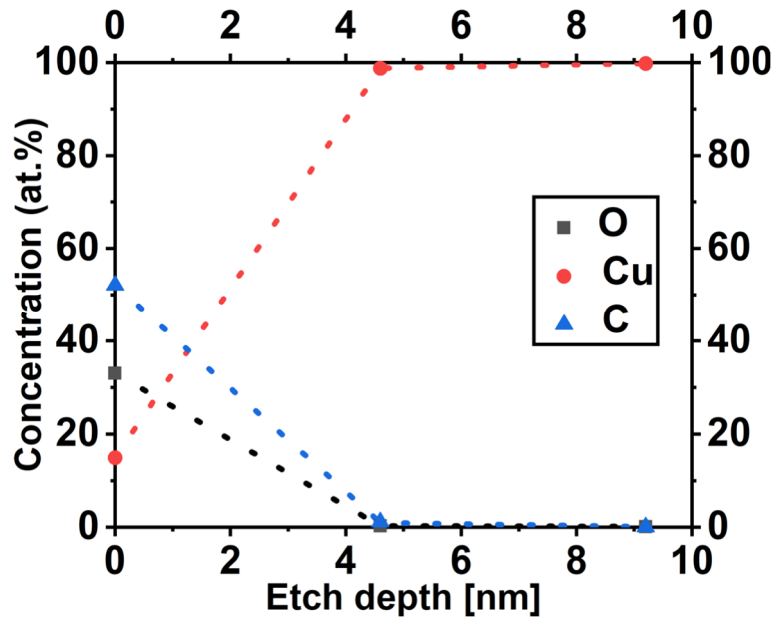
Fig. 30: Graph illustrating the depth-dependent elemental composition of a tensile-test structure from the BS surface of a MA which was in contact with photoresist during deposition. Surface contaminations with C and O were identified, but no contaminations in the bulk of the Cu layer were observed. Dashed lines act a guide for the eye.

2.7.5.4 Tensile-test experiments

For validation of the fabrication method and functionality of the tensile-test structures, pure Cu structures were fabricated, and tensile-tests were performed in the as-deposited state. The resulting stress-displacement graphs of two different, exemplary tensile experiments are shown in Fig. 31 a) and Fig. 32. The two experiments were selected to illustrate different effects that can occur during testing and their influence on the measurements.

The first experiment (Fig. 31 a)) was performed with a displacement rate of 40 nm/s (strain rate $\sim 4*10^{-4}$ s^{-1}) and the test was stopped before fracture to allow for post-mortem-analysis of the full tensile-test structure. In an ideal case, after initial contact of the gripper and the sample head, the stress should have increased linearly with increasing displacement in the elastic regime. For this experiment the stress-displacement did not show a linear regime and the slope increased directly after first contact of the gripper and structure. This was observed more clearly by plotting the first derivative (Fig. 31 a)) of the stress-displacement data, as it directly represents the slope. The initial increase for the first derivative was a result of a non-symmetric contact with the gripper and subsequent rotational deformation of the sample head as indicated in Fig. 31 b). This deformation was superimposed with the elastic regime and therefore it was not possible to measure the Young's modulus of the tested material. The initial misalignment might also have been responsible for the overall

shape of the curve with the two distinct stress maxima. The maxima correlated with necking in the gauge and the formation of an additional crack at the transition region from the gauge to the sample head. The formation of the necking and the crack correlated with the first stress plateau. Propagation of the crack stopped at the end of the first stress plateau. Necking in the gauge continued with the failure and correlated with the second stress plateau. The crack at the sample head might have been caused by the deformation induced by the initial angular misalignment between the structure and gripper. The alignment error was estimated by post-mortem image-analysis to be approximately 2.5 ° (Fig. 31 b)). Additionally, the image-analysis showed deformation of the structure head in the contact area with the gripper (Fig. 31b)). The deformation in displacement direction was estimated to approximately 1.5 - 2 µm. It was assumed that the deformation was caused by the small contact area of the vertical gripper and rounded structure sidewall during the initial contact (Fig. 28 b)). With increasing deformation, the contact area increased, which resulted in a decrease of the local stress until no further deformation occurred. Both, the displacement from the plastic deformation within the gauge section and additional deformation effects from the clamping were superimposed in the stress-displacement data. As a result, it was not possible to confidently identify the elastic regime and transition from elastic to plastic deformation with the associated mechanical properties. In this case the ultimate tensile strength was the main parameter that could be utilized for characterization, as it reflected the load that was definitively carried by the gauge and therefore the minimum strength of the material.
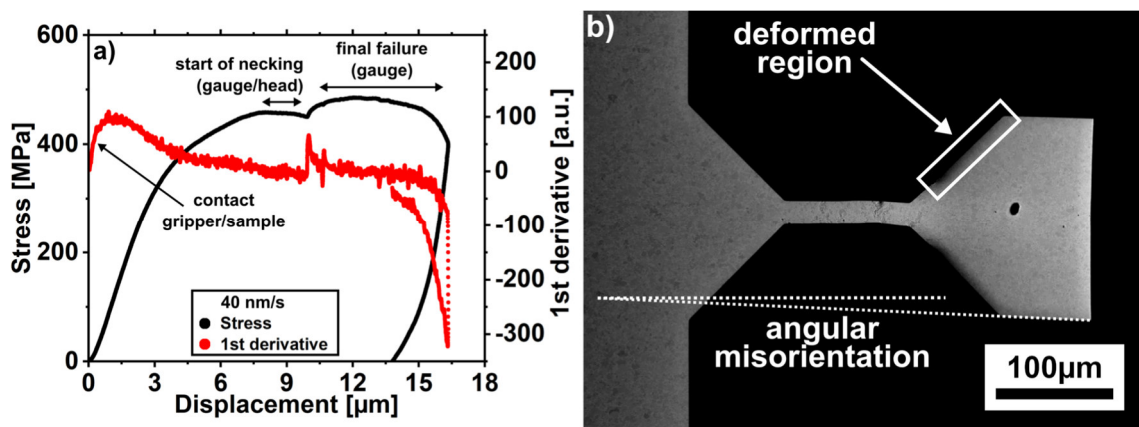
Fig. 31: a) Graphs of the stress-displacement data of a tensile-test experiment and the corresponding first derivative (red). The experiment was performed with a displacement rate of 40 nm/s. The experiment was stopped before fracture for post-mortem image acquisition. b) SEM BSED image of a strained tensile-test structure before fracture.

A second experiment (Fig. 32) was performed with a displacement rate of 400 nm/s (strain rate $\sim 4*10^{-3}$ s^{-1}) until fracture. The setup was well aligned and no significant

deformation of the tensile-test structure upon initial contact with the gripper was observed, as indicated by the linear behavior of the stress-displacement data. This was supported by the first derivative curve (Fig. 32), which showed an approximately constant slope for the elastic regime. With the better alignment only a single instance of necking occurred, followed by fracture in the gauge. The reduction of alignment-related errors allowed for evaluation of the linear elastic part of the stress-displacement curve. For this experiment, the Young's modulus was evaluated to approximately 90 GPa, which was approximately 23% lower compared to literature [70]. The compliance of the system was not considered for the experiments. Digital image correlation, as used by Smolka et al. [39] in a comparable setup, could be utilized here to obtain information regarding system compliance which would help to provide more realistic data on the elastic material behavior and accurate strain values. Due to these uncertainties, it was difficult to accurately separate elastic and plastic regimes and subsequently to evaluate Young's moduli. Therefore, the ultimate tensile strength (UTS) was used as the main parameter for mechanical characterization in this approach. Both experiments showed similar behavior during failure and approximate UTS of 485 and 528 MPa respectively. The average grain size (GS) of as-deposited Cu tensile-test structures was approximately 360 nm in the gauge area. The UTS values were in good agreement with literature values for tensile-test experiments which featured microscale dimensions or nanoscale GS, if GS dependent effects on the mechanical properties (e.g. Hall-Petch) were considered [35,36,39,71–76].
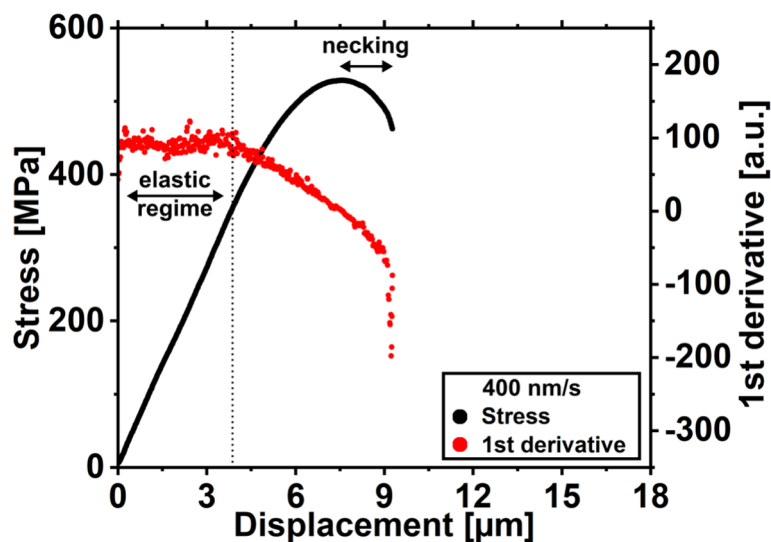
Fig. 32: Stress-displacement data of a tensile-test experiment and the corresponding first derivative (red). The experiment was performed with a displacement rate of 400 nm/s and the tensile-test structure was strained until fracture.

With this approach a throughput of approximately 2 MAs (6 tensile-test structures) per hour was achieved during testing at RT. The limiting factors were the preparation of the tensile-test structure assembly with the glued Si plates for clamping (approximately 15 min per MA) and the execution of the experiment in the utilized straining system (approximately 30 min per MA), which showed that the latter was the more important limitation for this specific constellation. The straining experiments required approximately 75 s per tensile-test structure (400 nm/s strain rate and 30 μm maximum displacement) and the remaining time was used for handling. Possible approaches to increase throughput were optimization of the structure insertion in the setup and automation of the alignment process. With faster processing of the structures in the test setup the main limitation would have shifted to the manual preparation of the tensile-test structure assembly. As automation of the assembly preparation would be a difficult process, a more targeted optimization would have been to avoid the required preparation steps by directly adapting a clamping mechanism in the straining device for direct clamping at the handle section of the MAs. This could have eliminated most manual handling in between structure release and testing.

2.7.5.5 Conclusion V3

This approach presented the first investigation process where both, the fabrication of the tensile-test structures and subsequent tensile-testing were executed successfully. The fabrication process itself was striking due to the simplicity and throughput for structure fabrication. Structuring was done exclusively by photolithography and no wet etching was required, because of which the process could be applied to practically all materials processable by sputter deposition. This was a significant advantage for the combinatorial fabrication of multinary MLs. With only a single exposure step and no backside processing of the wafer substrate it was also very simple to adapt the geometry of the tensile-test structures to investigate e.g., different size regimes or adapt geometry to a different nominal structure thickness. Limitations of the approach were primarily connected to the time required for handling of the structures after lift-off and execution of the straining experiments. Because the structures remained as freestanding thin-films after lift-off an additional handling structure had to be attached, which was difficult to automate and presented a significant time factor. The manual handling also introduced small variation in the handle in between different MAs which had to be adjusted during alignment in the test setup. To improve time efficiency, it is recommended to develop a fixture that could be utilized to clamp the structures in the test setup

in a pre-aligned state without the need to attach an additional handle to reduce manual handling. Furthermore, it would be possible to automate alignment in the setup by image analysis and a motorized stage to further improve automation. Beside throughput, the experiments were limited with regards to measurement quality and properties that could be acquired consistently due to the rounded sidewall geometry of the structures. A modified process for fabrication of improved geometries is presented in approach V5. Similar to approach V1, approach V3 was also limited in terms of possible heat treatments due to the use of photoresist during sputter deposition. The deposition was constrained to RT processes, as it was performed on top of resist for structuring, and it was only possible to perform annealing during post processing of the released structures. The most important limitation for the application of this process to combinatorial processing was the influence of residual stress on the structures. Depending on the stress characteristics, structures could deform significantly after release and be unusable for testing. Especially if more extensive composition spreads (e.g., full ternary system) were fabricated, it could be expected that stresses would vary over a ML. Stress optimization by adaption of process parameters would have been possible, but by design, modification of process parameters are aimed at optimization of target properties first and stress optimization second. Furthermore, optimization in one compositional region of the ML could negatively impact stress in other regions of the ML and it would need to be evaluated if acceptable stress over a full ML could be achieved while maintaining target properties.

2.7.6 Approach V4 – Corrugated structure fabrication by lift-off lithography

2.7.6.1 V4 Design

Approach V4 was developed as a modification of approach V3 to improve the mechanical stability of the tensile-test structure head to reduce deformations during testing. Approach V4 was developed to suppress bending and buckling under load in the "top side up" arrangement to avoid imaging of the additional layer on the structure BS and provide better in-situ observation. An effective mechanism for mechanical stabilization of thin films is the fabrication of corrugations to increase moment of inertia of the structure [77]. To fabricate the tensile-test structures and corrugations in a single deposition, the lift-off process was adapted by utilizing negative tone photoresists instead of the prior positive tone resist and an additional resist layer to structure the corrugations. This way only limited changes to the established process flow were required and lithography masks could be retained. But as the negative tone resist was no longer soluble in acetone it was required to utilize different solvents such as NMP, or DMSO. To limit chemical reactions of these solvents with the Cu base material exposure times during lift-off had to be limited. Similar to the approach V3, it was required to prepare a separate handling structure for testing and constraints in terms of in-plane structure geometries and structure thickness were similar due to the closely adapted lift-off process.

Different layouts of the corrugation structures were tested among multiple MAs where corrugations were fabricated on the handle structure and on the head of the tensile-test structures. An overview of the layouts and combinations that were tested was shown in Fig. 33. Handle structures were fabricated a) without, b) with hexagonal and c) with line-geometry corrugation layout. With three tensile-test structures per MA, two different corrugation layouts were tested for each MA with one tensile-test structure without corrugations as a reference (Fig. 33 d-e)). Similar to the handle structure, line-geometry and hexagonal corrugation layouts were tested. The orientation of the layout was adjusted to align with the forces introduced during contact with the gripper device in a tensile experiment to achieve better resistance against bending induced by actuation with the gripper.
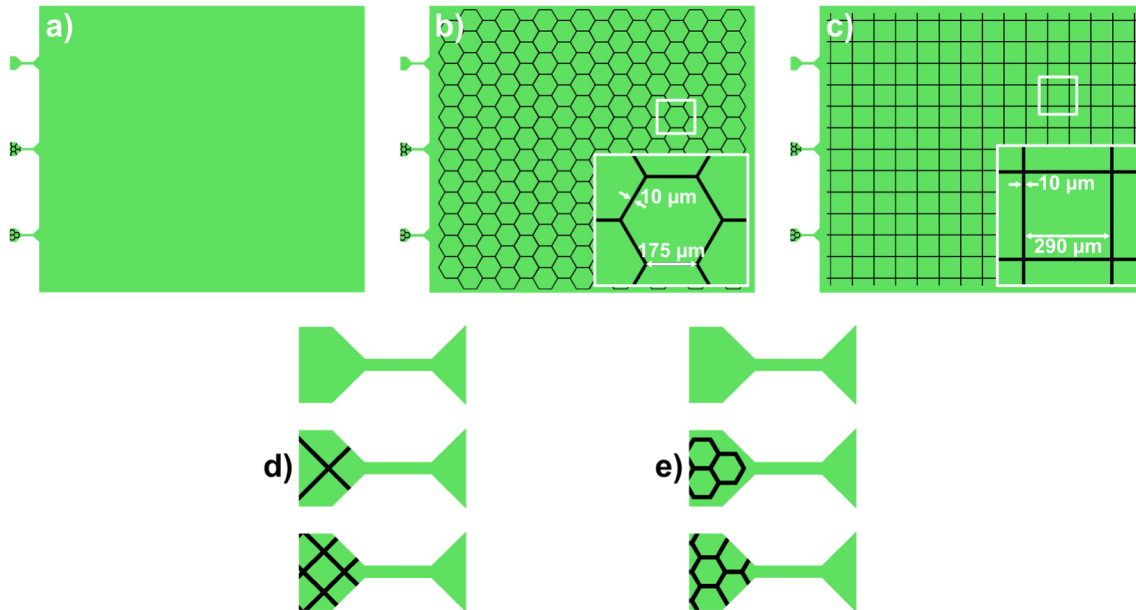
Fig. 33: Schematic illustration of tested corrugation geometries with a) one tensile-test structure without corrugations and two tensile-test structures with different corrugation geometries each and no corrugations on the handle, b) one tensile-test structure without corrugations and two tensile-test structures with different corrugation geometries each and hexagonal corrugations on the handle, c) one tensile-test structure without corrugations and two tensile-test structures with different corrugation geometries each and line-geometry corrugations on the handle. Corrugation geometries on the tensile-test structures were d) line-geometries with varying densities on the structure head, oriented orthogonal to the contact surface with the gripper and e) hexagonal geometries with different arrangements on the structure head.

2.7.6.2 Tensile-test structure fabrication process and material synthesis

Thermally oxidized 4-inch diameter Si (100) wafer substrates with a 1.5 µm thick SiO_2 diffusion barrier were used as a substrate for the fabrication process (Fig. 34 a)). In a first step a bilayer of non-photosensitive lift-off photoresist (LOR 20 B, MicroChem Corp.) with a combined thickness of approximately 6.6 µm was spin coated (Fig. 34 b)). The resist thickness was selected to be higher than the nominal thickness of the tensile-test structures (in the order of 2/3 of the resist thickness) to ensure a successful lift-off process. The two layers were deposited by two successive spin coating steps which were performed with a waiting time of 5 s in between the coatings. The individual coatings were performed with a dynamic dispense at a rotational speed of approximately 8.3 1/s (500 revolutions per minute (rpm)) over a time of 5 s, with a final rotation speed of approximately 16.7 1/s (1000 rpm) for 35 s and an acceleration of approximately 183.3 rad/s² (1750 rpm/s). After deposition of the bilayer a softbake was performed at 160 °C for 120 s. In the next step a negative tone photoresist with a thickness of approximately 6 µm (AZ 15nXT 115 cps, Microchemicals) was spin coated (Fig. 34 c). The

coating was performed with a dynamic dispense at a rotational speed of approximately 8.3 1/s (500 revolutions per minute (rpm)) over a time of 5 s, with a final rotation speed of approximately 16.7 1/s (1000 rpm) for 35 s and an acceleration of approximately 183.3 rad/s^2 (1750 rpm/s). After deposition, a softbake was performed at 120 °C for 120 s. Exposure of the top resist was performed (Fig. 34 d)) on a mask aligner (MA6/BA6, Süss Microtec) with a broadband UV Hg-vapor lamp with an I-line dose of approximately 300 mJ/cm^2 (approximated by 40 % of the broadband dose of the mercury vapor lamp). After exposure, the resist system was partially developed by immersion development in an aqueous-alkaline developer (AZ 726 MIF, Microchemicals) for approximately 10 s, followed by a rinsing cascade in deionized water (Fig. 34 e). Exposure was followed by spin coating of a second photoresist layer (AZ 15nXT 115 cps, Microchemicals) with a thickness of approximately 6 μm (Fig. 34 f)). The coating was performed with a dynamic dispense at a rotational speed of approximately 8.3 1/s (500 revolutions per minute (rpm)) over a time of 5 s, with a final rotation speed of approximately 16.7 1/s (1000 rpm) for 35 s and an acceleration of approximately 183.3 rad/s^2 (1750 rpm/s). After deposition, a softbake was performed at 120 °C for 120 s. Exposure of the top resist was performed on a mask aligner (MA6/BA6, Süss Microtec) with a broadband UV Hg-vapor lamp with an I-line dose of approximately 300 mJ/cm^2 (Fig. 34 g)). The exposure mask was aligned to structures fabricated during partial development of the first photoresist layer. After exposure, the resist system was partially developed by immersion development in an aqueous-alkaline developer (AZ 726 MIF, Microchemicals). Due to the combined thickness of all resist layers the immersion time was adjusted by optical observation of the progress during development. After development, the wafer was cleaned in a rinsing cascade with deionized water (Fig. 34 h)). After fabrication of the resist lift-of structure the deposition of the tensile-test structure material was performed (Fig. 34 i)). For deposition, a magnetron sputter system with a confocal target setup was used. The thin film was deposited by simultaneous sputtering of two diametrically opposed Cu targets (4-inch diameter, 99.999 at.% purity). The deposition powers (direct current) for both Cu targets were adjusted for a similar sputter rate of approximately 0.18 - 0.2 nm/s. Depositions were performed with an additional substrate bias (3 W, ~52 V, radio frequency) at a pressure of approximately 0.133 Pa (1 mTorr) with an Ar plasma at room temperature and a base pressure $< 2.7 \times 10^{-5}$ Pa. Deposition time was adjusted to achieve a film thickness of up to 5 μm. Sputter parameters were adjusted to achieve low stress variations and low porosity within the freestanding films. Low sputter pressure and additional bias were used to achieve increased incident energy during deposition resulting in dense films. Literature sources were used as an initial guide to achieve stress

compensation: low sputter pressure, typically resulting in compressive stress, could be compensated by substrate bias, which can result in tensile stress [67–69]. After deposition of the tensile-test structure material the lift-off was performed by dissolving the photoresist system in DMSO, followed by a cleaning cascade of acetone and isopropanol to remove possible contaminations (Fig. 34 j)). Exposure time to DMSO was limited to approximately 1800 s. Longer lift-off times in DMSO were only performed when the photoresist was not fully resolved, and structures were still attached.

After lift-off, the freestanding structures were fixed in between two rectangular Si plates with Ag glue (G 3692, PLANO GmbH) to have a mechanically more stable assembly for subsequent handling and attachment to a holder that was fitted into the setup for mechanical testing.
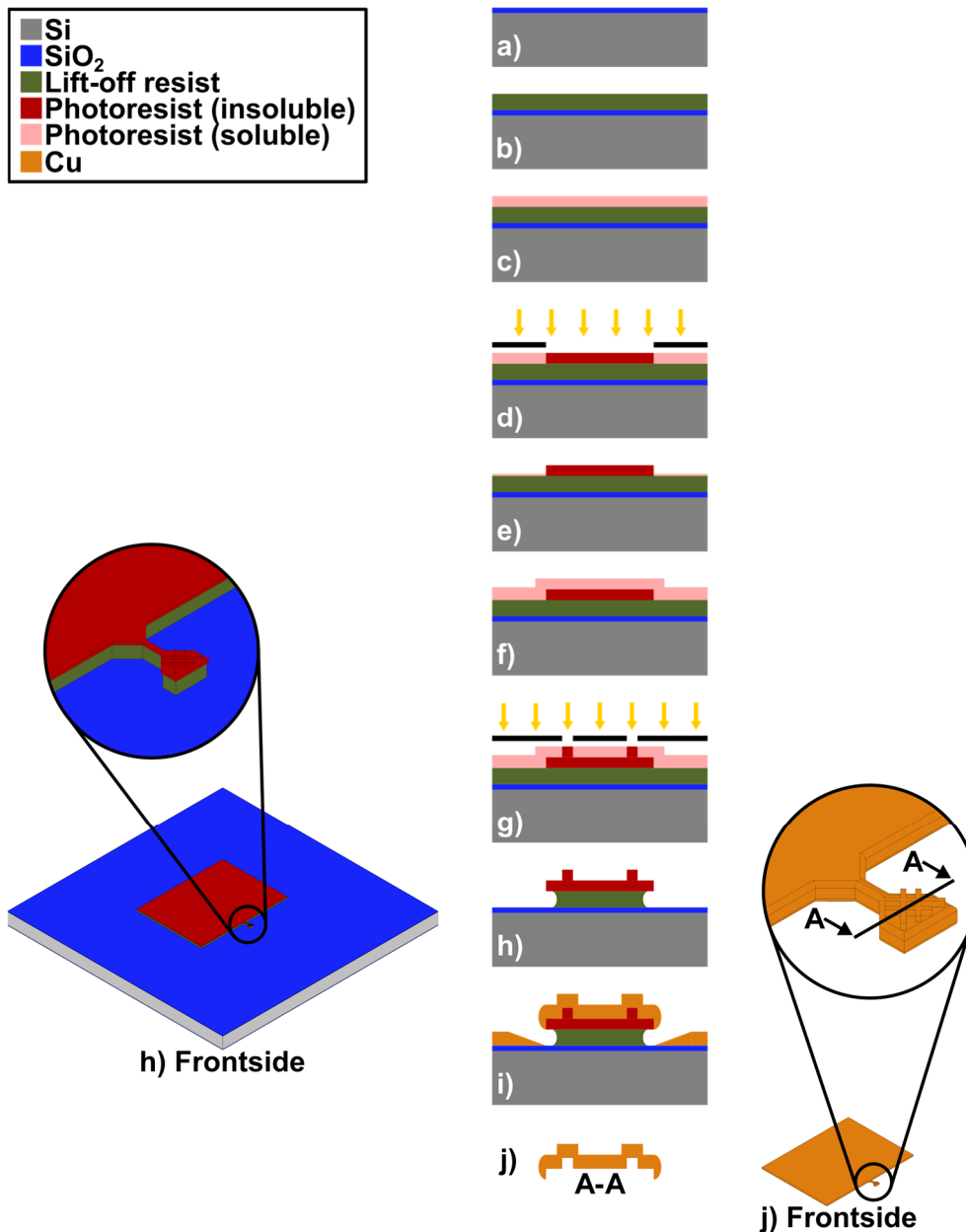
Fig. 34: Schematic process flow for fabrication approach V4 (not to scale). (a) thermally oxidized Si wafer, (b-c) FS bi-layer lift-off resist deposition, (d-e) FS photolithographic structuring of the top-layer photoresist and resist development was stopped before the top-layer photoresist was fully removed, (f) FS deposition of photoresist, (g-h) FS photolithographic structuring of the full resist system, (i) FS Cu deposition, (j) structure lift-off in DMSO and final rinsing cascade with acetone and isopropanol.

2.7.6.3 Important design features

In the following sub-section selected features are described/reiterated with the aim to clarify their purpose within the design. The features are presented in a separate section to highlight their importance, as they were essential to the overall process.

78

The first important design choice was the change from a positive to a negative tone photoresist. To achieve a time-efficient fabrication of the corrugated structure it was important to fabricate the tensile-test structure and the corrugations in a single deposition. This required 3-dimensional patterning of the photoresist to incorporate the lateral geometry of the tensile-test structure and elevated structures for the corrugations. The approach that was selected to achieve the 3-dimensional structure was by stacking multiple layers of a negative tone photoresist. The concept was based on the polymer cross-linking of negative resists during exposure which generated a layer that was insoluble during development. With the generation of a continuous, cross-linked resist structure with the lateral geometry of the tensile-test structure it was possible to perform an additional exposure on an additional photoresist layer coated on top of the first layer. This was possible, because a second exposure (see Fig. 34 g)) of the underlying layer during the second exposure for the corrugation structures only resulted in further cross-linking of the bottom resist and had no effect on the already insoluble state.

A second important process element was the partial development of the first AZ 15nXT photoresist (see Fig. 34 e)) opposed to fully developing the lift-off resist structure (AZ 15nXT and LOR 20 B). The partial development was selected to improve mask alignment during the second photolithography and secondly for better thickness homogeneity and step coverage during coating of the second AZ 15nXT layer (see Fig. 34 g)). The combined thickness of almost 13 µm and characteristic undercut of the LOR 20 B and AZ 15nXT resist system after full development would have resulted in resist pileups and inhomogeneous coverage of the lift-off structure. With partial development, only the approximately top 2 µm of the AZ 15nXT layer were dissolved and no undercut was generated, because the LOR 20 B layer was not developed. Due to the small step in the resist, it was possible to apply the second AZ 15nXT coating with improved homogeneity. The approximate 18.6 µm thickness of all resist layers (6.6 µm LOR 20 B + 6 µm AZ 15nXT + 6 µm AZ 15nXT) also required the fabrication of alignment marks close to the resist surface for the second exposure process (see Fig. 34 g)). Fabrication of the marks at the substrate surface was not possible, because the achievable alignment accuracy was insufficient due to the low image quality that could be acquired through the thick resist with the mask aligner optics. With the partial development it was possible to generate a structure closer to the top surface that allowed for precise alignment for the second exposure.

2.7.6.4 Discussion

To evaluate the stability of the structures against bending due to intrinsic stresses, as well as externally applied stress during tensile testing, pure Cu test structures were fabricated according to the prior process flow and tensile tests were performed. The geometry of the corrugations was successfully fabricated, exemplarily shown for a set of corrugated tensile-test structures in Fig. 35. The shown MA had no corrugations at the structure handle and (Fig. 35 b) and c)) hexagonal corrugations at the head structures with one reference head without corrugations (Fig. 35 d)). As observed in Fig. 35, the thin-film showed significant bending towards the handle edges and along the length of the tensile-test structures. This was not due to intrinsic stress, as the thin film was deposited under conditions identical to the structures in approach V3, where no extensive stress and bending was observed. Instead, the bending was a result of a fabrication error during structure lift-off in DMSO (see Fig. 34 i) to j)). The lift-off process had to be interrupted, and to limit the exposure of the Cu film to DMSO the wafer was transferred from the DMSO filled beaker to a beaker filled with acetone while the handle structures were still attached to the partially dissolved resist. After immersion of the wafer in acetone, the acetone rapidly removed the DMSO from the surface. But within this replacement process the structures were bend away from the wafer and the deformation partially remained afterwards. In Fig. 35 a) this could be especially observed at the handle section. Only the area of the handle close to the edge was bend upwards, whereas the central region, which was still attached to the resist structure, remained flat throughout the lift-off process.
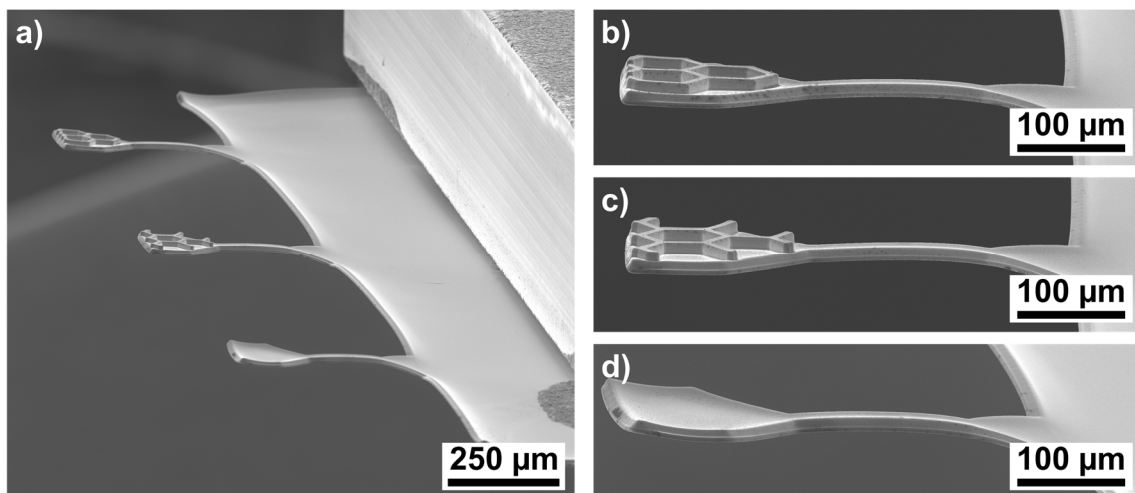
Fig. 35: SEM SED images of a) a tensile-test structure MA without corrugations on the handle after lift-off and with glued Si plates for mounting with respective magnified images of the tensile-test structure heads with b-c) hexagonal corrugation geometries and d) a reference head without corrugations.

Nonetheless, the increased stability due to the corrugations against material stress and external deformation was evident. Fig. 36 a-c) show a reference head structure and two head structures with line-geometry corrugations. Notable was the curvature along the width of the head which resulted from the intrinsic stress. The reference head showed the highest curvature which decreased with the increasing density of the fabricated corrugations (Fig. 36 d)). For the structure with the highest density of corrugations the stress was almost fully compensated and almost no curvature remained. While this example demonstrated the increased stability, the deformation due to the error during the lift-off process had to be avoided in future processes. To achieve this, it was important to perform the entire lift-off in DMSO in a single, uninterrupted process and only conduct cleaning in acetone after full removal of the structures from the resist.
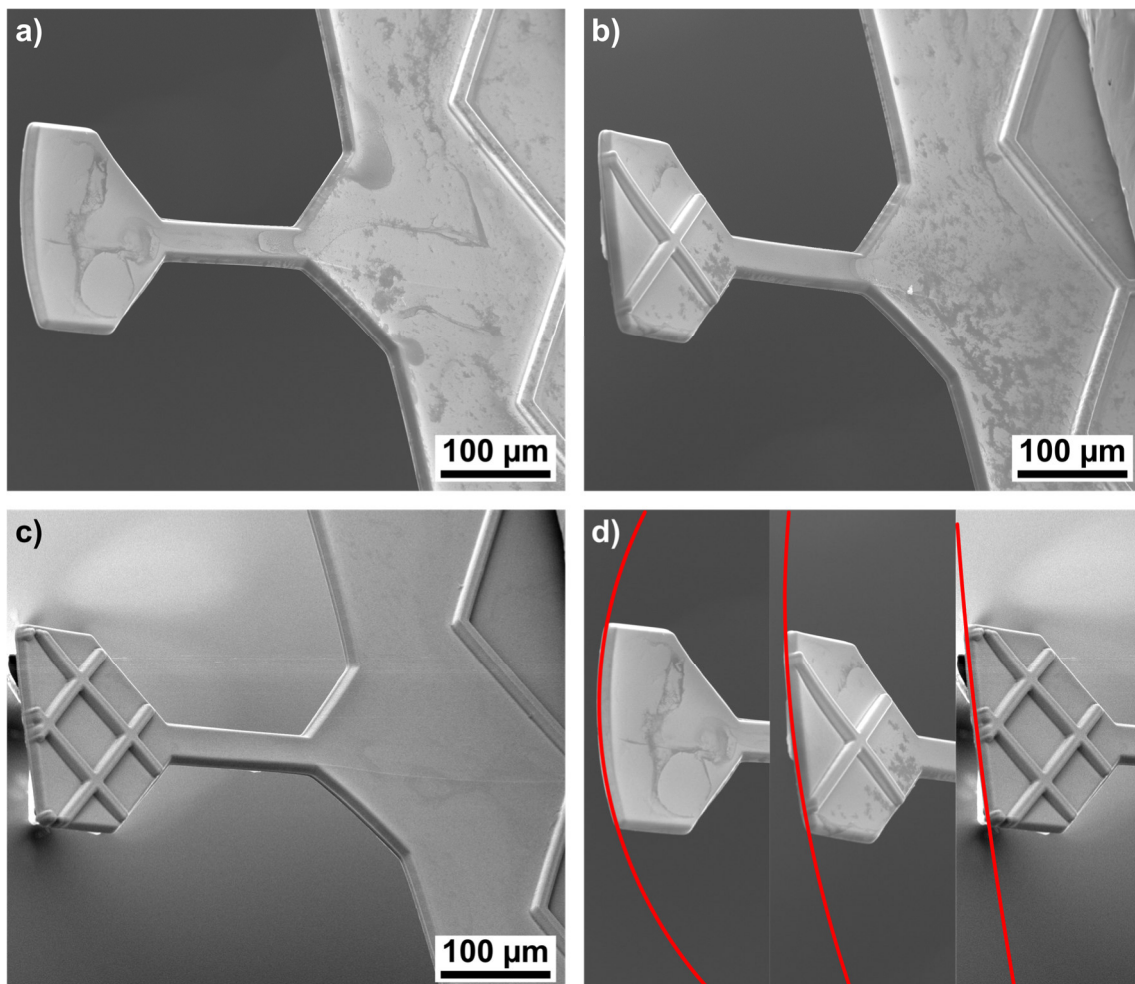
Fig. 36: SEM SED images of three tensile-test structure heads with from one MA with a) one reference head without corrugations, b) one head with two line-geometry corrugations and c) one head with four line-geometry corrugations. Image d) showed a side-by-side comparison of all structure heads to illustrate the influence of the corrugations on the structure deformation (bending radius indicated in red).

An interesting geometrical feature of the fabricated structures was a difference in sidewall geometry of the corrugations and the edge of the tensile-test structure. Both geometries were generated by deposition on the sidewall of similarly processed AZ 15nXT photoresist. Difference was that the sidewall of the tensile-test structure was formed by deposition on the bottom resist layer, and the corrugation sidewall by deposition on the top resist. Both sidewall geometries are shown in Fig. 37 a). Sidewalls of the tensile-test structure were angled by approximately 25° from the vertical whereas corrugation sidewalls had a vertical geometry with a radius at the top and bottom. The reason for this difference was of interest because a vertical geometry would have been beneficial to reduce bending during interaction with the gripper in a tensile experiment. But the reason for the geometry remained unclear. The only difference in the processing parameters for both photoresist layers was heat treatment, as the bottom photoresist was heat treated a second time during softbake of the top photoresist layer. Reflow of the bottom resist layer during softbake of the top layer was excluded as a reason, because the bottom photoresist was only partially developed during the process flow (Fig. 34 e), and therefore the generation of a sloped sidewall along the entire resist thickness was not possible. Reflow due to elevated temperatures during deposition was also excluded, as the top photoresist structure would have also been subjected to reflow and developed a sloped sidewall, but the structure remained vertical. Because the origin of the difference could not be identified, it was not possible to utilize this effect to improve the sidewall geometry of structures as they were fabricated in approach V3.

A drawback of this approach was the change to a negative-tone photoresist. Due to the increased polymer cross-linking during lithography, the photoresist was more difficult to remove during lift-off, despite the use of the stronger solvent DMSO. This was enhanced by the limitations with regards to process time, as extended exposure to the DMSO resulted in damage to the Cu due to chemical reactions. Consequently, the tensile-test structure BS and especially the corrugated structures had to be inspected individually for all MAs, because lift-off time to separate resist and thin film was typically insufficient to remove all resist residues from the trenches of the corrugations. Fig. 37 b) shows the BS of a corrugated head structure after lift-off with remaining photoresist. Removal of the resist in these areas was difficult, because the solvent could only penetrate slowly into the trench and resist residues had strong adhesion due to the large surrounding surface area of the trenches. Additional agitation (e.g., ultrasonic) for accelerated cleaning was not available due to the potential risk of damaging the tensile-test structures. With repeated cleaning cascades and visual inspection, it was possible to consistently remove the photoresist and allow for mechanical testing of the structures.
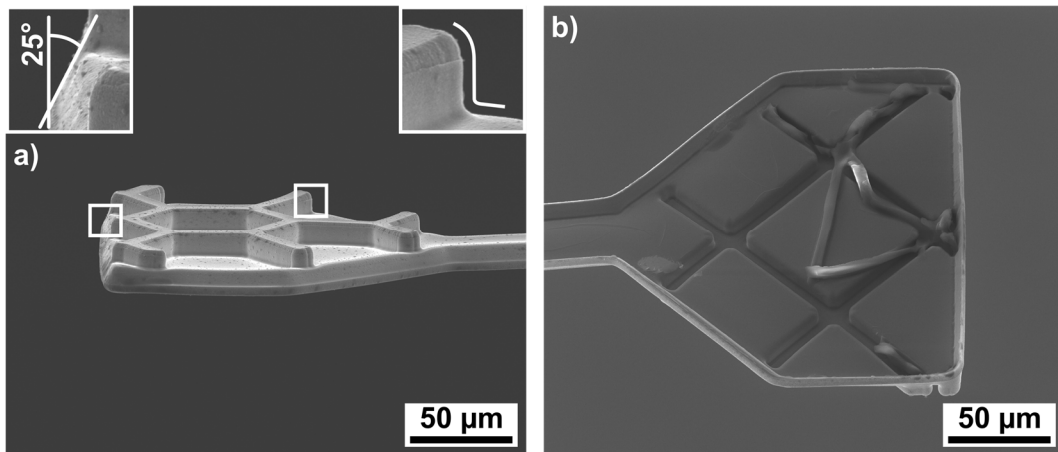
Fig. 37: SEM SED images of a) a corrugated tensile-test structure head from the FS with magnified inserts to illustrate sidewall and corrugation geometry, b) a corrugated tensile-test structure head from the BS with photoresist residues in the corrugations due to insufficient cleaning time.

After cleaning, the structures were prepared for mechanical testing according to the method established in approach V3. The structure handle was fixed in between two Si plates with Ag glue for better handling and the assembly was subsequently attached to a sample holder with Ag glue. During preparation it was observed that the corrugations in the handle area acted as mechanical weak points during manual manipulation with tweezers and during clamping in between Si plates and multiple structures were damaged (Fig. 38). Consequently, only structures without corrugations in the handle area were used for testing because the damaged corrugations significantly influenced the tensile experiments by deformation/failure in addition to the tensile-test structure.
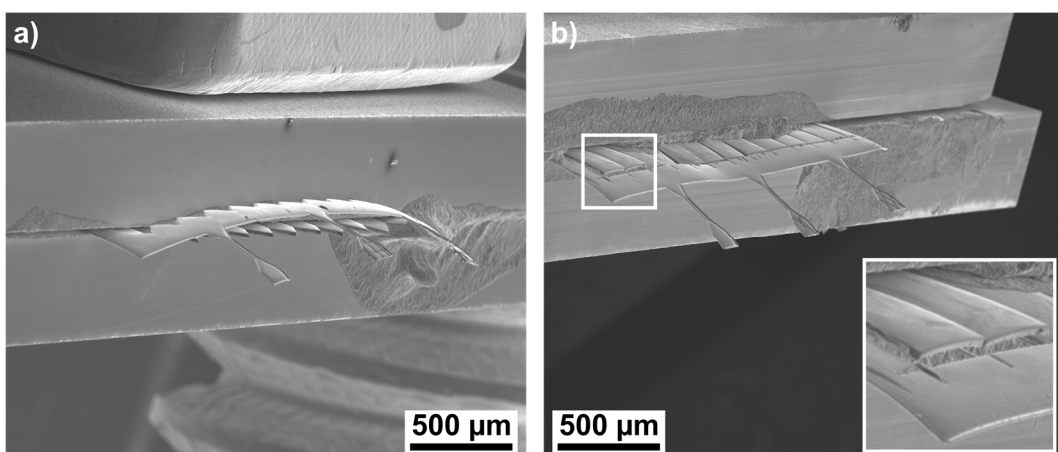
Fig. 38: SEM SED images tensile-test MAs with corrugated handle structures after gluing to Si plates for mounting. a) MA with hexagonal corrugations at the handle which fractured along the corrugation during clamping and gluing and b) MA with line-geometry corrugations at the handle with localized fracture of some corrugations due to manual handling.

But subsequent tensile-testing revealed, that the corrugations at the structure head also showed mechanical weak points under stress. In the initial stages of the straining experiments deformations at the structure head were significantly reduced, but with increasing stress the corrugations fractured along their top surface (Fig. 39 a)). After fracture, the structures either bent and buckled similar to structures tested in "top side up" configuration in approach V3, or fracture propagated through the rest of the head structure and the head was fully detached (Fig. 39 c)). Which case occurred was dependent on the corrugation layout. When corrugations were placed further away from the gauge (Fig. 39 b)) partial fracture with subsequent deformation was observed and when corrugations were placed closer to the gauge (Fig. 39 d)) structures fractured fully with detachment of the head. A closer look at a partially fractured structure revealed that the initial fracture occurred along an apparent interface located close to the top surface of the corrugations (Fig. 39 b)). This behavior was also observed for structures that fractured fully (Fig. 39 d)) where a clean fracture surface with low roughness was observed. The clean fracture surface further indicated a preferential failure along a mechanically weaker interface. It was assumed that the fracture surface represented a growth interface that formed during sputter deposition. The fabrication of the corrugations utilized deposition on a rectangular photoresist structure. During the deposition the main material flux was deposited on the top and sidewall surface of the photoresist. These films subsequently grew and connected at the corner in between both surfaces where the observed interface was formed. The interface was angled at approximately 45° which correlated with the assumption, that the interface grew simultaneously with the deposition on the side and top surface and started at the corner of the rectangular resist structure. Due to formation of the mechanically weak interface all tensile tests executed within this approach were unsuccessful due to premature fracture at the corrugations. It might have been possible to avoid interface formation by adjusted sputter conditions. An increased sputter pressure for example would have led to higher scattering of sputtered species, and potentially better coverage and more random microstructure close to the corner which could have reduced formation of such a localized interface. This approach was not tested, because the deposition pressure is an important parameter for adjustment of material properties in combinatorial sputtering and the structure fabrication process should not severely limit the range of available process parameters. Finally, the approach was not tested further, because the testing according to approach V3 in "bottom side up" configuration presented a simpler approach to limit deformations at the structure head.
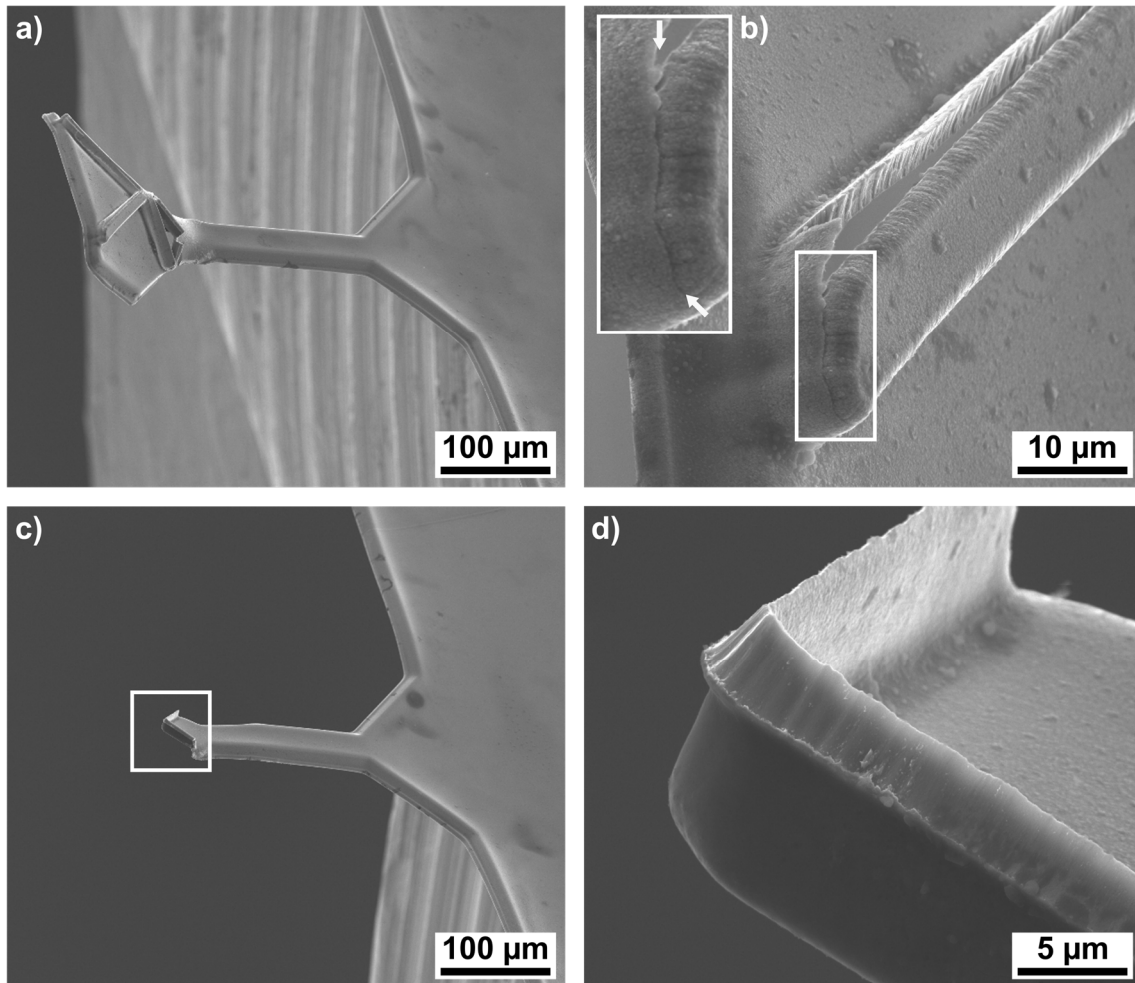
Fig. 39: SEM SED images of tensile-test structures with corrugated heads after straining in "top side up" configuration. a) Tensile-test structure with line-geometry corrugations which showed an upwards bend head and fracture along the length of the corrugations with b) a magnified view which showed that fracture occurred along a visible interface (marked in insert) along the top edge of the corrugations. c) Tensile-test structure with line-geometry corrugations which showed a removed head due to fracture along the length of the corrugations with b) a magnified view which showed the fracture interface, oriented at the top edge of the corrugations.

2.7.6.5 Conclusion V4

The process was specifically developed to improve the stability of the freestanding tensile-test structures against deformations from stress induced during displacement and intrinsic stress by fabrication of corrugations. Tensile testing revealed that the corrugation structures preferentially fractured under load at convex corners along what was assumed to be a growth interface. This prevented successful testing for all tested structures. It might have been possible to reduce growth defects by adaption of the deposition parameters (e.g., higher deposition pressure). But as mentioned prior, the main focus for selection of process parameter is the optimization of the target properties (e.g. the electrical conductivity here), whereas

optimization of intrinsic stress is only considered as a secondary target. It could have been possible to overcome the limited stability by changing the corrugation geometry (increasing the radius in between sidewall and top surface) and therefore avoiding the growth interface, but such geometry would have been difficult to fabricate. In terms of general properties, the main fabrication characteristics were similar to approach V3 with regards to the utilized techniques and the process consequently showed similar advantages and constraints.

The modifications for this approach had no relevant impact on high fabrication throughput established for approach V3, as only one additional lithographic step had to be added prior to the sputter deposition for fabrication of the corrugation structures. The fabrication of the corrugation required the change to negative tone photoresists which negatively impacted the applicability of the process to arbitrary materials due to the requirement for stronger chemicals during structure release. Consequently, for application of the approach to a material system the compatibility with the utilized chemicals should be tested before fabrication.

2.7.7 Approach V5 – Freestanding structure fabrication by lift-off lithography

2.7.7.1 V5 Design

The last investigated approach was a modification of approach V3 to improve structure geometry and subsequently reduce deformations during the tensile tests. In approach V3 it was concluded that especially the rounded geometry of the structure sidewalls led to bending of the structure head under load and ultimately failure of the experiments. This was overcome by placing the tensile-test structure in "bottom side up" configuration. But it was not possible to fully exclude detrimental influences on the mechanical testing in this configuration, as the stress that caused the bending/buckling was still exerted on the head structure and only the deformation was suppressed. For this approach, the structure layout from approach V3 was retained and an additional lift-off structure was fabricated in close proximity around the tensile-test structure with a defined gap in between both structures. The additional structure was intended to block the material flux that deposited on the sidewalls of the tensile-test structure. Without the structure continuous deposition occurred on the sidewalls which resulted in a rounded sidewall geometry (Fig. 40 left side). By simultaneous growth of a secondary structure

86

in close proximity, the material flux that would have been deposited on the sidewalls was blocked with increasing thin-film thickness, thus reducing the rounded geometry (Fig. 40 right side).

The gap in between the tensile-test and additional structure was varied over multiple structures to evaluate the influence of the gap on coating of the undercut of the lift-off geometry and the separation of the deposited structures. The gap was changed in a range of approximately 3.5 µm to 7.5 µm. Smaller gaps were not tested due to the resolution limit of the laser lithography system that was utilized for fabrication of the exposure mask.
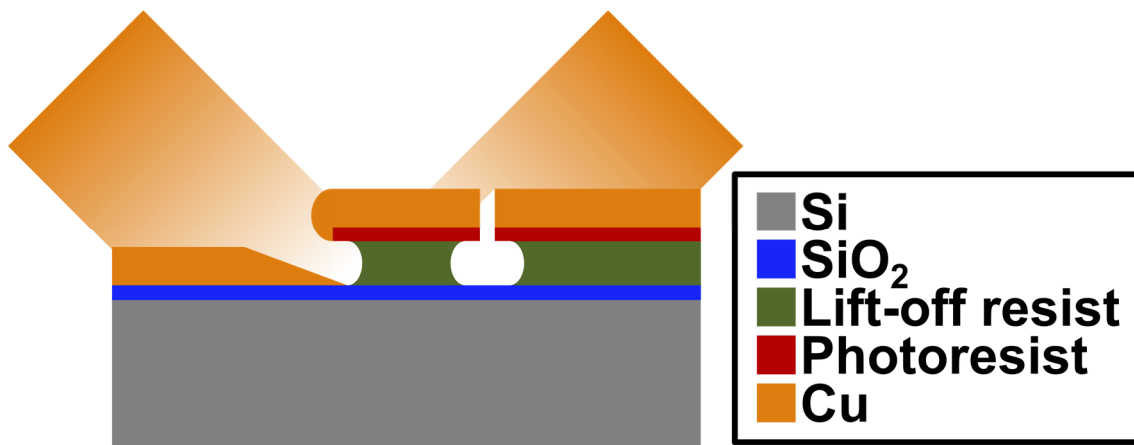
Fig. 40: Schematic illustration of the concept for approach V5. A secondary photoresist structure was fabricated in close proximity to the main structure. During Cu deposition the additional structure shields the sidewall of the growing Cu layer from the material flux to achieve a more vertical sidewall in contrast to the rounded geometry that is obtained on an unshielded sidewall.

2.7.7.2 Tensile-test structure fabrication process and material synthesis

Thermally oxidized 4-inch diameter Si (100) wafer substrates with a 1.5 µm thick SiO_2 diffusion barrier were used as a substrate for the fabrication process (Fig. 41 a)). In a first step a non-photosensitive lift-off photoresist (LOR 20 B, MicroChem Corp.) was spin-coated with a thickness of approximately 2.8 µm (Fig. 41 b)). The coating was performed with a dynamic dispense at a rotational speed of approximately 8.3 1/s (500 revolutions per minute (rpm)) over a time of 5 s, with a final rotation speed of approximately 100 1/s (6000 rpm) for 35 s and an acceleration of approximately 183.3 rad/s^2 (1750 rpm/s). After deposition, a softbake was performed at 160 °C for 120 s. In the next step a positive tone photoresist with a thickness of approximately 0.4 µm (AZ1505, Microchemicals) was spin coated (Fig. 41 c)). The dispense was performed dynamically at a rotational speed of approximately 8.3 1/s (500 rpm) over a time of 5 s, with a final rotation speed of approximately 100 1/s (6000 rpm) for 30 s and an

acceleration of approximately 183.3 rad/s^2 (1750 rpm/s). The softbake was performed at 100 °C for 50 s. Exposure of the top resist was performed on a mask aligner (MA6/BA6, Süss Microtec) with a broadband UV Hg-vapor lamp with a dose of approximately 55 mJ/cm^2 (Fig. 41 d)). After exposure, the resist system was processed by immersion development in an aqueous-alkaline developer (AZ 726 MIF, Microchemicals) for approximately 45 s, followed by a rinsing cascade in deionized water (Fig. 41 e)).

After fabrication of the resist lift-of structure the deposition of the tensile-test structure material was performed (Fig. 41 f)). For deposition, a magnetron sputter system with a confocal target setup was used. The thin film was grown by simultaneous sputtering of two diametrically opposed Cu targets (4-inch diameter, 99.999 at.% purity). The deposition powers (direct current) for both Cu targets were adjusted for a similar sputter rate of approximately 0.18 - 0.2 nm/s. Depositions were performed with an additional substrate bias (3 W, ~52 V, radio frequency) at a pressure of approximately 0.133 Pa (1 mTorr) with an Ar plasma at room temperature and a base pressure < 2.7*10^{-5} Pa. Deposition time was adjusted to achieve a film thickness of up to 10 µm. Sputter parameters were adjusted to achieve low stress variations and low porosity within the freestanding films. Low sputter pressure and additional bias were used to achieve increased incident energy during deposition resulting in dense films. Literature sources were used as an initial guide to achieve stress compensation: low sputter pressure, typically resulting in compressive stress, could be compensated by substrate bias, which can result in tensile stress [67–69].

After deposition of the tensile-test structure material the lift-off was performed by dissolving the top photoresist layer in acetone (Fig. 41 g)). The bottom resist layer was selected to be insoluble in acetone, which ensured a clean and consistent lift-off of the tensile-test structure. Lift-off was continued until the structures were fully detached from the substrate and photoresist residues on the structure surface were fully dissolved. After lift-off, the structures were removed from the acetone individually and cleaned with a rinsing cascade of acetone and isopropanol to remove possible contaminations.
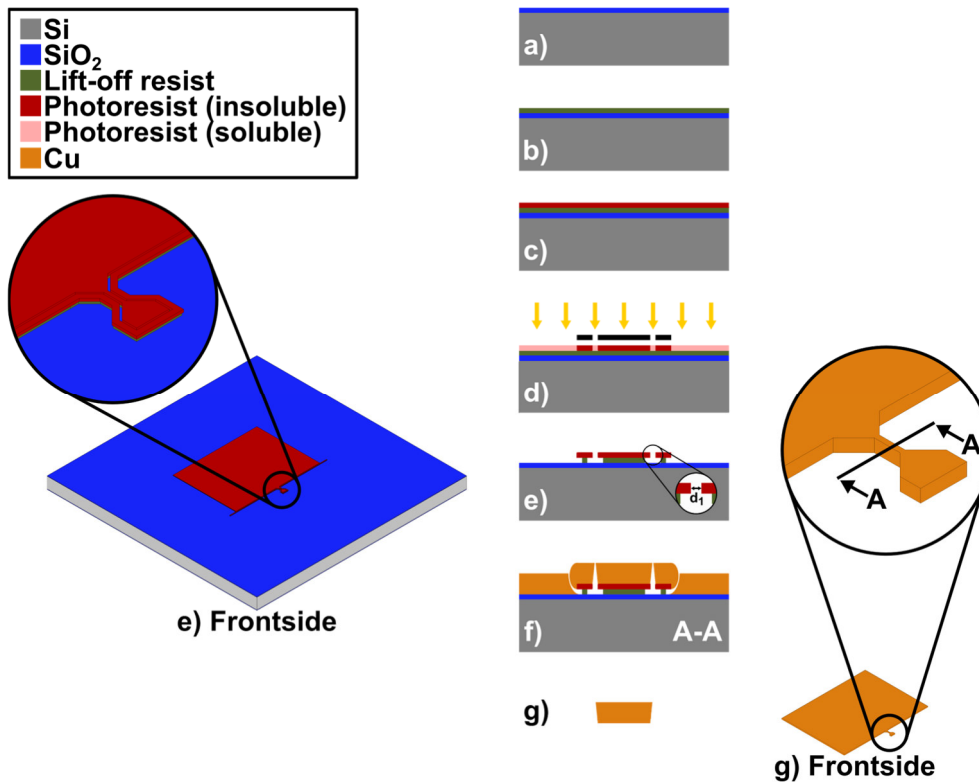
Fig. 41: Schematic process flow for fabrication approach V5 (not to scale). (a) thermally oxidized Si wafer, (b-c) FS bi-layer lift-off resist deposition, (d-e) FS photolithographic structuring of photoresist, (f) FS Cu deposition, (g) structure lift-off in acetone and final rinsing cascade with acetone and isopropanol.

2.7.7.3 Important design features

In the following sub-section selected features are described/reiterated with the aim to clarify their purpose within the design. The features are presented in a separate section to highlight their importance, as they were essential to the overall process.

The first important design feature was the distance d_1 (Fig. 41 e)) in between the top layer of the photoresist structures. For effective shadowing of the sputtered material flux, varying distances d_1 were explored with the aim to fabricate the gap as small as possible under restrictions of the utilized fabrication systems, as optimal tensile-test structure geometry was expected for a minimal gap.

The second important design feature was the thickness of the lift-off resist. The spin-coating parameters were selected to deposit the layer as thin as possible within the limitations of the coating system. A low thickness was selected, because there was very low risk of continuous deposition on the resist sidewalls at the tensile-test structure due to the shadowing by the additional structure. The reduction in resist thickness was important because it resulted in lower immersion times during resist development and subsequently, lower

undercut of the lift-off resist. With a smaller undercut the top resist layer was structurally supported over a wider area, which reduced the freestanding resist overhang that was prone to deformations during deposition (see approach V3). The added stability against deformation was expected to improve the final geometry of the fabricated tensile-test structures.

2.7.7.4 Discussion

Tensile-test structures were fabricated with a thickness of approximately 10 µm to test the limits of the lift-off process. It was expected to observe a relation in between gap d_1 and thickness that could be deposited before the separately deposited tensile-test and additional sides structures grew together. Interestingly, all deposited tensile-test structures remained separated from the material deposited on the additional structure. SEM observations of the top surface indicated that the lift-off was easy to perform in acetone due to the structure separation without a need for further agitation (Fig. 42 (a,b,c)). SEM observation of the structures showed the improvement in sidewall verticality with decreasing structure gap (Fig. 42 (d,e,f)). To characterize the structure geometry, structure separation and coating of the resist undercut cross-sectional cuts of structures with different gaps were fabricated by FIB milling (Fig. 42 (g,h,i)). These showed, that for all structures the transition from the bottom surface to sidewall and sidewall to top surface were always rounded with different radii that depended on the structure gap and the position towards the top, or bottom surface. Generally, the bottom radius was bigger than the top radius for all structures and radii decreased with decreasing structure gap. When the sum of both radii on a structure were smaller than the deposited thickness, the sidewall area in between the radii was defined by a straight section. As in approach V3, it was observed that a part of the material flux was deposited on the structure sidewalls and formed an overhanging structure. The width of the overhang decreased with decreasing structure gap. This was attributed to the shadowing effect of the additional structure which was more effective for smaller gaps. Image analysis (Fig. 42 (g,h,i)) indicated that the top gap d_2 and approximate overhang d_3 decreased with decreasing initial gaps d_1 for the investigated structure geometries. Structures were investigated for three initial gaps d_1 and the resulting geometries are summarized in Table 2.

Table 2: Overview of investigated structure geometries of the tensile-test structures and the additional adjacent structure.

Structure	d_1 [µm]	d_2 [µm]	d_3 [µm]
#1 (Fig. 42 (a,d,g))	3.5	< 0.1	1.5
#2 (Fig. 42 (b,e,h))	4.5	< 0.25	2
#3 (Fig. 42 (c,f,i))	7.0	1.5	2.5

According to the dependence of d_1 and d_2 it should have been possible to further reduce the initial gap d_1 without the risk of the Cu structures growing together. Further testing with smaller initial gaps in the photoresist layer would be required to evaluate this characteristic. The material deposited on the substrate and on the additional structure did not grow together, despite the small separation along the film thickness. This could have indicated that the shadowing effect had a stronger influence with decreasing gap, which possibly enabled even smaller gaps than extrapolated by the currently measured data points. In the investigated regime, the best sidewall geometry with regards to a straight sidewall and verticality (inclination of approximately 2 ° - 4 ° from vertical) was observed for the structures with the smallest gap (Table 2 #1, Fig. 42 (a,d,g)). The high verticality was important for interaction with the gripper during tensile testing to avoid out-of-plane bending, buckling and deformations at the contact point. Additionally, for all structures the triangular area of the overhang (see Fig. 27 b) in approach V3) that was deposited on the side of the photoresist was significantly reduced in comparison to structure fabricated by approach V3. The reduced deposition artifact was attributed to shadowing of the material flux, as further deposition in the area of the overhang was suppressed with increased deposited film thickness. The reduction of the artifact and especially the sharp corner at the bottom was important to increase confidence in the tensile test results. With suppression of the sharp corner, it was possible to reduce stress concentrations which could have induced premature failure, especially for brittle materials. Reduction of the artifact also improved the geometry of the gauge cross-section towards a rectangular area which simplified area calculation for later data analysis.
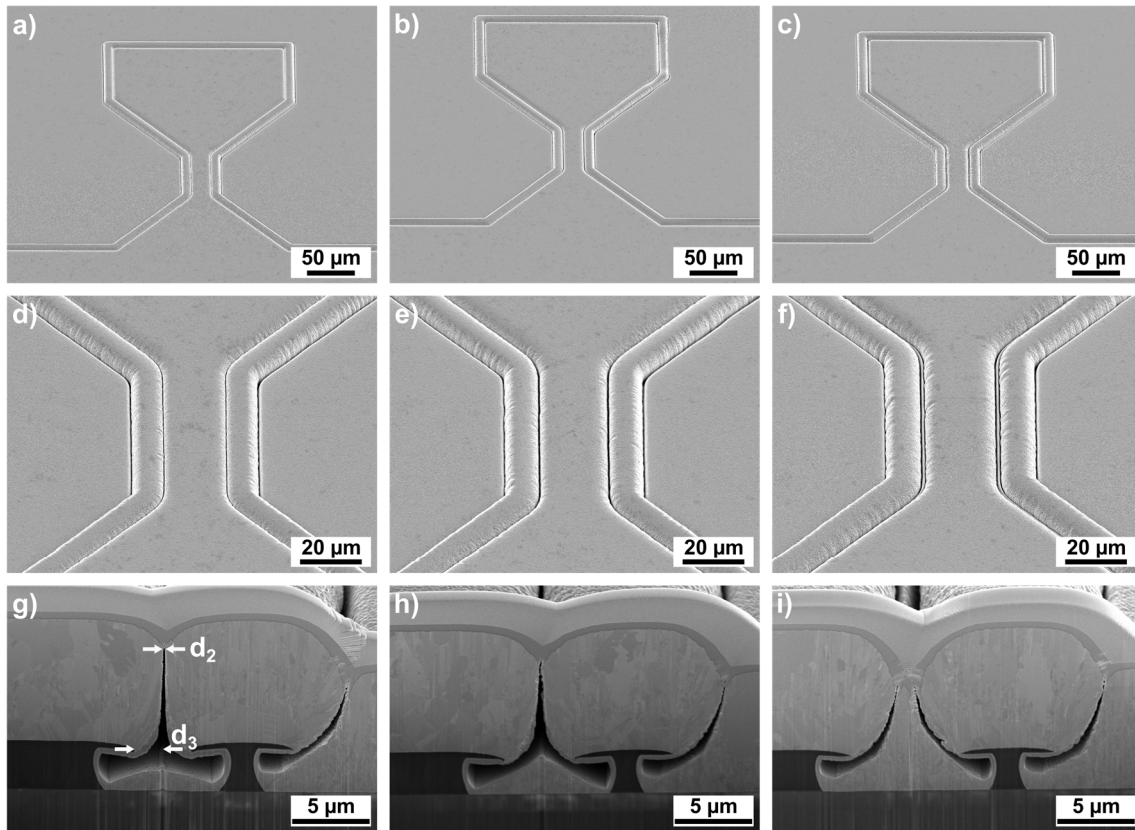
Fig. 42: SEM SED images of tensile-test structures before lift-off. a-c) Overview images of the structures with increasing gap d_1 with a) $d_1 \approx 3.5\ \mu m$, b) $d_1 \approx 4.5\ \mu m$, c) $d_1 \approx 7\ \mu m$, d-e) corresponding magnified images of the tensile gauge and g-i) FIB prepared cross-sectional images of the corresponding structures with a view of the gauge and additional side structure.

While formation of the triangular artifact was reduced, interestingly the deposition of material in the area of the resist undercut increased in comparison to approach V3. As approximately twice the Cu thickness was deposited in comparison to structures fabricated for approach V3 an increase of the layer thickness in the same order was expected, but a 10-fold increase was measured (Fig. 43 a)). The growth characteristics of the layer indicated that the layer was deposited after the geometry of the tensile gauge was already fabricated, because a clear interface was observed in between the layer and the gauge. Additionally, a layered microstructure was observed for the layer, whereas the gauge showed an isotopic distribution of grains. The layer was identified as Cu by area resolved EDX to exclude that Pt was deposited in the area during preparation for FIB milling. The layer might have been caused by redeposition of Cu during the FIB milling process which could explain the interface and layered microstructure. This was supported by the appearance of the layer after lift-off for a structure that was not FIB milled. In this case the gauge sidewall did not appear to have the attached layer on the gauge and the layer appeared thinner than the thickness of 220 nm (Fig. 43 b)).
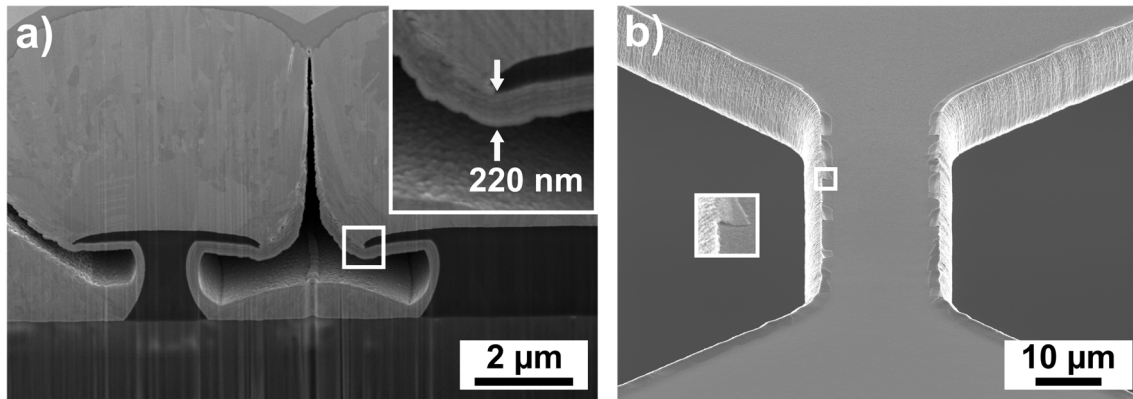
Fig. 43: a) SEM SED image of a FIB prepared cross-section of a tensile-test structure before lift-off fabricated with a gap $d_1 \approx 3.5$ µm with the thickness of the material layer deposited on the underside of the photoresist and sidewall of the lift-off resist indicated in the magnified insert. b) SEM SED image of the BS surface of the tensile gauge which showed the triangular overhang on the photoresist side and the additional layer from the photoresist underside that remained attached to the gauge after lift-off.

In comparison to fabrication method V3, V5-structures showed less curvature along the width of the gauge. This was achieved by the reduction of the lift-off resist thickness. With the thickness reduction it was possible to reduce the width of the lift-off resist undercut, which reduced the freestanding photoresist area which was bend and caused the curvature. Further reduction of the curvature at the edges would have been possible with a further reduced undercut. But as development rates were in the same order in horizontal and vertical direction, specific reduction of the horizontal development rate was difficult. It might have been possible to further reduce the lift-off resist thickness and therefore reduce the undercut, but this approach was not evaluated here.

2.7.7.5 Conclusion V5

Approach V5 was developed to primarily improve the sidewall geometry of the tensile-test structures and subsequently improve quality of the acquired data. The process was successfully modified from approach V3 and allowed for significant geometry improvements by fabrication of a secondary structure which reduced the material flux that contributed to the deposition on the sidewall. The geometry improvement depended primarily on the gap in between the secondary and tensile-test structure with improved geometry for decreasing gaps. The width of the smallest tested gap was defined by the resolution of the lithography equipment that was available, but it would be interesting to evaluate the influence of smaller gaps down to the limit of broadband-UV lithography on a mask aligner (approximately 0.8 µm – 1 µm) which could still achieve efficient fabrication throughput. It was not possible to test the structures due

to availability of the straining device and as such the influence of the improved geometry on the quality could not be demonstrated. In terms of general properties, the main fabrication characteristics were similar to approach V3 with regards to the utilized techniques. As such the process showed similar advantages and constraints.

3 Material investigations

3.1 Cu

Cu was selected for evaluation of the fabrication process and mechanical testing. Cu is widely used in the electronics industry due to its excellent electrical and thermal conductivity which is superior to other commonly used materials such as Al while being less costly in comparison to other materials with high conductivity such as Au and Ag. Substrate-bound and tensile-test Cu structures were fabricated to perform reference measurements of mechanical and electrical properties as a benchmark to determine possible influences of the used material synthesis and for comparison to literature, as well as subsequent investigations of alloyed structures.
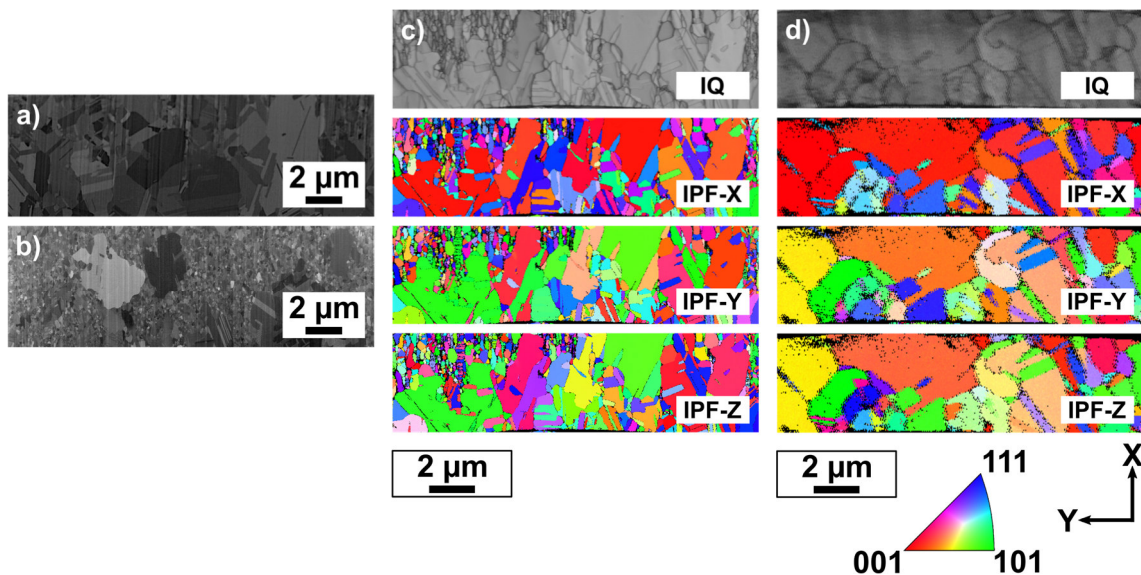
Fig. 44: SEM BSED images of a) a cross-sectional cut through the gauge of an as-deposited Cu tensile-test structure MA and b) a cross-sectional cut through an as-deposited, substrate-bound Cu MA. c) EBSD analysis with image quality (IQ) and crystal orientation (IPF-X/Y/Z) maps for an as-deposited Cu tensile-test structure MA. d) EBSD analysis with image quality (IQ) and crystal orientation (IPF-X/Y/Z) maps for an annealed Cu tensile-test structure MA. The X-axis represented the growth direction of the thin-film.

The average grain size (GS) of as-deposited Cu tensile-test structures was determined at cross-sectional cuts through the gauge section. The microstructure predominantly consisted of big grains (diameter > 2400 nm) with a low quantity that occupied the main area fraction and clusters of smaller grains (diameter < 1200 nm) located towards the top side of the structure

(Fig. 44 a)). In contrast, the microstructure of as-deposited Cu substrate-bound structures consisted predominantly of small grains with a high quantity and a low number of big grains (Fig. 44 b)). The position of the big grains did not exhibit a preferential orientation on the cross-section. Average GS of the substrate-bound structures was approximately 75 % of the GS in comparison to tensile-test structures with 358 nm to 274 nm respectively for as-deposited structures and 1186 nm to 915 nm respectively for annealed structures. After annealing tensile-test and substrate-bound structures, the cross-sectional microstructure consisted only of bigger grains and no small grains were observed anymore. A summary of the GS for Cu structures subjected to different heat treatments is summarized in Table 3. The microstructure of the investigated pure Cu structures did not show preferential crystal orientation for as-deposited structures as observed through EBSD measurements (Fig. 44 c)). For annealed structures, a preferential (001) crystal orientation in growth direction was observed (Fig. 44 d) IPF-Z) with no preferential orientation for the X- and Y-axis.

Table 3: Summary of average GS for Cu tensile-test and substrate-bound structures in the as-deposited and annealed state.

Cu reference		
T as-dep Cu GS	[nm]	358
T as-dep Cu std dev	[nm]	479
S as-dep Cu GS	[nm]	274
S as-dep Cu std dev	[nm]	382
T annealed Cu GS	[nm]	1186
T annealed Cu std dev	[nm]	928
S annealed Cu GS	[nm]	915
S annealed Cu std dev	[nm]	710

T → Tensile-structure MA
S → Substrate-bound MA

Mechanical characterization was performed through tensile testing of structures fabricated according to approach V3 and nanoindentation. Tensile tests were performed on structures in the as-deposited state at RT (Cu-T-AD-RT), in an annealed state (1800 s at 400 °C) at RT (Cu-T-A-RT) and in-situ at an elevated temperature of 400 °C where the structure was annealed (1800 s at 400 °C) prior to the test (Cu-T-A-IS). Nanoindentation measurements were performed on substrate-bound structures in the as-deposited state at RT (Cu-S-AD-RT) and annealed (1800 s at 400 °C) state at RT (Cu-S-A-RT).
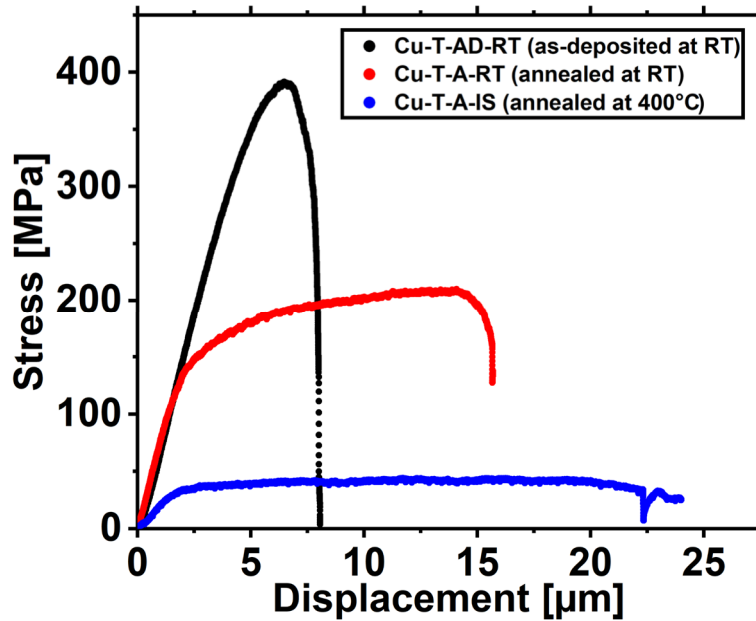
Fig. 45: Stress-displacement graphs for Cu tensile-test structure MAs with an as-deposited Cu structure tested at RT (●), an annealed Cu structure tested at RT (●) and an annealed Cu structure tested in-situ at 400 °C (●).

Stress-displacement data was obtained through tensile testing as described in section 2.6. A decrease in mechanical strength for different structure states was observed with UTS of approximately 400 MPA (Cu-T-AD-RT) in the as-deposited state, to approximately 200 MPa in the annealed state (Cu-T-A-RT), down to approximately 40 MPa at 400 °C (Fig. 45). Contrary to the UTS, the displacement to failure as well as plastic deformation in the gauge area increased with annealing and at elevated temperatures. Post-mortem investigations were performed on the structures to further characterize deformation and failure under load. As-deposited structures (Cu-T-AD-RT) showed only low ductility during failure with almost no necking in proximity of the fracture (Fig. 46 a-c)). Failure occurred quickly along a shear plane oriented at an angle of approximately 30 °, commonly observed for ductile materials [78]. Plastic deformations were only observed in confined areas distributed along the gauge. For annealed structures tested at RT (Cu-T-A-RT) failure occurred slowly with pronounced plastic deformation and fracture along an angle of approximately 15 ° (Fig. 46 d-f)). Plastic deformations were observed throughout the entire surface of the gauge and necking occurred before failure. For annealed structures tested in-situ at 400°C (Cu-T-A-IS) the further decrease in UTS was accompanied by a significant increase in elongation to fracture. During straining of the gauge pronounced intergranular failure was observed throughout the entire gauge which was not observed at RT (Fig. 46 g-i)). As with Cu-T-A-RT structures, failure occurred slowly with fracture along an angle of approximately 15°. The appearance of the intergranular failure also indicated that continuous grain growth occurred during testing at elevated temperatures

97

where average GS appeared to be in the µm-range. The ductile behavior of pure Cu and transition to intergranular fracture for elevated temperatures was also observed by Laporte et al. [79], and Ashby et al. [45,78] who summarized this behavior in deformation mechanism maps for different tensile stresses, temperatures, and GS. The significant increase in ductility at elevated temperatures was also consistent with literature results for tests performed with low impurity pure Cu, which were comparable to the conditions within this study.
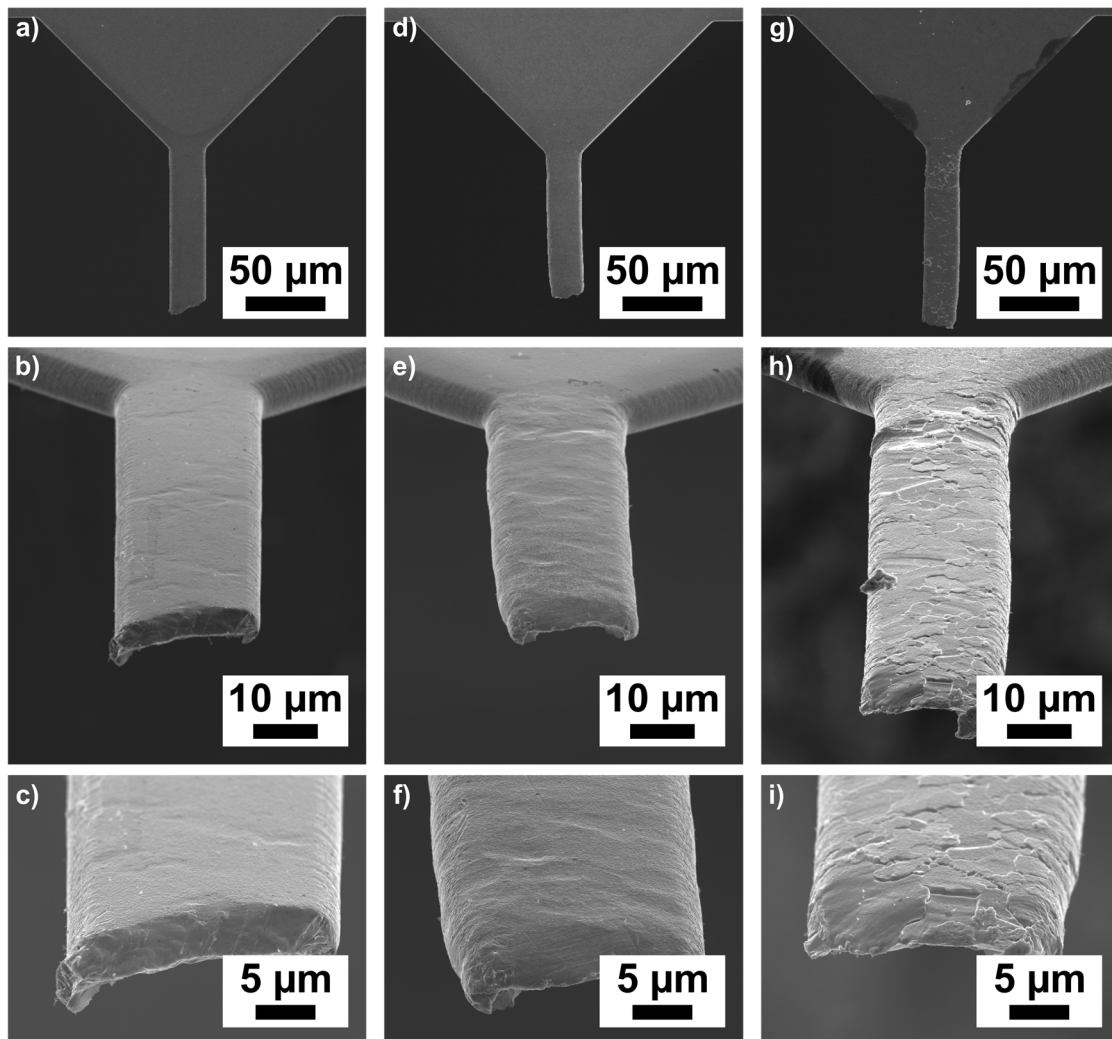
Fig. 46: SEM SED images of Cu tensile-test structures after testing. (a-c) Post-mortem images of an as-deposited structure after testing at RT with a) a top-down view of the FS, b) a magnified angled view of the gauge and fracture surface and c) a magnified view of the fracture surface. (d-f) Post-mortem images of an annealed structure after testing at RT with a) a top-down view of the FS, b) a magnified angled view of the gauge and fracture surface and c) a magnified view of the fracture surface. (g-i) Post-mortem images of an annealed structure after in-situ testing at 400 °C with a) a top-down view of the FS, b) a magnified angled view of the gauge and fracture surface and c) a magnified view of the fracture surface.

As indicated, a decline in UTS and increase in ductility were observed from as-deposited to annealed tensile-test structures tested at RT. The decline in UTS was attributed primarily to

grain coarsening, as described by the Hall-Petch relation which introduced a general correlation in between GS and mechanical properties [5,10]. The Hall-Petch relationship is shown in equation Eqn.1 with σ_y being the yield strength, σ_0 and k material specific constants and d the GS.

$$\sigma_y = \sigma_0 + \frac{k}{\sqrt{d}}$$

Eqn. 1

In this study, UTS values observed for pure Cu structures tested at RT were in good agreement with literature values for tensile-test experiments if GS dependent effects on the mechanical properties (e.g. Hall-Petch) were considered [35,36,39,71–76]. Fig. 47 shows a collection of UTS values plotted over GS with data points taken from this study and investigations from literature which featured microscale dimensions, or nanoscale GS. Approximation of the data by a linear fit resulted in a slope of approximately 2900 MPa / $d^{-1/2}$ nm$^{-1/2}$ for the development of UTS with decreasing GS.
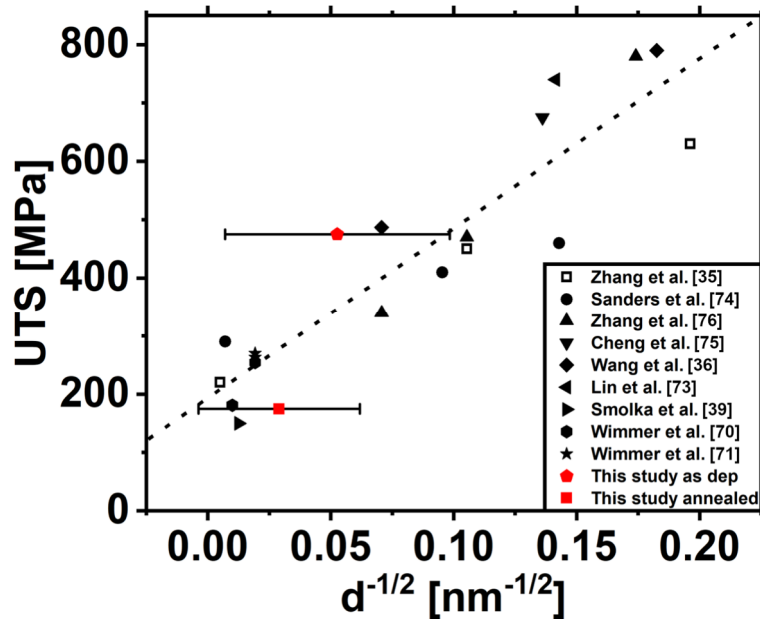
Fig. 47: Graph of UTS over inverse GS with data points of various studies from literature and from this study. The dashed line indicates the linear fit over data points acquired from literature. [35,36,39,71–76]

Nanoindentation hardness measurements were performed for comparison on as-deposited (Cu-S-AD-RT) and annealed (Cu-S-A-RT), substrate-bound MAs. Measured hardness was approximately 1600 MPa and 1400 MPa respectively. The observed strengthening with decreasing GS was consistent with the approximation assumed for tensile

tests (Fig. 48). The verification of this behavior by nanoindentation served as a confirmation for the development of the mechanical properties that were acquired through the newly developed straining device [80].
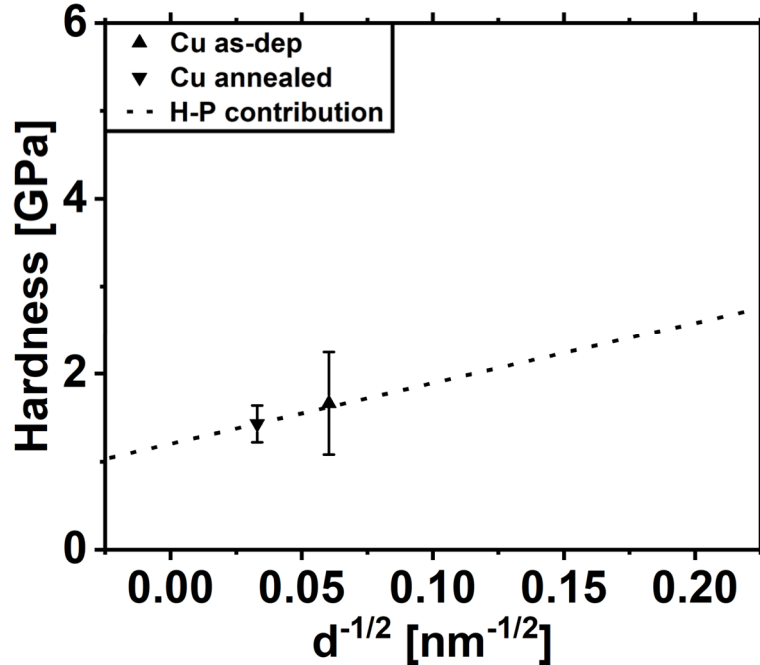
Fig. 48: Nanoindentation hardness over GS of substrate-bound Cu MAs obtained for MAs in the as-deposited and annealed state with measurements at RT. The dashed line indicated the expected contribution of GS dependent H-P strengthening.

For as-deposited structures deviations in the measurements were observed, indicated by the error bar (Fig. 48) which was expected to be a result of the microstructure. For as-deposited MAs (Fig. 49 (a,b)) the average GS was quantitatively dominated (~ 90 %) by grains with a diameter < 600 nm. But with regards to area fraction, > 60 % of the MA cross-section were covered by grains with a diameter > 2400 nm which quantitatively represented less than 5 % of the grains. For annealed MAs (Fig. 49 (c,d)) the average GS was quantitatively dominated (~ 70 %) by grains with a diameter < 1200 nm. But with regards to area fraction, ~ 50 % of the MA cross-section was covered by grains with a diameter > 2400 nm which quantitatively represent less than 5 % of the grains. As such, it was highly likely that idents were located in regions dominated by grains with above-average size where Hall-Petch strengthening would have been negligible, or with below-average size where Hall-Petch strengthening would have been more pronounced. This likely resulted in the high observed scatter.
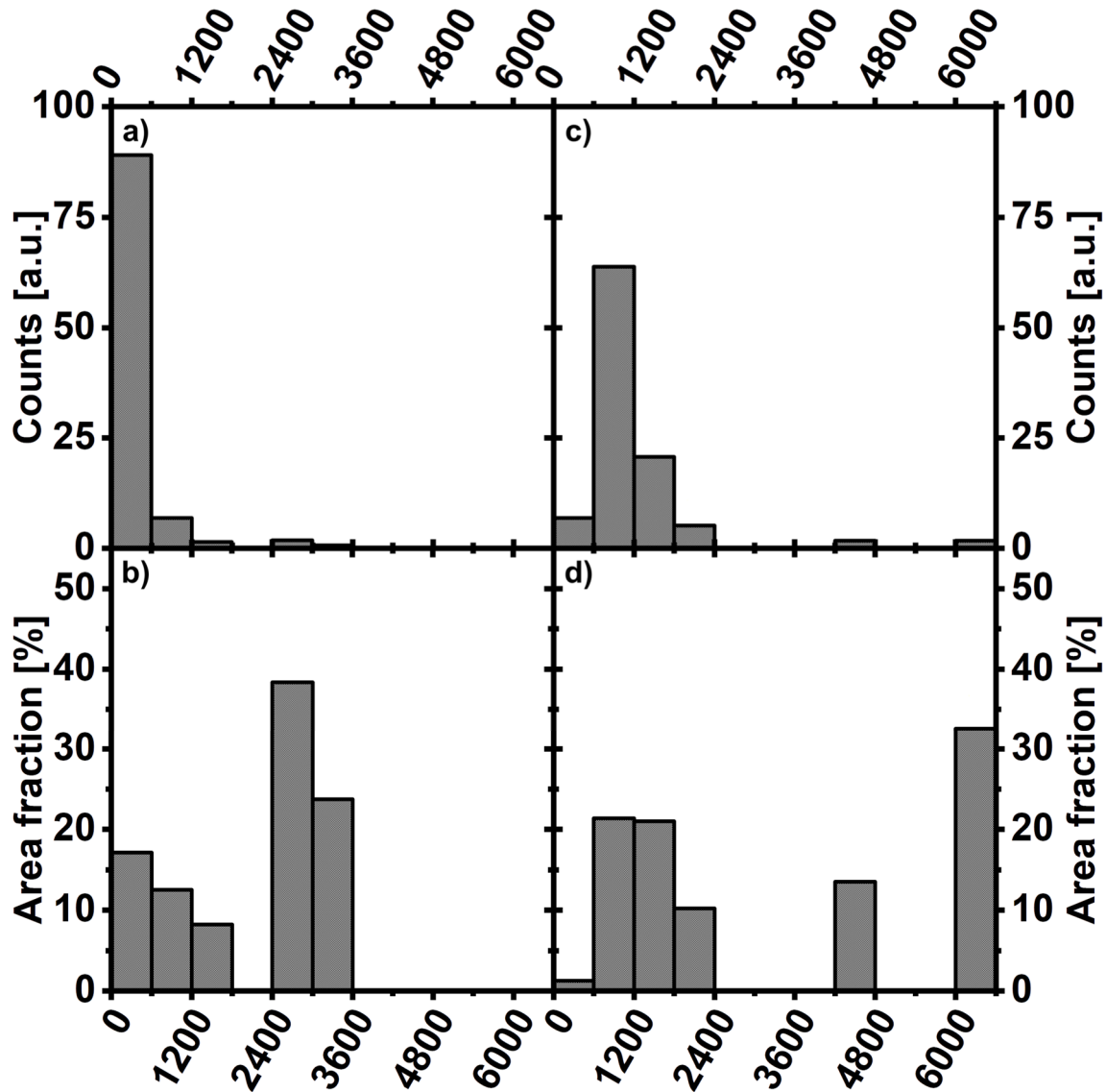
Fig. 49: Comparison of the GS distribution by quantity of grains (counts) and area fraction of grains for GS increments of 600 nm. Graphs show the comparison for substrate-bound (a,b) as-deposited and (c,d) annealed MAs.

To evaluate electrical properties of the deposited pure Cu material sheet resistivity measurements were executed on substrate-bound MAs. For as-deposited MAs a resistivity of $1.95*10^{-8}$ Ωm was measured. After annealing the resistivity showed a further reduction to $1.78*10^{-8}$ Ωm which corresponded to a conductivity of 97 % of the IACS [81]. Fig. 50 shows a comparison of the measured resistivity with a calculated approximation for pure Cu. The measurements were close to the expected resistivity with respect to the actual GS of the MAs, which indicated that the synthesized base material did not contain a significant amount of contaminations. Calculations were performed according to a model from Mayadas and Shatzkes [82] according to Eqn. 2. Calculations were performed with an assumed Cu bulk resistivity of $\rho_i = 1.7*10^{-8}$ Ωm [83], Cu electron mean free path of e = 39 nm [84] and reflection coefficient R = 0.47 [83]. Interestingly, the resistivity for the as-deposited MA was below the calculated

value which was most likely caused by the heterogenous size distribution of the Cu grains, as networks of adjacent grains with above-average size could have allow for easier electron transport in comparison to a more homogenous distribution of grains with similar size. This effect was more pronounced at smaller average GS, as the resistivity increased significantly with a non-linear behavior when the GS approached the electron mean free path of a material.

$$\rho = \rho_i * 1 + \left(\left(\frac{3}{2} \right) * \left(\frac{e}{GS} \right) * \left(\frac{R}{1-R} \right) \right) \qquad \text{Eqn. 2}$$
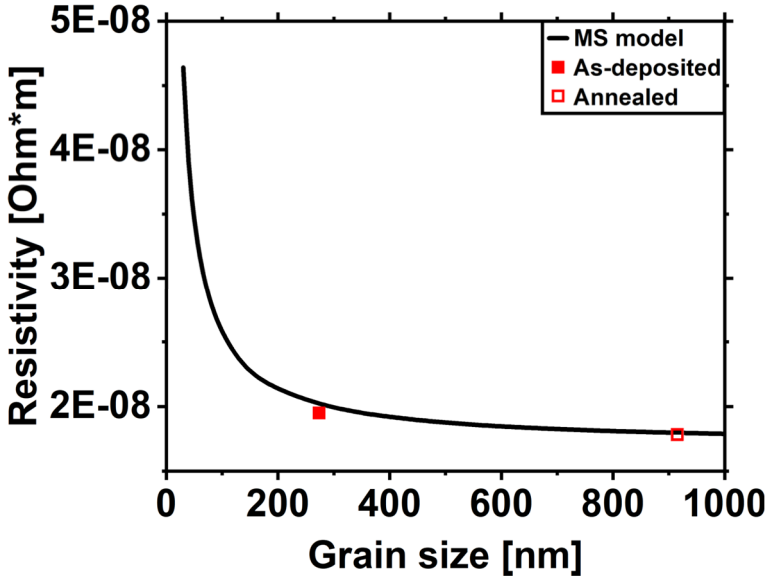
Fig. 50: Plot of electrical resistivity over GS for substrate-bound Cu MAs measured in the as-deposited and annealed state. The black line indicated the calculated resistivity over GS after Eqn. 2.

3.2 Cu-Ag

For a second study the Cu-Ag system was selected as a model system to validate the developed approach for utilization in a combinatorial investigation. Cu-Ag was especially suitable for investigation, because a linear behavior of the target properties was expected with increasing Ag content due to the expected linear evolution of GS and Ag precipitates with increasing Ag content. Further, Cu-Ag was of interest because of the high potential for application due to good electrical properties that were observed in bulk and thin film, as well as a lack in literature with regards to mechanical investigations for thin-film applications.

Cu-Ag is a eutectic system with limited solubility of Ag in Cu at RT and a very large compositional range where Cu and Ag are immiscible (Fig. 51). Consequently, for microstructure, a solid solution and supersaturated solid solution were expected throughout the synthesized compositional range for the as-deposited state, as the RT deposition likely would not have provided sufficient energy to enable the formation of Ag precipitates. In the annealed state, due to the low solubility of Ag in the Cu lattice, it was expected that most Ag content formed precipitates with increasing precipitate quantity/size for increasing Ag content. But final precipitate quantity/size was difficult to predict and would depend on the actual annealing conditions. This behavior did significantly simplify validation of the experimental results, as alloys with the expected microstructure would have exhibited linear relationships in between composition and electrical/mechanical properties. Therefore, non-linear trends in the development of the functional properties would have directly indicated inconsistencies in the measurements, or additional influences on the properties.
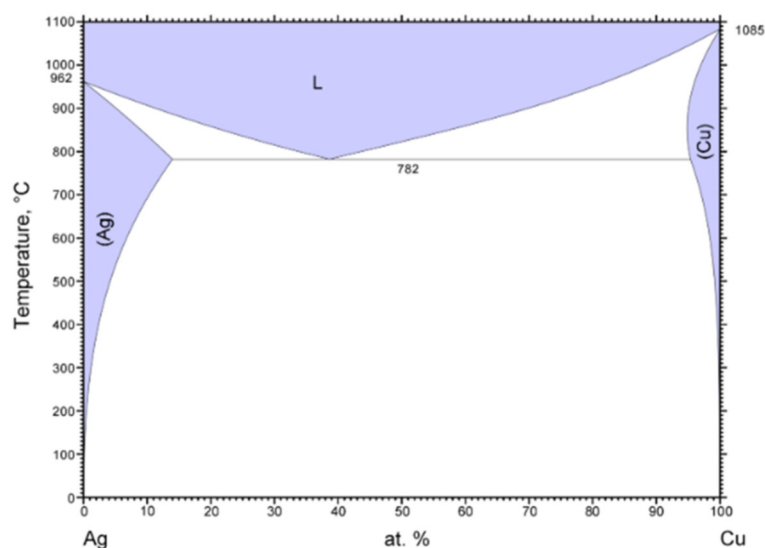
Fig. 51: Ag-Cu phase diagram. [85]

Additionally, Cu-Ag was selected due to good electrical properties which results from the good electrical conductivity of the base materials. Electrical properties of Cu-Ag were investigated primarily for bulk materials through bulk/top-down approaches [86–98]. In recent years, bottom-up approaches [99–109] such as thin-film growth were explored more extensively due to the potential application of Cu-Ag in the semiconductor industry. But only few studies exist where the mechanical properties, or a direct correlations of mechanical, electrical and microstructural properties [110] were investigated. Here, the developed approach enabled to perform a comprehensive study of all target properties in a fast investigation process.

3.2.1 Thin-film synthesis and annealing

Multiple thin film libraries were fabricated with a combinatorial sputter system by co-deposition. The MLs were fabricated with composition gradients of the Cu-Ag system. In total six MLs, which covered different composition gradients of $Cu_{100-x}Ag_x$ ($1 < x < 2$; $2.5 < x < 5$; $4.5 < x < 8$) were fabricated to encompass an overall composition of $Cu_{100-x}Ag_x$ ($1 < x < 8$). Substrates were prepared with both, freestanding tensile-test structure (see section 2.7.5) and substrate-bound thin-film MLs (see section 2.7.2). A magnetron sputter system (AJA ATC 2200-V) with a confocal target setup was used for the deposition and subsequent annealing. The thin film libraries were grown by simultaneous sputtering of two diametrically opposite Cu targets (4-inch diameter, 99.999 at.% purity) and a single Ag target (4-inch diameter, 99.99 at.% purity) at an orthogonal position to the Cu targets. The deposition powers for both Cu targets were adjusted for a similar sputter rate of approximately 0.18 - 0.2 nm/s and Ag deposition rate of 0.02 - 0.16 nm/s, depending on the fabricated composition range of the ML. Depositions were performed with an additional substrate bias (3 W, ~52 V, radio frequency) at a pressure of approximately 0.133 Pa (1 mTorr) with an Ar plasma at room temperature (RT) with a base pressure $< 6.7*10^{-6}$ Pa. Deposition times were adapted to achieve a film thickness of up to 5 µm. MLs were investigated in the as-deposited and the annealed state (400 °C, 1800 s, pressure $< 6.7*10^{-6}$ Pa) to simulate the accelerated effects of the operating conditions of an electrical system. Annealings were performed with a heater incorporated in the ATC 2200-V sputter system. For sample handling during annealing substrate-bound libraries were placed on a Si/SiO_2 carrier wafer identical to substrates utilized during library fabrication and for freestanding structure a Si wafer with an etched cavity was utilized for annealing. Freestanding structures were placed in the cavity to restrict movement of the structures due to movement/vibration of the heating stage.

3.2.2 Results and Discussion

Fig. 52 shows thickness and compositional gradients of the fabricated MLs. The thickness of all libraries varied in the range of approximately 4.1 - 4.8 µm. Thickness values were highest for the geometrical center of the MLs and dropped off towards the edges due to the configuration of the deposition system. By utilizing two opposing Cu targets the thickness variation along the composition gradient was reduced to improve the comparability of MAs with different Ag contents. The composition gradient (Fig. 52) covered most of the targeted composition range, with only a small gap in the range of $Cu_{100-x}Ag_x$ ($2 < x < 2.5$) in between the MLs.
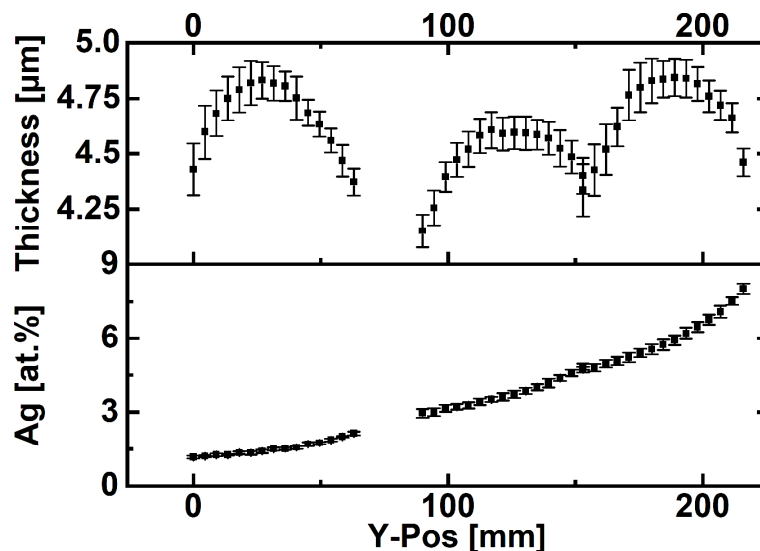
Fig. 52: Film thickness and composition values from the fabricated MLs. Thickness and composition were plotted over the position of the measurement areas along the composition gradient. The measurement areas were placed with a spacing of 4.5 mm. Three individual MLs were fabricated, visibly distinguished by the characteristic arc shape of the thickness distribution.

As a basis for evaluation of the mechanical and electrical properties the microstructure with regards to GS, elemental distribution and crystal orientation was investigated for the different alloy compositions and test conditions. In the as-deposited state, Ag was evenly distributed throughout the volume of the Cu-Ag films in form of an oversaturated solid solution. The Ag distribution was confirmed by TEM imaging (Fig. 53 a)) and elemental distribution analysis (Fig. 53 b)). An overlay of both images indicated that the Ag distribution did not correlate with the film microstructure and was homogenous throughout the material (Fig. 53 c)).
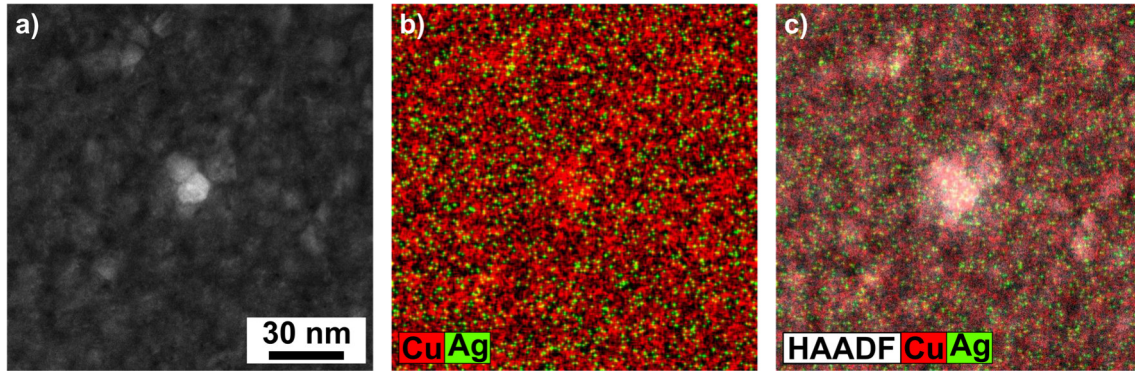
Fig. 53: TEM analysis of an as-deposited Cu-Ag MA prepared from a freestanding thin-film. Images show a) a high angle annular darkfield (HAADF) image, the corresponding elemental composition map measured by EDX and c) a superimposed image of a) and b).

As-deposited GS was evaluated by TEM analysis for tensile-structure MAs with Ag contents of approximately 1 and 8 at.% (Fig. 54). Intermediate Ag contents MAs were not investigated, because a linear dependency of GS and Ag content was expected. The average GS decreased from approximately 51 nm to 38 nm for 1 and 8 at.% Ag respectively. In comparison to the Cu reference, no abnormal grain growth was observed, and size distribution was more homogenous.
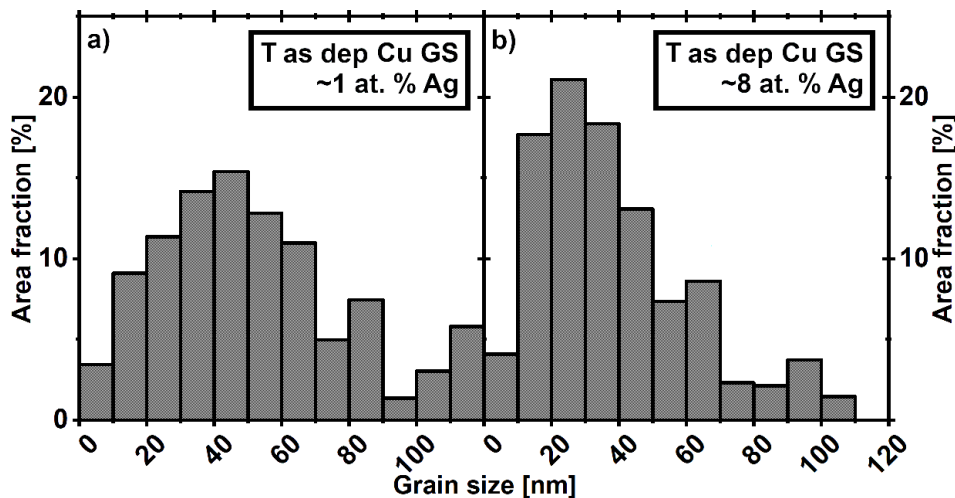
Fig. 54: GS distribution by grain area fraction over GS in 10 nm increments for as-deposited Cu-Ag tensile-test structure MAs with a) an Ag content of approximately 1 at.% and b) an Ag content of approximately 8 at.%.

In addition to GS, crystal orientation measurements were performed during TEM investigation. Fig. 55 shows results for MAs of low and high Ag content with maps of the image quality (IQ) and crystal orientations (IPF-X/Y/Z) in dependence of the orientation of the MA. The Z-axis represented the growth direction of the thin-film and the X-/Y-axis the plane of the wafer surface. For Ag contents of approximately 1 at.% and 8 at.% measurements indicated a preferential (101) orientation in growth direction.

106
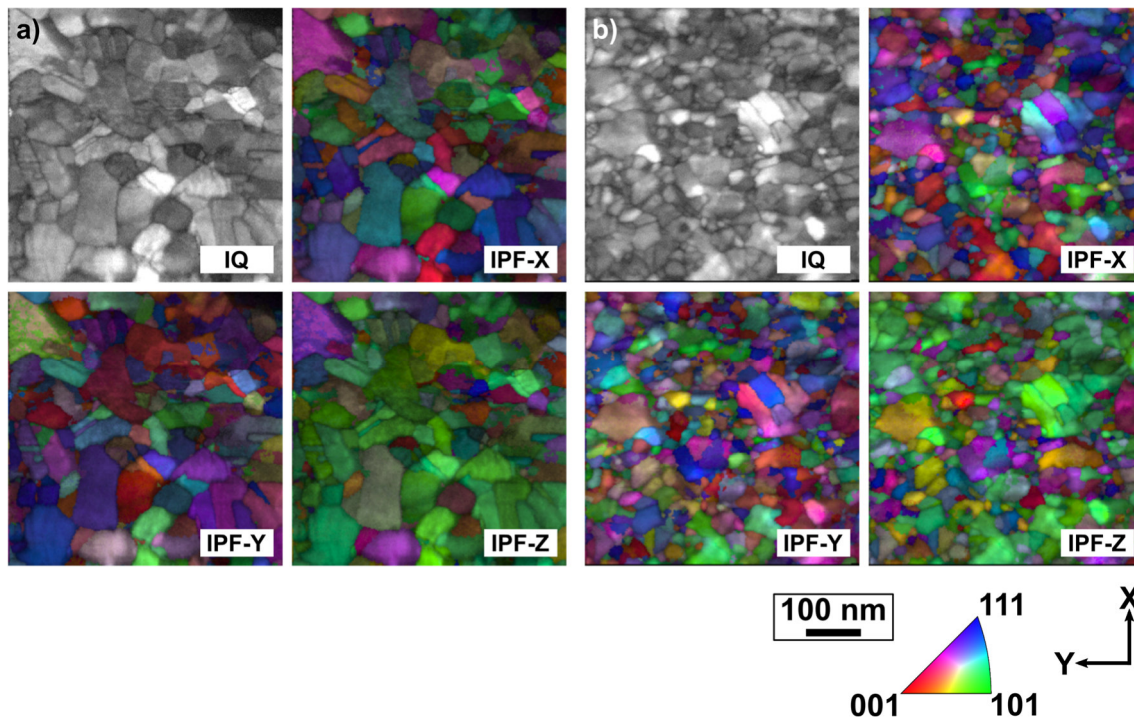
Fig. 55: TEM grain analysis with IQ and IPF-X/Y/Z crystal orientation maps for as-deposited Cu-Ag tensile-test structure MAs with a) an analysis for an Ag content of approximately 1 at.% and b) an analysis for an Ag content of approximately 8 at.%. Cuts were prepared orthogonal to the film growth direction. The Z-axis represented the growth direction of the thin-film.

Investigations of microstructural properties in the annealed state were performed for different Ag contents to give a representative overview of the microstructural evolution. Upon annealing the Ag formed precipitates, and grain growth occurred with the final GS distribution depending on the Ag content. Precipitate formation was indicated by several studies for Cu-Ag alloys [111–114] and was confirmed within this study for the combination of synthesis and processing parameters. The formation of Ag precipitates was confirmed through XRD and SEM image analysis and subsequent Ag GS characterization was performed by SEM image analysis. Verification of phase formation through XRD (Fig. 56) was performed on substrate-bound MAs in the as-deposited and annealed state (400 °C, 1800 s) for Ag contents of approximately 1 and 8 at.%. As-deposited, diffractograms showed intensity maxima which correlated with pure Cu and no maxima which correlated with Ag, which indicated the solid solution. After annealing, the formation of pure Ag precipitates was observed. Angular shifts in between intensity maxima of the as-deposited and annealed state that were attributed to the same phase (e.g., Cu (200)) were observed in the diffractograms. These were primarily caused by differences in temperature during the measurement, as the as-deposited state was investigated at RT, and the annealed state in-situ at 400 °C.
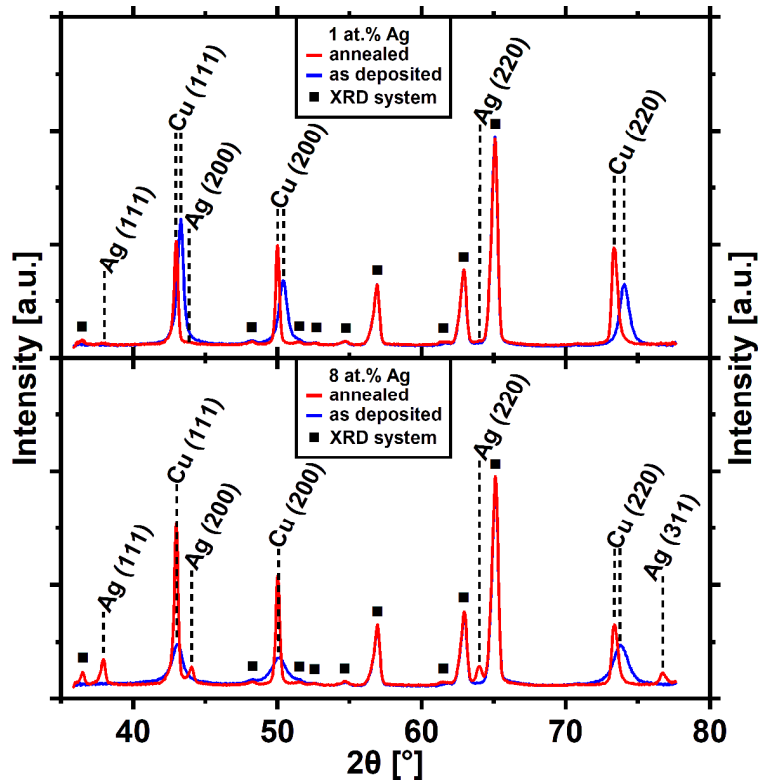
Fig. 56: XRD diffractograms of substrate-bound MAs with Ag contents of 1 and 8 at.% in the as-deposited (blue) and annealed (red) state. Intensity maxima that originate from the annealing stage of the XRD system were denoted with solid black squares.

For GS distribution of the Ag precipitates cross-sectional cuts were prepared through ion-beam etching and characterization was performed through analysis of SEM images taken with a BSE detector which provided high contrast between Ag and Cu. Characterizations were performed on tensile and substrate-bound MAs in the annealed state (400 °C, 1800 s) for Ag contents of approximately 1, 4.5 and 8 at.%. In addition, the cross-sections were utilized for investigation of GS distribution for Cu grains through EBSD analysis. GS distributions for Cu and Ag are shown in Fig. 57 for the substrate-bound (a-f) and tensile-test structure (g-l) MAs. For substrate-bound MAs the Cu average GS decreased only slightly with increasing Ag content from 299 nm to 276 nm to 266 nm (~ 5 nm per at.% Ag) and Ag GS varied from 36 nm to 47 nm to 41 nm for 1, 4.5 and 8 at.% Ag respectively. For tensile-test structure MAs the average Cu GS decreased more significantly with increasing Ag content from 434 nm to 291 nm to 199 nm (~ 34 nm per at.% Ag) and Ag GS varied from 37 nm to 39 nm to 35 nm for 1, 4.5 and 8 at.% Ag respectively. GS values for the Cu-Ag structures are summarized in Table *4*. Parameters for pure Cu MAs were include for reference.

Table 4: Summary of average GS for Cu-Ag tensile-test structure and substrate-bound MAs in the as-deposited and annealed state with average Cu GS for reference.

Cu reference				
T as-dep Cu GS	[nm]	358		
T as-dep Cu std dev	[nm]	479		
S as-dep Cu GS	[nm]	274		
S as-dep Cu std dev	[nm]	382		
T annealed Cu GS	[nm]	1186		
T annealed Cu std dev	[nm]	928		
S annealed Cu GS	[nm]	915		
S annealed Cu std dev	[nm]	710		
Cu-Ag				
Ag cont.	**[at.%]**	**~1**	**~4.5**	**~8**
Cu-Ag Tensile as-deposited				
T as-dep Cu GS	[nm]	51		38
T as-dep Cu std dev	[nm]	28		23
Cu-Ag Tensile annealed				
T annealed Cu GS	[nm]	434	291	199
T annealed Cu std dev	[nm]	300	206	103
T annealed Ag GS	[nm]	37	39	35
T annealed Ag std dev	[nm]	27	30	30
Cu-Ag Substrate annealed				
S annealed Cu GS	[nm]	299	276	266
S annealed Cu std dev	[nm]	191	169	175
S annealed Ag GS	[nm]	36	47	41
S annealed Ag std dev	[nm]	28	41	47

T → Tensile-structure MA
S → Substrate-bound MA
as-dep → as-deposited MA
annealed → 30 min at 400 °C

The generally reduced GS in comparison to pure Cu was expected due to the alloying with Ag which constrained grain growth after precipitation. But GS evolution with increasing Ag content showed unexpected characteristics. Under identical heat treatment conditions, very similar microstructural evolution for the different MA types would have been expected. But for tensile-test structure MAs the average Cu GS at low Ag content (approximately 1 at.%) was higher in comparison to the corresponding substrate-bound MA, at intermediate Ag content (approximately 4.5 at.%) Cu GSs for both MA types were comparable, and at high Ag content Cu GS was lower in comparison to the substrate-bound MA. Average Ag GS was comparable for tensile-test structure MAs of all Ag contents and substrate-bound MAs with Ag content of approximately 1 at.%, while substrate-bound MAs with approximately 4.5 and 8 at.% Ag exhibited a shift towards grains with bigger maximum size of up to 240 nm.
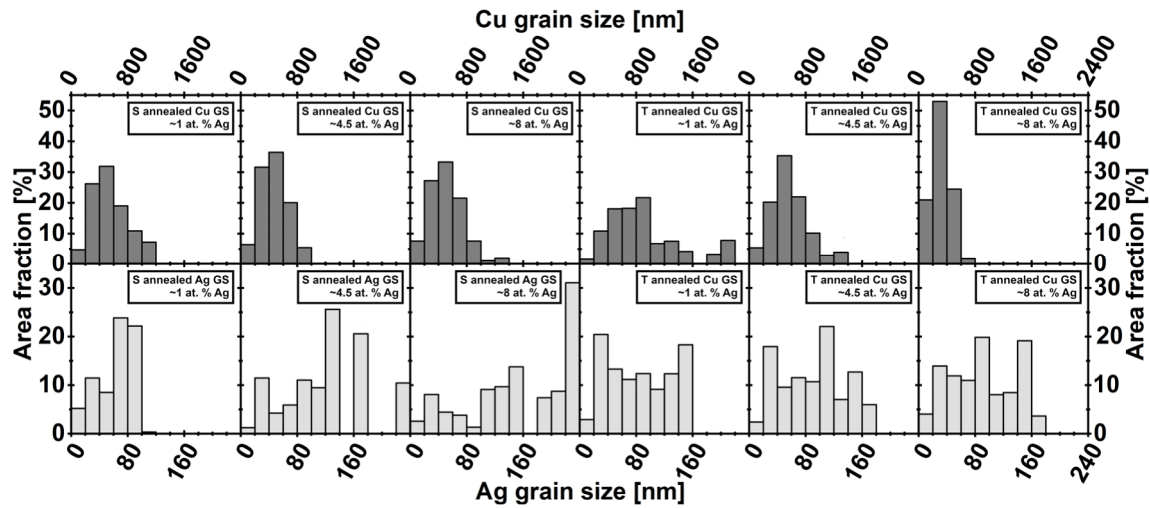
Fig. 57: GS distributions of annealed, substrate-bound and tensile-test structure MAs for different Ag concentrations (1, 4.5 and 8 at.% Ag). Note different scales for GS of Cu (top) and Ag (bottom).

The differences could be partially explained by differences in the actual annealing conditions. For substrate-bound MAs the Cu-Ag thin-film remained on the wafer which was cut into smaller pieces and placed on a carrier wafer on top of the heating stage. Tensile-structure MAs were annealed after lift-off from the substrate as freestanding films and were placed on a carrier wafer on top of the heating element. Because heat transport in vacuum happened primarily through conduction and radiation, substrate-bound MAs were expected to have better heat transfer due the direct contact of the thin-film to the substrate. For freestanding tensile-test structure MAs even slight curvatures reduced the area contact with the substrate to a line contact, which significantly impeded transfer by conduction. On the other hand, tensile-test structure MAs had significantly lower mass (approximately 3 %) relative to substrate-bound MAs to be heated. These different conditions could have resulted in variations with regards to heating rate, actual temperature and temperature homogeneity and might have explained the observed microstructural variation. Due to the small size of both MAs and difficult access due to the vacuum conditions, direct measurements of the temperature during annealing were not performed here.

For later characterization of the functional properties, it was additionally investigated if the Ag content fully segregated into precipitates, or if a fraction remained as a solid solution in the Cu matrix. This characteristic was important to identify the underlying mechanisms that contributed to the measured functional properties. Analysis was performed on SEM BSED images which provided high image contrast in between Cu and Ag and image analysis of the Cu to Ag area fraction. Atomic Ag content of the precipitates was approximated by calculation with a lattice constant of $a_{Ag} = 4.079$ Å [115] without lattice defects. Fig. 58 showed a plot of

110

the calculated Ag content over the nominal Ag content measured by EDX. The dashed line indicated the state where the entire Ag content segregated into precipitates. It was observed that nominal Ag contend matched closely to the calculated Ag content within the precipitates. This indicated that for all MA types and Ag contents the Ag segregated into precipitates and no significant content remained in solid solution.
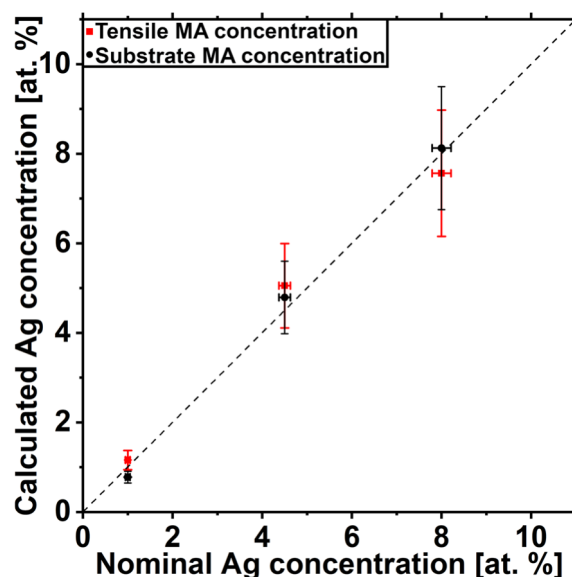
Fig. 58: Plot of calculated Ag concentration over nominally measured (EDX) Ag concentration for annealed tensile-test structure and substrate-bound MAs. The dashed line indicated the match in between calculated and measured Ag concentration.

In addition, crystal orientation measurements were performed on annealed MAs by EBSD analysis. Fig. 59 shows results for tensile-structure MAs of low, intermediate, and high (1, 4.5, 8 at.%) Ag content with maps of the IQ and crystal orientations in dependence of the orientation of the MA. Investigations were performed on cross-sectional cuts fabricated by ion beam milling. The X-axis represents the growth direction of the thin film and the Y-/Z-axis the plane of the wafer surface. Similar to as-deposited MAs, measurements indicated a slight preferential (101) orientation in growth direction for Ag contents of approximately 1 and 8 at.%. For an Ag content of approximately 4.5 at.% no obvious preferential orientation was observed.
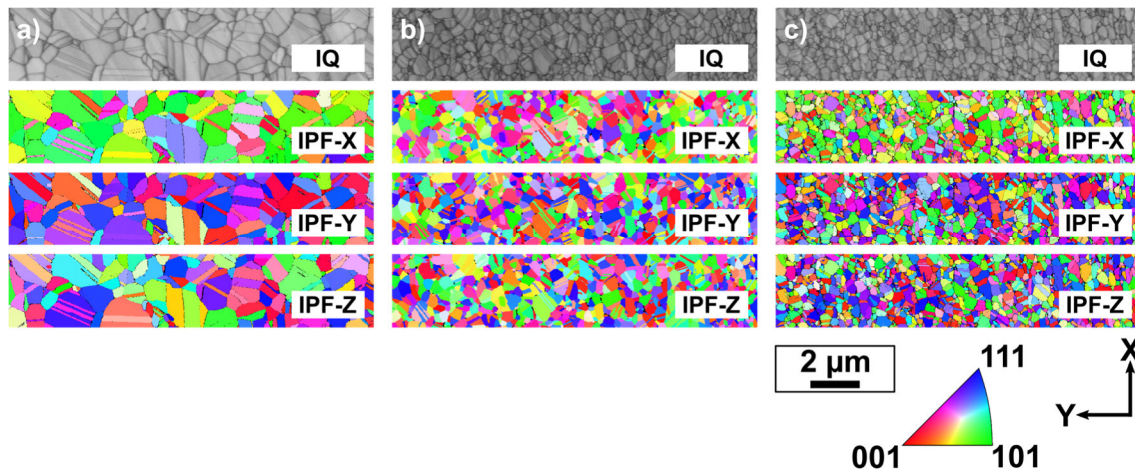
Fig. 59: EBSD analysis of cross-sectional cuts through annealed, Cu-Ag tensile-test structure MAs. IQ and crystal orientation (IPF-X/Y/Z) maps MAs with approximate Ag contents of a) 1 at.%, b) 4.5 at.%, c) 8 at.%. The X-axis represented the growth direction of the thin-film.

Crystal orientations of annealed substrate-bound MAs were investigated with the same procedure for MAs of low, intermediate, and high (1, 4.5, 8 at.%) Ag content (Fig. 60). For substrate-bound MAs no obvious preferential orientation was observed for all investigated compositions. The absence of preferential orientations in comparison the tensile-structure MAs might have been caused by differences in deposition conditions such as the substrate surface (SiO$_2$ vs. photoresist) and resulting parameters such as actual deposition temperature, or differences in actual annealing conditions due to MA design (e.g., geometry, volume, materials).
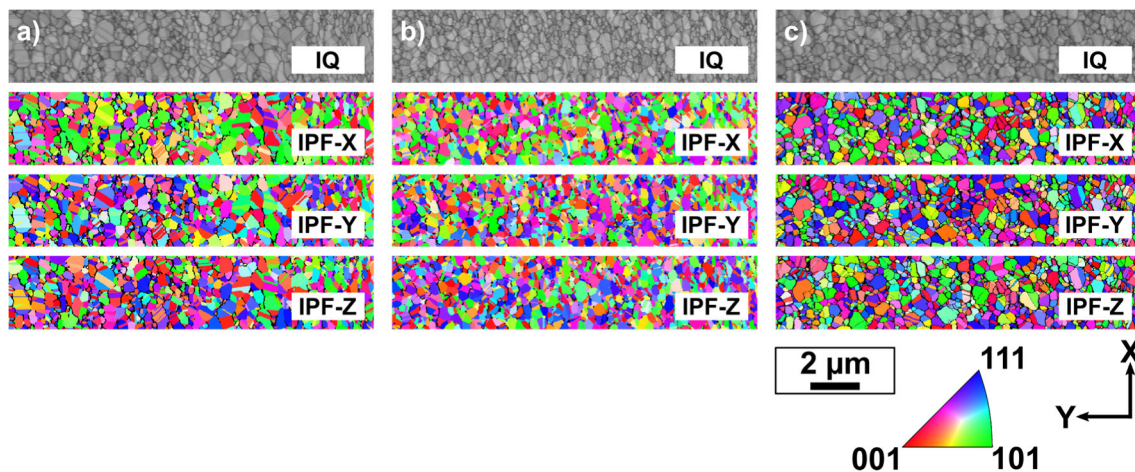
Fig. 60: EBSD analysis of cross-sectional cuts through annealed, Cu-Ag substrate-bound MAs. IQ and crystal orientation (IPF-X/Y/Z) maps MAs with approximate Ag contents of a) 1 at.%, b) 4.5 at.%, c) 8 at.%. The X-axis represented the growth direction of the thin-film.

Investigated functional properties of the Cu-Ag alloys comprised electrical and mechanical properties. Electrical properties were investigated by sheet resistivity, and

112

mechanical properties through nanoindentation and tensile experiments. Fig. 61 shows electrical and mechanical properties in dependence of Ag content, as well as Cu reference measurement values for comparison. All tests were performed on as-deposited and annealed MAs. Annealings were performed for 30 minutes at 400 °C under vacuum.
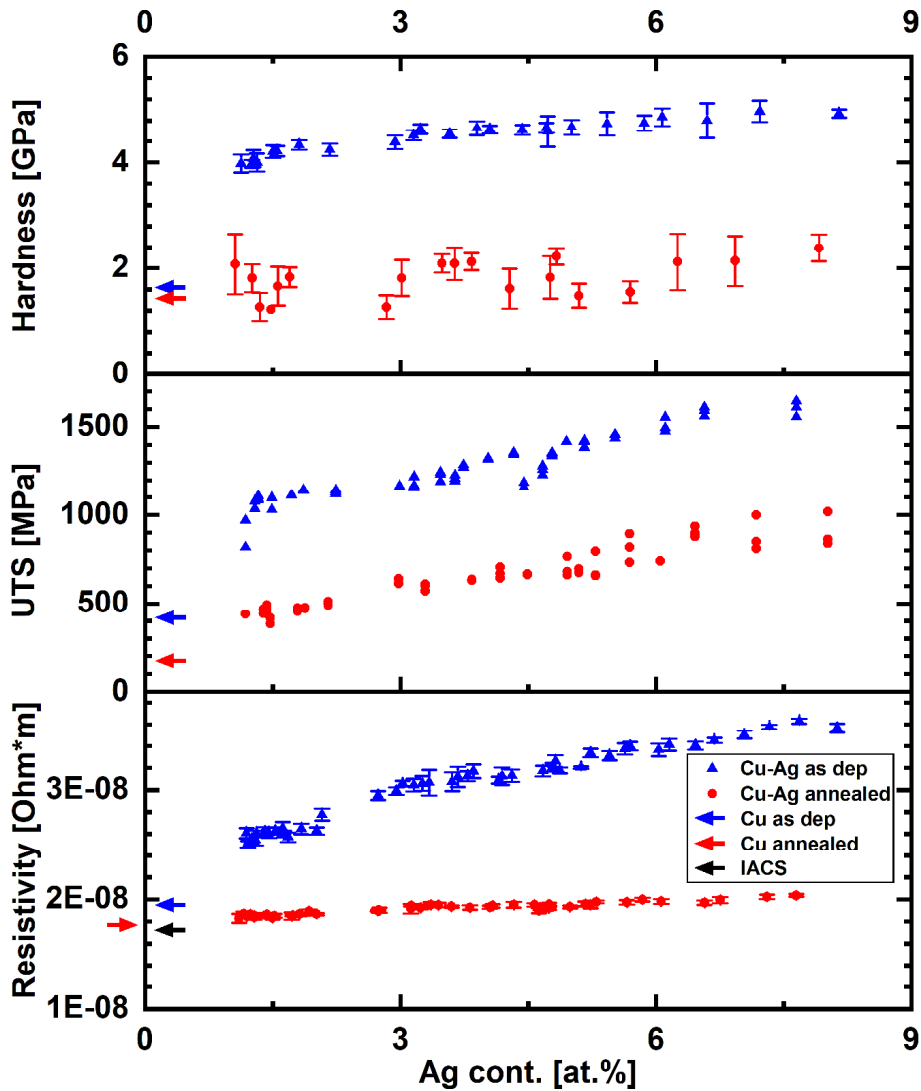
Fig. 61: Compilation of characterization results for a) hardness, b) UTS and c) electrical resistivity in dependence of the Ag content of the fabricated MLs.

Resistivity measurements (Fig. 61) showed a linear increase with increasing Ag content with a higher slope in the as-deposited state, compared to the annealed state ($\sim 1.6^{-9}\,\Omega * m/at.\%$ vs. $\sim 2.8^{-10}\,\Omega * m/at.\%$). Compared to the IACS, the Cu-Ag alloys achieved values of 85 - 94 % in the annealed state and 48 - 69 % in the as-deposited state with increasing resistivity for increasing Ag contents.

Hardness and ultimate tensile strength (UTS) increased approximately linearly with increasing Ag content in the as-deposited and annealed state. Values were lower in the annealed

state for both, hardness and UTS. Hardness for as-deposited MAs increased from approximately 4 GPa to 5 GPa with a slope of approximately 0.13 GPa / at.% Ag and for annealed MAs hardness increased from approximately 1.5 GPa to 2 GPa with a slope of approximately 0.08 GPa / at.% Ag. High scatter of the hardness data for annealed MAs was attributed to increased surface roughness after annealing. UTS for as-deposited MAs increased from approximately 1000 MPa to 1500 MPa (Fig. 62 a)) with an increase of approximately 93 MPa / at.% Ag and for annealed MAs UTS increased from approximately 400 MPa to 900 MPa (Fig. 62 b)) with an increase of approximately 75 MPa / at.% Ag.
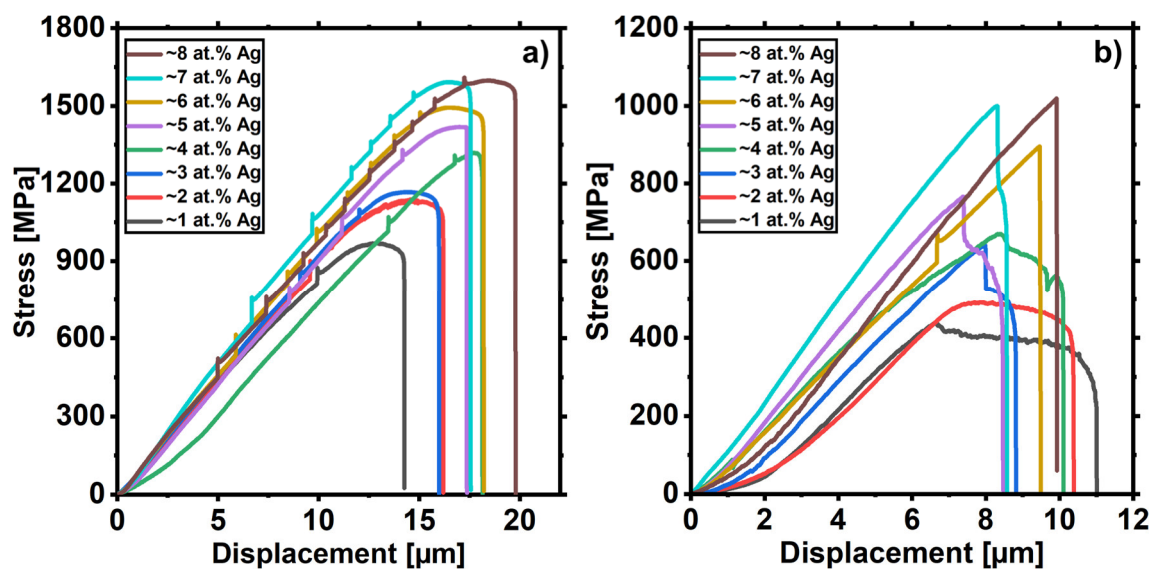
Fig. 62: Stress-displacement plots of Cu-Ag MAs with increasing Ag contents tested at RT for a) as-deposited MAs and b) annealed MAs.

During preparation of tensile-test structure MAs more pronounced bending of the Cu-Ag thin-films was observed in comparison to Cu MAs. An exemplary arrangement of MAs after lift-off is shown in Fig. 63 for MAs with a composition from approximately 1 at.% Ag to 2 at.% Ag. The bending was clearly observable through surface reflections. The axis of the bending was generally oriented orthogonal to the tensile-gauge axis and angular changes of the orientation with changing Ag content / position on the substrate were small. This was consistent with prior observations of homogenous microstructure along the thickness of the MAs and no significant changes in crystal orientation for different Ag contents. But especially for crystal orientation available data points were limited and a more detailed study with investigation of more Ag contents would have been required for confirmation. The bending was still unproblematic for manual handling and mounting the MAs as illustrated in Fig. 26, as gluing of the MAs in between Si plates helped to fix the MAs in a flat state. But the remaining

curvature in the gauge could have resulted in small misalignments with the straining device which could have influenced the measured mechanical properties.
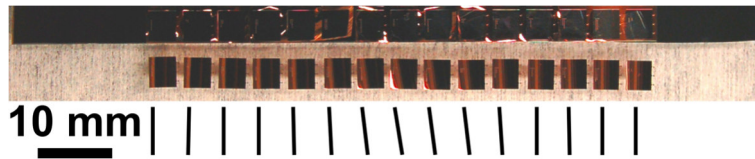
Fig. 63: Photograph of one column from a Cu-Ag ML along the compositional gradient after lift-off arranged next to the Si wafer substrate. Lines below the placed MAs indicated the change in orientation of the axis around which the MAs were bend due to intrinsic stress.

In the as-deposited state all tensile-structures throughout the investigated composition range exhibited ductile fracture with generally low plastic deformation. The scale of plastic deformation was similar for all Ag contents as indicated by the stress-displacement data (Fig. 62 a)) and optical appearance of the tensile-test structures. Post-mortem investigations showed that fracture occurred under an angle of approximately 30° - 40° (Fig. 64 (b,e,h)) from the length axis of the gauge with a shearing motion, commonly observed for ductile materials [78]. After an initial plastic deformation all structures failed spontaneously on the remaining cross-section which showed a characteristic dimpled surface structure (Fig. 64 (d,f,i)). Due to the abrupt failure, it was not possible to retain the structure heads for post-mortem investigations, as they were forcefully ejected from the straining device and could not be recovered.
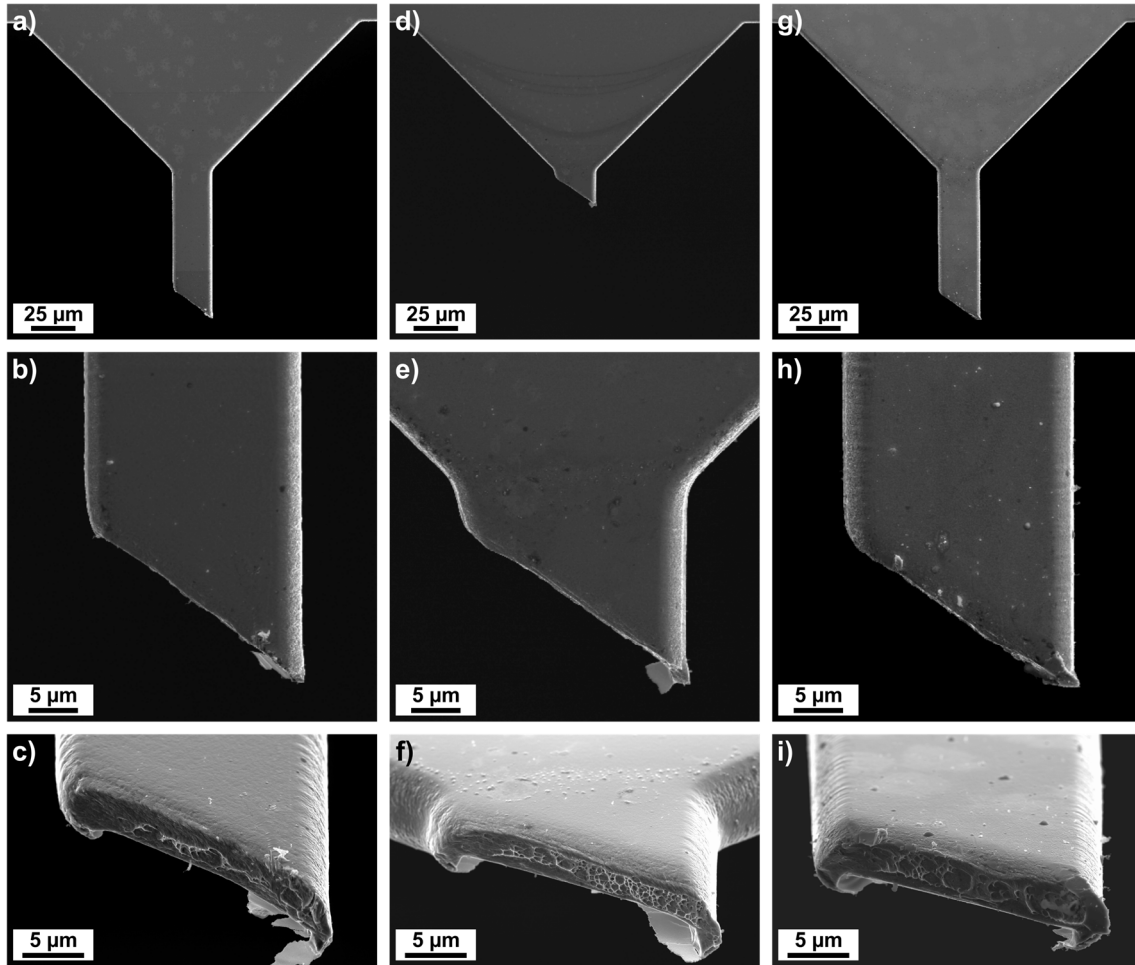
Fig. 64: SEM SED images of Cu-Ag tensile-test structures after testing with post-mortem images of as-deposited structures after testing at RT with a top-down view of the FS, a magnified view of the gauge and a magnified view of the fracture surface for Ag contents of (a,b,c) approximately 1 at.%, (d,e,f) approximately 4.5 at.% and (g,h,i) approximately 8 at.%.

After annealing, tensile-test structures still exhibited ductile fracture for all tested Ag contents, but the mechanical behavior showed an additional transition from high to low plastic deformation (Fig. 62 b)). The amount of plastic deformation decreased with increasing Ag content and from the stress-displacement data no plastic deformation was observed for Ag contents > 5 at.% (Fig. 62 b)). The necking was visualized through post-mortem analysis for MAs with compositions of approximately 1 and 4 at.%, whereas no necking was observed for a composition of ~ 8 at.% ((Fig. 65 (b,e,h))). For all compositions fracture occurred under an angle of approximately 30° - 40° (Fig. 65 (b,e,h)) from the length axis of the gauge with a shearing motion and slanted edges of the fracture surface, commonly observed for ductile materials [78]. The shearing motion could be directly observed for the MA with an Ag content of approximately 1 at.%, as the long plastic deformation allowed to stop the experiment close to removal of the structure head (Fig. 65 (b)). The structure clearly showed the offset of the length axis in between structure head and remaining section of the gauge.
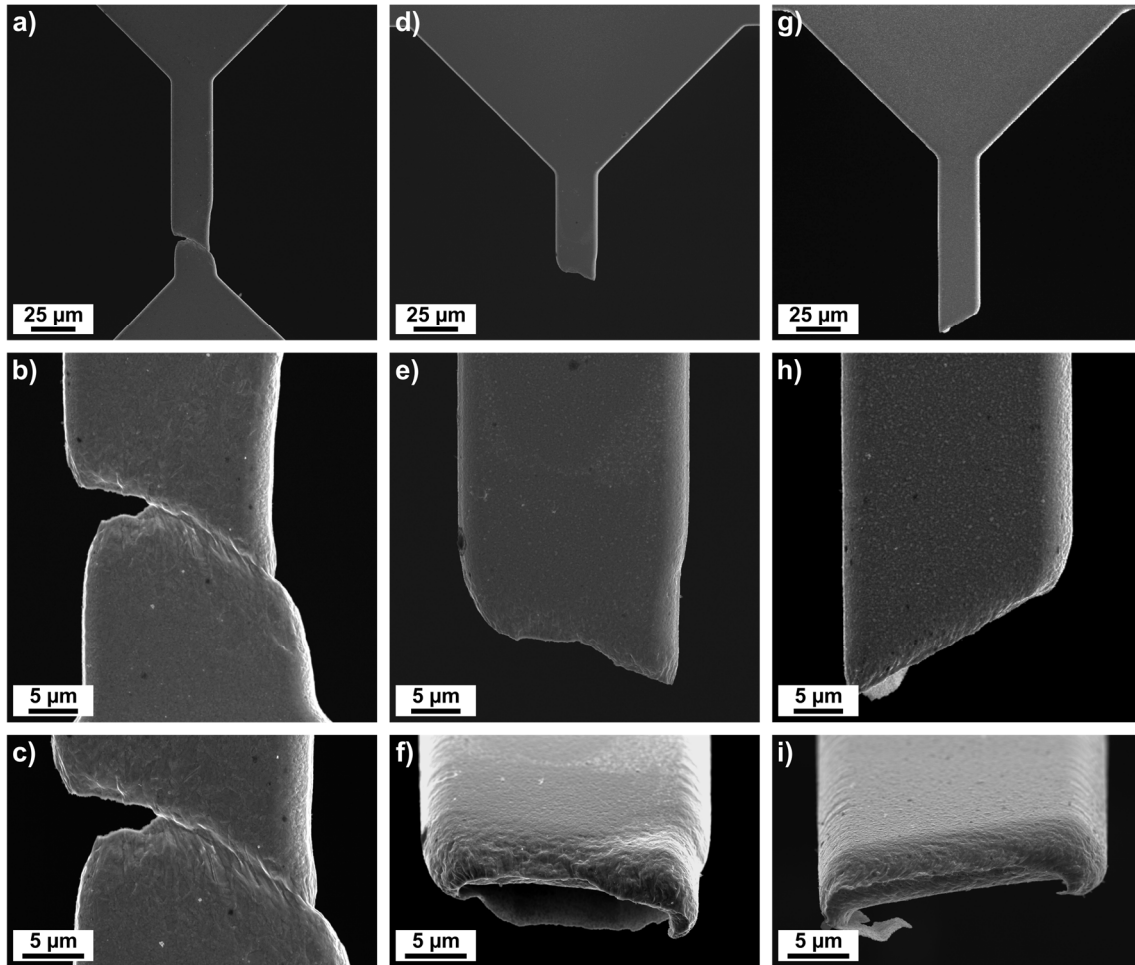
Fig. 65: SEM SED images of Cu-Ag tensile-test structures after testing with post-mortem images of annealed structures after testing at RT with a top-down view of the FS, a magnified view of the gauge and a magnified view of the fracture surface for Ag contents of (a,b,c) approximately 1 at.%, (d,e,f) approximately 4.5 at.% and (g,h,i) approximately 8 at.%.

To better simulate mechanical behavior at elevated temperatures, tensile structures were additionally tested in-situ at 400 °C. Due to the added complexity of the in-situ testing, experiments were performed for MAs of selected Ag content which represented low (~ 2 at.%), intermediate (~ 3.5 at.%) and high (~ 7.5 at.%) Ag contents from the synthesized compositional range. At elevated temperatures all tested compositions showed ductile behavior. Exact quantification of the mechanical properties was not possible for the in-situ tests, as the displacement range of the test setup was insufficient to achieve fracture for the Cu-Ag structures. Qualitatively, Cu-Ag structures showed an improvement in the displacement required for fracture in comparison to pure Cu reference structures, which could be fractured within the displacement range of the straining device. For the low Ag content (~ 2 at.%) first necking was observed, indicated by the reduction in stress above a displacement of approximately 22 µm (Fig. 66). UTS was low at approximately 70 MPa, which was

approximately 30 MPa (75 %) higher in comparison to Cu. For higher Ag contents (~ 3.5 at.% and ~ 7.5 at.%) only strain hardening, and no necking was observed (Fig. 66).
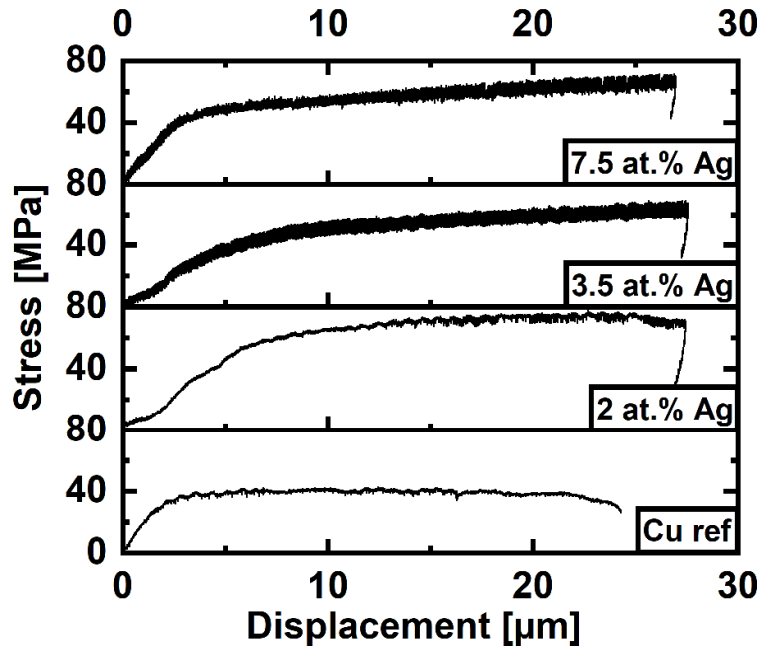
Fig. 66: Comparison of in-situ tensile experiments performed at 400 °C. The displacement range of the setup was insufficient to fracture tested Cu-Ag structures, whereas the Cu reference fractured within the range (approximately 25 µm).

Changes in resistivity were primarily explained by the Cu GS evolution and Ag distribution. Resistivity for as-deposited and annealed Cu-Ag MAs was plotted over GS for MAs where both properties were available (Fig. 67). For comparison, additional reference values of Cu MAs and a calculated approximation for pure Cu (see section 3.1) were included. For as-deposited MAs resistivity was governed by GS and scattering by impurity atoms such as the Ag atoms in solid solution. Impurity scattering should always have resulted in increased resistivity in comparison to impurity-free Cu, but interestingly resistivity for as-deposited Cu-Ag MAs were either comparable, or below the calculated resistivity of Cu. This deviation was most likely caused by the fact that GS values for the as-deposited states were only measured for tensile-structure MAs and might not have been representative of the actual GS of substrate-bound MAs with similar Ag content.

For annealed Cu-Ag MAs, the average GS (299 nm) was significantly smaller in comparison to annealed Cu (915 nm), but still sufficiently bigger than the electron mean free path of Cu (39 nm [84]) and therefore only had a limited effect on resistivity. Interestingly, resistivity decreased for annealed MAs with increasing Ag content and decreasing GS. For substrate-bound MAs an increased Ag content resulted in an increased number and size of Ag

118

precipitates which decreased resistivity due to the lower resistivity of Ag ($1.578*10^{-8}$ Ω/m) in comparison to Cu. Reduced GS on the other hand should have resulted in an increase in resistivity due to increased grain boundary scattering. The net reduction in resistivity observed here was attributed to two effects. Similar to Cu MAs, the numerical determination of the average GS did not well reflect the area fraction occupied by grains with bigger size. As indicated by the high standard deviation of the GS, a high number of grains with above average size were observed on the MA cross-section. These grains could have dominated electron transport and therefore resulted in a smaller resistivity as expected for the average GS. Additionally, an increased presence of twin boundaries was observed for the Cu grain of annealed Cu-Ag MAs. Such boundaries could have exhibited reduced electron scattering due to lower defects in comparison to regular boundaries and additionally contributed to a reduction in resistivity. The combined interaction of both effects could be the reason for the lower resistivity.
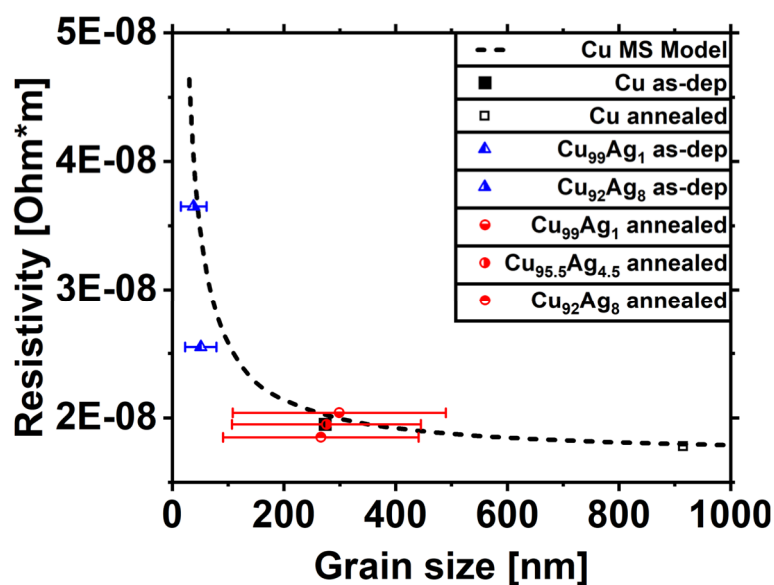
Fig. 67: Plot of electrical resistivity over GS for substrate-bound Cu-Ag MAs measured in the as-deposited and annealed state. Cu reference measurements were included for comparison. The black line indicates the calculated resistivity for Cu over GS after Eqn. 2.

The mechanical properties were primarily governed by three strengthening mechanisms which were Hall-Petch (H-P) strengthening, solid solution strengthening and particle strengthening. H-P strengthening (see Eqn. 1), describes the increase of mechanical strength with decreasing GS of a material.

Solid solution strengthening describes the influence of second element atoms in the form of a solid solution on the mechanical strength of a material. The influence of this effect is governed by Eqn. 3 and described the increase in shear stress $\Delta\tau$ required to move dislocations

through a material with increasing solute atom concentration c. Further components of the formula are constants with the shear modulus G, the Burgers vector b and the lattice strain ϵ introduced by the solute atoms.

$$\Delta\tau = G * b * \epsilon^{\frac{3}{2}} * \sqrt{c} \ [116]$$

Eqn. 3

Precipitate strengthening is governed by equation Eqn. 4 which describes the sheer stress τ required to bow dislocations around particles. The strength increase is primarily influenced by particle spacing L and particle radius r. Further components of the formula are constants with the shear modulus G, the Burgers vector b.

$$\tau = \frac{G*b}{L-2*r}$$

Eqn. 4

For as-deposited MAs the primary strengthening mechanisms were H-P due to the GS changes on the nanoscale level and solid solution strengthening, through added Ag that formed a substitutional, supersaturated solid solution. For annealed MAs the mechanical strength was also governed by H-P strengthening due to the GS changes with changing Ag addition and solid solution strengthening was replaced by particle strengthening, as the Ag content agglomerated to Ag particles distributed throughout the thin film. The mechanical strength for both, as-deposited and annealed Cu-Ag was more than two times higher in comparison to the Cu reference, which showed the effect of the strengthening mechanisms. For quantification of the individual strengthening contributions to the final strength, the H-P contribution was approximated according to strengthening effect observed for the UTS of Cu (Fig. 47). The resulting H-P contribution was plotted together with the measured UTS for all MAs where data for GS and Ag content was available as well (Fig. 68).
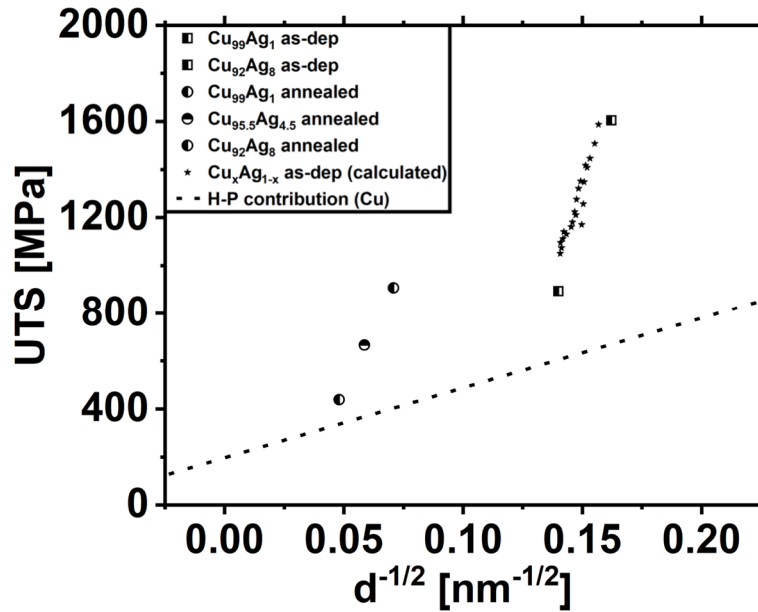
Fig. 68: Plot of Cu-Ag UTS over inverse GS of as-deposited and annealed MAs for all data points where both properties were available. For an approximation of as-deposited properties intermediated Ag contents GS values were interpolated by assumption of a linear behavior. The dashed line indicates the expected H-P contribution of Cu for reference.

In the as-deposited state the H-P contribution to the UTS was thereby approximated as 600 MPa for 1 at.% Ag and 660 MPa for 8 at.% Ag, as GS decreased with increasing Ag content. This corresponded to a H-P contribution of approximately 67 % and 41 % to the total UTS for 1 and 8 at.% Ag respectively.

The contribution of the solid solution strengthening was subsequently calculated by subtraction of the H-P approximation from the UTS. The resulting contributions by solid solution strengthening were approximately 290 MPa and 940 MPa for 1 and 8 at.% Ag respectively, which corresponded to a respective contribution to the total UTS of approximately 33 % and 59 %. To verify if the increase in Ag content was consistent with the assumed increase in solid solution strengthening, it was evaluated if the strength increase was proportional to the increase in Ag content (Fig. 69). For evaluation, the increase in UTS attributed to solid solution strengthening was plotted over the Ag content by $c^{1/2}$ (Fig. 69 a)), as described by Eqn. 3. Labusch et al. [117] suggested that experimental results could also follow a relation of $c^{2/3}$ for solid solution strengthening which was also plotted (Fig. 69 b)) for comparison. It could be seen that the strength increase showed good proportionality to the increase in Ag content for both plots. This further indicated that the strength increase could be attributed to the contribution of solid solution strengthening.
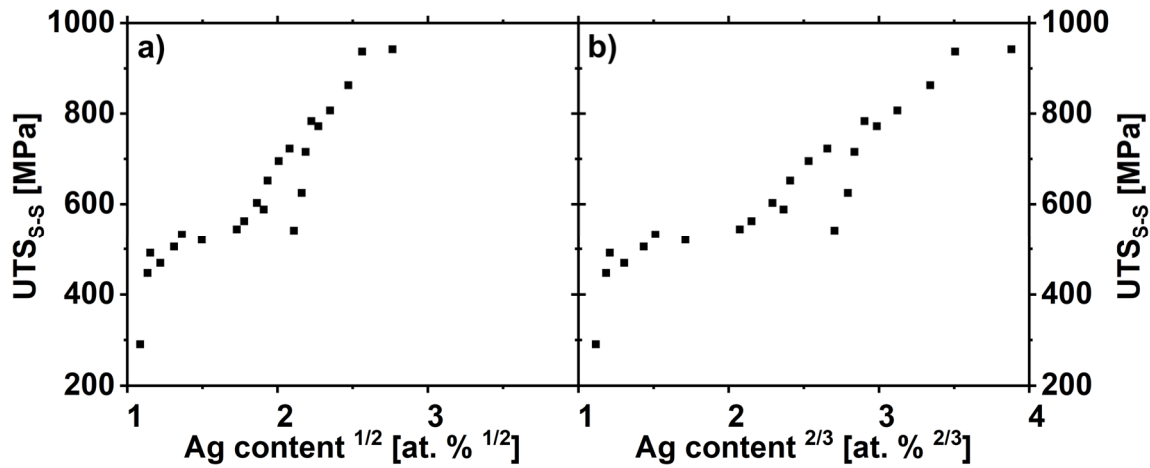
Fig. 69: Plot of calculated contribution for solid solution strengthening to the UTS (UTS$_{S-S}$) over a) the Ag content to the power of 1/2 and b) the Ag content to the power of 2/3.

In the annealed state, UTS was approximately 30 - 50 % lower in comparison to the as-deposited state (Fig. 62). Underlying strength contributions were primarily attributed to H-P due to GS and particle strengthening due the formation of Ag precipitates. For quantification of the separate contributions, the H-P strengthening was approximated by utilizing the H-P approximation for Cu. This simplification was used due to the low overall Ag content and Ag grain quantity of the investigated MLs, and the subsequently low expected influence of Ag on the H-P contribution. The resulting contribution was approximated to 330 MPa, 360 MPa and 400 MPa for 1, 4.5 and 8 at.% Ag which corresponded to a respective contribution of approximately 76 %, 55 % and 44 % to the total UTS.

The contribution of the particle strengthening was subsequently calculated by subtraction of the H-P approximation from the measured UTS (Fig. 70). The resulting contributions were approximately 100 MPa, 300 MPa and 500 MPa for 1, 4.5 and 8 at.% Ag, which corresponded to a respective contribution of approximately 24 %, 45 % and 56 % to the total UTS.

A possible contribution of twin strengthening due to the presence of twin boundaries was not considered here, as twining did not occur with a high density and only a negligible contribution was expected.
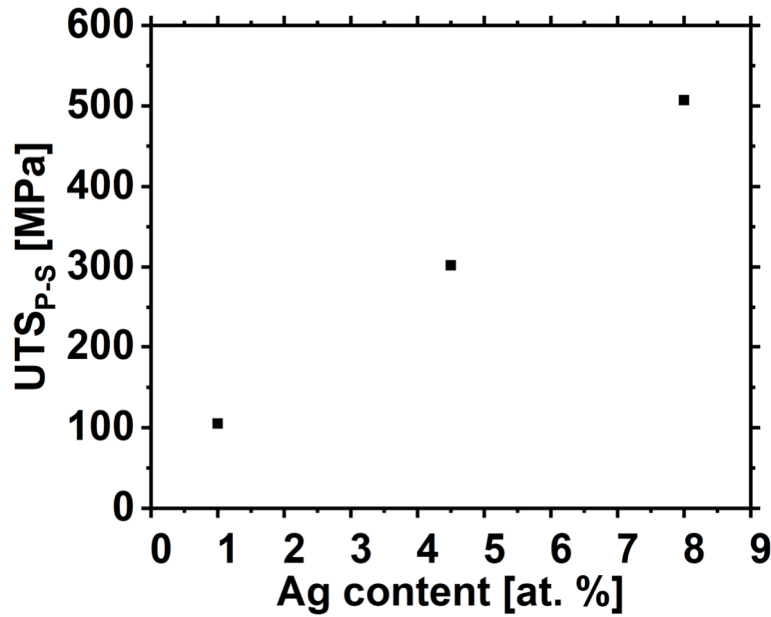
Fig. 70: Approximated contribution of particle strengthening (UTS_{P-S}) to the UTS of annealed Cu-Ag MAs plotted over the Ag content.

For validation of the mechanical properties obtained through tensile-test experiments, results were evaluated by comparison with the hardness evolution of substrate-bound MAs by nanoindentation (Fig. 71).

In the as-deposited state the H-P contribution to the hardness was approximated as 2.1 GPa for 1 at.% Ag and 2.3 GPa for 8 at.% Ag which corresponded to approximately 55 % and 47 % of the total hardness. For H-P strengthening the GS for approximation was taken from tensile-structure MAs with corresponding composition. The contribution of the solid solution strengthening was subsequently calculated by subtraction of the H-P approximation from the measured UTS. The resulting contributions by solid solution strengthening were approximately 1.8 GPa, 2.6 GPa for 1 and 8 at.% Ag respectively, which corresponded to a contribution of approximately 54 % and 53 % to the total hardness.

In the annealed state the H-P contribution to the hardness was approximated as 2.1 GPa, 2.2 GPa and 2.4 GPa for 1, 4.5 and 8 at.% Ag which corresponded to approximately 77 %, 73 % and 68 % of the total hardness. The contribution of the solid solution strengthening was subsequently calculated by subtraction of the H-P approximation from the measured UTS. The resulting contributions by solid solution strengthening were approximately 0.5 GPa, 0.6 GPa and 0.8 GPa for 1, 4.5 and 8 at.% Ag respectively, which corresponded to a contribution of approximately 23 %, 27 % and 32 % to the total hardness.

For the as-deposited state the distribution of the strengthening contributions was close to the tensile-structure MAs with deviations < 6 %, which could have been caused by errors due to the GS assumption. In contrast, the increase in mechanical properties was significantly lower

for hardness (25 % increase from 1 to 8 at.% Ag) in comparison to UTS (100 % increase from 1 to 8 at.% Ag). This more significant deviation might have been caused by the direct comparison in between the two different properties, but the definite reason remained unclear.

For the annealed state, the distribution of the strengthening contributions was close to the tensile-test structure MAs with deviations < 1 % for MAs with 1 at.% Ag. For MAs with 4.5 and 8 at.% Ag deviations were higher in the order of 20 % to 25 %. The close match for 1 at.% Ag was unexpected, as GS for both MA types deviated by a factor of approximately 2. Instead, a closer match at 4.5 at.% Ag was expected, as GS was comparable for both MA types. The increase in mechanical properties was again significantly lower for hardness (20 % increase from 1 to 8 at.% Ag) in comparison to UTS (125 % increase from 1 to 8 at.% Ag). The deviations might have been caused by uncertainties during GS determination, especially differences in between the numerical average of the GS and corresponding area fractions, as well as issues of comparability in between the two different properties. Same as for as-deposited MAs, the definitive reason remained unclear and would have required further studies for clarification.
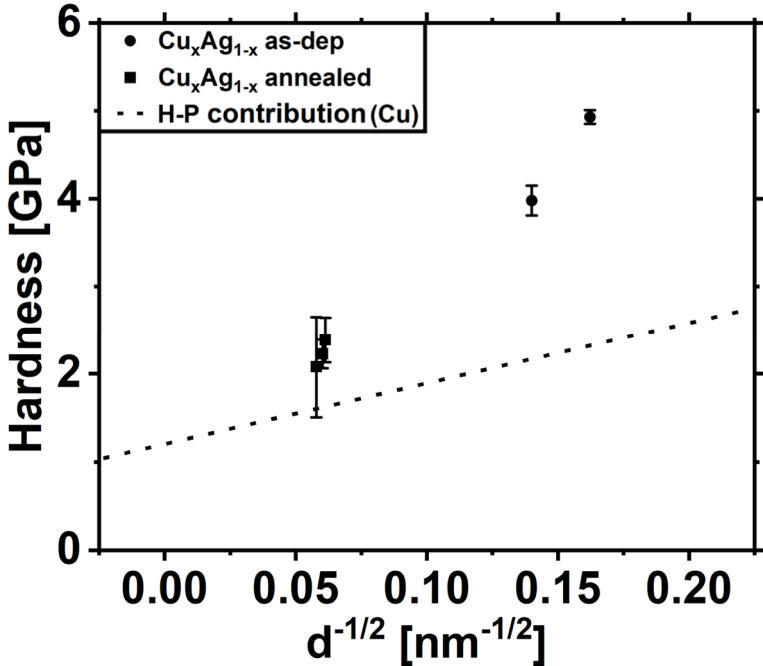
Fig. 71: Plot of Cu-Ag hardness over inverse GS of as-deposited and annealed substrate-bound MAs for all data points where both properties were available. The dashed line indicated the expected H-P contribution of Cu for reference.

3.3 Cu-Zr

After successful investigation of the Cu-Ag system, the Cu-Zr system was selected for a third study and second application of a combinatorial investigation. The Cu-Zr system was selected to test a material system with higher microstructural complexity in comparison to Cu-Ag to evaluate the robustness of the fabrication and characterization process, and because literature reports indicated possible improvements for mechanical performance and electromigration. The Cu-Zr phase diagram shows low solubility of Zr in Cu at RT and the existence of multiple phases in dependence of the composition (Fig. 72). Further, studies indicated that preferential segregation of Zr to grain boundaries occurred during heat treatment which could counteract grain boundary embrittlement. Such microstructural characteristics can potentially complicate characterization due to e.g., additional formation of intrinsic stress and can show limitations of the developed approach. So far, most studies have investigated Cu-Zr alloys with Zr contents > 20 at.%, which lead to amorphous, metallic glasses [118–121]. The addition of small amounts of immiscible alloying elements into Cu which can lead to an improved lifetime of microelectronic devices is limited. As described, alloying of Cu with Zr lead to the formation of precipitates, which improve the electromigration lifetime of Cu interconnects by up to two orders of magnitude [122,123], as well as the mechanical properties [124,125] by segregation of Zr to grain boundaries. But comprehensive studies which correlate mechanical and electrical performance with compositional and microstructural data were limited to few discrete compositions [126–130].
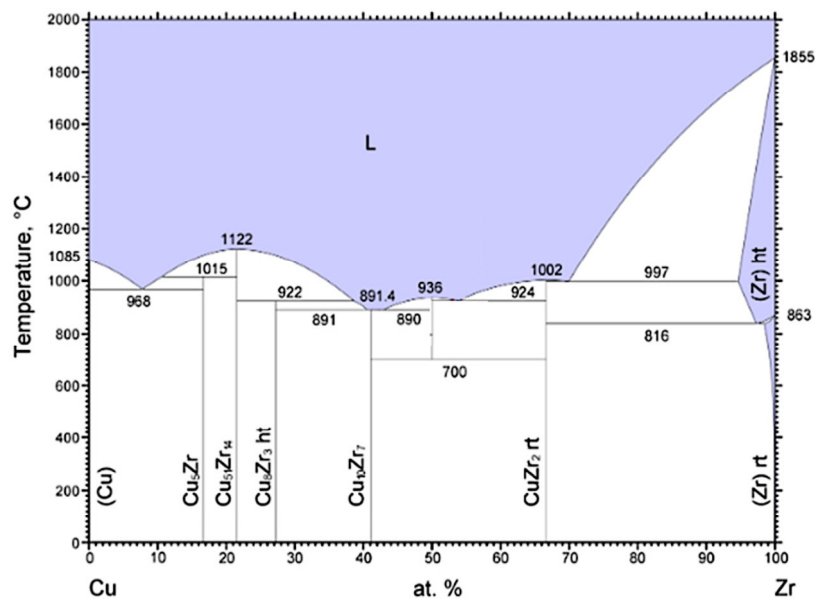
Fig. 72: Cu-Zr phase diagram. [131]

For combinatorial testing, MLs were synthesized over a composition range of $Cu_{(100-x)}Zr_x$ $(1 < x < 5.5)$. A low Zr content was selected to try and retain the good electrical properties of Cu. For this composition range a solid solution and supersaturated solid solution were expected in the as-deposited state, as the RT deposition likely would not have provided sufficient energy for phase formation. In the annealed state the formation of Cu_5Zr was expected, as indicated by the phase diagram.

3.3.1 Thin-film synthesis and annealing

Multiple thin film-libraries were fabricated with a combinatorial sputter system by co-deposition. The MLs were fabricated with composition gradients of the binary Cu-Zr system. Six MLs, which covered composition gradients of $Cu_{100-x}Zr_x$ $(1 < x < 1.5;\ 2.0 < x < 4;$ $4 < x < 5.5)$ were fabricated to encompass an overall composition of $Cu_{100-x}Zr_x$ $(1 < x < 5.5)$. Depositions were performed on Si wafers according to approach V3. Substrates were prepared with both, freestanding tensile-test structure and substrate-bound thin-film MLs. A magnetron sputter system (AJA ATC 2200-V) with a confocal target setup was used for the deposition. The MLs were grown by simultaneous sputtering of two diametrically opposite Cu targets (4-inch diameter, 99.999 at.% purity) and a single Zr target (4-inch diameter, 99.95 at.% purity) at an orthogonal position to the Cu targets. The deposition powers for both Cu targets were adjusted for a similar sputter rate of approximately 0.18 - 0.2 nm/s and Zr deposition rate of 0.02 - 0.13 nm/s, depending on the fabricated composition range of the ML. Depositions were performed at a pressure of approximately 0.133 Pa (1 mTorr) with an Ar plasma at RT with a base pressure $< 6.7 \times 10^{-6}$ Pa. Deposition times were adapted to achieve a film thickness of up to 5 µm. MLs were investigated in the as-deposited, and the annealed state (400 °C, 1800 s, pressure $< 1 \times 10^{-3}$ Pa) to simulate the accelerated effects of the operating conditions of an electrical system. For the heat treatment an "ANNEALSYS AS-One" rapid thermal processing system was used which utilized infrared lamps for heating.

After synthesis and release of the tensile-test structures a significant challenge for mechanical testing was observed. The as-deposited structures showed pronounced bending in comparison to Cu-Ag, easily observed on the handle area of the released structure (Fig. 73 a)). During initial annealing tests the structures exhibited even further bending and curled up all the way into a roll (Fig. 73 b)). The bending prevented consistent and proper fixation of the handle to the Si plates during preparation for testing. For as-deposited structures it was possible to

perform the preparation, but bending was still observed along the freestanding tensile gauge and head. For annealed structures, the preparation process was not possible due to the high bending.
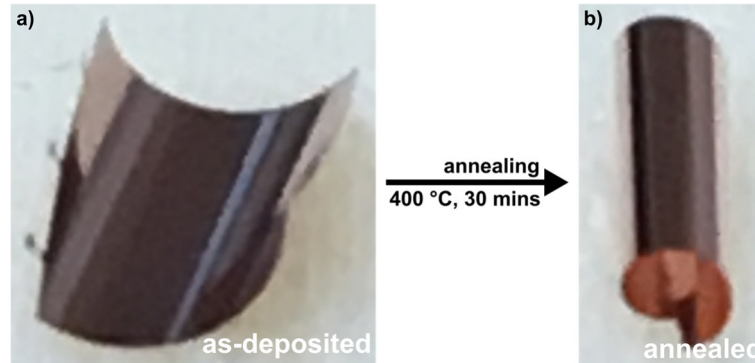
Fig. 73: Photo of a Cu-Zr tensile-test MA after lift-off in a) the as-deposited state and b) in the annealed state.

To counteract further bending during heat treatment the annealing procedure was adapted. Bending was suppressed by annealing the MAs in a geometrically constrained flat shape, achieved by clamping of the MAs in between a graphite carrier and wafer substrate (Fig. 74). In this assembly intrinsic stress of the MAs was relaxed during annealing while bending of the MAs was reduced by clamping. For heat transfer, the annealing assembly was covered with a graphite lid to aid absorption of the infrared light. For consistent annealing conditions substrate-bound MAs were annealed with the same setup without the Si/SiO$_2$ cover wafer.

Fig. 74: Schematic illustration of the annealing assembly utilized for suppression of bending and flattening of the freestanding tensile-test structure MAs.

3.3.2 Results and Discussion

Fig. 75 shows thickness and compositional gradients of the fabricated MLs. The thickness of all libraries varied in the range of approximately 4.25 - 4.9 μm. Thickness values were typically highest for the geometrical center of the MLs and dropped off towards the edges due to the configuration of the deposition system. By utilizing two opposing Cu targets the thickness variation along the composition gradient was reduced which improved comparability

of MAs with different Zr contents. The composition gradient (Fig. 75) covered most of the targeted composition range, with only a small gap in the range of $Cu_{100-x}Zr_x$ (1.5 < x < 2).
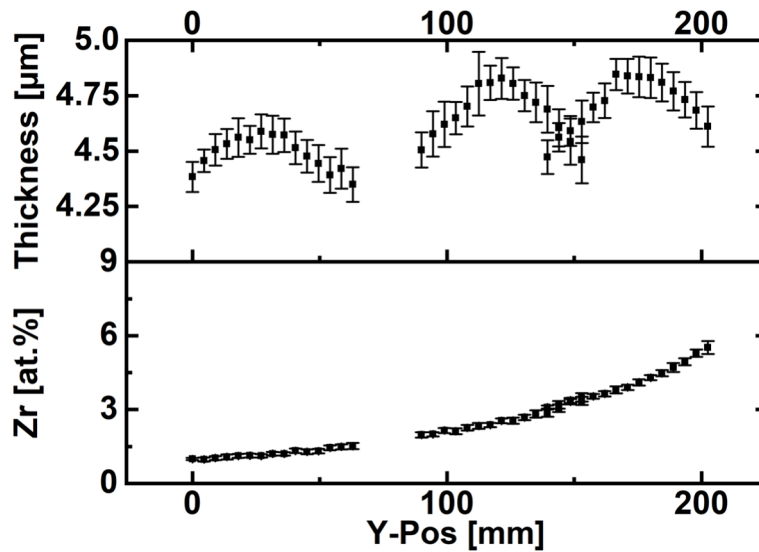
Fig. 75: Film thickness and composition of the fabricated MLs plotted over the position of the measurement areas along the composition gradient. The measurement areas were placed with a spacing of 4.5 mm. Three individual MLs were fabricated, visibly distinguished by the characteristic arc shape of the thickness distribution.

As a basis for evaluation of the mechanical and electrical properties the microstructure with regards to GS, elemental distribution and crystal orientation was investigated for the different compositions and test conditions.
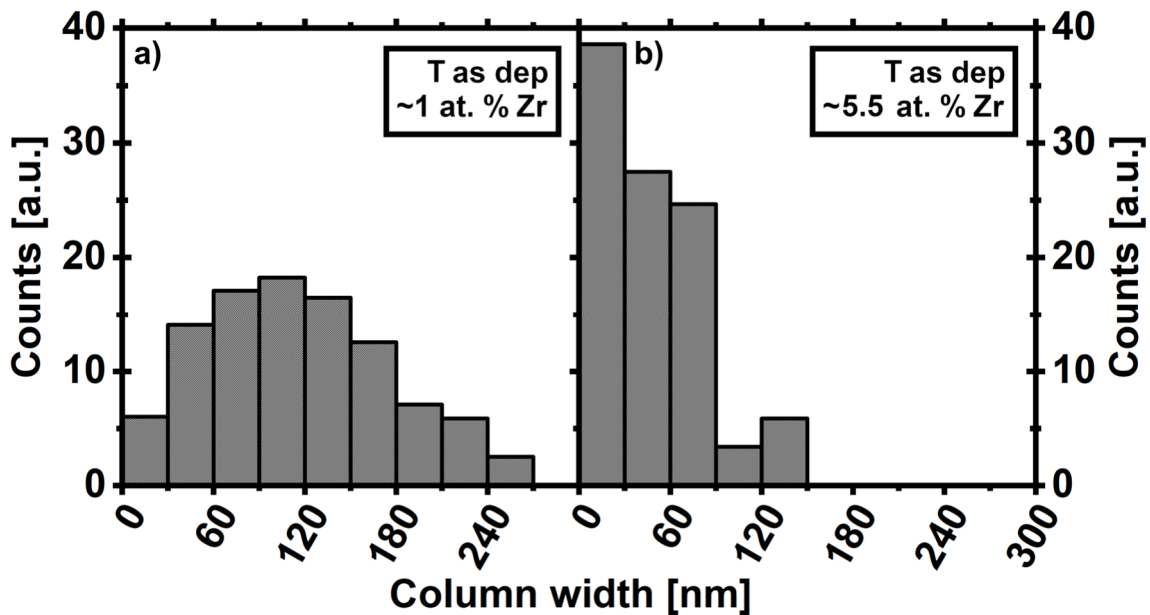
Fig. 76: GS distribution by grain quantity over GS in 30 nm increments for as-deposited Cu-Zr tensile-test structure MAs with a) an Zr content of approximately 1 at.% and b) an Zr content of approximately 5.5 at.%.

As-deposited GS was evaluated by TEM analysis for tensile-test structure MAs with Zr contents of approximately 1 and 5.5 at.%. Intermediate Zr contents MAs were not investigated, because a linear dependency of GS and Zr content was expected. The average GS decreased from approximately 114 nm to 45 nm for 1 and 5.5 at.% Zr respectively (Fig. 76). In comparison to the Cu reference, no abnormal grain growth was observed, and size distribution was more homogenous.
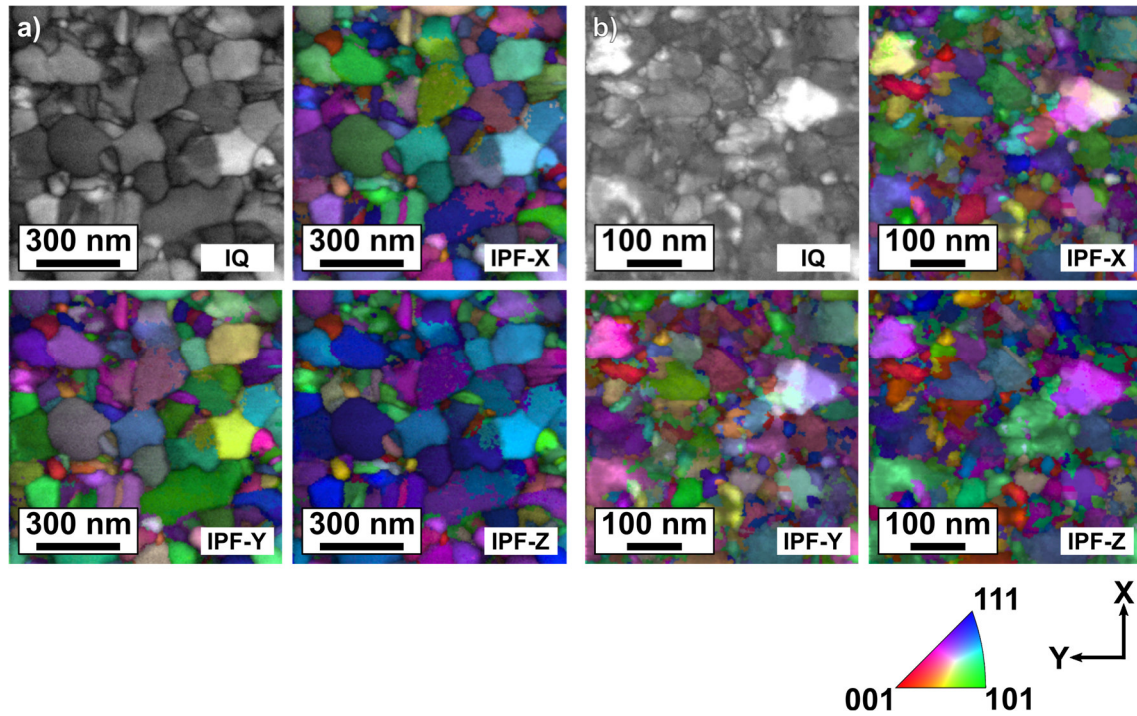
Fig. 77: TEM grain analysis with IQ and crystal orientation (IPF-X/Y/Z) maps for as-deposited Cu-Zr tensile-test structure MAs with a) an analysis for a Zr content of approximately 1 at.% and b) an analysis a Zr content of approximately 5.5 at.%. Cuts were prepared orthogonal to the film growth direction and the Z-axis represented the growth direction of the thin-film.

In addition to GS, crystal orientation measurements were performed during TEM investigation. Fig. 77 shows results for MAs of low and high Zr content with maps of the image quality and crystal orientations in dependence of the orientation of the MA. The Z-axis represents the growth direction of the thin film and the X-/Y-axis the plane of the wafer surface. For low contents, measurements indicated a preferential (111) orientation in film growth direction and for high Zr contents no apparent preferential orientation was observed.

Investigations of microstructural properties in the annealed state were performed for different Zr contents to evaluate the microstructural evolution. Upon annealing Cu_5Zr precipitates formed and grain growth was observed for a part of the investigated compositions (Fig. 78). From literature primarily two behaviors were observed which were grain boundary

segregation of Zr up to a Zr content of approximately 1 at.% and formation of Cu_xZr_y precipitates for higher Zr contents [132], and grain boundary segregation of Zr up to a Zr content of approximately 1 at.% and formation of an Zr rich amorphous phase at the grain boundaries for higher Zr contents [124,125]. For this study the formation of Cu_5Zr precipitates, which was consistent with the phase diagram, was confirmed through XRD and SEM image analysis and subsequent GS characterization was performed by SEM image analysis. Verification of phase formation through XRD was performed on substrate-bound MAs in the as-deposited and annealed state (400 °C, 1800 s) for Zr contents of approximately 1 and 5.5 at.%. As-deposited, diffractograms showed intensity maxima which correlated with Cu and no maxima which correlated with Zr and Cu_5Zr, which indicated the expected solid solution. After annealing, the formation of Cu_5Zr precipitates was observed.
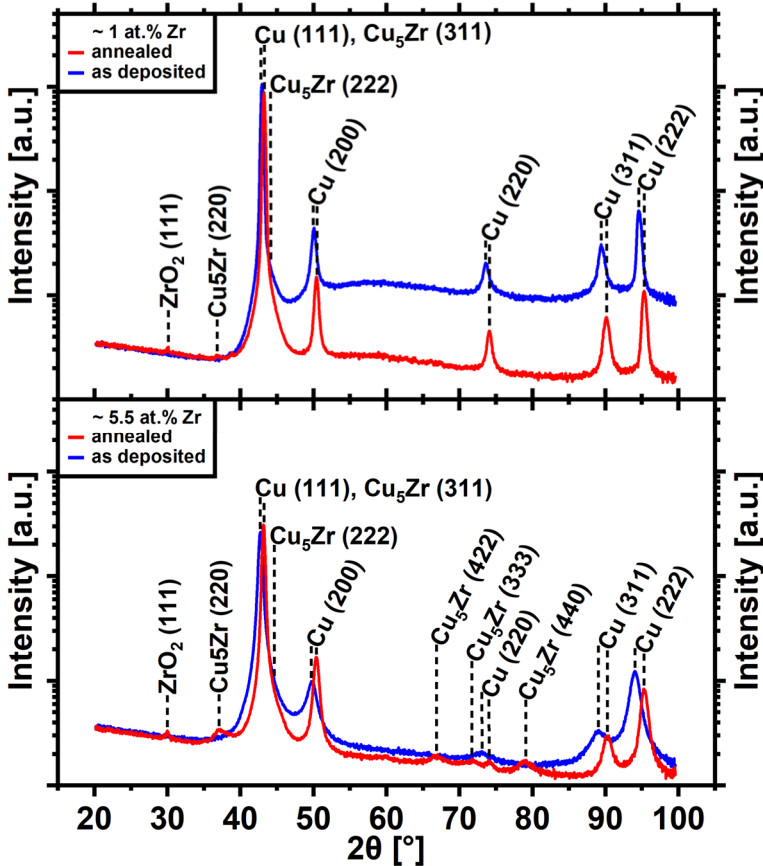
Fig. 78: XRD diffractograms of substrate-bound MAs with Zr contents of 1 and 5.5 at.% in the as-deposited (blue) and annealed (red) state.

For investigation of GS distribution cross-sectional cuts were prepared through ion-beam etching and characterization was performed through analysis of BSED SEM which provided elemental contrast. Characterizations were performed on tensile-test structure (Fig. 79) and substrate-bound (Fig. 80) MAs in the annealed state (400 °C, 1800 s) for Zr contents

130

of approximately 1, 3.5 and 5.5 at.%. Both, tensile-test structure and substrate-bound MAs showed clear columnar structure at 1 at.% Zr with a high density of twin boundaries oriented perpendicular to the growth direction. With an increased Zr content of 3.5 at.% the columnar microstructure was retained, and for the tensile-structure MAs the column height decreased in addition. Twin boundaries were no longer observable by SEM. For a Zr content of 5.5 at.% the columnar microstructure was still visible, but columns were reduced in height in comparison to lower Zr contents. Additionally, no twins were observed by SEM. Twin formation in Cu-Zr was observed by Zhang et al. [124] and Zhao et al. [125], and by Niu et al. for nanolayered Cu Zr [133] who attributed twin formation to high internal stresses. High internal stress was also observed for the Cu-Zr structures in this study, as indicated by the high bending of the freestanding tensile-structure MAs which could have contributed to twin formation.
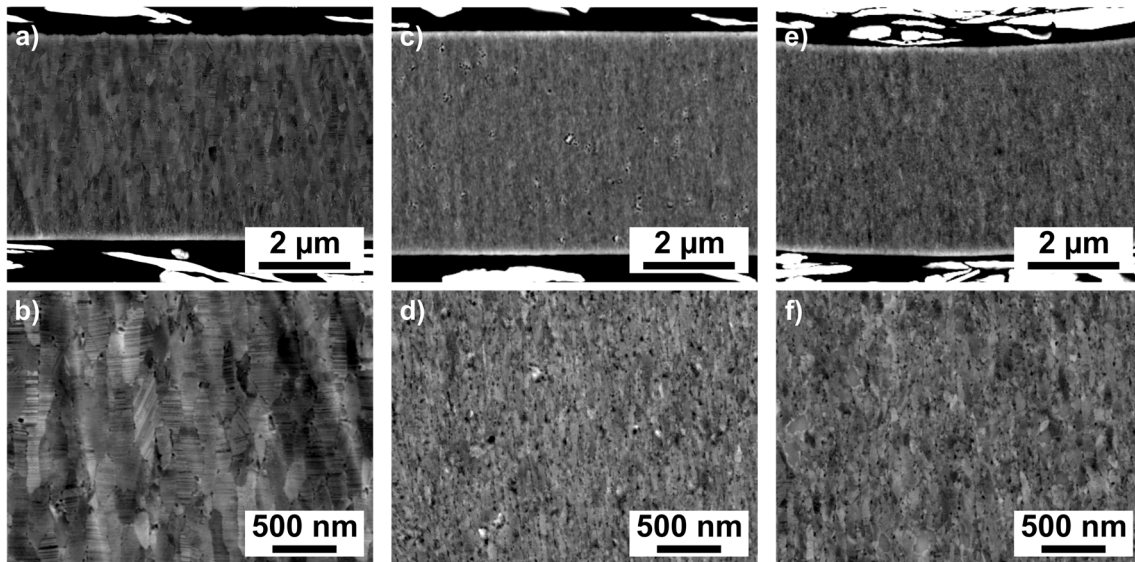
Fig. 79: SEM BSED images of cross-sectional cuts prepared from tensile-test structure MAs in the annealed state with an overview image and a high magnification image for Zr contents of approximately a, b) 1 at.%, c, d) 3.5 at.% e, f) 5.5 at.%.
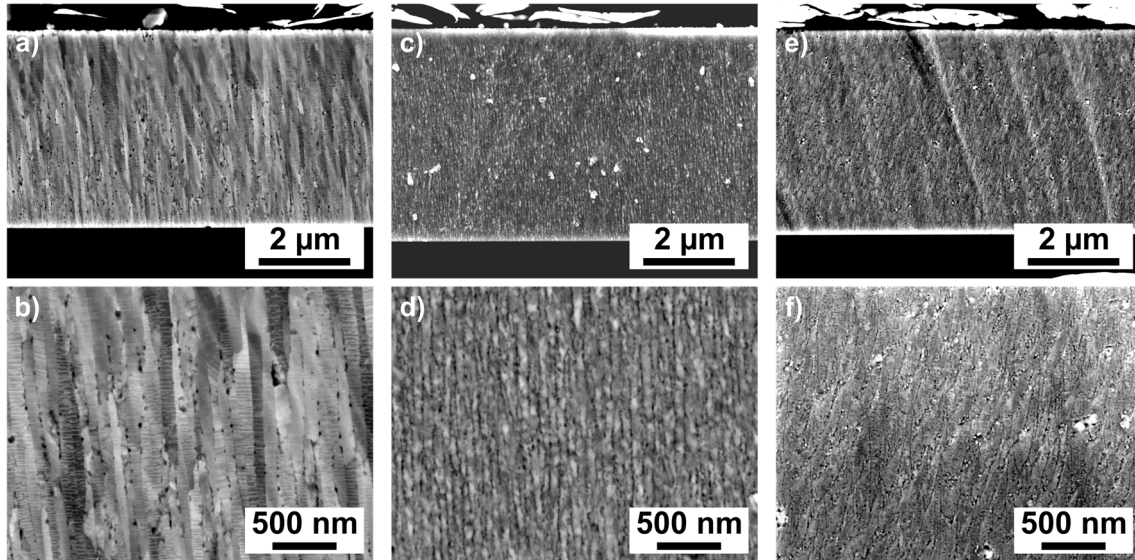
Fig. 80: SEM BSED images of cross-sectional cuts prepared from substrate-bound MAs in the annealed state with an overview image and a high magnification image for Zr contents of approximately a, b) 1 at.%, c, d) 3.5 at.% e, f) 5.5 at.%.

The cross-sections were utilized for investigation of GS and crystal orientation for Cu grains through EBSD analysis (Fig. 81). Due to high drift during measurements, it was not possible to automatically determine GS by EBSD analysis. EBSD images showed a highly preferential (111) texture along the Y-axis, which corresponded to the in-plane direction of the film. The preferential orientation was not observed in the as-deposited state and only appeared after heat treatment. The texture was assumed to be induced by the high internal stress which was similarly oriented for all MAs. This effect was observed during a prior study by Seita et al. who demonstrated thin-film growth with out-of-plane texture due to ion-bombardment induced stress during synthesis of Ag thin films [134].
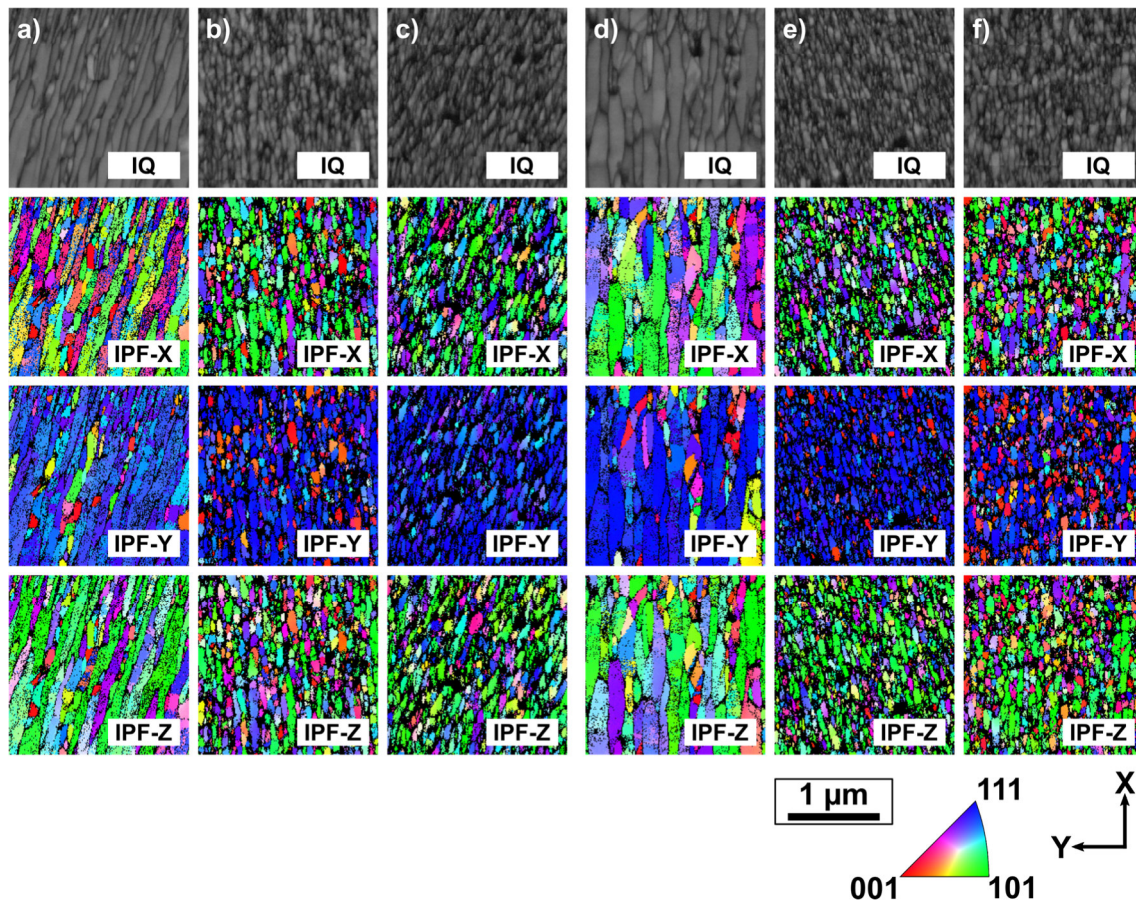
Fig. 81: EBSD analysis of cross-sectional cuts through annealed, (a, b, c) substrate-bound and (d, e, f) tensile-test structure Cu-Zr MAs. IQ and crystal orientation (IPF-X/Y/Z) maps with approximate Zr contents of a) 1 at.%, b) 3.5 at.%, c) 5.5 at.% for substrate-bound MAs and d) 1 at.%, e) 3.5 at.%, f) 5.5 at.% for tensile-test structure MAs. The X-axis represented the growth direction of the thin film.

GS was determined with the intercept method, as EBSD analysis was not viable due to high drift in combination with the small GS. Because grains primarily consisted of columns along the growth direction, intercepts were analyzed along 5 lines orthogonal to the film growth direction to acquire column width. Column width distributions are shown in Fig. 82 (a-c) for the substrate-bound MAs. Average column width decreased only slightly with increasing Zr content from 81 nm to 61 nm for 1 and 3.5 at.% Zr and remained approximately constant for increasing Zr content with 70 nm at 5.5 at.% Zr. For tensile-test structure MAs (Fig. 82 (d-f)) the average column width showed similar behavior with 109 nm to 63 nm to 67 nm for 1, 3.5 and 5.5 at.% Zr respectively. Column width values for the Cu-Zr structures are summarized in Table 5. Parameters for Cu MAs are included for direct comparison.
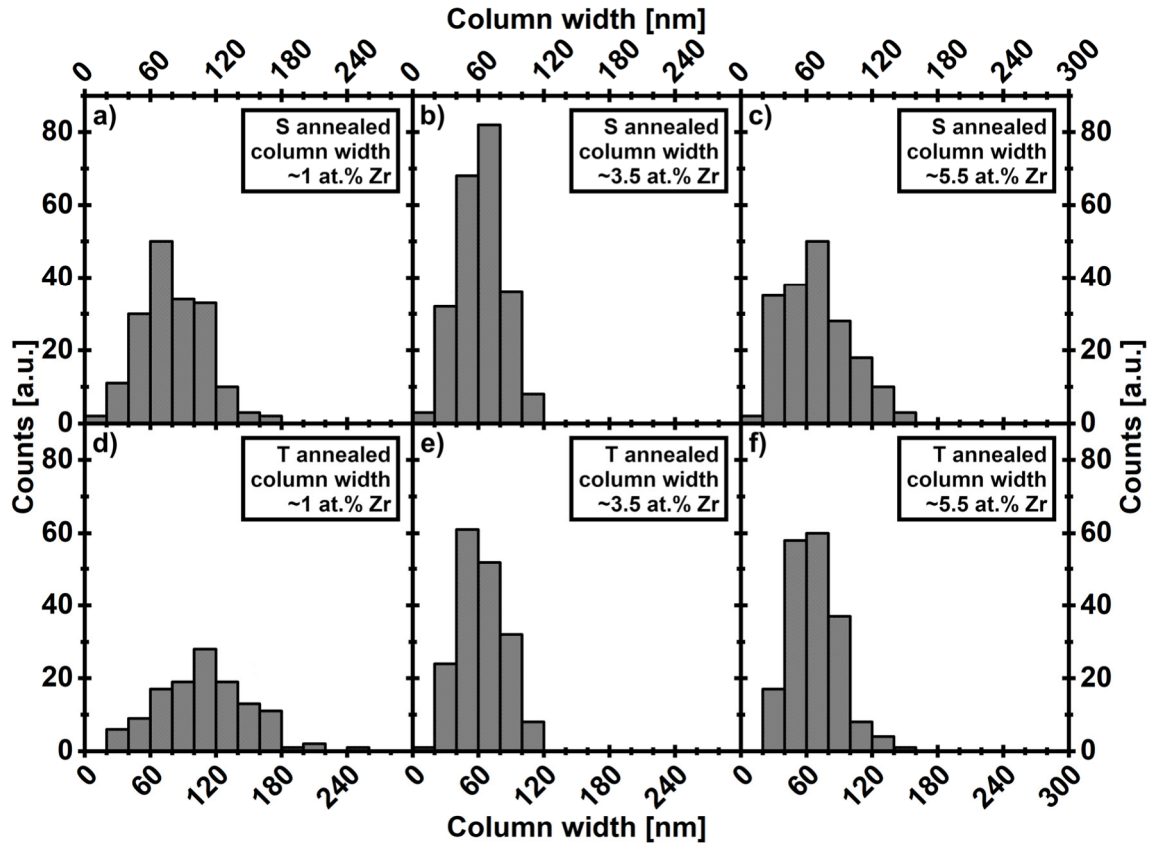
Fig. 82: Column width distributions of annealed, substrate-bound (a, b, c) and tensile-test structure (d, e, f) MAs for different Zr concentrations (1, 3.5 and 5.5 at.% Zr).

GS values of substrate-bound and tensile-structure MAs were very similar for corresponding compositions. In comparison to Cu-Ag, the behavior was more consistent in between substrate-bound and tensile-test structure MAs and GS was generally lower. The general reduction in GS relative to Cu, as well as the similar GS of substrate-bound and tensile-structure MAs were expected due to the formation of Cu_5Zr precipitates, which were reported for effectively constraining grain growth and stabilization of the microstructure [124–126,132]. Influences from the utilized annealing setup on the observed GS characteristics of the different ML types was not expected. For substrate-bound MAs the Cu-Zr thin film remained on the wafer which was cut into smaller pieces and placed on the graphite carrier. Tensile-structure MAs were annealed after lift-off from the substrate as freestanding films and were placed clamped in between the graphite carrier and a wafer substrate on top (Fig. 74). The annealing system utilized infrared lamps, so heating was primarily achieved by radiation from the top. As the assembly was slightly different for both MA types heating times might have differed slightly. But due to the high heating rate (approximately 20 K/s) influences of varying temperature ramp up times (approximately 20 s) were negligible as the hold time of 1800 s at 400 °C were significantly longer. Additionally, differences in heating/cooling rates in between the utilized annealing setups were small (< 60 s heating, < 300 s cooling).

134

Table 5: Summary of average column width for Cu-Zr tensile-test structure and substrate-bound MAs in the as-deposited and annealed state with average Cu GS for reference.

Cu reference				
T as-dep Cu GS	[nm]	358		
T as-dep Cu std dev	[nm]	479		
S as-dep Cu GS	[nm]	274		
S as-dep Cu std dev	[nm]	382		
T annealed Cu GS	[nm]	1186		
T annealed Cu std dev	[nm]	928		
Cu-Zr				
Zr cont.	**[at.%]**	**~1**	**~3.5**	**~5.5**
Cu-Zr Tensile as-deposited				
T as-dep Cu GS	[nm]	114		48
T as-dep Cu std dev	[nm]	57		33
Cu-Zr Tensile annealed				
T annealed Cu GS	[nm]	109	63	67
T annealed Cu std dev	[nm]	41	21	22
Cu-Zr Substrate annealed				
S annealed Cu GS	[nm]	81	61	70
S annealed Cu std dev	[nm]	30	20	30

T → Tensile-structure MA
S → Substrate-bound MA
as-dep → as-deposited MA
annealed → 30 min at 400 °C

For later evaluation of the functional properties, the distribution of the Cu_5Zr precipitates in the microstructure was investigated. In contrast to the bright appearance of Ag precipitates, the elemental contrast of BSED SEM images appeared dark for Zr containing precipitates (Fig. 83 a)). Local EDS investigations were performed to confirm the presence of Zr (Fig. 83 b)). Line scans indicated an elevated Zr content in the area of the dark particles (Fig. 83 c)). Along the performed line-scans a constant Zr content of approximately 0.75 at.% was measured which was caused by the interaction volume of the electron beam with the material. As measurements were performed on cross-sectional cuts and not thin lamellas, the electron beam did interact with the volume behind the cross-section surface, which caused the increased Zr content. For a precise quantification of the Zr content an EDS investigation on a thin lamella would have been required to minimize the electron interaction with the material. The Cu_5Zr particles were preferentially located along the grain boundaries for Zr contents of 1 and 3.5 at.%. For higher contents of 5.5 at.% the size of the dark particles was either significantly reduced for tensile-structure MAs, or no longer visible in case of substrate-bound MAs. This might have been caused by a finer distribution of Cu_5Zr along the grain boundaries, but this could not be confirmed due to the insufficient resolution of the analysis by SEM.
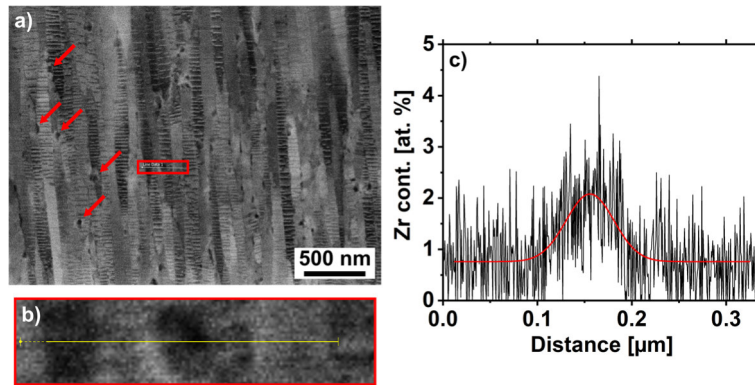
Fig. 83: a) SEM BSED image of a cross-sectional cut through a substrate-bound MA in the annealed state with a nominal Zr content of 1 at.%. Local areas with dark elemental contrast were observed, exemplary marked by arrows. b) Area investigated by EDS line-scan. c) Plot of Zr content over distance corresponding to the marked area. Fit of the measurement data was marked in red.

Investigated functional properties of the Cu-Zr alloys comprised electrical and mechanical properties. Electrical properties were investigated by sheet resistivity, and mechanical properties through nanoindentation and tensile experiments. Fig. 84 shows an overview of the electrical and mechanical properties in dependence of Zr content, as well as Cu reference measurement values for comparison. All tests were performed on as-deposited and annealed MAs. Annealings were performed 30 minutes at 400 °C under vacuum.

Resistivity measurements showed a linear increase with increasing Zr content with a higher slope in the as-deposited state, compared to the annealed state ($\sim 1.6^{-8} \, \Omega * m/at.\%$ vs. $\sim 7.6^{-8} \, \Omega * m/at.\%$). Compared to the IACS, the Cu-Zr alloys achieved values of 13 - 44 % in the annealed state and 3 - 15 % in the as-deposited state with increasing resistivity for increasing Zr contents.

Hardness increased approximately linearly in the as-deposited state and remained approximately constant in the annealed state for increasing Zr contents. Hardness was consistently lower in the annealed state and measurements were only performed up to a Zr content of approximately 3.5 at.% due to delamination of the thin films from the substrate for higher contents during annealing. For as-deposited MAs hardness increased from approximately 4.5 GPa to 6.5 GPa with a slope of approximately 0.41 GPa / at.% Zr. For annealed MAs, the hardness was approximately constant at 3.2 GPa. Reliability of measurements on annealed MAs was constrained by an increase in surface roughness and film delamination after annealing which rendered multiple measurements unusable.

Stress measurements were inconsistent over the investigated composition range and experiments were significantly influenced by pre-bending of the tensile-test structures, deformation of the structure heads under strain, and premature fracture due to the out of plane

136

bending of the structures. Due to these uncertainties, it was not possible to confidently identify the UTS and only the maximum stress (MS) during the measurement was determined. For as-deposited structures maximum stress started at approximately 1350 MPa and reduced to approximately 1000 MPa for Zr contents of 1 to 1.5 at.% which corresponded to the first ML. For Zr contents of 2 to 3.5 at.%, which corresponded to the second ML, MS again started higher at approximately 1250 MPa and reduced to approximately 400 MPa with increasing Zr content. No results were given for the third ML (3.5 at.% - 5.5 at.%), as it was not possible to perform the measurements due to high bending of the structures due to residual film stress. The main restriction was, that bending prevented proper positioning and gripping of the structure head, which prevented displacement of the structure. For annealed structures, the MS started with approximately 1200 MPa and reduced to approximately 1000 MPa for Zr contents of approximately 1 to 1.5 at.% which corresponded to the first ML. The MS showed a minimum of approximately 800 MPa for a Zr content of approximately 2.5 at.%. Maximum stress increased again and remained approximately constant for increasing Zr contents in the range of 3 to 4 at.%. In the range of 4 to 5 at.% Zr the MS decreased to approximately 1000 MPa and increased again to approximately 1350 MPa for a Zr content of approximately 5.5 at.%.
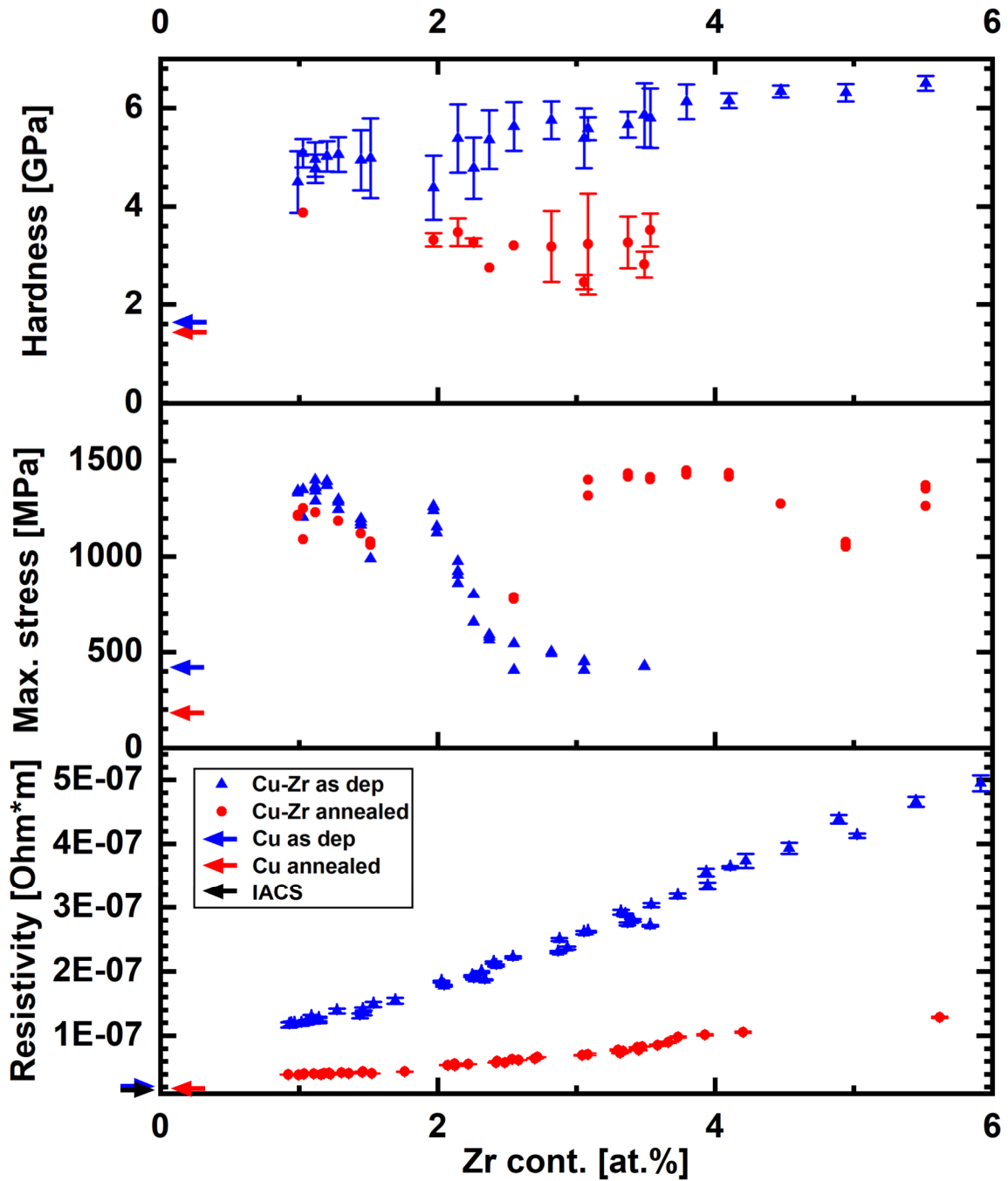
Fig. 84: Compilation of characterization results for a) hardness, b) maximum measured stress and c) electrical resistivity in dependence of the Zr content of the fabricated MLs.

As shown, the MS was inconsistent over the investigated compositional space and did not show a systematic behavior with increasing Zr content. But the measured MS was consistent within the set of redundant tensile-test structures of the individual MAs. This indicated that failure did not occur at random but was instead governed by the MA properties. To illustrate the reason for the changes in MS, multiple MAs along the composition gradient with different failure characteristics were characterized by stress-displacement measurements (Fig. 85-1), and corresponding images of the structure in the straining device before testing (Fig. 85-2), at

approximately 50 % of the MS (Fig. 85-3), directly before fracture (Fig. 85-4) and after fracture (Fig. 85-5). For as-deposited MAs the MS decreased with increasing Zr content (Fig. 85 a1 - c1). Deflection on the structure surface revealed, that the initial bending of the structures at the beginning of the test increased with the MS and the Zr content (Fig. 85 a2 - c2). Similarly, deformation of the head structures under load at approximately 50 % displacement increased for MAs with higher MS. For the MA with highest MS (~ 1200 MPa at ~ 1 at.% Zr) the head primarily straightened under load and did not deform significantly (Fig. 85 a3). For MAs with intermediate (~ 850 MPa at ~ 2 at.% Zr) and lowest (~ 400 MPa at ~ 3.5 at.% Zr) MS clear buckling of the head occurred under load (Fig. 85 b3 - c3). For all structures, deformation further increased with increasing displacement. Deformations were primarily characterized by increasing buckling of the head with decreasing MS (Fig. 85 b4 - c4). For all as-deposited MAs, structures failed by fracture close to the head (Fig. 85 b5 - c5). For the annealed state MAs with different failure behaviors were selected for illustration which were a MA with low Zr content (~ 1 at.%) with high MS (~ 1200 MPa), the MA with highest MS of all annealed MAs (~ 1400 MPa at ~ 4 at.% Zr) and a MA which showed a significantly reduced MS (~ 1000 MPa at ~ 5 at.% Zr) in comparison to surrounding MAs (Fig. 85 d1 - f1). Deflection on the structure surface showed, that the initial bending of the structures before testing was different for all selected MAs, even though all were annealed in the same clamped assembly to reduce bending. The MA with lowest Zr content and high MS showed high bending at the handle edges, though the gauge and head structure appeared straight without bending (Fig. 85 d2). This was attributed to the experimental procedure, as structure heads were sometimes straightened during contact and positioning of the gripper while the handle remained unaffected. The MA with a Zr content of approximately 4 at.% and high MS showed low bending in all film areas (Fig. 85 e2) and the last MA at approximately 5 at.% Zr with lower MS showed high bending at the handle edges and along the gauge/head. Under load at approximately 50 % displacement all MAs showed buckling of the head (Fig. 85 d3 - f3). MAs with a Zr contents of approximately 1 and 4 at.% did show increasing buckling (Fig. 85 d4, f4) and did not fail by fracture. Instead, the structures were "pulled through" the opening of the gripper with increasing load (Fig. 85 d5, f5). The MA with approximately 5 at.% Zr and low MS also showed increasing buckling (Fig. 85 e4) but failed by fracture (Fig. 85 e5).

For the presented structures, no clear systematic behavior was observed during overall testing. While as-deposited MA behavior indicated that higher bending of the structures due to intrinsic stress resulted in premature failure at lower stress due to bending of the structure head, annealed MAs were able to achieve high MS even though a high degree of bending at the

structure head was observed. This might have been caused by differences in mechanical behavior of the material after annealing, but this could not be confirmed due to the inconsistent results.
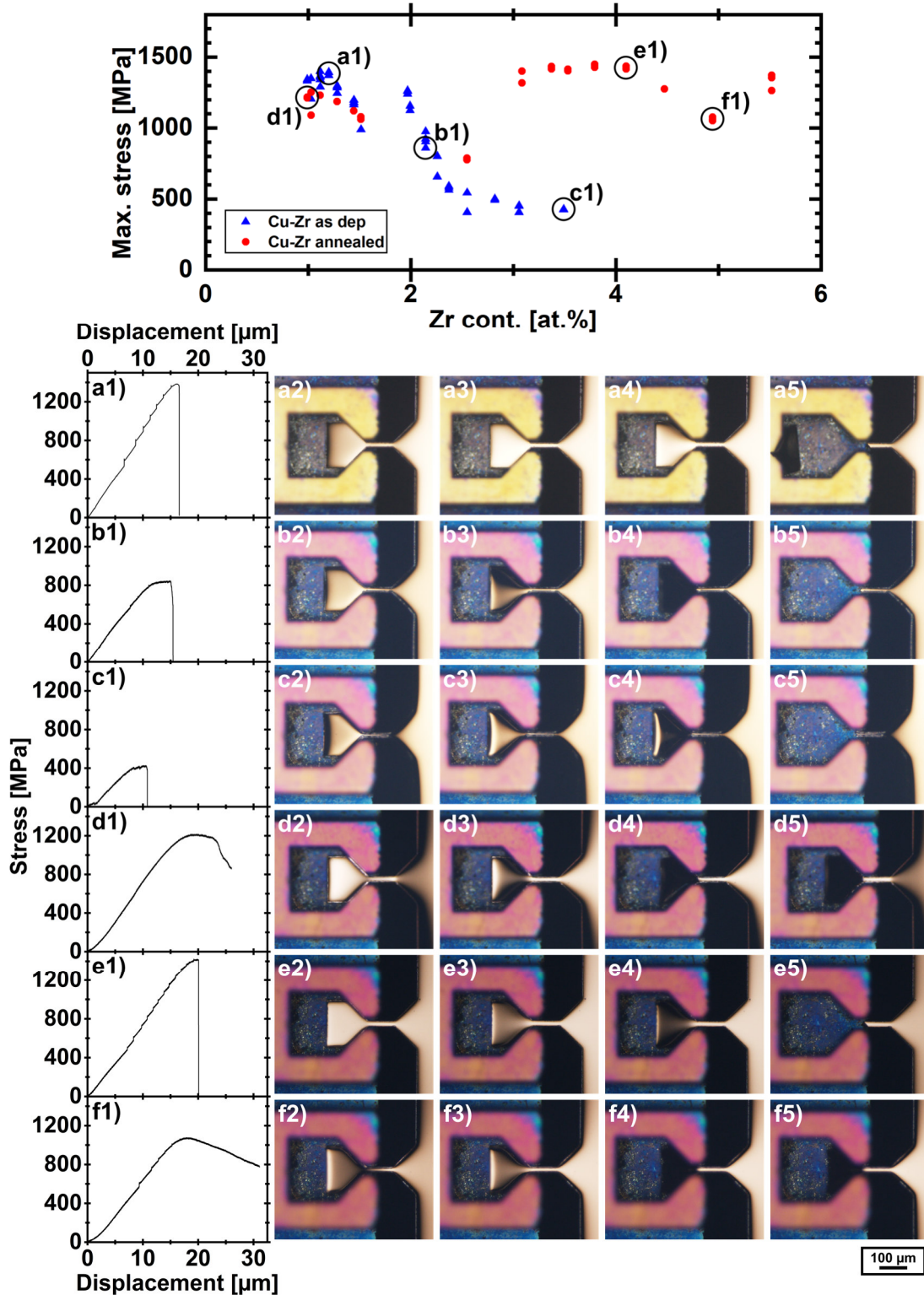
Fig. 85: (1) Plots of stress-displacement data and optical microscope images of corresponding structures at (2) initial contact between structure and gripper, (3) at approximately 50 % strain of the corresponding experiment, (4) before fracture and (5) after fracture. The presented structures (a-f) were marked in the preceding stress-displacement graph.

140

The inconsistent bending of the structures due to intrinsic stress was assumed to be the main reason for the observed inconsistencies in mechanical behavior, as the bending resulted in misalignments in between the MA and gripper and application of force outside of the gauge length-axis. An exemplary arrangement of MAs after lift-off is shown in Fig. 86 for MAs with a composition from approximately 3 at.% Zr to 5.5 at.% Zr to illustrate the behavior of bending along the composition gradient of a ML. The bending was clearly observable by eye through surface reflections. The axis of the bending was generally oriented orthogonal to the tensile-gauge axis and angular changes of the orientation were observed with changing Zr content. The observed bending was higher in comparison to Cu-Ag by qualitative assessment of the bending radius. The increase in bending might have been caused by preferential orientation of internal stress due to the preferential crystal orientation that was observed for all Cu-Zr MAs. The increased bending complicated manual handling and mounting the MAs as according to Fig. 26 and bending was still visible at the structure gauge and head after assembly and mounting of the MAs.
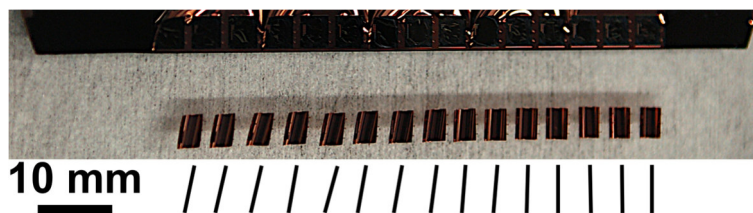
Fig. 86: Photograph of one column from a Cu-Zr ML along the compositional gradient after lift-off arranged next to the Si substrate. Lines below the placed MAs indicate the change in orientation of the axis around which the MAs were bend due to intrinsic stress.

To simulate mechanical behavior at elevated temperatures, tensile-test structures were tested in-situ at 400 °C. Similar to investigations at RT, deformations of the tensile-test structure heads were observed which ranged from bending under load with subsequent fracture to combined bending and buckling without fracture where structures were "pulled through" the opening of the gripper. In addition, testing was not possible for multiple MAs, because structures bend out-of-plane under elevated temperature which prevented insertion to the gripper. Fig. 87 shows tensile-test experiments of MAs with selected intermediate and high Zr contents of 2.5, 3, 5 and 5.5 at.% to illustrate the mechanical behavior. MAs with a Zr content of 2.5 and 5.5 at.% did not fracture with increasing strain and the slow decrease in stress after the maximum was attributed to continuous bending and buckling of the structure head. MAs with a Zr content of 3 and 5 at.% did fail with fracture. Mechanical behavior appeared ductile with regards to the stress-displacement data. But optical evaluation of the experiments showed

significant out-of-plane bending with increasing load which influenced stress-displacement characteristics and prevented confirmation of ductile behavior. Maximum stress that was observed was high for all MAs with approximates of 500 MPa at 2.5 at.%, 725 MPa at 3 at.%, 725 MPa at 5 at.% and 650 MPa at 5.5 at.%. MS was significantly higher in comparison to Cu by a factor of approximately 12 to 18 depending on the specific MA. No consistent increase of MS with increasing Zr was observed and it was assumed that mechanical behavior with increasing displacements was primarily governed by the unwanted deformation at the structure head.
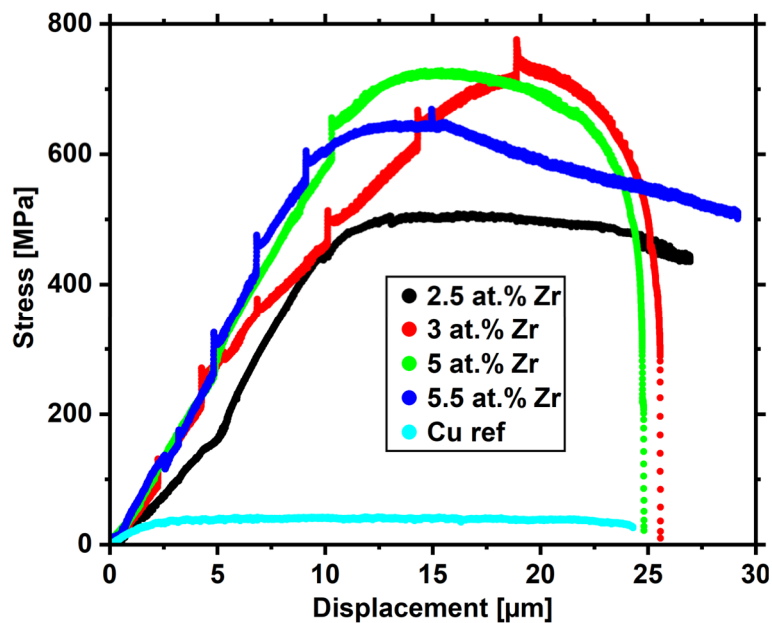
Fig. 87: Comparison of in-situ tensile experiments for Cu-Zr tensile-test structure MAs at 400 °C. No fracture occurred for MAs with a Zr content of approximately 2.5 and 5.5 at.% due to bending and buckling of the structure head under load.

Changes in resistivity were primarily explained by the microstructure evolution of the Cu GS and the Zr distribution. For evaluation of the electrical properties the GS was approximated by the column width measured for annealed MAs, because electron transport for sheet resistivity measurements occurred in line with the column width.

Resistivity for as-deposited and annealed Cu-Zr MAs was plotted over GS for MAs where both properties were available (Fig. 88). For comparison, additional reference values of Cu MAs and a calculated approximation for Cu (section 3.1) were included. For as-deposited MAs resistivity was governed by GS and scattering by impurity atoms such as the Zr atoms in solid solution. The increase in resistivity from a Zr content of 1 to 5.5 at.% was significant by approximately half an order of magnitude ($\sim 4.5*10^{-7}$ $\Omega*m$). The change was superimposed with a reduction in GS to 48 nm which was close to the electron mean free path of Cu

(39 nm [84]). With regards to GS only the Cu grains were considered, as Zr was distributed throughout the Cu matrix and no Zr grains were observed. The alloyed Zr was characterized by a resistivity of approximately $4.2*10^{-7}$ $\Omega*$m. Both, GS close to the electron mean free path and high base resistivity of Zr explained the increased resistivity with increasing Zr content. But it should also be noted that uncertainties in the actual as-deposited resistivity values were possible because column width values were only measured for tensile-structure MAs and might not have been representative of the actual GS of substrate-bound MAs with similar Zr content.

The reduction in resistivity for annealed MAs was primarily attributed to the reduction in impurity scattering due to the formation of Cu_5Zr precipitates. No significant influence was expected due to GS evolution as GS remained approximately constant in comparison to as-deposited GS. The linear increase in resistivity was consistent with GS and Zr content as GS was approximately proportional to the increase in Zr content which increased approximately linearly over the shown MAs. The calculated approximation for Cu was consistent with the measured lower bound resistivity for 1 at.% Zr as the overall resistivity was primarily governed by Cu grains due to the low Zr content whereas the higher absolute resistivity was likely explained by additional scattering due to the distributed Cu_5Zr precipitates. The increase in resistivity relative to the increase in Zr content was unexpectedly high (approximately $2*10^{-8}$ $\Omega*$m per at.% Zr) in comparison to the resistivity of pure Zr (approximately $4.2*10^{-7}$ $\Omega*$m). This might have been a result of additional influences such as a possible preferential distribution of fine precipitates toward the grain boundaries and observed twin boundaries, but more in-depth investigations would have been required for confirmation.
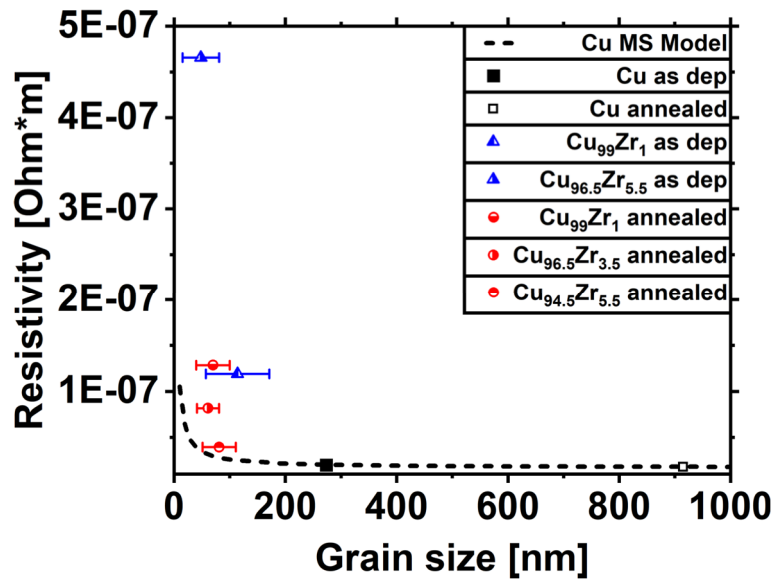
Fig. 88: Plot of electrical resistivity over GS for substrate-bound Cu-Zr MAs measured in the as-deposited and annealed state. Cu reference measurements were included for comparison. The dashed black line indicates the calculated resistivity for Cu over GS after Eqn. 2.

In depth analysis of mechanical properties acquired by tensile testing and quantification of the contributing strengthening mechanisms was not possible for Cu-Zr because of the inconsistent measurements caused by structure deformation under load. As such, only a qualitative evaluation of the mechanical performance was carried out. For tensile experiments, the main characteristic that was useable for evaluation of mechanical properties was the maximum stress during measurement, as it was the maximum load that was definitively carried by the tensile gauge and was therefore representative of the minimum strength of the material. Overall tensile experiments for Cu-Zr showed very interesting and promising mechanical behavior for selected MAs that failed by fracture without extensive deformation at the structure head. For such MAs high MS was observed which was retained to a high degree after annealing and also partially during in-situ testing at elevated temperatures.

For low Zr contents of approximately 1 at.% a reduction in MS by only 150 MPa from approximately 1350 to 1200 MPa was observed after annealing. For increasing Zr contents a direct comparison was not possible due to the bending induced fracture and subsequent reduction in MS for as-deposited MAs. But the increased MS for annealed MAs at Zr contents of approximately 3 to 4 at.% indicated that the material strength was at least constant and was expected to increase with increasing Zr content. Main strength contributions that were expected in the as-deposited state were H-P strengthening and solid-solution strengthening, whereas main expected contributions in the annealed state were H-P strengthening, precipitate strengthening and twin strengthening. Twin strengthening might also have contributed in the as-deposited state, but this could not be confirmed as microstructure investigations were

144

performed on material volumes that were oriented orthogonal to the film growth-axis, parallel to the expected twin orientation which might have prevented identification of existing twins. Considering the contributing strengthening mechanisms, the retention of mechanical strength for annealed MAs was primarily attributed to the stability of the microstructure. With the stability of Cu GS during heat treatment and twinning, the resulting contribution of H-P strengthening and twin strengthening in combination to the added precipitate strengthening were expected to explain the strength retention.

In-situ testing at 400 °C showed MS in the range of approximately 500 to 700 MPa for all tested Zr contents which was a significant increase in the order of 12- to 18-fold over the UTS of Cu tested under the same conditions. This further indicated the microstructural stability at elevated temperatures with retention of the small GS, distribution of twin boundaries and dispersed precipitates, which was paramount for the retention of the high mechanical performance.

The decreased MS for as-deposited tensile-test structure MAs was attributed to the unwanted deformation at the structure head. This was supported by mechanical properties measured by nanoindentation on substrate-bound MAs. The approximately linear increase in hardness with increasing Zr content indicated that a similar increase in MS during tensile testing should have been expected. No conclusive trend was observed for hardness of annealed MAs with increasing Zr contents, but the approximately constant hardness indicated that mechanical performance was at least retained and that uncharacteristic reductions in MS for selected Zr contents during tensile testing were likely caused by the previously mentioned deformations.

4 Summary and conclusions

4.1 Tensile-test structure investigations

Several concepts for tensile-test structure fabrication were evaluated with three base concepts and two improved iterations. The two approaches that required wet chemical etching of the Si substrate were unsuccessful due to failure of the etch barriers, or failures during dicing and separation of the structures. The third, purely lithographic approach was executed successfully, and the fabricated structures were characterized with respect to geometry, composition, microstructure, and mechanical properties. During the initial investigation with Cu as a structure material the functionality and reliability of the fabrication and characterization process was confirmed, but it was observed that the stability of the tensile-test structure head under load was insufficient under certain conditions. Two further iterations were investigated to improve stability of the structure head and general structure behavior under load through fabrication of corrugations at the head and general optimization of the tensile structure geometry. However, corrugated structures were detrimental to the head stability due to defects in the structure material during fabrication. An adaption of the fabrication process for the second iteration showed significant improvement in the structure geometry, but the impact of the improvement was not verified by testing. Results for the individual fabrication concepts are summarized in the following.

- Fabrication concept V1 showed high susceptibility for fabrication failures and issues in the fundamental design. Due to the intrinsic design issues and because the process provides no unique advantages, a further development, or optimization is not recommended.
- The high susceptibility for fabrication failures of V2 was caused by high intrinsic stress in the SiO_2 etch barrier during KOH etching. Optimization of the process would be possible by utilization of a low stress etch barrier to reduce failures during etching and by substitution of wet etching by dry etching processes to improve compatibility with combinatorial fabrication. With successful fabrication the approach V2 provides the advantage of a stable Si handle for handling and fixation, as well as better compatibility heat treatment processes. It is recommended to further explore this approach if suitable deposition and dry etching systems are available.

- Approach V3 showed good repeatability and low susceptibility to fabrication failures. The tensile-test structure geometry was sufficient for testing, but further optimizations to improve reliability and accuracy during tensile testing were required. The approach showed sufficient throughput for application to combinatorial processes. But for execution of combinatorial investigations a different straining device must be utilized to reduce required manual handling and adjustments. To improve applicability of the approach, further studies to control intrinsic stress of deposited material should be performed, as deformation due to stress presents the main limitation during structure fabrication. Due to the sensitivity of the process to intrinsic stress and the limited throughput due to restrictions of the straining device it is recommended to perform tensile tests in a second stage after other combinatorial investigations. This way it is possible to identify regions of interest in a first step and constrain mechanical characterization to these regions. This limits the quantity of measurements and the compositional regions that need to be synthesized, which in turn reduces the risk of significant intrinsic stress variations due to steep compositional gradients.

- The addition of corrugations in approach V4 was successful in reducing the influence of intrinsic stress. But ultimately the corrugations provided no net advantage, as they caused consistent and premature fractured under mechanical load along an interface that formed during sputtering.

- Approach V5 provided significant improvements in the tensile-test structure geometry which potentially solves restrictions of structure orientation during testing and deformation of the head under load. As the process flow is identical to approach V3 it is recommended to apply the optimizations to all fabrication processes that follow the concept of approach V3.

4.2 Material investigations

Functional properties of the three selected material systems Cu, Cu-Ag and Cu-Zr were investigated with varying success. Electrical and mechanical properties of the fabricated Cu structures matched well with references from literature. The Cu-Ag system, after heat treatment, showed a high retention of electrical properties and increased mechanical properties with a moderate increase for testing at RT and a minor increase for testing at elevated temperatures. Investigation of the Cu-Zr system was only partially successful due to high intrinsic stress of the material. After heat treatment Cu-Zr showed only intermediate electrical conductivity for the synthesized compositions. Exact mechanical properties could not be acquired due to frequent failures in the measurements, but results indicated a significant improvement at RT and at elevated temperatures in comparison to Cu and Cu-Ag.

- Validation of MAs fabricated by approach V3 was achieved with pure Cu under idealized conditions of a homogenous materials with low intrinsic stress.
- Compatibility of the tensile-test structure fabrication and characterization processes with combinatorial synthesis was demonstrated successfully with Cu-Ag for a defined compositional variation and a material with low intrinsic stress.
- Limitations for approach V3 were observed for materials with high intrinsic stress during investigation of Cu-Zr, which potentially limits the applicability of the approach.
- Cu showed good agreement with reference properties and was utilized for validation of the reliability of the applied characterization techniques.
- Cu-Ag showed promising performance for application in electronics devices after annealing with high electrical conductivity at RT and superior mechanical properties in comparison to Cu at RT and at elevated temperatures.
  - Mechanical properties in the annealed state were attributed to a combination of Hall-Petch and particle strengthening.
  - High conductivity after annealing was attributed to the increase in Cu GS (> 200 nm) during annealing and the formation of uninterrupted Cu pathways for conduction due to the segregation of Ag into isolated particles.
- Cu-Zr showed significantly higher mechanical performance in comparison to Cu and Cu-Ag after annealing and testing at RT and at elevated temperatures, but the electrical

conductivity was insufficient for application in electronics applications which require high conductivity.

- o Mechanical properties in the annealed state were partially attributed to Hall-Petch strengthening. Contribution of additional strengthening mechanisms was expected but could not be confirmed.
- o The intermediate conductivity was attributed to the combination of small Cu GS (< 80 nm) and the formation of Cu_5Zr precipitates at grain boundaries.

5 Outlook

While a successful tensile-test structure fabrication process was developed and successful investigations with different materials were performed, especially the structure fabrication and characterization process showed further potential for optimization. The main recommendation for future improvements is the optimization of aspects which target the overall throughput, as this represents the main limitation for application to combinatorial approaches.

- To reduce time for structure preparation before testing, the clamping mechanism of the straining device should be modified to clamp the tensile-test structures without further modification.
- Analog positioning systems for structure and gripper alignment should be replaced by digitally operated and motor driven alignment mechanisms for quicker and more precise alignment. For further optimization, automated alignment procedures through e.g., camera and sensor-controlled alignment should be implemented.
- To reduce time for structure exchange in between handling, it should be explored if the area of MAs can be increased along the direction orthogonal to the gauge axis. With this it would be possible to increase the quantity of structures that can be inserted into the straining device for investigation which would decrease handling time.

In addition to aspects concerning throughput, the current tensile-test structure fabrication process should be refined to further optimize the structure geometry and subsequently improve quality of the measurements. Approach V5 is recommended as a basis for optimizations as it yields the best geometry.

- For approach V5 the influence of the gap width in between the tensile-test structure and the parasitical side structure should be investigated for gaps < 3.7 μm. Smaller gaps should result in better sidewall geometries geometry and gaps down to approximately 1 μm should be within the capabilities of the fast broadband UV mask aligner fabrication.

- For approach V5 the substitution of the lift-of resist LOR 20 B with a different resist should be investigated to reduce the thickness of the lift-off resist layer. A lower thickness would result in a lower undercut which would improve structure geometry in the area of the undercut.

- As approach V5 allows the fabrication of tensile-test structures with low thickness lift-off structures the substitution of resists with dielectrics such as SiO_2 and Si_3N_4 should be investigated if dry etching machines for structuring are available. The reduced thickness of the lift-off system is in a range where fabrication with dielectric layers fabricated by chemical vapor deposition is viable and the structuring of the layers is possible by dry chemical etching. This approach could enable annealing of structures directly on the substrate, depositions at elevated temperatures, or also the anchoring of the tensile-test structure to the substrate for better structure handling.

Further investigations should be performed to improve the applicability of the current fabrication approach to combinatorial processes for investigation of MLs with compositional variations.

- As deformation due to intrinsic stress was one of the main limitations for execution of tensile tests, investigations should be performed to explore the possibility for optimization of intrinsic stress within the limitations of the utilized approach. Due to the deposition of photoresist, process parameters are restricted to low temperature processes which restrict parameters such as e.g., heating, substrate bias, or deposition rate.

Figures

158

6 References

(1) Moore, G. E. Cramming more components onto integrated circuits, Reprinted from Electronics, volume 38, number 8, April 19, 1965, pp.114 ff. *IEEE Solid-State Circuits Society Newsletter* **2006**, *11* (3), 33–35. DOI: 10.1109/N-SSC.2006.4785860.

(2) M. Madou. *Fundamentals of Microfabrication and Nanotechnology Vol. 3, From MEMS to Bio MEMS and Bio NEMS*; CRC Press, 2012.

(3) Lion, K. S. Transducers: Problems and Prospects. *IEEE Transactions on Industrial Electronics and Control Instrumentation* **1969**, *IECI-16* (1), 2–5. DOI: 10.1109/TIECI.1969.229858.

(4) Bergveld, P. The tip of the iceberg. Silicon Sensors. By S. Middelhoek and S. A. Audet. Academic Press, London 1989. xi, 376 pp., hardcover, £ 37.50.- ISBN 0-12-495051-5. *Advanced Materials* **1990**, *2* (9), 433–434. DOI: 10.1002/adma.19900020911.

(5) PETCH, N. J. The Cleavage Strength of Polycrystals. *Journal of the Iron and Steel Institute* **1953**, *174*, 25–28.

(6) Nix, W. D. Mechanical properties of thin films. *Metallurgical Transactions A* **1989**, *20* (11), 2217. DOI: 10.1007/BF02666659.

(7) Kraft, O.; Gruber, P. A.; Mönig, R.; Weygand, D. Plasticity in Confined Dimensions. *Annual Review of Materials Research* **2010**, *40* (1), 293–317. DOI: 10.1146/annurev-matsci-082908-145409.

(8) Julia R. Greer; Jeff Th.M. De Hosson. Plasticity in small-sized metallic systems: Intrinsic versus extrinsic size effect. *Progress in Materials Science* **2011**, *56* (6), 654–724. DOI: 10.1016/j.pmatsci.2011.01.005.

(9) Gerhard Dehm. Miniaturized single-crystalline fcc metals deformed in tension: New insights in size-dependent plasticity. *Progress in Materials Science* **2009**, *54* (6), 664–688. DOI: 10.1016/j.pmatsci.2009.03.005.

(10) E O Hall. The Deformation and Ageing of Mild Steel: III Discussion of Results. *Proceedings of the Physical Society. Section B* **1951**, *64* (9), 747–753. DOI: 10.1088/0370-1301/64/9/303.

(11) Armstrong, R. W. The influence of polycrystal grain size on several mechanical properties of materials. *Metallurgical and Materials Transactions B* **1970**, *1* (5), 1169–1176. DOI: 10.1007/BF02900227.

(12) Adelaide Nespoli; Stefano Besseghini; Simone Pittaccio; Elena Villa; Stefano Viscuso. The high potential of shape memory alloys in developing miniature mechanical devices: A

review on shape memory alloy mini-actuators. *Sensors and Actuators A: Physical* **2010**, *158* (1), 149–160. DOI: 10.1016/j.sna.2009.12.020.

 (13) Mohd Jani, J.; Leary, M.; Subic, A.; Gibson, M. A review of shape memory alloy research, applications and opportunities. *Materials & Design* **2014**, *56*, 1078–1113. DOI: 10.1016/j.matdes.2013.11.084.

 (14) George, E. P.; Raabe, D.; Ritchie, R. O. High-entropy alloys. *Nature Reviews Materials* **2019**, *4* (8), 515–534. DOI: 10.1038/s41578-019-0121-4.

 (15) Senkov, O. N.; Miracle, D. B.; Chaput, K. J.; Couzinie, J.-P. Development and exploration of refractory high entropy alloys—A review. *Journal of Materials Research* **2018**, *33* (19), 3092–3128. DOI: 10.1557/jmr.2018.153.

 (16) Unold, T.; Schock, H. W. Nonconventional (Non-Silicon-Based) Photovoltaic Materials. *Annual Review of Materials Research* **2011**, *41* (1), 297–321. DOI: 10.1146/annurev-matsci-062910-100437.

 (17) Polman, A.; Knight, M.; Garnett, E. C.; Ehrler, B.; Sinke, W. C. Photovoltaic materials: Present efficiencies and future challenges. *Science* **2016**, *352* (6283). DOI: 10.1126/science.aad4424.

 (18) Potyrailo, R.; Rajan, K.; Stoewe, K.; Takeuchi, I.; Chisholm, B.; Lam, H. Combinatorial and High-Throughput Screening of Materials Libraries: Review of State of the Art. *ACS Combinatorial Science* **2011**, *13* (6), 579–633. DOI: 10.1021/co200007w.

 (19) McGinn, P. J. Thin-Film Processing Routes for Combinatorial Materials Investigations—A Review. *ACS Combinatorial Science* **2019**, *21* (7), 501–515. DOI: 10.1021/acscombsci.9b00032.

 (20) Maier, W. F.; Stöwe, K.; Sieg, S. Combinatorial and High-Throughput Materials Science. *Angewandte Chemie International Edition* **2007**, *46* (32), 6016–6067. DOI: 10.1002/anie.200603675.

 (21) A Ludwig; J Cao; J Brugger; I Takeuchi. MEMS tools for combinatorial materials processing and high-throughput characterization. *Measurement Science and Technology* **2004**, *16* (1), 111–118. DOI: 10.1088/0957-0233/16/1/015.

 (22) Hintsala, E. D.; Hangen, U.; Stauffer, D. D. High-Throughput Nanoindentation for Statistical and Spatial Property Determination. *JOM* **2018**, *70* (4), 494–503. DOI: 10.1007/s11837-018-2752-0.

 (23) Xiaokun Zhang; Yong Xiang. Combinatorial approaches for high-throughput characterization of mechanical properties. *Journal of Materiomics* **2017**, *3* (3), 209–220. DOI: 10.1016/j.jmat.2017.07.002.

(24) Gregoire, J. M.; van Campen, D. G.; Miller, C. E.; Jones, R. J. R.; Suram, S. K.; Mehta, A. High-throughput synchrotron X-ray diffraction for combinatorial phase mapping. *Journal of Synchrotron Radiation* **2014**, *21* (6), 1262–1268. DOI: 10.1107/S1600577514016488.

(25) Robert Zarnetta. Combinatorial development and discovery of ternary and quaternary shape memory alloys. Doctoralthesis, Ruhr-Universität Bochum, Universitätsbibliothek, 2010.

(26) Salomon, S.; Hamann, S.; Decker, P.; Savan, A.; Meshi, L.; Ludwig, A. Combinatorial synthesis and high-throughput characterization of the thin film materials system Co–Mn–Ge: Composition, structure, and magnetic properties. *physica status solidi (a)* **2015**, *212* (9), 1969–1974. DOI: 10.1002/pssa.201532075.

(27) Ruoxi Xia; Christoph J. Brabec; Hin-Lap Yip; Yong Cao. High-Throughput Optical Screening for Efficient Semitransparent Organic Solar Cells. *Joule* **2019**, *3* (9), 2241–2254. DOI: 10.1016/j.joule.2019.06.016.

(28) Ludwig, A. Discovery of new materials using combinatorial synthesis and high-throughput characterization of thin-film materials libraries combined with computational methods. *npj Computational Materials* **2019**, *5* (1), 70. DOI: 10.1038/s41524-019-0205-0.

(29) Doerner, M. F.; Gardner, D. S.; Nix, W. D. Plastic properties of thin films on substrates as measured by submicron indentation hardness and substrate curvature techniques. *Journal of Materials Research* **1986**, *1* (6), 845–851. DOI: 10.1557/JMR.1986.0845.

(30) J. B. Pethicai; R. Hutchings; W. C. Oliver. Hardness measurement at penetration depths as small as 20 nm. *Philosophical Magazine A* **1983**, *48* (4), 593–606. DOI: 10.1080/01418618308234914.

(31) G. Dehm; H.P. Wörgötter; S. Cazottes; J.M. Purswani; D. Gall; C. Mitterer; D. Kiener. Can micro-compression testing provide stress–strain data for thin films?: A comparative study using Cu, VN, TiN and W coatings. *Thin Solid Films* **2009**, *518* (5), 1517–1521. DOI: 10.1016/j.tsf.2009.09.070.

(32) Uchic, M. D.; Dimiduk, D. M.; Florando, J. N.; Nix, W. D. Sample Dimensions Influence Strength and Crystal Plasticity. *Science* **2004**, *305* (5686), 986–989. DOI: 10.1126/science.1098993.

(33) Hong, S.; Weihs, T. P. Residual stresses in thin films using microcantilever beams In Thin Films: Stresses and Mechanical Properties, edited by JC Bravman; WD Nix; DM Barnett, & DA Smith. In *Mater. Res. Soc. Proc*, 1989, Vol. 130; pp 93–98.

(34) Haque, M. A. and Saif, M. T. A. A review of MEMS-based microscale and nanoscale tensile and bending testing. *Experimental Mechanics* **2003**, *43* (3), 248–255. DOI: 10.1007/BF02410523.

(35) Zhang, H. Z.; Zhang, H.; Liu, L. Microstructures and Tensile Properties of Electrodeposited Cu Sheets with Grain Sizes from Nanocrystalline to Ultrafine Scale. In *Materials Processing Technology II*; Trans Tech Publications, 2012, Vol. 538; pp 1611–1614. DOI: 10.4028/www.scientific.net/AMR.538-541.1611.

(36) Y.M. Wang; K. Wang; D. Pan; K. Lu; K.J. Hemker; E. Ma. Microsample tensile testing of nanocrystalline copper. *Scripta Materialia* **2003**, *48* (12), 1581–1586. DOI: 10.1016/S1359-6462(03)00159-3.

(37) Oh, Y.; Cyrankowski, E.; Shan, Z.; Syed Asif, S. A. Micro/nano-mechanical test system employing tensile test holder with push-to-pull transformer.

(38) Xiaodong Li; Bharat Bhushan. A review of nanoindentation continuous stiffness measurement technique and its applications. *Materials Characterization* **2002**, *48* (1), 11–36. DOI: 10.1016/S1044-5803(02)00192-4.

(39) Smolka, M.; Motz, C.; Detzel, T.; Robl, W.; Griesser, T.; Wimmer, A.; Dehm, G. Novel temperature dependent tensile test of freestanding copper thin film structures. *Review of Scientific Instruments* **2012**, *83* (6), 64702. DOI: 10.1063/1.4725529.

(40) Tsuchiya, T.; Tabata, O.; Sakata, J.; Taga, Y. Specimen size effect on tensile strength of surface-micromachined polycrystalline silicon thin films. *Journal of Microelectromechanical Systems* **1998**, *7* (1), 106–113. DOI: 10.1109/84.661392.

(41) L I J C Bergers; J P M Hoefnagels; M G D Geers. On-wafer time-dependent high reproducibility nano-force tensile testing. *Journal of Physics D: Applied Physics* **2014**, *47* (49), 495306. DOI: 10.1088/0022-3727/47/49/495306.

(42) J. Gaspar; M. E. Schmidt; J. Held; O. Paul. Wafer-Scale Microtensile Testing of Thin Films. *Journal of Microelectromechanical Systems* **2009**, *18* (5), 1062–1076. DOI: 10.1109/JMEMS.2009.2029210.

(43) Gravier, S.; Coulombier, M.; Safi, A.; Andre, N.; BoÉ, A.; Raskin, J.-P.; Pardoen, T. New On-Chip Nanomechanical Testing Laboratory - Applications to Aluminum and Polysilicon Thin Films. *Journal of Microelectromechanical Systems* **2009**, *18* (3), 555–569. DOI: 10.1109/JMEMS.2009.2020380.

(44) Saurabh Gupta; Olivier N. Pierron. MEMS based nanomechanical testing method with independent electronic sensing of stress and strain. *Extreme Mechanics Letters* **2016**, *8*, 167–176. DOI: 10.1016/j.eml.2016.01.005.

(45) Magagnosc, Daniel J. and Ligda, Jonathan P. and Sano, Tomoko and Schuster, Brian E. Femtosecond Laser Machining of Micro-tensile Specimens for High Throughput Mechanical Testing. In *Micro and Nanomechanics, Volume 5*; Starman, LaVern and Hay, Jenny, Ed.; Springer International Publishing: Cham, 2018; pp 7–9.

(46) N. André; M. Coulombier; V. De Longueville; D. Fabrègue; T. Gets; S. Gravier; T. Pardoen; J.-P. Raskin. Microfabrication-based nanomechanical laboratory for testing the ductility of submicron aluminium films. *Microelectronic Engineering* **2007**, *84* (11), 2714–2718. DOI: 10.1016/j.mee.2007.05.039.

(47) Fabregue, D.; André, N.; Coulombier, M.; Raskin, J. P.; Pardoen, T. Multipurpose nanomechanical laboratory: Five thousands micromachines on a wafer. *Micro Nanolett* **2007**, *2*, 13--16.

(48) R. C. Jaeger. *Introduction to Microelectronic Fabrication 2nd Edition*; Addison Wesley Pub Co Inc, 2001.

(49) Allresist GmbH. *Product Data Sheet, AR-P 5400 - AR-P 3510*.

(50) MicroChemicals GmbH. *Product Data Sheet, AZ nLOF 2000 series*.

(51) D. Naujoks. Röntgenphotoelektronenspektroskopische Untersuchungen zum Einfluss der Schichtdicke auf das Phasenumwandlungsverhalten von Ti51Ni38Cu11 Formgedächtnislegierungs-Dünnschichten. bachelor thesis, Ruhr-Universität-Bochum, 2012.

(52) D. M. Mattox. *Handbook of Physical Vapor Deposition (PVD) Processing - Film Formation, Adhesion, Surface Preparation and Contamination Control*; Noyes Publications, 1998.

(53) D. A. Glocker, S. I. Shah. *Handbook of Thin Film Process Technology*; Institute of Physics Publishing, 1995.

(54) Thornton, J. A. Influence of apparatus geometry and deposition conditions on the structure and topography of thick sputtered coatings. *Journal of Vacuum Science and Technology* **1974**, *11* (4), 666–670. DOI: 10.1116/1.1312732.

(55) Thornton, J. A. The microstructure of sputter-deposited coatings. *Journal of Vacuum Science & Technology A* **1986**, *4* (6), 3059–3065. DOI: 10.1116/1.573628.

(56) André Anders. A structure zone diagram including plasma-based deposition and ion etching. *Thin Solid Films* **2010**, *518* (15), 4087–4090. DOI: 10.1016/j.tsf.2009.10.145.

(57) S. I. Wright. Random thoughts on non-random misorientation distributions. *Materials Science and Technology* **2006**, *22* (11), 1287–1296. DOI: 10.1179/174328406X130876.

(58) Thienhaus, S.; Zamponi, C.; Rumpf, H.; Hattrick-Simpers, J.; Takeuchi, I.; Ludwig, A. High-throughput characterization of shape memory thin films using automated temperature-

dependent resistance measurements. *MRS Proceedings* **2005**, *894*, 0894-LL06-06. DOI: 10.1557/PROC-0894-LL06-06.

(59) Smits, F. M. Measurement of Sheet Resistivities with the Four-Point Probe. *Bell System Technical Journal* **1958**, *37* (3), 711–718. DOI: 10.1002/j.1538-7305.1958.tb03883.x.

(60) Valdes, L. B. Resistivity Measurements on Germanium for Transistors. *Proceedings of the IRE* **1954**, *42* (2), 420–427. DOI: 10.1109/JRPROC.1954.274680.

(61) Arigela, V. G.; Oellers, T.; Ludwig, A.; Kirchlechner, C.; Dehm, G. Development of a high-temperature micromechanics stage with a novel temperature measurement approach. *Review of Scientific Instruments* **2019**, *90* (7), 73904. DOI: 10.1063/1.5086261.

(62) Arigela, V. G. *Development and application of a high-temperature micromechanics stage with a novel temperature measurement approach*; Ruhr-Universität Bochum, 2020.

(63) Xu, Y. K.; Adachi, S. Properties of light-emitting porous silicon photoetched in aqueous HF/FeCl3 solution. *Journal of Applied Physics* **2007**, *101* (10), 103509. DOI: 10.1063/1.2733752.

(64) Çak\i r, O. Review of Etchants for Copper and its Alloys in Wet Etching Processes. In *Optics Design and Precision Manufacturing Technologies*; Trans Tech Publications Ltd, 2008, Vol. 364; pp 460–465. DOI: 10.4028/www.scientific.net/KEM.364-366.460.

(65) Williams, K. R.; Gupta, K.; Wasilik, M. Etch rates for micromachining processing-Part II. *Journal of Microelectromechanical Systems* **2003**, *12* (6), 761–778. DOI: 10.1109/JMEMS.2003.820936.

(66) P.J French; P.M Sarro; R Mallée; E.J.M Fakkeldij; R.F Wolffenbuttel. Optimization of a low-stress silicon nitride process for surface-micromachining applications. *Sensors and Actuators A: Physical* **1997**, *58* (2), 149–157. DOI: 10.1016/S0924-4247(96)01397-0.

(67) Windischmann, H. Intrinsic stress in sputter-deposited thin films. *Critical Reviews in Solid State and Materials Sciences* **1992**, *17* (6), 547–596. DOI: 10.1080/10408439208244586.

(68) Lim, J.-W.; Ishikawa, Y.; Miyake, K.; Yamashita, M.; Isshiki, M. Influence of Substrate Bias Voltage on the Properties of Cu Thin Films by Sputter Type Ion Beam Deposition. *MATERIALS TRANSACTIONS* **2002**, *43* (6), 1403–1408. DOI: 10.2320/matertrans.43.1403.

(69) Pletea, M.; Brückner, W.; Wendrock, H.; Kaltofen, R. Stress evolution during and after sputter deposition of Cu thin films onto Si (100) substrates under various sputtering pressures. *Journal of Applied Physics* **2005**, *97* (5), 54908. DOI: 10.1063/1.1858062.

(70) Freund, L. B.; Suresh, S. *Thin film materials: stress, defect formation and surface evolution*; Cambridge University Press, 2004.

(71) Wimmer, A.; Smolka, M.; Heinz, W.; Detzel, T.; Robl, W.; Motz, C.; Eyert, V.; Wimmer, E.; Jahnel, F.; Treichler, R.; Dehm, G. Temperature dependent transition of intragranular plastic to intergranular brittle failure in electrodeposited Cu micro-tensile samples. *Materials Science and Engineering: A* **2014**, *618*, 398–405. DOI: 10.1016/j.msea.2014.09.029.

(72) Wimmer, A.; Heinz, W.; Leitner A.; Detzel, T.; Robl, W.; Kirchlechner C.; Dehm, G. Micro-tension study of miniaturized Cu lines at variable temperatures. *Acta Materialia* **2015**, *92*, 243–254. DOI: 10.1016/j.actamat.2015.03.056.

(73) Lin, M.-T. and Tong, C.-J. and Shiu, K.-S. Novel Microtensile Method for Monotonic and Cyclic Testing of Freestanding Copper Thin Films. *Experimental Mechanics* **2010**, *50* (1), 55–64. DOI: 10.1007/s11340-009-9221-1.

(74) Sanders, P. G.; Eastman, J. A.; Weertman, J. R. Elastic and tensile behavior of nanocrystalline copper and palladium. *Acta Materialia* **1997**, *45* (10), 4019–4025. DOI: 10.1016/S1359-6454(97)00092-X.

(75) Cheng, S.; Ma, E.; Wang, Y. M.; Kecskes, L. J.; Youssef, K. M.; Koch, C. C.; Trociewitz, U. P.; Han, K. Tensile properties of in situ consolidated nanocrystalline Cu. *Acta Materialia* **2005**, *53* (5), 1521–1533. DOI: 10.1016/j.actamat.2004.12.005.

(76) Zhang, H.; Jiang, Z.; Lian, J.; Jiang, Q. Bulk Nanostructured Cu with High Strength and Good Ductility. *Advanced Engineering Materials* **2008**, *10* (1-2), 41–45. DOI: 10.1002/adem.200700237.

(77) Maryna Lishchynska; Victor Bourenkov; Marc A.F. van den Boogaart; Lianne Doeswijk; Juergen Brugger; James C. Greer. Predicting mask distortion, clogging and pattern transfer for stencil lithography. *Microelectronic Engineering* **2007**, *84* (1), 42–53. DOI: 10.1016/j.mee.2006.08.003.

(78) M.F. ASHBY; C. GANDHI; D.M.R. TAPLIN. OVERVIEW NO. 3 - FRACTURE-MECHANISM MAPS AND THEIR CONSTRUCTION FOR F.C.C. METALS AND ALLOYS. In *Perspectives in Creep Fracture*; M.F. ASHBY, L.M. BROWN, Eds.; Pergamon, 1983; pp 1–31. DOI: 10.1016/B978-0-08-030541-7.50005-9.

(79) V Laporte; A Mortensen. Intermediate temperature embrittlement of copper alloys. *International Materials Reviews* **2009**, *54* (2), 94–116. DOI: 10.1179/174328009X392967.

(80) Arigela, V. G.; Oellers, T.; Ludwig, A.; Kirchlechner, C.; Dehm, G. Development of a high-temperature micromechanics stage with a novel temperature measurement approach. *Review of Scientific Instruments* **2019**, *90* (7), 73904. DOI: 10.1063/1.5086261.

(81) S. W. Stratton. *COPPER WIRE TABLES*, 1914.

(82) Mayadas, A. F.; Shatzkes, M. Electrical-Resistivity Model for Polycrystalline Films: the Case of Arbitrary Reflection at External Surfaces. *Phys. Rev. B* **1970**, *1* (4), 1382–1389. DOI: 10.1103/PhysRevB.1.1382.

(83) Sun, T.; Yao, B.; Warren, A. P.; Barmak, K.; Toney, M. F.; Peale, R. E.; Coffey, K. R. Surface and grain-boundary scattering in nanometric Cu films. *Phys. Rev. B* **2010**, *81* (15), 155454. DOI: 10.1103/PhysRevB.81.155454.

(84) W. Zhang; S.H. Brongersma; O. Richard; B. Brijs; R. Palmans; L. Froyen; K. Maex. Influence of the electron mean free path on the resistivity of thin metal films. *Microelectronic Engineering* **2004**, *76* (1), 146–152. DOI: 10.1016/j.mee.2004.07.041.

(85) Villars, Pierre and Okamoto, Hiroaki. *Ag-Cu Binary Phase Diagram 0-100 at.% Cu: Datasheet from "PAULING FILE Multinaries Edition - 2012" in SpringerMaterials (https://materials.springer.com/isp/phase-diagram/docs/c_0101004)*; Springer-Verlag Berlin Heidelberg & Material Phases Data System (MPDS), Switzerland & National Institute for Materials Science (NIMS), Japan. https://materials.springer.com/isp/phase-diagram/docs/c_0101004.

(86) Champion, Y.; Bourgon, J.; Sauvage, X. Modified strain rate regime in ultrafine grained copper with silver micro-alloying. *Materials Science and Engineering: A* **2016**, *657*, 1–5. DOI: 10.1016/j.msea.2016.01.044.

(87) Coddet, P.; Verdy, C.; Coddet, C.; Debray, F. Effect of cold work, second phase precipitation and heat treatments on the mechanical properties of copper–silver alloys manufactured by cold spray. *Materials Science and Engineering: A* **2015**, *637*, 40–47. DOI: 10.1016/j.msea.2015.04.008.

(88) Coddet, P.; Verdy, C.; Coddet, C.; Debray, F. On the mechanical and electrical properties of copper-silver and copper-silver-zirconium alloys deposits manufactured by cold spray. *Materials Science and Engineering: A* **2016**, *662*, 72–79. DOI: 10.1016/j.msea.2016.03.049.

(89) Dodla, S.; Thiem, P.; Krüger, M.; Dietrich, D.; Bertram, A. Microstructure, flow behavior, and bulk texture evolution of cold drawn copper–silver composites. *Journal of Alloys and Compounds* **2015**, *647*, 519–527. DOI: 10.1016/j.jallcom.2015.06.145.

(90) Frommeyer, G.; Wassermann, G. Anomalous properties of in-situ-produced silver-copper composite wires I. Electrical conductivity. *phys. stat. sol. (a)* **1975**, *27* (1), 99–105. DOI: 10.1002/pssa.2210270112.

(91) Han, K.; Vasquez, A.A.; Xin, Y.; Kalu, P.N. Microstructure and tensile properties of nanostructured Cu-25wt%Ag. *Acta Materialia* **2003**, *51* (3), 767–780. DOI: 10.1016/S1359-6454(02)00468-8.

(92) Hong, S. I. Superplastic Behavior and Activation Energies for Plastic Flow in Cu–Ag Mocrocomposites. *Advanced Engineering Materials - ADV ENG MATER* **2001**, *3.* DOI: 10.1002/1527-2648(200111)3:113.0.CO;2-0.

(93) Hong, S. I.; Hill, M. A. Mechanical stability and electrical conductivity of Cu–Ag filamentary microcomposites. *Materials Science and Engineering: A* **1999**, *264* (1), 151–158. DOI: 10.1016/S0921-5093(98)01097-1.

(94) Hu, J.-l.; Zhang, J.-d.; Meng, L. Morphology evolution of two-phase Cu-Ag alloys under different conditions. *Journal of Zhejiang University-SCIENCE A* **2009**, *10* (3), 458–463. DOI: 10.1631/jzus.A0820389.

(95) Pilyugin, V. P.; Solodova, I. L.; Tolmachev, T. P.; Antonova, O. V.; Chernyshev, E. G.; Patselov, A. M. On the Possibility of Formation and Properties of Copper–Silver Solid Solutions Under Severe Plastic Deformation. *Russian Physics Journal* **2016**, *58* (9), 1339–1346. DOI: 10.1007/s11182-016-0652-8.

(96) Sakai, Y.; Inoue, K.; Asano, T.; Wada, H.; Maeda, H. Development of high-strength, high-conductivity Cu–Ag alloys for high-field pulsed magnet use. *Applied Physics Letters* **1991**, *59* (23), 2965–2967. DOI: 10.1063/1.105813.

(97) Y. Sakai; K. Inoue; T. Asano; H. Maeda. Development of a high strength, high conductivity copper-silver alloy for pulsed magnets. *IEEE Transactions on Magnetics* **1992**, *28* (1), 888–891. DOI: 10.1109/20.120021.

(98) Yao, D. W.; Meng, L. Effects of solute, temperature and strain on the electrical resistivity of Cu–Ag filamentary composites. *Physica B: Condensed Matter* **2008**, *403* (19), 3384–3388. DOI: 10.1016/j.physb.2008.04.038.

(99) Fang, J. S.; Liu, Y. S.; Chin, T. S. Atomic layer deposition of copper and copper silver films using an electrochemical process. *Thin Solid Films* **2015**, *580*, 1–5. DOI: 10.1016/j.tsf.2015.03.015.

(100) Hakamada, M.; Nakamoto, Y.; Matsumoto, H.; Iwasaki, H.; Chen, Y.; Kusuda, H.; Mabuchi, M. Relationship between hardness and grain size in electrodeposited copper films. *Materials Science and Engineering: A* **2007**, *457* (1), 120–126. DOI: 10.1016/j.msea.2006.12.101.

(101) Ko, Y. K.; Jang, J. H.; Lee, S.; Yang, H. J.; Lee, W. H.; Lee, J. G.; Reucroft, P. J. Thickness effect on grain growth and precipitate coarsening of a copper-silver thin film in an

170

advanced metallization process. *Journal of Materials Science: Materials in Electronics* **2003**, *14* (2), 103–108. DOI: 10.1023/A:1021956703967.

(102) Menzel, S.; Strehle, S.; Wendrock, H.; Wetzig, K. Effect of Ag-alloying addition on the stress–temperature behavior of electroplated copper thin films. *Applied Surface Science* **2005**, *252* (1), 211–214. DOI: 10.1016/j.apsusc.2005.01.120.

(103) Sheng, H.W.; Wilde, G.; Ma, E. The competing crystalline and amorphous solid solutions in the Ag–Cu system. *Acta Materialia* **2002**, *50* (3), 475–488. DOI: 10.1016/S1359-6454(01)00374-3.

(104) Strehle, S.; Bartha, J. W.; Wetzig, K. Electrical properties of electroplated Cu(Ag) thin films. *Thin Solid Films* **2009**, *517* (11), 3320–3325. DOI: 10.1016/j.tsf.2008.11.146.

(105) Strehle, S.; Menzel, S.; Bartha, J. W.; Wetzig, K. Electroplating of Cu(Ag) thin films for interconnect applications. *Microelectronic Engineering* **2010**, *87* (2), 180–186. DOI: 10.1016/j.mee.2009.07.010.

(106) Strehle, S.; Menzel, S.; Wendrock, H.; Acker, J.; Gemming, T.; Wetzig, K. Thermo-mechanical behavior and microstructural evolution of electrochemically deposited low-alloyed Cu(Ag) thin films. *Microelectronic Engineering* **2004**, *76* (1), 205–211. DOI: 10.1016/j.mee.2004.07.055.

(107) Strehle, S.; Menzel, S.; Wendrock, H.; Acker, J.; Wetzig, K. Microstructural investigation of electrodeposited CuAg-thin films. *Microelectronic Engineering* **2003**, *70* (2), 506–511. DOI: 10.1016/S0167-9317(03)00422-2.

(108) Strehle, S.; Reiche, R.; Hoffmann, V.; Acker, J.; Gemming, T.; Wetzig, K. Sulfur incorporation in electroplated Cu(Ag) thin films. *Microchimica Acta* **2006**, *156* (1), 167–172. DOI: 10.1007/s00604-006-0607-9.

(109) Zhao, B.; Kim, H.; Shimogaki, Y. Effects of Ag Addition on the Resistivity, Texture and Surface Morphology of Cu Metallization. *Japanese Journal of Applied Physics* **2005**, *44* (No. 41), L1278-L1281. DOI: 10.1143/jjap.44.l1278.

(110) Hsieh, J.; Hung, S. *The Effect of Cu:Ag Atomic Ratio on the Properties of Sputtered Cu–Ag Alloy Thin Films*; Materials, Vol. 9, 2016. DOI: 10.3390/ma9110914.

(111) Roberto Bernasconi; James L. Hart; Andrew C. Lang; Luca Magagnin; Luca Nobili; Mitra L. Taheri. Structural properties of electrodeposited Cu-Ag alloys. *Electrochimica Acta* **2017**, *251*, 475–481. DOI: 10.1016/j.electacta.2017.08.097.

(112) Ko, Y. K.; Jang, J. H.; Lee, S.; Yang, H. J.; Lee, W. H.; Lee, J. G.; Reucroft, P. J. Thickness effect on grain growth and precipitate coarsening of a copper-silver thin film in an

advanced metallization process. *Journal of Materials Science: Materials in Electronics* **2003**, *14* (2), 103–108. DOI: 10.1023/A:1021956703967.

(113) C.C. Chama; J.J. Vlassak; W.O. Soboyejo. Stress evolution in copper–silver thin films during thermal-cycling. *Materials Science and Engineering: A* **2012**, *532*, 414–419. DOI: 10.1016/j.msea.2011.11.005.

(114) B.B. Straumal; V. Pontikis; A.R. Kilmametov; A.A. Mazilkin; S.V. Dobatkin; B. Baretzky. Competition between precipitation and dissolution in Cu–Ag alloys under high pressure torsion. *Acta Materialia* **2017**, *122*, 60–71. DOI: 10.1016/j.actamat.2016.09.024.

(115) Slater, J. C. Atomic Radii in Crystals. *The Journal of Chemical Physics* **1964**, *41* (10), 3199–3204. DOI: 10.1063/1.1725697.

(116) Pelleg, J. Strengthening Mechanisms. In *Mechanical Properties of Materials*; Springer Netherlands, 2013; pp 195–257. DOI: 10.1007/978-94-007-4342-7_4.

(117) Labusch, R. A Statistical Theory of Solid Solution Hardening. *physica status solidi (b)* **1970**, *41* (2), 659–669. DOI: 10.1002/pssb.19700410221.

(118) Almyras, G. A.; Matenoglou, G. M.; Komninou, P.; Kosmidis, C.; Patsalas, P.; Evangelakis, G. A. On the deposition mechanisms and the formation of glassy Cu–Zr thin films. *Journal of Applied Physics* **2010**, *107* (8), 84313. DOI: 10.1063/1.3366715.

(119) Barbee, T. W.; Walmsley, R. G.; Marshall, A. F.; Keith, D. L.; Stevenson, D. A. Phase separation in vapor quench synthesized noncrystalline copper zirconium alloys. *Applied Physics Letters* **1981**, *38* (3), 132–135. DOI: 10.1063/1.92275.

(120) C.J. Chen; J.C. Huang; H.S. Chou; Y.H. Lai; L.W. Chang; X.H. Du; J.P. Chu; T.G. Nieh. On the amorphous and nanocrystalline Zr–Cu and Zr–Ti co-sputtered thin films. *Journal of Alloys and Compounds* **2009**, *483* (1), 337–340. DOI: 10.1016/j.jallcom.2008.07.188.

(121) Li, Y.; Guo, Q.; Kalb, J. A.; Thompson, C. V. Matching Glass-Forming Ability with the Density of the Amorphous Phase. *Science* **2008**, *322* (5909), 1816–1819. DOI: 10.1126/science.1163062.

(122) Igarashi, Y.; Ito, T. Electromigration properties of copper-zirconium alloy interconnects. *Journal of Vacuum Science & Technology B: Microelectronics and Nanometer Structures Processing, Measurement, and Phenomena* **1998**, *16* (5), 2745–2750. DOI: 10.1116/1.590237.

(123) Nobuyoshi Awaya; Toshio Kobayashi. Effect of Thin-Film Texture and Zirconium Diffusion on Reliability against Electromigration in Chemical-Vapor-Deposited Copper

Interconnects. *Japanese Journal of Applied Physics* **1998**, *37* (Part 1, No. 3B), 1156–1161. DOI: 10.1143/jjap.37.1156.

(124) P. Zhang; J.Y. Zhang; J. Li; G. Liu; K. Wu; Y.Q. Wang; J. Sun. Microstructural evolution, mechanical properties and deformation mechanisms of nanocrystalline Cu thin films alloyed with Zr. *Acta Materialia* **2014**, *76*, 221–237. DOI: 10.1016/j.actamat.2014.04.041.

(125) J.T. Zhao; J.Y. Zhang; L.F. Cao; Y.Q. Wang; P. Zhang; K. Wu; G. Liu; J. Sun. Zr alloying effect on the microstructure evolution and plastic deformation of nanostructured Cu thin films. *Acta Materialia* **2017**, *132*, 550–564. DOI: 10.1016/j.actamat.2017.05.007.

(126) A. Kauffmann; D. Geissler; J. Freudenberger. Thermal stability of electrical and mechanical properties of cryo-drawn Cu and CuZr wires. *Materials Science and Engineering: A* **2016**, *651*, 567–573. DOI: 10.1016/j.msea.2015.10.119.

(127) Hisamichi Kimura; Hiroaki Matsumoto; Akihisa Inoue. Effect of Cold Drawing on Electrical and Mechanical Properties of Cu-5 at% Zr Alloy. *MATERIALS TRANSACTIONS* **2007**, *advpub*, 708270179. DOI: 10.2320/matertrans.MRA2007074.

(128) Hisashi Suzuki; Motohiro Kanno. Effect of a Small Addition of Transition Elements on Annealing Characteristics of Cold-Worked Pure Copper. *Transactions of the Japan Institute of Metals* **1985**, *26* (1), 69–77. DOI: 10.2320/matertrans1960.26.69.

(129) Naokuni Muramatsu; Takashi Goto. Microstructures and Mechanical and Electrical Properties of Hypoeutectic Cu-1, C-3 and Cu-5 at%Zr Alloy Wires Preprocessed by Spark Plasma Sintering. *MATERIALS TRANSACTIONS* **2013**, *54* (7), 1213–1219. DOI: 10.2320/matertrans.M2013011.

(130) R. Busch; E.D. McClanahan. Copper-based materials formed by high rate sputtering. *Thin Solid Films* **1977**, *47* (3), 291–306. DOI: 10.1016/0040-6090(77)90044-X.

(131) Villars, Pierre and Okamoto, Hiroaki. *Cu-Zr Binary Phase Diagram 0-100 at.% Zr: Datasheet from "PAULING FILE Multinaries Edition - 2012" in SpringerMaterials (https://materials.springer.com/isp/phase-diagram/docs/c_0101118)*; Springer-Verlag Berlin Heidelberg & Material Phases Data System (MPDS), Switzerland & National Institute for Materials Science (NIMS), Japan. https://materials.springer.com/isp/phase-diagram/docs/c_0101118.

(132) Mark A. Atwater; Ronald O. Scattergood; Carl C. Koch. The stabilization of nanocrystalline copper by zirconium. *Materials Science and Engineering: A* **2013**, *559*, 250–256. DOI: 10.1016/j.msea.2012.08.092.

(133) J.J. Niu; P. Zhang; R.H. Wang; J.Y. Zhang; G. Liu; G.J. Zhang; J. Sun. Formation of multiple twins and their strengthening effect in nanocrystalline Cu/Zr multilayer films. *Materials Science and Engineering: A* **2012**, *539*, 68–73. DOI: 10.1016/j.msea.2012.01.046.

(134) Matteo Seita; Christina M. Pecnik; Stephan Frank; Ralph Spolenak. Direct evidence for stress-induced texture evolution and grain growth of silver thin films upon thermal treatment and self-ion bombardment. *Acta Materialia* **2010**, *58* (19), 6513–6525. DOI: 10.1016/j.actamat.2010.08.014.

Lebenslauf

Persönliche Daten

Name	M.Sc. Tobias Oellers
	geb. 13. März 1985 in Schwerte

Ausbildung

06/2014 – 07/2019	**Wissenschaftlicher Mitarbeiter** und **Doktorand,** Lehrstuhl Werkstoffe der Mikrotechnik, Ruhr-Universität Bochum
05/2013 – 05/2014	**Master of Science,** Maschinenbau, Ruhr-Universität Bochum
04/2009 – 05/2013	**Bachelor of Science,** Maschinenbau, Ruhr-Universität Bochum
10/2005 – 04/2009	**Grundstudium,** Diplom Maschinenbau, TU Dortmund
1995 – 2004	**Abitur,** Phoenix Gymnasium, Dortmund

Publications

- J. Chakraborty, **T. Oellers**, R. Raghavan, A. Ludwig, G. Dehm, *Microstructure and residual stress evolution in nanocrystalline Cu-Zr thin films*, (**2022**), 896, 162799
  10.1016/j.jallcom.2021.162799

- V.G. Arigela, **T. Oellers**, A. Ludwig, C. Kirchlechner, G. Dehm, *Development of a high-temperature micromechanics stage with a novel temperature measurement approach*, Rev. Sci. Instrum. (**2019**), 90, 073904
  10.1063/1.5086261

- S. Geiger, O. Kasian, M. Ledendecker, E. Pizzotiol, A.M. Mingers, W.T. Fu, O. Diaz-Morales, Z. Li, **T. Oellers**, L. Fruchtner, A. Ludwig, K.J.J. Mayrhofer, Marc T.M. Koper, S. Cherevko, *The stability number as a metric for electrocatalyst stability benchmarking*, Nat. Catal. (**2018**), 1, 508-515
  10.1038/s41929-018-0085-6

- **T. Oellers**, R. Raghavan, J. Chakraborty, C. Kirchlechner, A. Kostka, C.H. Liebscher, G. Dehm, A. Ludwig, *Microstructure and mechanical properties in the thin film system Cu-Zr*, Thin Solid Films (**2018**), 645, 193-202
  10.1016/j.tsf.2017.10.030

- **T. Oellers**, D. König, A. Kostka. S. Xie, J. Brugger, A. Ludwig, *Shape Memory Micro- and Nanowire Libraries for the High-Throughput Investigation of Scaling Effects*, ACS Comb. Sci. (**2017**), 19 (9), 574-584
  10.1021/acscombsci.7b00065

- H. Zhang, **T. Oellers**, W. Feng, T. Abdulazim, E.N. Saw, A. Ludwig, P.A. Levkin, N. Plumere, *High-Density Droplet Microarray for Individually Addressable Electrochemical Cells*, Anal. Chem. (**2017**), 89 (11), 5832-5839
  10.1021/acs.analchem.7b00008